2019

Topographic reconstructions of the Variscan Belt of Western Europe through the study of fossil hydrothermal systems

Dusseaux, Camille

UNIVERSITY OF
PLYMOUTH

TOPOGRAPHIC RECONSTRUCTIONS OF THE VARISCAN BELT OF WESTERN EUROPE THROUGH THE STUDY OF FOSSIL HYDROTHERMAL SYSTEMS

by

CAMILLE DUSSÉAUX

A thesis submitted to the University of Plymouth

in partial fulfilment for the degree of

DOCTOR OF PHILOSOPHY

School of Geography, Earth and Environmental Sciences

April 2019

Signed:

Dated: 7th August 2019

TOPOGRAPHIC RECONSTRUCTIONS OF THE VARISCAN BELT OF WESTERN EUROPE THROUGH THE STUDY OF FOSSIL HYDROTHERMAL SYSTEMS

Camille Dusséaux

This thesis presents the first stable isotope quantification of paleoaltimetry for the Variscan Belt of Western Europe that integrates late-Carboniferous hydrogen isotope ratios of meteoric water in the internal zones in the Armorican Massif (AM) and the French Massif Central (FMC) with age-equivalent precipitation records in the foreland Bourbon l'Archambault basin (BA) and the Montagne Noire (MN).

Combined microstructural, hydrogen and oxygen stable isotope, thermometry and geochronology data allow the calculation of the isotopic composition of meteoric water in the internal zones of the orogen where surface-derived fluids infiltrated the ductile segment of the Quiberon, Piriac (AM) and Felletin (FMC) detachment shear zones during high temperature deformation and post-orogenic extension.

When compared to age-equivalent isotopic composition of surface-derived fluids based on freshwater shark remains found in the BA basin near sea level, the composition of meteoric water obtained from synkinematic muscovite in the detachment footwalls are consistent with a minimum elevation difference of 2500 ± 900 m in the AM and 3300 ± 1000 m for the FMC.

This study suggests that the internal zones (AM and FMC) of the Variscan Belt of Western Europe were characterized by a mean elevation typical for medium-sized mountain belts. These results are in good agreement with the view of the Variscan belt as a hot orogen characterized by abundant syntectonic crustal melting and high-grade metamorphism that profoundly affected its tectonic evolution.

RECONSTRUCTIONS TOPOGRAPHIQUES DE LA CHAINE VARISQUE DE L'EUROPE DE L'OUEST PAR L'ETUDE DES SYSTEMES HYDROTHERMAUX FOSSILES

Camille Dusséaux

Cette thèse présente la première quantification de la paléoaltitude de la Chaîne Varisque de l'Europe de l'Ouest par la méthode des isotopes stables, qui intègre la composition isotopique en hydrogène des eaux météoriques dans le Massif Armorican (MA) et le Massif Central (MC) avec des enregistrements contemporains provenant du bassin d'avant-pays de Bourbon l'Archambault (BA) et de la Montagne Noire (MN).

La combinaison des données microstructurales, des isotopes stables de l'hydrogène et de l'oxygène, thermométriques et géochronologiques permet de calculer la composition isotopique des eaux météoriques dans les zones internes, où des eaux de surface ont infiltré le segment ductile des zones de détachement de Piriac, Quiberon (AM) et Felletin (MC) pendant l'extension post-orogénique.

Comparée à des enregistrements isotopiques d'eaux de surface d'âge équivalent basés sur des fossiles de requins d'eau douce du bassin de BA, la composition des eaux météoriques obtenue à partir des muscovites dans les murs des détachements est cohérente avec une altitude moyenne minimale de 2500 ± 900 m dans le MA et 3300 ± 1000 m dans le MC.

Cette étude suggère donc que les zones internes de la Chaîne Varisque de l'Europe de l'Ouest ont atteint une altitude plutôt moyenne. Ces résultats sont en accord avec une vision de la Chaîne Varisque comme un orogène chaud caractérisé par une fusion partielle syntectonique abondante et un métamorphisme de haut grade qui ont profondément affecté son évolution tectonique.

ACKNOWLEDGMENTS

To start with, I would like to thank my supervisor Aude Gébelin. She has given me a humongous amount of her time, always showing a lot of passion for the beauty of geology and the magnificence of mountain ranges. It is hard to summarize all the professional and personal skills I gained thanks to her. Alors… Mille fois merci! Pour avoir pensé ce projet formidable et m'avoir aidé à le mener à bien. Désolée pour les tempêtes en Bretagne Sud, la neige dans le Limousin et la canicule dans la Montagne Noire… Merci pour ces trois ans, ainsi que les années à venir !

Many thanks to my second supervisor, Stephen Grimes, for his support and understanding throughout the project. Thank you for the great scientific conversations at the university, sometimes at the JSV, and for correcting my poor English until the last day. I promise not to chase you down to your allotment for further corrections!

Merci à Phillippe Boulvais, who is certainly one of the best guide to discover the Armorican Massif with amazing enthusiasm and humour. I am very thankful for the support he has offered along this project. Merci à toute l'équipe Géosciences Rennes (Yannick, Marc, Nathan, Thibault, Rémi) pour les bons moments sur le terrain et les bons papiers à venir! Merci à Gilles Ruffet pour les magnifiques âges plateaux réalisés sur les muscovites.

I am grateful to Andreas Mulch who welcomed me in Frankfurt and has helped me all along the project. Many thanks to Ulricht Treffert, Jens Fiebig. Maud and Katharina for the laboratory support and the hundreds of hydrogen isotope measurements in Frankfurt, without which this study would not have been possible.

I cannot acknowledge enough Michel Dubois for his endless support throughout my studies. He was kind enough to have me back at the University of Lille for my PhD and taught me about the wonderful tiny world of fluid inclusions. Apart from his academic support, I would like to thank him for his friendship and the good times we have had sharing our passion for rock(s), music and beer.

Many thanks to Veronique Gardien, for having shared the field in the Armorican Massif under the storm and carrying on the study by measuring the isotope composition of fluid inclusions in Lyon.

Thanks to Catherine Mottram and Glen for hosting me and sharing the excitement of dating rocks at the University of Portsmouth.

Thanks to Christophe Nevado, Sylvie Reigner and Cédric Demeurie who made all sorts of sections, and sometimes in emergency. Many thanks to Fabrice Barou for the EBSD support at the University of Montpellier. Merci à Bernard Boyer de l'Université de Montpellier et Séverine Bellayer de l'Université de Lille pour m'avoir aidé à utiliser la microsonde SX100. Thanks to Benita Putlitz for oxygen isotope measurement at the University of Lausanne. Many thanks to Laurent Beccaletto for providing advice, documents over the years and his expertise of the French Variscan geology.

Thanks to Ian King, Jodie Fischer and Rob Hall for the lab support and happy mood. I also want to thank Mark Davies that shared scientific advice and good music (Comfort Eagle by Cake is one of the best album in the world indeed) in the lab as well as at the Maker.

I am very grateful to Aude, Colin, Arjan, Uwe, Mathew, Chris, Luca and to all the amazing lecturers of Plymouth that I have had the pleasure to assist during almost 4 years of demonstrating during the practicals. Subsequently, I would like to thank all Plymouth undergraduate students that I have bothered with 3D drawings and stupid jokes, coupled with English misunderstandings. I hope that they still enjoyed the practicals and the field as much as I did. Seriously, demonstrating was one of the best parts of my degree in Plymouth so thanks to you all.

I would also like to thank Cesar Witt and Alain Chauvet, my BSc and MSc supervisors as they have been a great support during all of my studies. It is always a pleasure to meet with you in Lille or Montpellier, and I hope that we will collaborate in future projects (and finish on-going projects!).

Thanks to all the Plymouth PhD crew, met by accident but being friends by love. To Wycliff who will always make my heart sing, Madeleine who made me cry of laugh, Louise and her explosive and caring temperament, Giulia my structural-metamorphism buddy and drama queen, Francesca (thanks for the EBSD!), Matt (Nemo Magneto), Hoayda, Tom, Grant & Sarah, Killian, Bugra, Josh and Jesse. A special mention goes to Anne who visited a few months but definitely left her trace in Plymouth. I would like to thank Timothy Webster and Romain Richaud who helped during the project through lab-based internships and became dear friends of mine (for sure!).

To all 'non-academic' friends from Plymouth who helped me get away from ancient times to set foot in the present and share music, food, hikes and road trips: Vanessa, Alba, Phil, Adriana, Xiquito as well as the Cave crew. Thanks also to Dan and Mike from Mad Dog for the Sundays spent playing music on Dartmoor.

Of course, je remercie Max, qui me suit dans mes pérégrinations et m'offre plus que tout le support dont je puisse rêver. J'ai conscience d'avoir beaucoup de chance.

Merci à mes parents et mon frère Tom. C'est certainement ma famille de troglodytes, ouverte d'esprit et encourageante qui a été mon fil d'Ariane. J'étais heureuse que vous puissiez assister à la RST, à Lille et en ~~ch'timi~~ français, à défaut de pouvoir assister à ma soutenance privée de l'autre côté de la Manche !

Merci en général à ma famille adorée ! Ça en fait du monde, il me faudrait une thèse entière pour tous les citer. J'ai une pensée émue pour mes grands-parents, et spécialement Pépé à qui je pense beaucoup en griffonnant tous ces schémas et ces jolies cartes. Je pense également à mon arrière-grand-père Jean, qui m'ouvert les yeux sur l'immensité des sciences et de l'univers.

Merci à Camille, Matilde et Lucie qui ont toujours été là et qui prouvent que l'amitié ne se tarit pas avec la distance, apparemment !

To finish, I would like thank most warmly the team that examined my thesis on the 21st of June 2019: Pr. Richard Law, Dr. Arjan Dijkstra and Dr Ruth Weaver. Thanks to you, my viva was a very pleasant and thrilling discussion! Thank you very much.

AUTHOR'S DECLARATION

At no time during the registration for the degree of Doctor of Philosophy has the author been registered for any other University award without prior agreement of the Doctoral College Quality Sub-Committee.

Work submitted for this research degree at the University of Plymouth has not formed part of any other degree either at the University of Plymouth or at another establishment.

This study was financed with the aid of the University of Plymouth. The author also acknowledges the analytical help of the University of Portsmouth (UK), Goethe Universität Germany), and the Universités de Rennes 1, Montpellier and Lille (France), as well as the financial support of the Plymouth Doctoral Training Centre and the Société Géologique de France to attend conferences.

A programme of advanced study was undertaken, which included Research Skills and Research Methods modules. Relevant scientific seminars and conferences were regularly attended at which work was often presented; relevant training and workshops were also attended; several papers were prepared for publication.

The following external institutions were visited for consultation purposes:

- Joint Goethe university/BiK-F, Frankfurt, Germany (Hydrogen isotope geochemistry)
- University of Montpellier, France (microprobe and EBSD)
- University of Rennes 1, France (fieldwork and sample preparation)
- University of Lille 1, France (Fluid inclusions microthermometry and microprobe)
- University of Portsmouth, UK (U-Th/Pb La-ICP-MS on monazite)

Peer-reviewed publications:

Dusséaux C., Gébelin A., Boulvais P., Gardien V., Grimes S., Mulch A. (in press) *Meteoric fluid-rock interaction in Variscan shear zones*. Terra Nova. DOI: https://doi.org/10.1111/ter.12392

Publications in preparation:

Dusséaux C., Gébelin A., Grimes S., Boulvais, P., Ruffet, G., Poujol, M., Branquet, Y., Cogné, N., Mottram C., Barou, F., Mulch A. (in prep.) *Timing of fluid-rock infiltration and microstructure development in the Quiberon detachment zone, Armorican Massif, France*. Tectonics

Published abstracts:

Dusséaux C., Gébelin A., Boulvais P., Gardien V., Dubois M., Ruffet G., Poujol M., Branquet Y., Grimes S., Mulch A. (2019) Characterisation of meteoric water infiltration in Variscan shear zones. Goldschmidt abstracts – session 03g Geochemical tracers of fluids in crustal systems, Barcelona, Spain (oral)

Boulvais P., Poujol M., Branquet Y., Cogné N., Duretz T., Ballouard C., Tartèse R., Dusséaux C., Gébelin A. (2019) The uranium metallogenic system in the South Armorican detachment zones, Variscan belt, France : geology, tracing in space and time, numerical modelling. 15th Biennial Meeting SGA 2019, Glasgow, Scotland

Boulvais P., Branquet Y., Duretz T., Poujol M., Ballouard C., Tartèse R., Cogné N., Ruffet G., Dusséaux C., Gébelin A. (2018) *Mobilisation et dépôt d'uranium dans les structures extensives varisques en Bretagne Sud : "set-up" de la modélisation numérique Mon-U (Projet NEEDS)*, Journées Uranium, Paris, France.

Dusséaux C., Gébelin A., Boulvais P., Dubois M., Ruffet G., Poujol M., Branquet Y., Barou F., Mulch A. (2018) *Late-Carboniferous infiltration of meteoric water in Variscan shear zones*, Réunion des Sciences de la Terre (RST), Lille, France (oral)

Dusséaux C. (2018) *Study of hydrothermal systems and its use as a paleoaltimeter.* Earth sciences research seminar, Plymouth, UK (oral - 1h)

Dusséaux C., Gébelin A., Boulvais P., Dubois M., Gardien V., Grimes S., Mulch A. (2018) *Meteoric fluid-rock interaction in Variscan ductile shear zones.* Tectonic and Metamorphic Studies Groups (TSG-MSG) Joint Conference, Fluid flow in the lithosphere, Plymouth, UK (poster)

Dusséaux C., Gébelin A., Boulvais P., Dubois M., Gardien V., Grimes S., Mulch A. (2017) *Deep penetration of meteoric water in Variscan ductile shear zones.* Goldschmidt abstracts - Crustal differentiation and specialization - Aqueous Fluids in the Crust, Paris, France (oral)

Dusséaux C., Gébelin A., Boulvais P., Gardien V., Mulch A., Grimes S., Dubois M. (2016) *How high was the Armorican Massif 300 million years ago?* Earth Sciences Research Conference, Plymouth, UK (oral - 1h)

Boulvais, P., Tartèse, R., Poujol, M., Boiron, M.-C., Ruffet, G., Branquet, Y., Gébelin, A., Dusséaux, C. (2016) *Exhumation des migmatites et infiltration d'eaux météoriques : le domaine hercynien sud-armoricain.* Réunion des Sciences de la terre (RST), Caen, France.

Boulvais, P., Tartèse, R., Poujol, M., Boiron, M.-C., Ruffet, G., Branquet, Y., Gébelin, A., Dusséaux, C. (2016) *Fluids in the South Armorican Shear Zone, France.* Goldschmidt abstracts - Integrated Fault Zone Investigations - Constraining Timing of Deformation Zones, Yokohama, Japan.

Conferences attended:

- 08/2019 - Goldschmidt Conference (Barcelona, Spain) – Oral presentation
- 11/2018 - Réunion des Sciences de la Terre (Lille, France) – Oral presentation
- 01/2018 - Tectonic and Metamorphic Studies Groups Joint Conference (Plymouth, UK) – Poster presentation
- 08/2017 - Goldschmidt Conference (Paris, France) – Oral presentation and part of the organizing team for the fieldtrip in the Armorican Massif
- 11/2016 CRES Research Conference (Plymouth, UK) – Oral presentation and part of the organizing team of the conference

- 09/2016 - 7th International Conference on UNESCO Global Geoparks (Torbay, UK) - Fieldtrip guide in the English Riviera UNESCO Global Geopark
- 06/2016 - The Variscan belt: correlations and plate dynamics - Special meeting of the French & Spanish Geological Societies (Galicia, Spain) – attendance only

Word count of main body of thesis: 49,423 words.

Signed:

Date: 7th August 2019

CONTENTS

FIGURES

TABLES

INTRODUCTION

The Variscan belt of Western Europe was built as a result of a Himalayan-type continental collision between two main lithospheric plates, Laurussia (Laurentia-Baltica) to the north and Gondwana to the south, which led to crustal nappes stacking and to the formation of foreland basins during the Carboniferous (e.g. Matte, 2001). This belt is now completely eroded but displays similarities with the Tibet-Himalaya orogen in its tectonic style and geochemistry of partially molten rocks exhumed in the footwall of detachment faults, leading to the suggestion that its thickened hinterland regions could have represented a topographic high similar to the Himalaya during the Carboniferous (e.g. Mattauer, 1986, Dörr and Zulauf, 2010). However, recent studies point to a subdued topography due to coeval orogenic-parallel extension and low-viscosity crustal material that would have counterbalanced crustal thickening and uplift (e.g. Franke, 2014). Therefore, the paleoaltitude of the Variscan Belt is at the core of considerable debate and no paleoaltimetry estimates have been acquired at this time. This project addresses this outstanding, first-order question by combining newly developed quantitative methods in geochemistry with classical geological techniques to decipher the long-term topographic evolution of the Variscan belt of Western Europe using stable isotope paleoaltimetry.

Obtaining paleoaltimetry estimates is important to climate modellers and scientists interested in paleoclimate because the topography of mountain ranges controls the atmospheric circulation (e.g. Seager et al., 2002). The best example of solid Earth affecting climate is the Himalaya-Tibet orogen, for which a direct link between the growth of topography and the intensification of the Asian monsoon has been recognized (e.g. Molnar and England, 1990; Boos and Kuang, 2010; Wu et al., 2012).

Palaeontologists and biologists that aim at correlating the evolution of species with geological landscapes are also interested in such studies (e.g. Hoorn et al., 2010; Favre et al., 2014; Mulch, 2016). Finally, reconstructing the topography of ancient orogens is of great interest to the geosciences community because it provides information on the deformational and geodynamic processes that occur at depth as the elevation of the Earth's surface is closely related to the processes that govern the internal part of orogens (e.g. Braun, 2010).

Stable isotope paleoaltimetry uses the oxygen ($\delta^{18}O$) and hydrogen (δD) isotope composition of meteoric water that scales with elevation in a predictable fashion on the windward side of a mountain range (~-2.8 ‰ in $\delta^{18}O$ or ~-22 ‰ in δD per km; Poage and Chamberlain, 2001). This is due to the Rayleigh distillation of heavy isotopes (^{18}O or D) through condensation and precipitation as air masses that rise across a mountain range cool adiabatically during ascent. Quantifying the temporal evolution of topography is challenging in eroded orogens because it is difficult to find proxies in the geological archives that have recorded the isotopic composition of ancient rainfall. The most commonly used geological materials, such as lacustrine carbonates, are not necessarily available and/or unaltered by diagenetic processes in eroded orogens. However, hydrous silicates that crystallize at depth during deformation-related fluid flow have been shown to be reliable proxies of such meteoric fluids (e.g. Mulch et al., 2004, 2007; Gébelin et al., 2011, 2017). Indeed, the low hydrogen (δD) and oxygen ($\delta^{18}O$) stable isotope values of synkinematic hydrous minerals have allowed researchers to document the infiltration of meteoric fluids in the footwall of detachment zones of metamorphic core complexes such as those in the North American Cordillera (e.g. Fricke et al., 1992; Losh, 1997; Mulch et al., 2004, 2006; Holk and Taylor, 2007; Gébelin et al., 2011, 2012,

2015, 2017; Gottardi et al., 2011; Methner et al., 2015; Quilichini et al., 2015, 2016), in the European Central Alps (Campani et al., 2012), in the Menderes Massif of Turkey (Hetzel et al., 2013) and the South Tibetan Detachment (Gébelin et al., 2013, 2017). Such minerals, even though (re)crystallised at significant depth, can be used as paleoelevation proxies if they can be temporally and kinematically linked to the shear zones evolution (e.g. Mulch et al., 2004; Campani et al., 2012; Gébelin et al., 2012, 2013).

The present study aims at quantifying the late-Carboniferous paleoelevation of the Variscan Belt of Western Europe by studying fossil hydrothermal systems that have recorded the isotope composition of Variscan surface-derived fluids. This work is subdivided into five chapters. The first chapter explains the aim of the study by giving an overview of the Variscan Belt of Western Europe geological framework and the associated debate on its paleoelevation. This introduction is followed by the principles and limitations of the stable isotope paleoaltimetry method, and ends with the main objectives of this study.

The second chapter presents the different methods used to achieve the study's goals. To recover the isotopic composition of ancient precipitation, the hydrogen isotope (δD) ratio of hydrous silicates that crystallized during high temperature deformation in the footwall of detachment zones of the internal zones is measured. In parallel, a similar study is conducted on fluid inclusions in quartz grains derived from identical mylonitic samples. To determine the temperature of isotopic exchange between the fluid and the minerals that is essential to calculate the isotope composition of the fluid present during deformation, different thermometry techniques have been used. A detailed microstructural study (including EBSD) is conducted on representative samples to estimate the temperature of deformation, but also to characterize and

understand the deformational and isotope exchange histories at the grain-scale. $^{40}Ar/^{39}Ar$ thermochronology on neocrystallized hydrous minerals allow us to constrain the timing and duration of recrystallization and fluid flow.

The main results of this study are presented in Chapters III and IV. Chapter III depicts the work conducted in the southern Armorican domain. Part A presents the hydrogen isotope ratios of muscovite from different shear zones. Following the identification of ancient precipitation in the Armorican detachments, part B presents a detailed study that characterises the thermomechanical context of fluid-rock interaction as well as the timing of meteoric fluid infiltration in the Quiberon detachment footwall. Part C presents the results obtained on fluid inclusions in the Armorican detachment footwalls. A similar study conducted in ductile shear zones of the western part of the French Massif Central is presented in Chapter IV.

Finally, Chapter V aims at quantifying the paleoelevation of the Variscan Belt of Western Europe during the Late Carboniferous. The hydrogen isotope record of precipitation in the hinterland is referenced to age-equivalent proxies that have preserved the isotope composition of rainfall near sea level. Two different proxies for meteoric water are presented for the foreland areas: teeth and spines from fresh-water sharks in foreland basins (Fischer et al., 2013) and hydrous silicates from the Espinouse detachment in the Montagne Noire. The isotope lapse rate between the isotope composition of meteoric water and elevation, and the difference in δD and $\delta^{18}O$ values of meteoric water in the internal and external zones allow us to get a first evaluation of the paleotopography of this part of the Variscan hinterland, consistent with a medium mean elevation, in agreement with a “hot orogen” model involving extensional thinning and flow of partially molten rocks.

I. THE VARISCAN BELT OF WESTERN EUROPE AND THE CONTROVERSY ON ITS TOPOGRAPHY

A. The Variscan Belt of Western Europe

1. The Variscan Belt

The convergence and subsequent collision of two main continents (Laurussia to the North and Gondwana to the South) led to the amalgamation of the Pangea super-continent between ~500 and 250 Ma (**Fig. I-1**). The collision was responsible for the formation of collisional orogen systems, including the Variscan belt of Western Europe (e.g. Matte, 2001; Kroner and Romer, 2013).

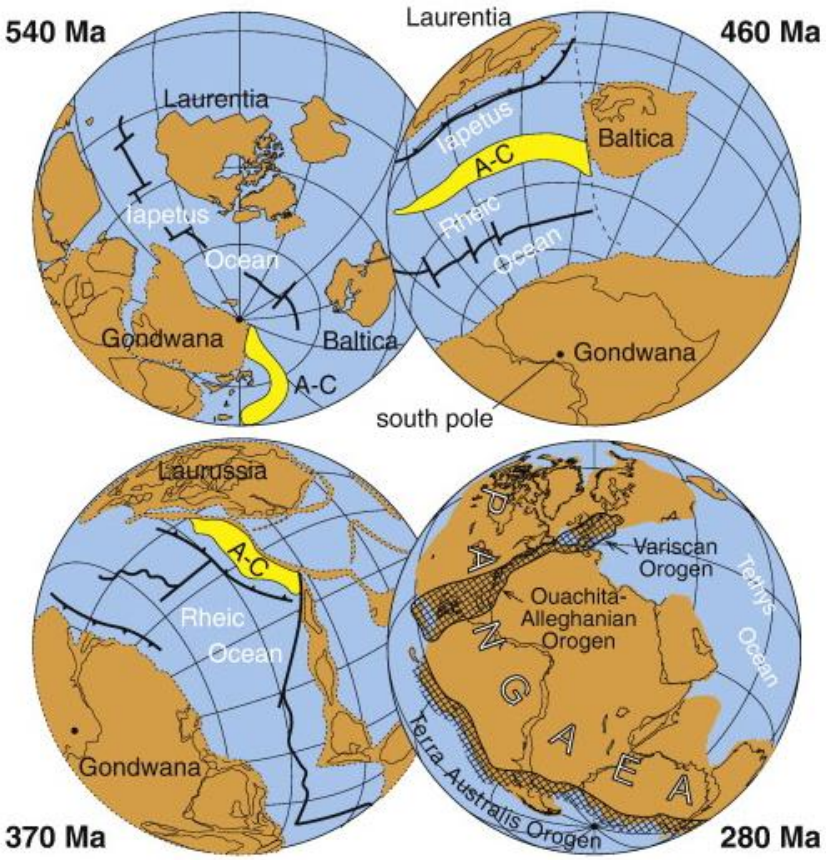

Figure I-1 Palaeozoic reconstructions ot the formation of the Variscan Belt.
- 540 Ma: formation of the Iapetus ocean between Laurentia and Gondwana
- 460 Ma: formation of the Rheic ocean that separates Avalonia–Carolinia (A–C) from Gondwana
- 370 Ma: Collision of Laurentia, Baltica and Avalonia–Carolina that forms Laurussia
- 280 Ma: Closure of the Rheic Ocean that forms Pangaea and both Variscan and Ouachita-Alleghanian orogens.
A-C: Avalonia-Carolina.
Figure from Nance et al., 2010; modified from Scotese, 1997; Cocks and Torsvik, 2002; Stampfli and Borel, 2002; Murphy et al., 2006; Cawood and Buchan, 2007.

In Western Europe, the Variscan terranes can be divided into 3 simplified tectonic and metamorphic zones: (1) a south-verging collisional wedge to the south and (2) a north-verging one to the north, and (3) the internal zones of the belt composed of high-grade metamorphic rocks (**Fig. I-2**). The south and north-verging collisional wedges gave rise to an E-W trending fan-shaped orogen (see cross-sections on **Fig. I-2**). The European Variscan internal zones are recognized in the Iberian Massif in Spain (Galicia and the Pyrenees), in the Armorican Massif in France (southern Brittany), in the French Massif Central, in Corsica, and in the Bohemian Massif (Germany). The North Variscan Front can be observed in the UK (SW Ireland, SW England and Wales) and in the north of France (N Brittany, Ardennes), and the South Variscan Front can be seen in Southern France (Montagne Noire, Vosges and Corsica), in Spain (Galicia, Pyrénées) and in Italy (Sardinia) (**Fig. I-2**).

Two main areas were targeted for this study: the Armorican Massif and the French Massif Central, which are part of the internal zones (**Fig. I-2**). These two Massifs have been extensively studied since the 19th century (e.g. Suess, 1887). However, the recent development of sophisticated methods have allowed researchers to get a precise idea of their nature (structural geology, petrology, palaeontology, stratigraphy, sedimentology, as well geochemistry and geochronology) and 3D geometry (geological mapping, airborne geophysics, seismic imagery).

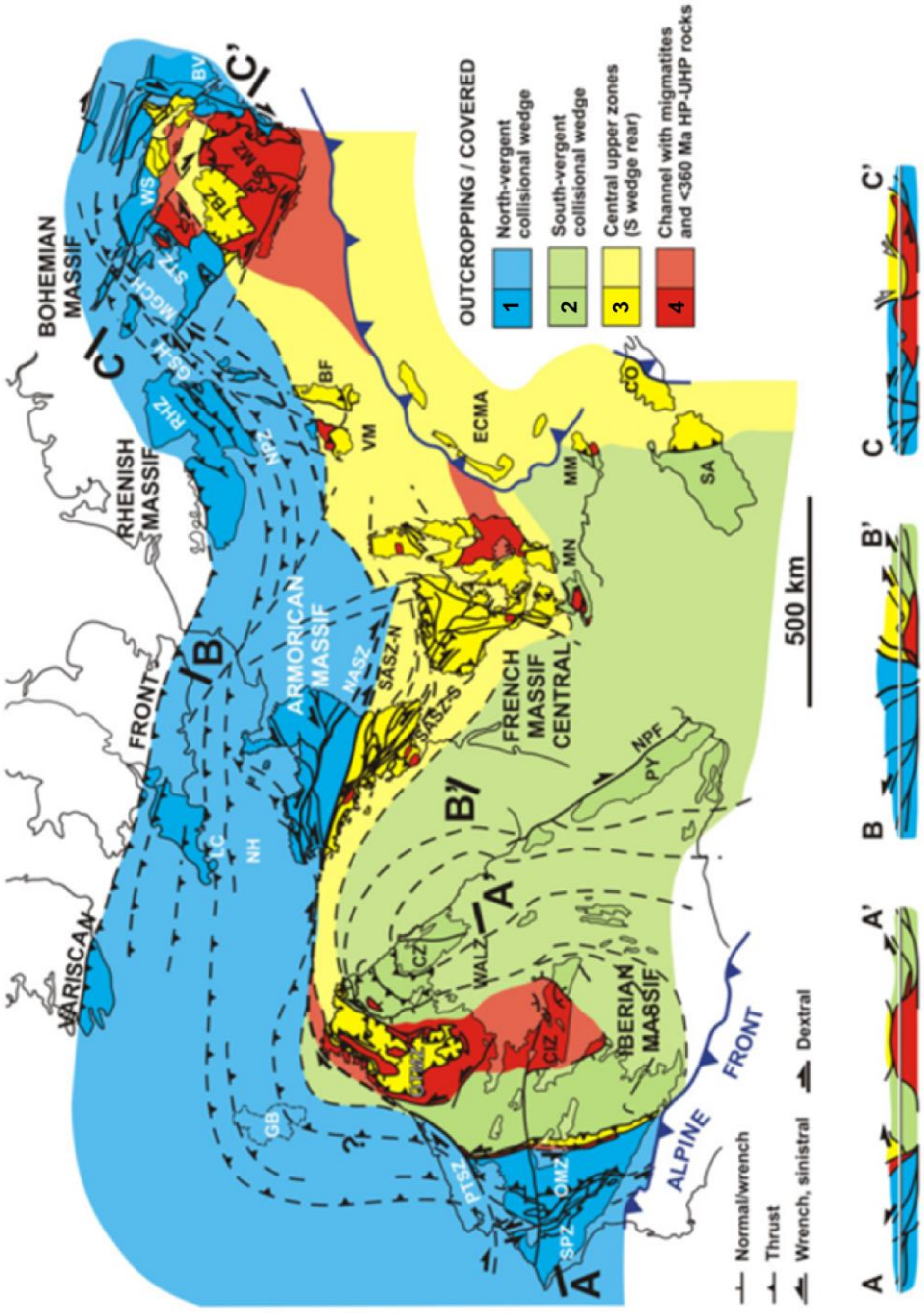

Figure I-2: Geodynamic sketch dividing the Variscan Orogen in Europe in four main domains: (1) north and (2) south opposite foreland wedges, (2) plateau-like upper structurally central regions of the hinterland and (4) underlying high grade orogenic crust. BF, Black Forest; BV, Brunovistulian; CCSZ, Córdoba-Coimbra Shear Zone; CIZ, Central Iberian Zone;CO, Corsica; CZ, Cantabrian Zone; ECMA, External Crystalline Massifs of the Alps; GB, Galicia Banks; GS-H: Giessen-Hartz; GTMZ, Galicia Trás-os-Montes Zone; LC, Lizard Complex; MGCH, Mid German Crystalline High; MN, Montagne Noire; MM, Maures Massif; MZ, Moldanubian Zone; NASZ, North Armorican Shear Zone; NH, Normannian High; NPF, North Pyrenean Fault; NPZ, Northern Phyllite Zone; OMZ, Ossa-Morena Zone; PTSZ, Porto-Tomar Shear Zone; PY, Pyrenees; RHZ, Rhenohercynian Zone; SA, Sardinia; SASZ, South-Armorican Shear Zone; SPZ, South Portuguese Zone; STZ, Saxo-Thuringian Zone; TBZ, Teplá-Barrandian Zone; VM, Vosges Massif; WALZ, West Asturian- Leonese Zone; and WS, West Sudetes (Rubio Pascual et al., 2016).

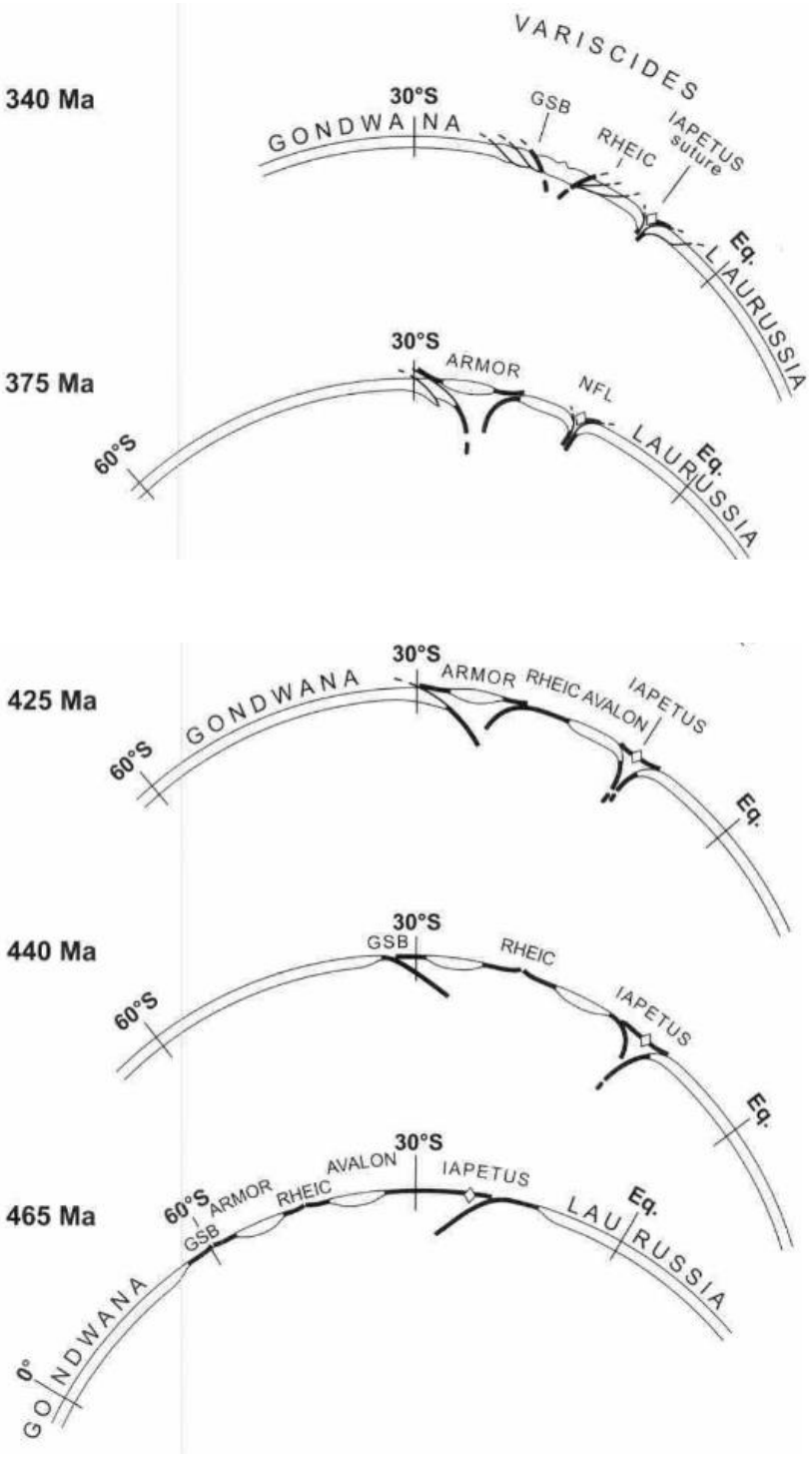

Figure I-3: Construction of the Variscan belt through progressive closures of oceanic basins. GSB: Galicia-Southern Brittany ocean and suture (Matte, 2001).

Two main models have been proposed to explain the tectonic evolution of the Variscan Belt of Western Europe. A monocyclic model proposed by Matte (1986b, 2001) and Lardeaux et al. (2001) which highlights a continuous convergence between Laurentia and Gondwana from the Silurian to the Early Carboniferous. This model is characterized by the progressive closure of two main oceanic basins, the Rheic Ocean to the north and the Galicia-Massif Central Ocean to the south of the belt, by intraoceanic subduction of opposite vergence, followed by obduction and intracontinental lithospheric subduction (**Fig. I-3**). It explains the progressive crustal thickening by nappe stacking and migration of the deformation through time from the sutures toward the external parts of the Variscan belt.

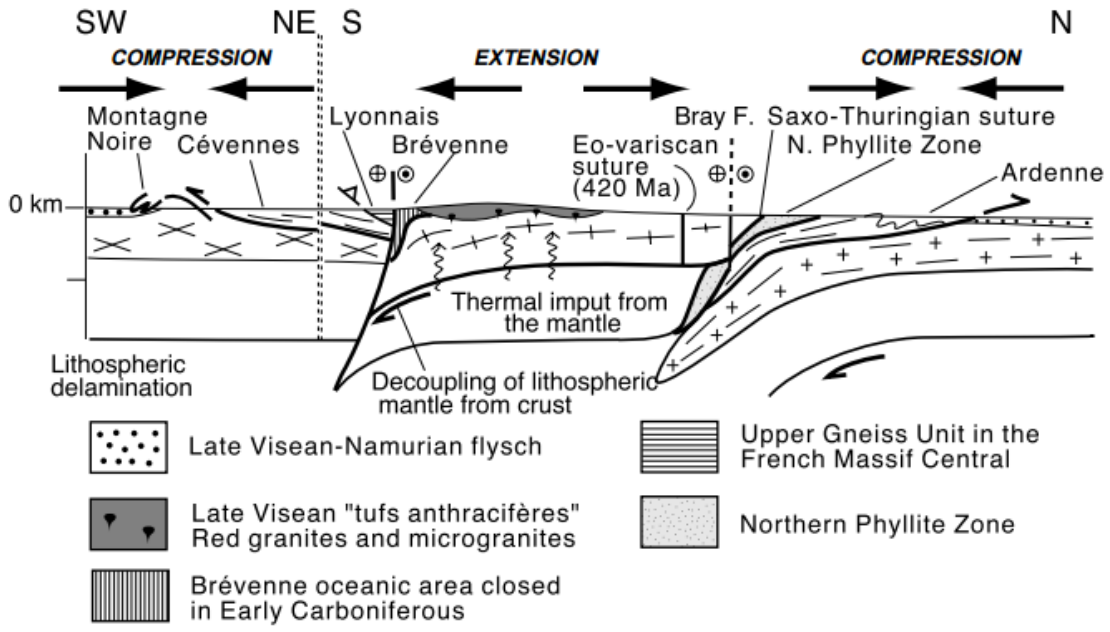

Figure I-4: Lithospheric-scale interpretative cross-section of the east Massif Central-Ardennes area showing the synchronism of extension in the internal and compression in the external parts of the orogen. In the internal parts, the thermal input from the mantle responsible for the Late Visean magmatism is related to mantle delamination. Plutons younger than Visean have been omitted (Faure et al., 2002).

In contrast, Pin (1990), Faure (1995); Faure et al., (1997; 2005, 2014) suggest a polycyclic evolution of the belt that involves: (1) a northward subduction that led to the closure of the Galicia-Massif Central ocean, followed by (2) a southward subduction of the Rheic Ocean. The latter was accompanied by localized extension that affected the upper plate in the internal zones while the externals parts were still in compression (**Fig. I-4**). Another model emphasizes the impact of ductile shear zones and associated partially molten rocks that accompanied the Variscan orogenic collapse in a transgressive regime (e.g. Gébelin et al., 2007, 2009 and Vanderhaeghe et al., 2018).

This study focusses on the late stages of the orogeny, when the mountain was already built and a certain altitude was very likely achieved before the post-orogenic collapse (see discussion below). Indeed, most of the studied crustal-scale shear zones played a major role in controlling the mean elevation of the belt during post-orogenic extension (e.g. Malavieille et al., 1990; Gapais et al., 2009).

2. The debate on the Variscan belt's paleoelevation

The ultimate goal of this study is to obtain paleoaltimetry estimates of the eroded Variscan Belt of Western Europe whose topography and associated tectonic processes are the focus of considerable debate. Principally, two competing models exist in the literature: 1) a Himalaya-Tibet-style high orogenic plateau that developed as a result of thickened hinterland regions (e.g. Dewey and Burke, 1973; Ménard and Molnar, 1988; Matte, 2001; Dörr and Zulauf, 2010), and 2) subdued topography due to coeval orogenic-parallel extension that counterbalanced crustal thickening and uplift (e.g. Franke, 2012, 2014).

a. Arguments for high elevation (≥ 4000m)

The Variscan Belt has often been compared to the Himalayas in terms of structural and metamorphic arrangement (**Fig. I-5**): both of these belts show an E-W trending axis and display a V-shaped geometry highlighted by West and East syntaxes (e.g. Dewey and Burke, 1973; Burg, 1983; Mattauer, 1986; Mattauer et al., 1988; Kroner and Romer, 2013; Stampfli et al., 2013). Both chains display major thrust zones developed in response to crustal thickening; the Main Central Thrust in the Himalayas has been compared to the 'Main Champtoceaux Thrust' in the Armorican Massif or the 'Main Massif Central Thrust' in the Massif Central (Mattauer et al., 1988; Mattauer and Matte, 1998; Ballèvre et al., 2013). Detachment zones parallel to the orogen are observed in both orogens: the South Tibetan Detachment in the Himalayas, and the Pilat detachment zone in the French Massif Central (FMC). The presence of normal faults perpendicular to the E-W trend of the belt that reflect orogen-parallel extension have been described in both the Himalayas (e.g. Leo Pargil, Ama Drime; Thiede et al., 2006; Jessup and Cottle, 2010) and the Variscan belt (e.g. Quiberon in the Armorican Massif, Argentat, Felletin or Nantiat in the FMC; Gapais et al., 1993, 2015; Roig et al., 2002; Gébelin et al., 2009).

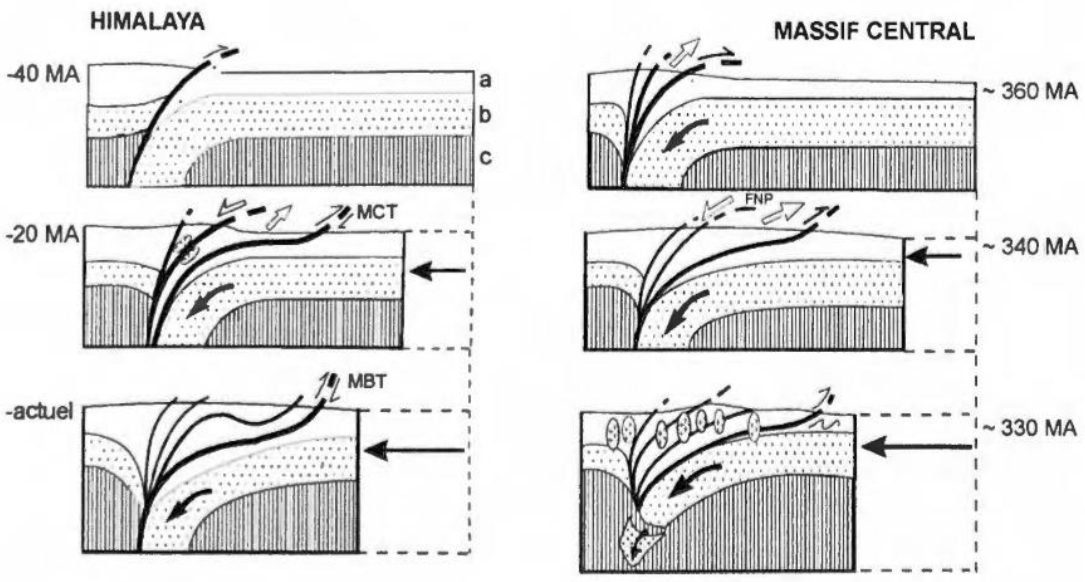

Figure I-5 (last page): Comparison between the Himalayas and the Southern French Massif Central at the end of the Palaeozoic. (a) Continental crust; (b) Lithospheric mantle; (c) Asthenosphere. MCT: Main Central Thrust; MBT: Main Boundary Thrust; FNP: Mont Pilat ductile normal fault. Crosses indicate the recent granitic massifs (Mattauer and Matte, 1998).

Synorogenic clastic sediments deposited in foreland basins indicates the presence of topographic relief in the internal zones of the Variscan belt of Western Europe (e.g. Franke and Engel, 1986; Schneider et al., 1999; Hartley and Otava, 2001; Pastor-Galán et al., 2013; Lin et al., 2016; Žák et al., 2018). Although controversial, periglacial deposits found in the French Massif Central and striated boulders in the Bohemian Massif were interpreted as the proof of a topographic high of ~4 km (Becq-Giraudon and Van Den Driessche, 1994; Becq-Giraudon et al., 1996). Crustal thickening in the internal zones of the Variscan orogen is supported by the presence of nappes emplaced during the Late Carboniferous and high-pressure metamorphism as attested by outcrops of blueschist and eclogite rocks (Ledru et al., 1989; Ballèvre et al., 2013; Rubio Pascual et al., 2016; Žák et al., 2017). For some authors, crustal thickening (up to 55km) in the internal zones of the belt led to a high-altitude plateau reaching Himalayan-type elevation of 3 to 4 km (e.g. Dörr and Zulauf, 2010). Furthermore, recent seismic section and gravity acquisitions reveal low resistivity and low velocity zones at the Moho depth in the internal zones of the Variscan belt, interpreted to represent the presence of partially molten lower crustal material comparable to those in the Himalaya (Beaumont et al., 2001; Guy et al., 2011).

b. Arguments for medium to low elevation (≤ 4000m)

Some authors acknowledge that surface uplift may have occurred only in "rather narrow belts along crustal-scale shear zones or active margins, in which Devonian-Carboniferous overstep sequences have not been detected" (Franke, 2014). Franke

(2014) argues that a high altitude would not have been achievable in the Variscan Belt because: (1) orogen-parallel extension and the activation of strike-slip shear zones (escape tectonics) would have reduced the amount of crustal thickening, (2) the subduction erosion of oceanic plates would have enhanced lithospheric thinning (e.g. Lardeaux et al., 2001; Franke, 2014), (3) the low viscosity of crustal materials in this « hot orogen » would have not been able to sustain high reliefs (e.g. Chardon et al., 2009; Franke, 2014; Vanderhaeghe et al., 2018). In summary, Franke (2014) compares the Variscan belt to the Alps where orogen-parallel extension compensated crustal thickening, uplift and erosion (Ratschbacher et al., 1989) and concludes that the Variscan Belt is “failed, but not collapsed” in terms of topography.

In addition, widespread fauna and flora found in European intra-montane coal-bearing basins are in agreement with medium to low elevation (**Fig. I-6**; Roscher and Schneider, 2006). The findings of periglacial deposits supporting a high elevation have been questioned as slip scars, slumps and water escape structures and do not necessarily constitute evidence for a cold climate (Becq-Giraudon and Van Den Driessche, 1994; Becq-Giraudon et al., 1996; Dörr and Zulauf, 2010; Franke, 2012, 2014). Moreover, atmospheric general circulation modelling applied to different configurations of Pangea points to a mean elevation of ~2000 to 3000 m (Fluteau et al., 2001). The presence of a flat Moho and a thin lithosphere in the Iberian Massif indicates a limited elevation (Torne et al., 2015).

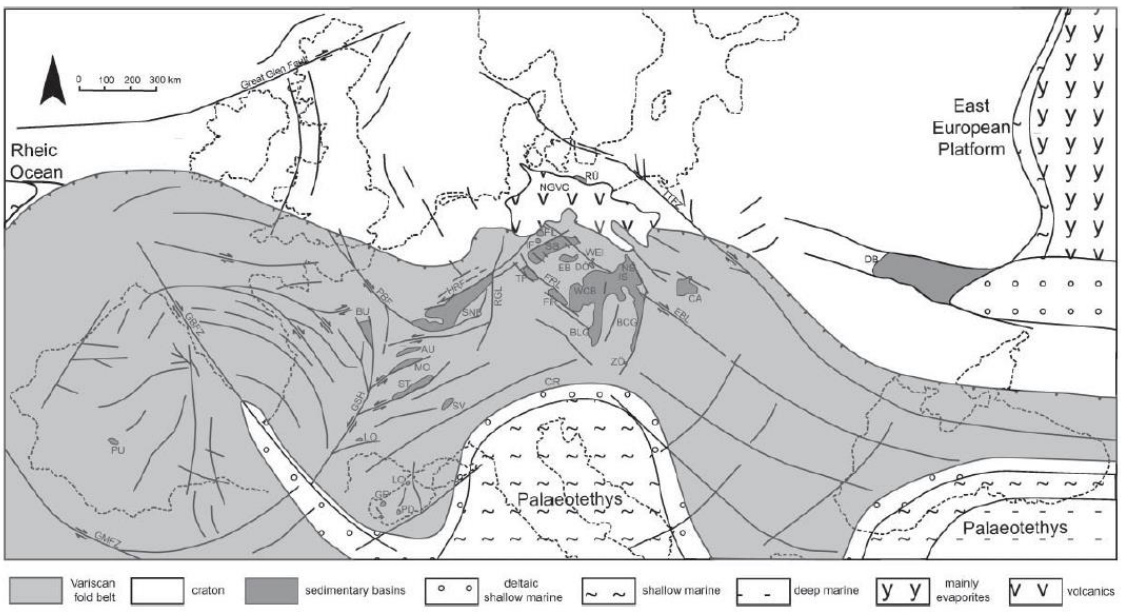

Figure I-6: Location of main Permo-Carboniferous basins in Western Europe (Roscher and Schneider, 2006)

As the Variscan Belt's topography is still at the core of the debate, it is important to quantify its topographic evolution through space and time. The principles and limitations of the method of stable isotope paleoaltimetry will be explained in the following section.

B. Stable Isotope Paleoaltimetry of the Variscan Belt of Western Europe

1. Principles of Stable Isotope Paleoaltimetry

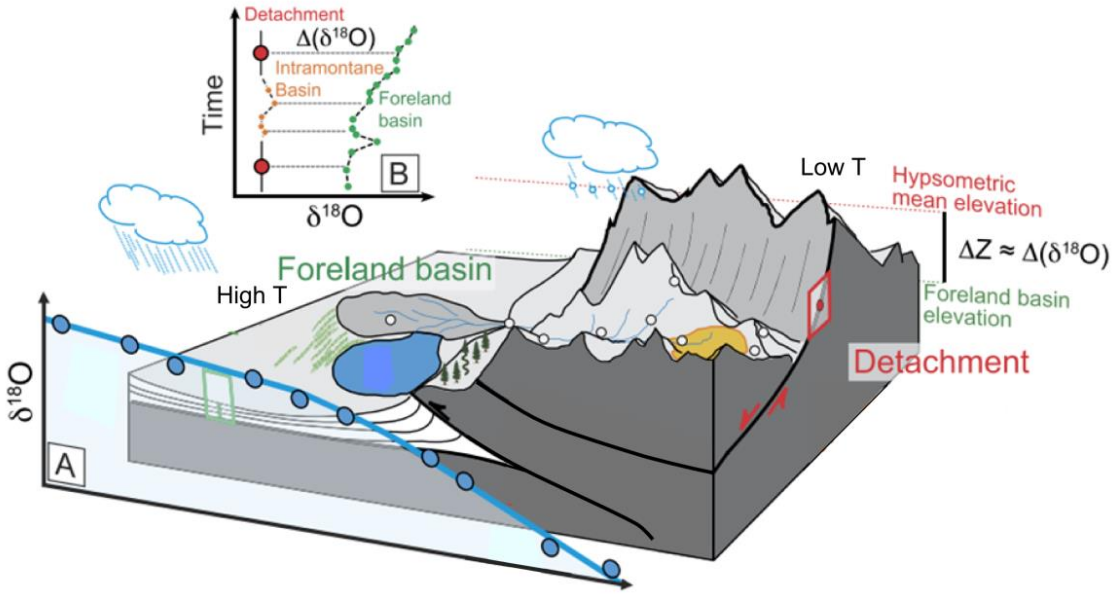

Figure I-7: Principle of stable isotope paleoaltimetry. (A) Lapse rate of $\delta^{18}O$ values of precipitation as a function of elevation. (B) $\Delta(\delta^{18}O)$ is the difference between the $\delta^{18}O$ values recovered from low elevation reference sites (foreland basin) and higher elevation sites (detachments) through time. Δz = difference in elevation between low elevation reference site and high elevation proxy record (Modified from Campani et al., 2012 and Mulch, 2016)

Stable isotope paleoaltimetry is based on the relationship between the isotopic composition of rainfall that scales with elevation. The process of Rayleigh's distillation (Dansgaard, 1964) is due to the decrease in temperature with increasing elevation (-6.5 °C/km) and implies that heavy isotopes concentrate in the condensate. Therefore, as air masses rise across a mountain range, the isotopic composition of meteoric water (the oxygen isotope composition is expressed in $\delta^{18}O$ values and the hydrogen isotope composition in δD values, see **part II-D**) becomes more negative as water vapour is more depleted in heavy isotopes (^{18}O and D) (**Fig. I-7**). A gradient has been identified from higher $\delta^{18}O$ and δD values of precipitation at low elevation where the temperature is

elevated to lower $\delta^{18}O$ and δD values of precipitation at high elevation associated with low temperature (**Figs. I-7 and I-8**). An average lapse rate has been defined for low and mid latitude at ~ -22‰ per km for δD values, and ~ -2.8 ‰ per km for $\delta^{18}O$ values (**Fig. I-8**; e.g. Poage and Chamberlain, 2001; Rowley and Currie, 2006; Rowley and Garzione, 2007).

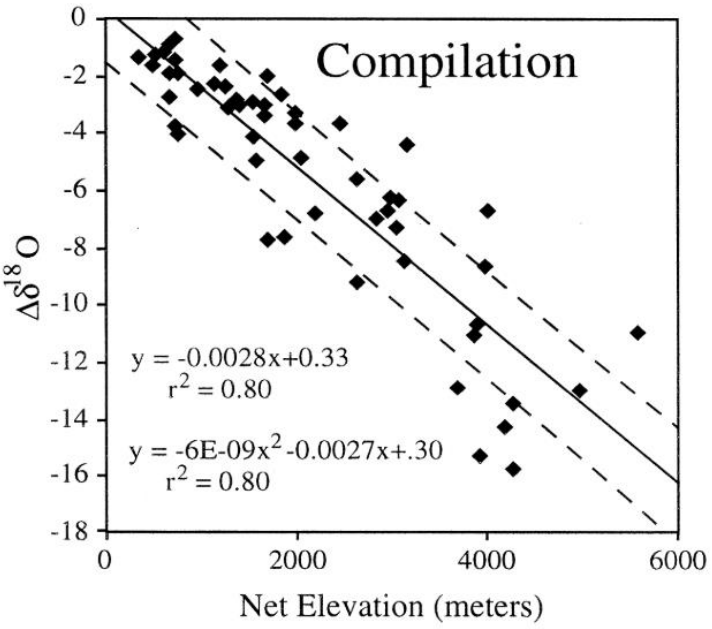

Figure I-8: The compilation of 68 studies revealed an empirical relationship between the net elevation and the isotope composition ($\delta^{18}O$) of meteoric water in mountain ranges (Poage and Chamberlain, 2001).

The method of stable isotope paleoaltimetry has evolved considerably since its infancy when single site isotope values were directly linked to elevation estimates (Ambach et al., 1968; Siegenthaler and Oeschger, 1980). A recent development allows us to reduce potential uncertainties relative to large-scale climate change effects on the stable isotope composition of precipitation by comparing an isotope record of rainfall sourced at high elevation (hinterland) with one sourced at low elevation (foreland) (**Fig. I-7**; e.g. Mulch et al., 2006a; Mulch and Chamberlain, 2007; Gébelin et al., 2012, 2013; Mulch, 2016). This means that both low and high altitude proxies will record the effects of upstream moisture recycling and atmospheric vapour transport, while the additional

effect of elevation will result in more negative isotope values for the high altitude proxies (e.g. Mulch, 2016). As shown on **Fig. I-7**, this method allows us to gain quantitative data on the hypsometric mean elevation of an area.

Stable isotope-based paleoaltimetry has allowed studies to reconstruct the past mean elevation of eroded mountain ranges using near-surface proxies in the Tibetan plateau (e.g. Garzione et al., 2000; Currie et al., 2005; Rowley and Currie, 2006; Quade et al., 2011; Xu et al., 2013; Hoke et al., 2014; Huntington et al., 2015), in the Rocky mountains, the North American Cordillera, the Cascades, the Basin and Range, the Sierra Nevada and Patagonia (e.g. Morrill and Koch; Drummond et al., 1993; Norris et al., 1996; Dettman and Lohmann, 2000; Mulch et al., 2004b, 2006a, 2008, 2015; Sjostrom et al., 2006; Horton and Chamberlain, 2006; Cassel et al., 2009; Chamberlain et al., 2012; Feng et al., 2013; Fan et al., 2014, 2017; Mix et al., 2016) and the Andes (e.g. Garzione et al., 2008; Mulch et al., 2010; Saylor and Horton, 2014). However, most of these studies are based on proxies that recorded the isotope composition of meteoric water in the near-surface record, whereas some recent studies are based on the isotope record of hydrous silicates that recrystallized and interacted with meteoric water at depth (e.g. Mulch et al., 2004b, 2007; Campani et al., 2012; Gébelin et al., 2012, 2013).

2. Limitations of paleoaltimetry reconstructions

a. Stable isotope-based paleoaltitude estimates

Stable isotope paleoaltimetry is based on an empirical relationship between the isotope composition of water and elevation (**Fig. I-8**; Poage and Chamberlain, 2001). This relationship is assumed to have remained stable over time. Indeed, the physical processes (Rayleigh's distillation) that regulated the isotope fractionation in air masses during Palaeozoic times would not be different from today. However, the lapse rate that

describes the isotope composition of meteoric water scaling with elevation depends on various parameters such as the latitude, the source of precipitation, the temperature of the moisture source and the air masses above it, and finally the distance to the source of precipitation (e.g. Rowley and Garzione, 2007). As such, evaluating the paleogeography and paleoclimate of Pangea at the end of the Carboniferous is essential (see section b below).

Nevertheless, these parameters are negligible compared to the effect of elevation on the isotope composition of precipitation (e.g. Rowley, 2007). Therefore, the uncertainty of the paleoaltitude estimates can be calculated by propagating the uncertainties observed in empirical data (mainly the isotope composition of minerals and the temperature of isotope exchange). Most stable isotope-based paleoaltitude studies exclude the uncertainty relying on the lapse rate, which can attain ± 700 m for model elevations of ~5000m (Rowley, 2007). This method has allowed us to estimate paleoaltitudes of ~5100 ± 400 m and ~5400 ± 350 m for the Mount Everest area (Gébelin et al., 2013) and 2350 (+700/-500) m for the European Alps (Campani et al., 2012), both during the Miocene.

b. Variscan paleogeography

Paleomagnetic data indicate that the Variscan Belt of Western Europe was located near by the Equator (**Fig. I-10**; Tait et al., 1996a, b, 1999, 2000; Zwing and Bachtadse, 2000; Domeier and Torsvik, 2014; Edel et al., 2018). Yet, the isotope composition of modern rainfall in equatorial regions display higher δD and $\delta^{18}O$ values than in low and mid latitudes (**Fig. I-9**, Rozanski et al., 1993). The different lapse rates calculated in many of the world's mountain belt give an average of −2.8‰/km for the $\delta^{18}O$ values and −22‰/km for the δD values (**Fig. I-8**, Poage and Chamberlain, 2001). However, this lapse

rate increases with latitude as shown by a recent study conducted in Ecuador that has revealed a much lower lapse rate of −2.2‰/km for the $\delta^{18}O$ values and −17‰/km for the δD values (Windhorst et al., 2013). As a consequence, using the lapse rate estimated by Poage and Chamberlain (2001) for low latitude areas might lead to an underestimation of the paleoaltitude.

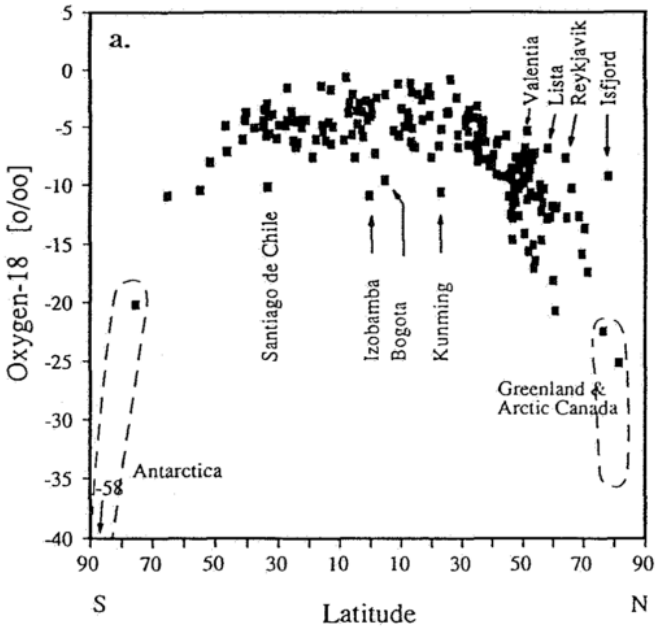

Figure I-9: Long-term annual mean $\delta^{18}O$ ratio in precipitation, derived from the database of the IAEA/WMO global network, plotted as a function of latitude (Rozanski et al., 1993). $\delta^{18}O$ values of precipitation can increase from low to high latitude by at least 20‰. It results in a lower isotope lapse rate between precipitation and attitude at the equator when compared to higher latitudes (Poage and Chamberlain, 2001; Windhorst et al., 2013).

c. Variscan paleoclimate

During the Late Carboniferous, the Southern part of Gondwana was covered by thick ice sheets, now found in South Africa, South America and southern Australia, that were 40% more extensive than today (**Fig. I-10**; Du Toit, 1921; Martin, 1975; Banks, 1985; Visser, 1987a,b; González-Bonorino and Eyles, 1995). The accumulation of large amounts of snow and ice, characterized by very low ^{18}O and D values, induces a positive increase of $\delta^{18}O$ and δD values of sea water (e.g. Blisniuk and Stern, 2005). As a result, the $\delta^{18}O$ values of sea water during the Carboniferous were probably 1.5‰ higher than today (Buggisch et al., 2008). In addition, the warm equatorial paleoclimate characterizing the Variscan Belt might have induced an increase in the oxygen and

hydrogen isotope ratios of precipitation that could also lead to an underestimate of the past mean elevation of eroded mountain ranges (Poulsen and Jeffery, 2011).

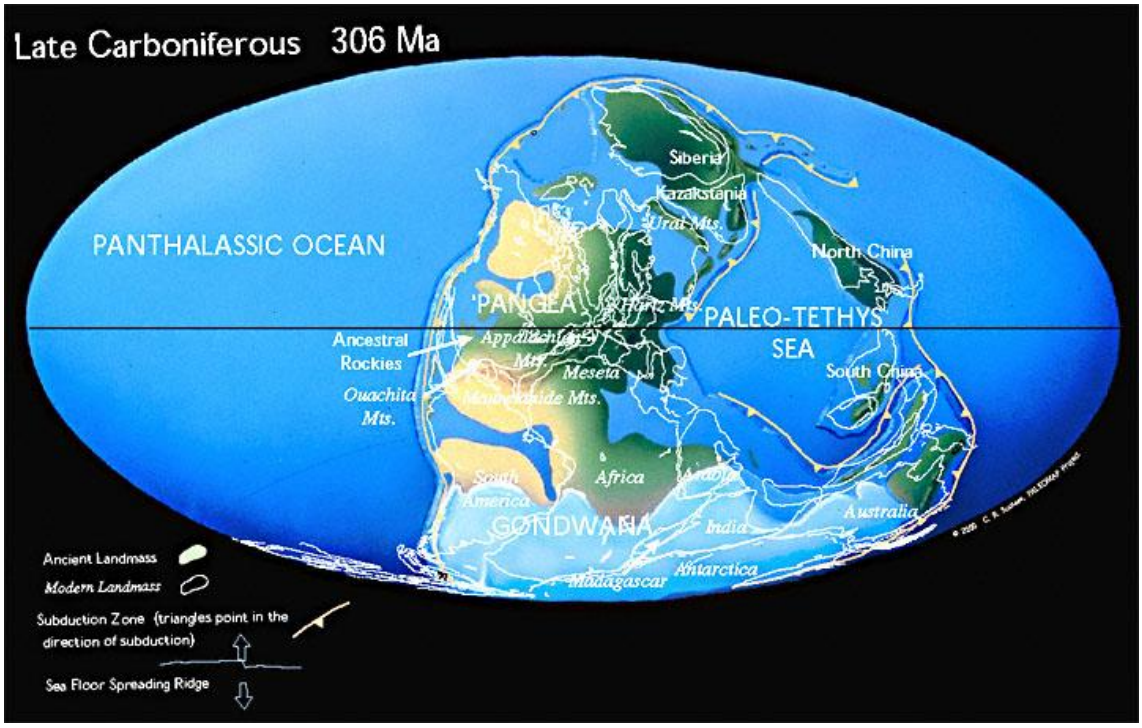

Figure I-10: Paleogeography of Pangea at the end of the Carboniferous (Scotese, 1997). Note the equatorial position of the Variscan Belt of Western Europe and the extensive ice sheet cover on southern Gondwana.

3. Proxies of late-Carboniferous rainfall in the Variscan Belt of Western Europe

The main goal of this study is to find proxies that have preserved the isotope composition of late-Carboniferous meteoric water. Indeed, most of the commonly used geologic material amenable to record the stable isotope composition of late-Carboniferous meteoric water is not preserved within this highly eroded belt. As this mountain range is 15 times older (≥ 300 Ma) than the orogens studied in previous stable paleoaltimetry studies (≤ 20 Ma), reconstructing the paleoelevation of the Variscan Belt of Western Europe is very challenging.

a. Proxies that interact with meteoric water at the Earth's surface

The most commonly used materials for stable-isotope paleoaltimetry reconstructions are found in the near surface record, such as lacustrine, palustrine and pedogenetic carbonates, paleosols, volcanic glasses or biogenic apatite from fossils (e.g. Kohn and Dettman, 2007; Mulch and Chamberlain, 2007; Quade et al., 2007). In Western Europe, late-Carboniferous post-orogenic basins are typically filled with siliciclastic sediments alternating with clay and coal, deposited in various environments (**Fig. I-6**; e.g. Châteauneuf et al., 1989). Scarce lacustrine carbonates are preserved, but the majority of the primary calcite has been replaced by secondary dolomite (e.g. Freytet et al., 1992). Hence, these surface records underwent later diagenesis and recrystallization that led to an increase of the $\delta^{18}O$ values and reset the isotope composition of primary calcite (e.g. Garzione et al., 2004). However, fresh-water shark remains are found in the Permo-Carboniferous basins in the external zones of the belt. They constitute a good target to recover the isotope composition of meteoric water at low elevation as the phosphate-oxygen bound in shark teeth fluorapatite is very resistant to diagenetic alteration (e.g. Kohn and Dettman, 2007; Fischer et al., 2013). Therefore, the oxygen isotope composition of biogenic fluorapatite from shark that evolved in fresh-water environments ~300 Ma ago could be used as a proxy for low-altitude meteoric water.

b. Proxies that interact with meteoric water in the crust

Recent studies indicate that meteoric water can penetrate the crust down to the brittle-ductile transition and interact with hydrous silicates during deformation (Fricke et al., 1992; Mulch et al., 2004; Mulch et al., 2006; Gottardi et al., 2011; Campani et al., 2012; Gébelin et al., 2011, 2012, 2015, 2017; Methner et al., 2015; Quilichini et al., 2015, 2016). Muscovite that crystallized at depth during deformation-related fluid flow

provides a reliable record to track meteoric-derived fluids that circulated in active ductile shear zones during high temperature deformation (~400-600°C; e.g. Gébelin et al., 2011, 2015; Methner et al., 2015). It allows us to calculate the hydrogen isotope ratio of the fluid (δD_{water}) if muscovite-water hydrogen isotope equilibrium was attained during deformation and crystallization and if the temperature of isotope exchange can be assessed (e.g. Fricke et al., 1992; Losh, 1997; Mulch and Cosca, 2004; Mulch et al., 2007; Gébelin et al., 2011, 2015). In addition, the high resistance of muscovite to post-deformational alteration and low-temperature isotope exchange makes it an excellent proxy (e.g. Guggenheim et al., 1987; Mulch et al., 2005; Mariani et al., 2006). Furthermore, this mineral can be dated using Ar/Ar geochronology that can help to determine the timing of meteoric fluid infiltration and duration of hydrogen isotope exchange between the fluid and the mineral.

In Western Europe, syntectonic two-mica leucogranites were emplaced in the footwall of detachment zones and along strike-slip zones during the Late Carboniferous (**Fig. I-11**; e.g. Jegouzo, 1980; Bernard-Griffiths et al., 1985; Gapais et al., 1993, 2015; Malavieille, 1993; Faure, 1995; Le Carlier de Veslud et al., 2004; Gébelin et al., 2007, 2009; Cartannaz et al., 2007; Rolin et al., 2009, 2014; Turrillot et al., 2009; Tartèse and Boulvais, 2010; Poilvet et al., 2011). The southern part of the Armorican Massif is bounded to the north by the South Armorican Shear zone that extends to the south-east in the western part of the Massif Central where it separates in a horse-tail structure along the internal zones of the belt (e.g. Cogné, 1960; Jegouzo, 1980; Gébelin et al., 2007). Detachment zones have been described in the French Variscan belt (e.g. Malavieille et al., 1990; Van Den Driessche and Brun, 1992; Gapais et al., 1993, 2015; Faure, 1995) and have been interpreted as expressing orogenic collapse similarly to

detachments found in the Tibetan plateau and the Basin and Range province (e.g. Mattauer et al., 1988; Ménard and Molnar, 1988; Malavieille et al., 1990). Therefore, this study is mainly based on the measurement of hydrogen and oxygen isotope ratios (δD and $\delta^{18}O$ values) of hydrous minerals from detachment zones that developed in both the hinterland and the foreland of the French Variscan Belt.

Ancient precipitation can also be trapped in fluid inclusions within minerals. The oxygen and hydrogen isotope composition of fluid inclusions has allowed us to identify the presence of meteoric water at depth (e.g. Kerrich et al., 1984; Siebenaller et al., 2013; Menzies et al., 2014; Carter et al., 2015; Gardien et al., 2016) and in some case can be used as proxies for paleoaltimetry reconstructions (Gardien et al., 2017). Therefore, the study of fluid inclusions can be used as a complementary tool and help to determine the isotope composition of ancient rainfalls.

c. Traces of surface-derived fluids in the Variscan Belt

In the Armorican Massif, albitic and chloritic alteration of mylonite samples point to the infiltration of meteoric fluids in crustal-scale ductile shear zones, as suggested (1) in detachment zones footwalls by the low-salinity fluid inclusions (1% NaCl eq.) and the high Sn and Cs content coupled to the low K/Rb, Nb/Ta and $\delta^{18}O_{whole\ rock}$ values of synkinematic leucogranites ($\delta^{18}O_{whole\ rock}$ values = 9.7‰; Ballouard et al., 2016, 2017), (2) in strike-slip shear zones by $\delta^{18}O_{whole\ rock}$ values as low as 1.7‰ in leucogranite (Tartèse et al., 2011, 2012), and (3) in crustal-scale quartz veins interpreted as giant tension gashes by $\delta^{18}O_{Quartz}$ values as low as -2‰ (Lemarchand et al., 2012).

In the SW of the Massif Central, muscovite hydrothermal alteration has been recognized in the hanging wall of the Argentat shear zone (Roig et al., 2002; Bellot, 2007, 2008; Courtnadge, 2016). Moreover, aqueous fluid inclusions studied in gold deposits

(e.g. Villeranges, North of the Massif Central) have low salinity and $\delta^{18}O_{water}$ values of -1 to +4‰ interpreted as the infiltration of depleted surface-derived fluids (Boiron et al., 2003).

In Permo-Carboniferous basins, the isotope composition of shark remains ($\delta^{18}O_p$ values from ~12 to 18‰ and $^{87}Sr/^{86}Sr$ ratios from 0.7085 to 0.7122) has shown that the sharks lived in aquatic environments influenced by meteoric waters (Fischer et al., 2013), including in the Bourbon l'Archambault basin located on **Fig. I-11**.

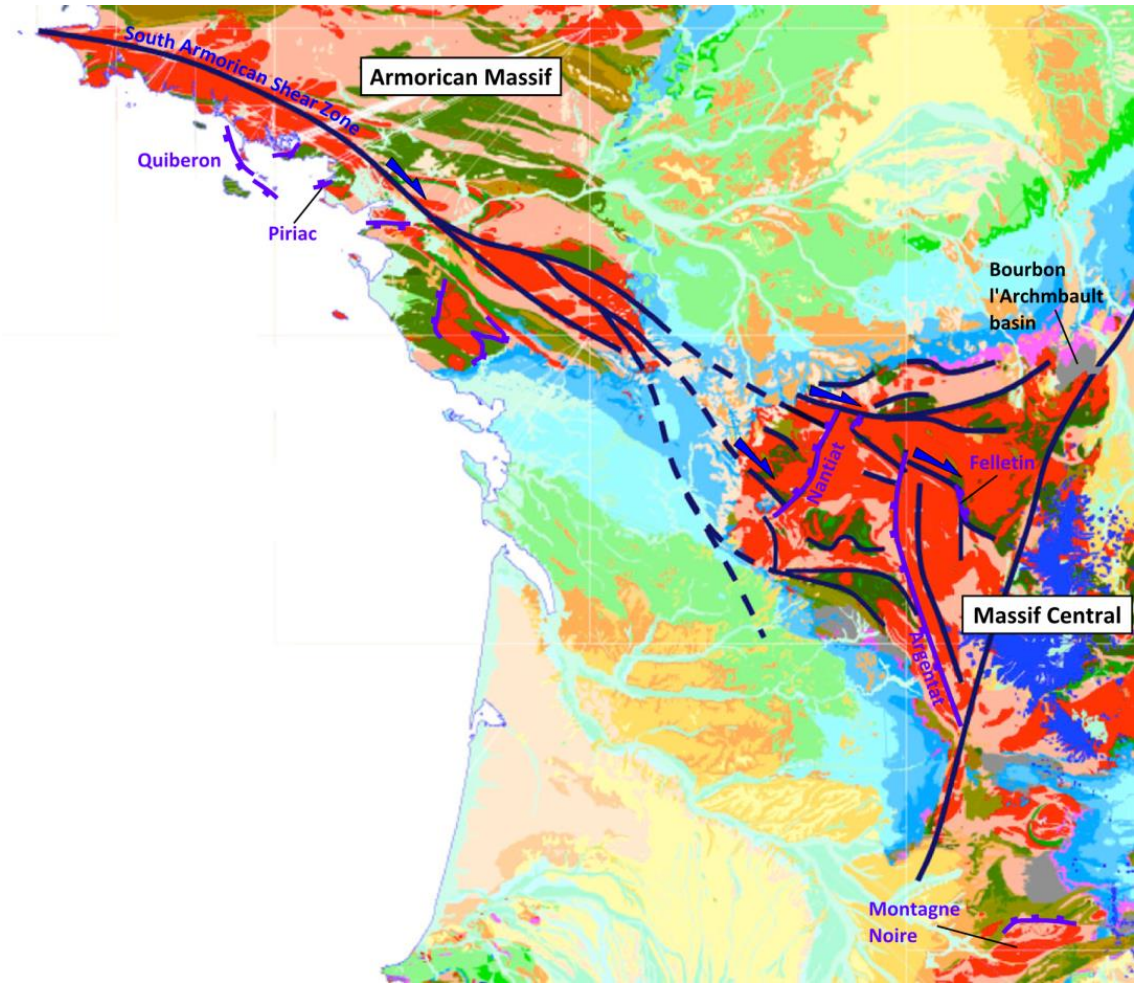

Figure I-11: Geological map of France (modified from BRGM, 2003). The Armorican and Central Massifs are defined by syntectonic granite (red) emplaced within strike-slip shear zones (deep blue lines) and detachments zones (purple lines). The Montagne Noire is a migmatite dome located in the foreland. The Bourchon l'Archambault basin is a foreland sedimentary basin.

4. Aims and objectives

The isotope composition of ancient precipitation in the internal and external zones needs to be recovered in order to reconstruct the paleoelevation of the Variscan belt of Western Europe (**Figs. I-11 and I-12**).

The objectives of this study are:

(1) Find meteoric water in fossil hydrothermal systems through the isotopic composition of hydrous silicates and fluid inclusions in the southern part of the Armorican Massif (**Chapter III**) and the western part of the French Massif Central (**Chapter IV**);

(2) Referencing the hinterland surface fluids records with age-equivalent isotope data from fresh-water sharks remains in the Bourbon l'Archambault foreland basin, and from hydrous silicates in the Espinouse detachment in the Montagne Noire supposed to have developed in the foreland (**Chapter V**).

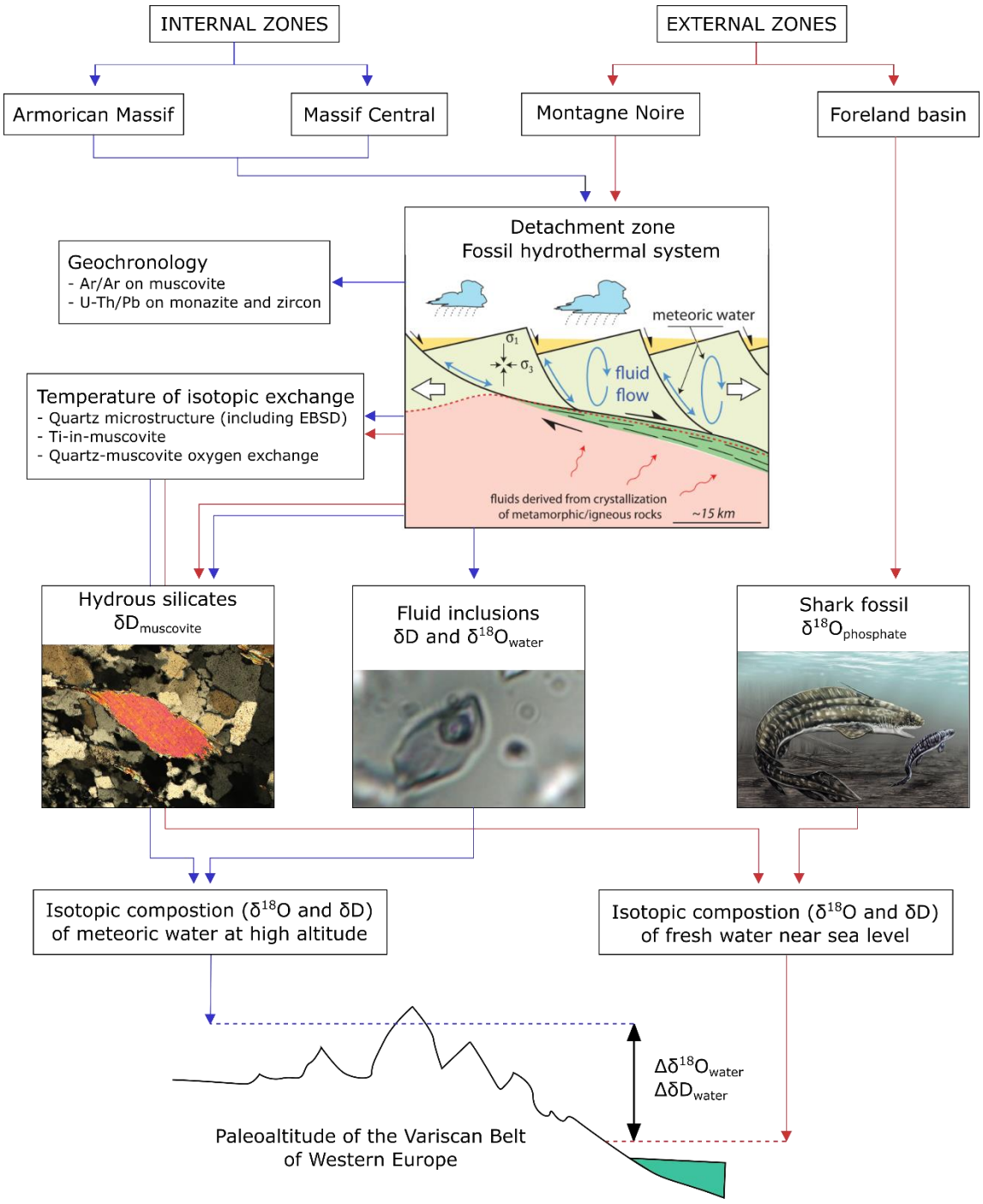

Figure I-12: Flow chart of the project that aims at reconstructing the paleoaltitude of the Variscan Belt of Western Europe by comparing the rainwater isotope composition preserved in the geological record (hydrous silicates, fluid inclusions, shark remains) in the internal and external zones of the belt (sketch of a detachment zone from Whitney et al., 2013).

II. METHODS

This study aims at reconstructing the spatial and temporal evolution of the Variscan belt of western Europe using the method of stable isotope paleoaltimetry based on the isotopic composition of rainfalls that scale with elevation. Therefore, the main objective of this study is to find ancient precipitation in the highly eroded Variscan Belt. As discussed in the first chapter, none of the commonly used geologic materials amenable to record the stable isotopic composition of late-Carboniferous meteoric water has been preserved within this old orogen. However, crustal-scale ductile shear zones represent fossil hydrothermal systems that are amenable to have preserved the hydrogen and oxygen stable isotope composition of surface-derived fluids at depth.

To be able to characterise and understand the deformational and isotopic exchange history from the mesoscopic to the microscopic scale, structural (**section II-A**) and microstructural (**section II-B)** data were systematically collected along structural sections from the top to the bottom of detachments zones into their mylonitic footwalls. Thermometry data were obtained based on quartz microstructures and muscovite geochemistry (**section II-B and C**) as the temperature of isotopic exchange was required to recover the isotopic composition of water (**section II-H**) that interacted with synkinematic minerals in the shear zone through experimentally calibrated parameters. These data also allowed us to decipher important events in the thermal and temporal history of the samples, even though deformation most likely continued after the thermal part of metamorphism.

The hydrogen (δD) and oxygen ($\delta^{18}O$) isotopic ratios of hydrous silicates (**section II-D and E**) were used as a proxy for the isotopic composition of water that interacted

and exchanged with minerals during deformation/recrystallization. As D and ^{18}O-depleted fluids are typically absent in the crust, low $\delta^{18}O$ and δD values of silicates were considered indicative of isotopic exchange with meteoric fluids. The stable isotope and thermometry data obtained from muscovite were then compared with the isotope signature and microthermometry of fluid inclusions from the same samples (**section II-F**). Finally, geochronology (Ar/Ar and U-Th/Pb) data allowed this study to constrain the timing and duration of recrystallization and fluid-flow in the hydrothermal systems (**section II-H**).

A. Structural study

Mountains ranges are characterised by crustal-scale ductile shear zones that accommodate the movement of relatively rigid wall-rock blocks. Shear zones are important source of geological information as their fabrics and mineral assemblages allow the unravelling of the Pressure-Temperature conditions of deformation, the kinematics, as well as the metamorphic and deformation history within the deformation zone (e.g. Passchier and Trouw, 2005). Ductile shear zones are sites of intense deformation and fluid circulation. During convergence and/or post-orogenic extension, low-angle normal detachment shear zones develop as a result of local extensional processes (**Fig. II-1**). They dissect the crust and create preferential pathways for deep crustal (magmatic and/or metamorphic) fluids, but also allow the downward infiltration of surface-derived fluids (**Fig. II-2**).

Previous studies have shown that detachment shear zones are preferential targets when looking for evidence of ancient precipitation: meteoric water can infiltrate the crust down to the brittle-ductile transition (~10 – 15 km depth) and more specifically within the first hundreds of meters into the footwall of detachment zones (**Fig. II-2**; e.g.

Fricke et al., 1992; Mulch et al., 2004a; Gébelin et al., 2011, 2012, 2013, 2015, 2017; Quilichini et al., 2015, 2016; Methner et al., 2015). From these studies, the essential conditions allowing the downwards infiltration of fluids imply a combined effect of brittle normal faults and fractures development in the upper crust, a high geothermal gradient and the presence of a hydraulic head (**Fig. II-2**; e.g. Mulch et al., 2004a; Person et al., 2007; Gébelin et al., 2011, 2015, 2017).

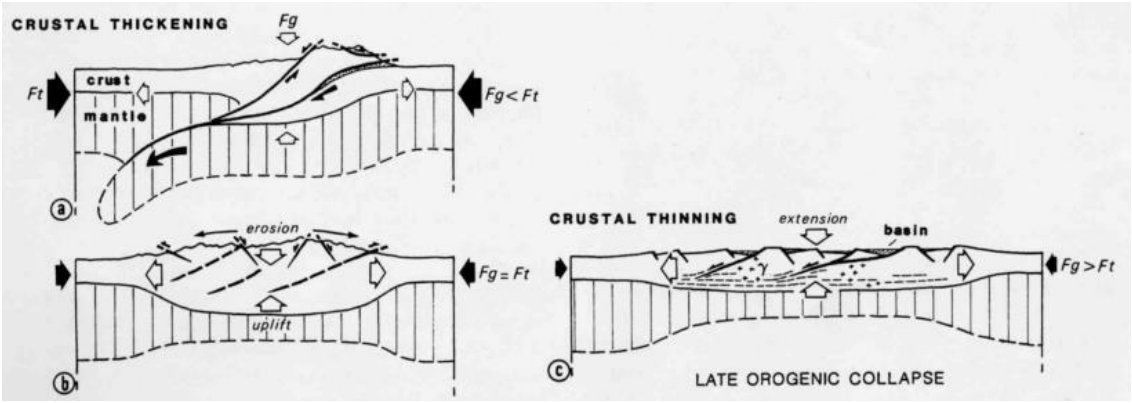

Figure II-1: Extension in mountain belts for different tectonic settings: (a and b) crustal shortening; (c) late-orogenic extension. Fg: gravitational forces, and Ft: tectonic forces (sketch from Malavieille, 1993)

Detachment systems separate the brittle unmetamorphosed upper crust from the ductile highly-metamorphosed (metamorphic, magmatic and partially molten) lower crust (e.g. Coney, 1980; Dewey, 1988; Vanderhaeghe, 1999). At large scale, a detachment shear zone represents a ten to hundreds-meter thick planar zone with low-angle dipping foliation and widespread stretching lineations (e.g. Malavieille, 1993; **Figs. II-2 and II-3**). As detachment zones continuously exhume lower-crustal material to the upper crust, brittle structures such as conjugated normal faults can overprint earlier ductile shearing fabrics at the outcrop scale (**Fig. II-3;** e.g. Davis, 1983; Malavieille, 1993).

Synkinematic granite can be emplaced in the footwall of the detachment and experience intense deformation that is expressed by an anastomosed network of shear

bands (such as C-S structures and C' planes, **Fig. II-3**). These foliated and mylonitic rocks contain stretching and mineral lineation highlighting the sense of movement and flow. Looking parallel to the direction of lineation and perpendicular to the foliation plane, shear sense indicators (delta and sigma clasts, mica fish and structural relationships) allow the kinematics of the shear zone to be determined. In particular, synkinematic hydrous silicates (re)crystallise during deformation and preserve the isotopic composition of the fluids that circulated within the shear zone (e.g. Person et al., 2007).

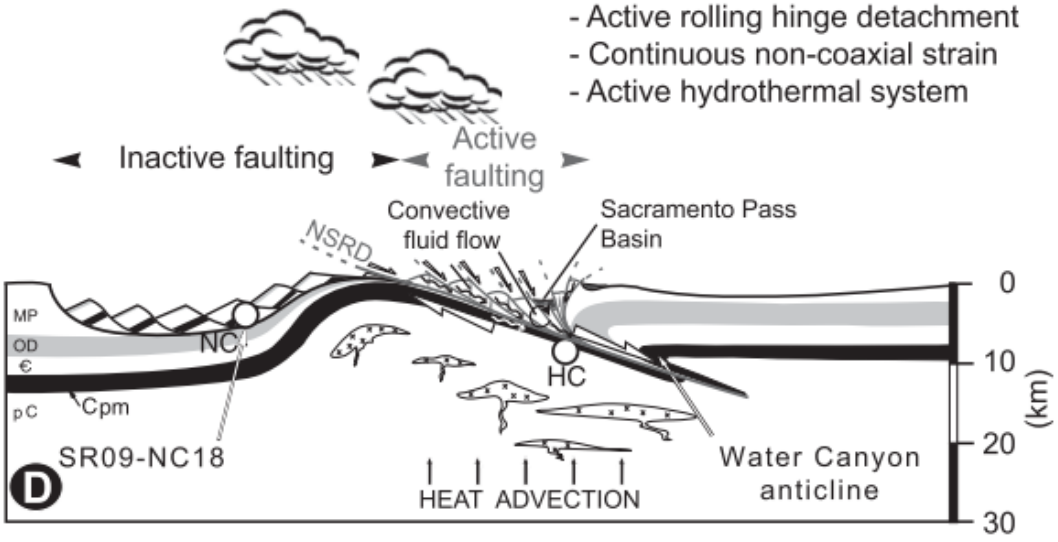

Figure II-2: Example of a detachment system in the northern Snake Range core complex (Nevada, USA) from Gébelin et al. (2015). Normal faults and tension fractures allow the downward infiltration of meteoric fluids to the active northern Snake Range detachment footwall, with high heat flow as driving force for hydrothermal fluid circulation in this part of the northern Snake Range detachment that was characterised by high topography (~4000m) during the Oligo-Miocene (Gébelin et al., 2012).

In this study, mylonitic rocks were systematically sampled across up to 500 m of structural section into the underlying mylonitic footwall of detachment zones. The sample distance to the hanging wall-footwall interface was estimated when observable. If the detachment interface could not be located due to erosional processes, the samples were referenced to the sample located at the very top of the section,

considered at 0 m from the detachment interface. Synkinematic mylonitic samples associated with strike-slip shear zones were also collected.

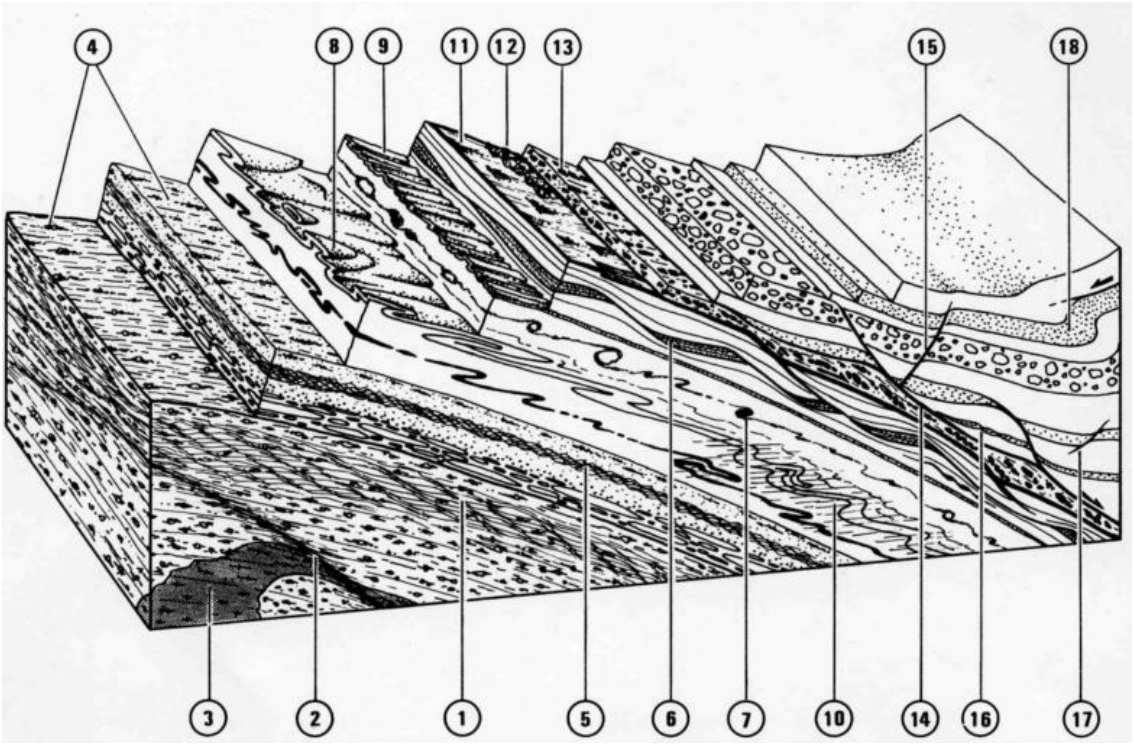

Figure II-3: Macrostructures in detachment zones: (1) foliated rocks with extensional shear bands (C' planes); (2) small scale normal shear zones; (3) synkinematic granite bodies or sill, mylonitized and boudinaged; (4) stretching and mineral lineations; (5) extensional crenulation cleavage; (6) boudinage at different scales; (7) shear criteria (rolling clasts); (8) sheath folds in zones of high shear strain; (9) folds with axes parallel to stretching lineations; (10) tight folds with subhorizontal axial planes; (11) slickensides on brittle detachment surfaces; (12) cataclastic breccia; (13) fractured pebbles, stretched and striated; (14) low-angle decollements in weak layer; (15) conjugated high angle brittle faults; (16) stretched layers; (17) synsedimentary hydroplastic faults; (18) gravity folding (from Malavieille, 1993).

All samples were carefully located, described and oriented in the field to allow the making of structural thin-sections parallel to the lineation direction. The thin-sections allowed a detailed microstructural and petrological study to be conducted (including classic microscopy and SEM-based techniques such as EBSD and microprobe – see sections **II - B, C and F** for more details). The collected samples were also crushed for mineral separation as part of the stable isotope or geochronology analyses (see **sections II – D, E and H**).

B. Microstructural study

Orientated polished thin sections and thick-sections were prepared for microstructural analysis with the aim of correlating deformation mechanism and fluid-mineral interactions during activity along the shear zones. For instance, previous studies have shown that there is a close relationship between fluid-rock interaction and quartz and silicates recrystallization within the top 200m of detachment zones, indicating that the quartz, silicate and fluid reached isotopic equilibrium during high temperature deformation (e.g. Gébelin et al., 2011). Polished thin-sections were made by the thin-section laboratories of the Universities of Montpellier and Lille, and the Thin Section Lab in Toul. Microstructural analyses using classical microscopy were performed at the Universities of Plymouth and Lille.

1. Mica microstructures

Mica fish can be used as shear sense indicators, as well as to determine the presence of multiple deformation histories due to their resistance to later deformation. To characterise syntectonic fluid-rock interactions, it is important to study the mechanisms of pressure-solution and diffusive mass transfer highlighted by the microstructural arrangement of minerals and the shapes of mica fish. Mica fish can be divided into 6 groups with different morphologies that reflect different mechanisms of formation, as well as different stages of evolution (**Fig. II-4;** ten Grotenhuis et al., 2003).

- Group 1 mica fish are lenticular and form by rotation and reduction on the upper and lower sides.
- Group 1 can evolve into group 2 fish with inclined tips by dragging along micro shear planes.

- Mica fish from group 3 that form by slip on (001) are rhomboidal with (001) parallel to the longest side of fish.
- Group 4 are rhomboidal with (001) parallel to the shortest side of the fish. They form from undeformed grains with a (001) cleavage at high angle to the foliation by antithetic slip on (001) and drag along micro shear zones.
- Mica fish from group 5 have a low aspect ratio and curved tails that form from irregular grains by rotation and grain size reduction along micro shear zones.
- Group 6 mica fish have a high aspect ratio and inverted stair stepping that form by slip on (001).

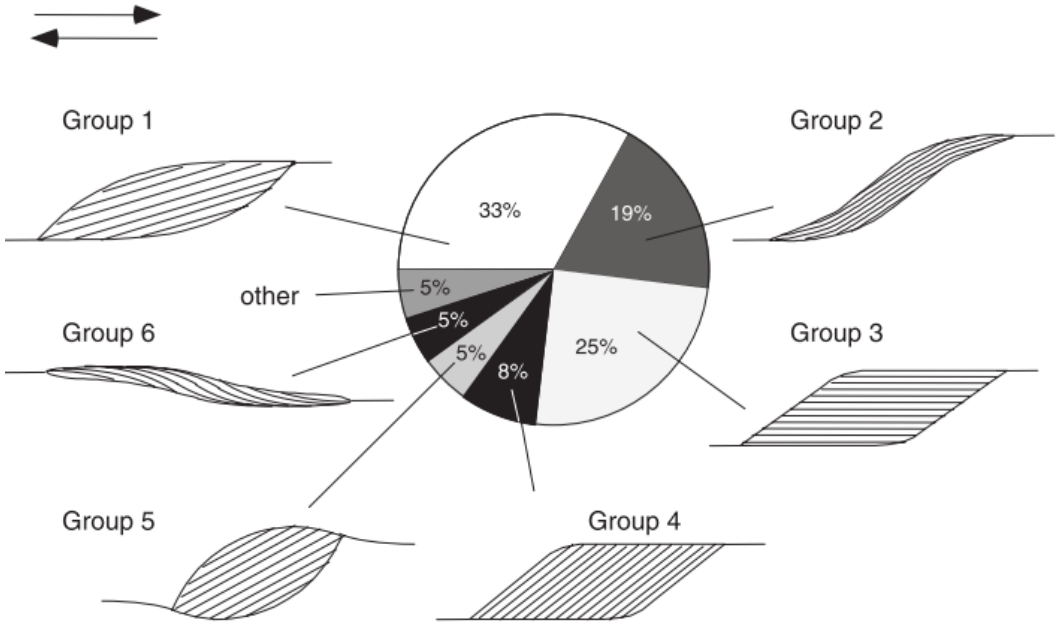

Figure II-4: Schematic drawings of the different morphological types of mica fish. Group 1, lenticular mica fish; group 2, lenticular fish with points inclined in the direction of the foliation; group 3, rhomboidal shaped fish with (001) parallel to longest side of the fish; group 4, rhomboidal shaped fish with (001) parallel to the shortest side of the fish; group 5, fish with small aspect ratio and curved tails; group 6, mica fish with high aspect ratio and inverted stair stepping; if considered out of their context, these structures could lead to an erroneous shear sense determination (from ten Grotenhuis et al., 2003).

In general, the final shape of mica fish results from rigid body rotation at the early stage of deformation accompanied by slip on basal planes, bending and folding, and

'tectonic erosion' along the rims mainly due to recrystallization, cataclasis and possibly pressure-solution and/or diffusional mass transfer (ten Grotenhuis et al., 2003). Synkinematic mica fish (that (re)crystallised during deformation) displaying evidence of recrystallization processes by solution-precipitation indicate that the isotope exchange between the fluid and the mineral occurred during mylonitisation.

2. Quartz microstructures

Quartz microstructures are a valuable tool to determine the temperature of deformation. This temperature can be used as an approximation for the temperature of isotope exchange between the hydrous minerals and the fluid circulating during deformation, if quartz and hydrous minerals share a common (re)crystallisation history. Three quartz dynamic recrystallization mechanisms corresponding to different deformation temperatures and strain rates have been defined by Hirth and Tullis (1992) and Stipp et al. (2002) (**Fig. II-5**): (a) Bulging recrystallization represent temperatures of deformation ranging between ~300 to 400°C; (b) sub-grain rotation recrystallization; deformation temperatures between ~400 to 500°C, and (c) grain boundary migration temperatures; temperatures above 500°C (Stipp et al., 2002).

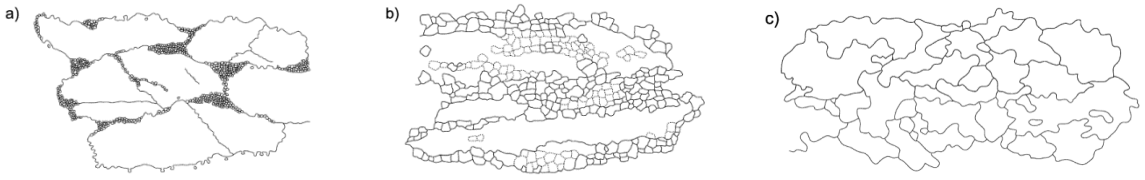

Figure II-5: Characteristic microstructures of the three dynamic recrystallization mechanisms of quartz shown at the same relative scale. (a) Bulging recrystallization (low temperature): bulges and recrystallized quartz grains are present along grain boundaries and to a lesser extent along micro cracks. (b) Sub grain rotation recrystallization (intermediate temperature): core and mantle structures of porphyroclastic ribbon grains and recrystallized sub grains. Polygonization by progressive sub grain rotation can completely consume the ribbon grains. (c) Grain boundary migration recrystallization (high temperature): irregular grain shapes and grain sizes; grain boundaries consists of interfingering sutures (Stipp et al., 2002).

C. Scanning Electron Microprobe-based techniques (SEM)

Scanning Electron Microscopy is a high-resolution imagery technique based on electron-matter interactions. An electron beam scans the sample surface that in response emit particles analysed by different detectors, such as EBSD or WDS that are described below. These methods have been used in this study as complementary techniques to estimate the temperature of synkinematic isotope exchange between the fluid and the minerals.

1. Electron backscatter diffraction (EBSD)

Electron backscatter diffraction is an SEM-based technique that helps identifying mineral phases, grain boundaries and crystal orientations in a rock sample. It consists of an electron beam bombarding the polished surface of a sample that is tilted at 70° from the horizontal. The diffracted electrons excite a phosphor screen that generates diffraction patterns called Kikuchi bands. Each crystal phase and orientation is related to a specific Kikuchi band. The Euler angles (φ1, φ2, φ3) are determined for each quartz grain and stored with the nature of the mineral. The whole procedure is carried out automatically. The precision of crystal orientations measured from electron backscattering patterns is better than 1° [Krieger Lassen, 1996]. EBSD data can be used to determine the Crystal Preferred Orientation (CPO) of specific minerals, highlighting the activated slip system that is related to temperature of deformation (**Fig. II-6**).

In this study, quartz CPO was evaluated from representative quartz ribbon. If the analysis of the [C] axis of the quartz (red on **Fig. II-6**) exhibit CPO maxima at the middle of the pole figure, it means that the prism <a> slip system was activated during deformation at temperatures ranging from ~400 to 500°C (e.g. Stipp et al., 2002). If the CPO maxima are located at the periphery of the pole figures around the foliation plane,

in the vicinity of the lineation, it means that the prism <c> slip system was dominant (e.g. Stipp et al., 2002). The <a> axis distribution also depends on the activation of slip systems related to temperature (**Fig. II-6**; e.g. Stipp et al., 2002).

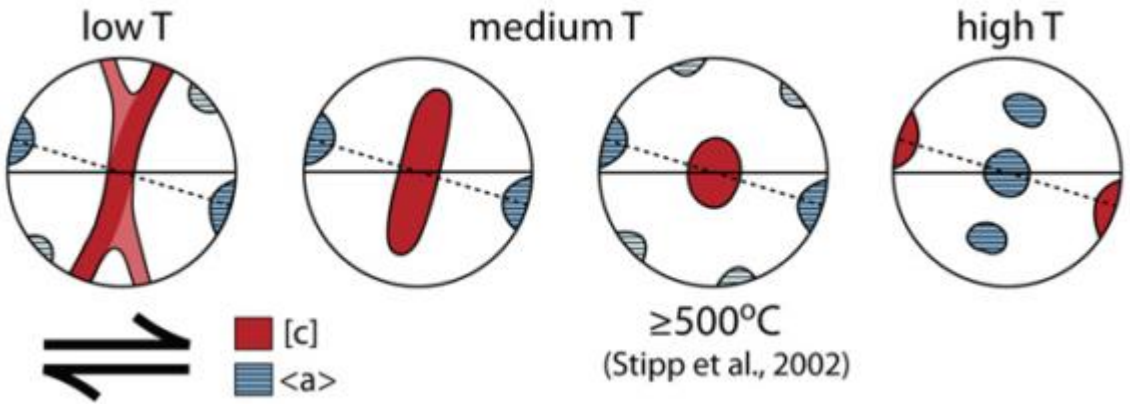

Figure II-6: Generalized quartz CPO patterns formed by simple shear under different temperatures (Singleton and Mosher, 2012, modified after Passchier and Trouw, 2005)

EBSD analyses were performed at the Plateforme de Microscopie Électronique et Analytique MEA of the University of Montpellier (France) using a Camscan Crystal Probe X500FE. It is an electron-scanning microscope with a field emission gun, equipped with a HKL NordlysNano EBSD detector for crystal analysis and an X-MaxN 20 mm² EDS detector for chemical analysis, both piloted by Aztec HKL software, leading to a resolution of about 10 nm. This EBSD-indexation was obtained from the comparison between acquired and simulated diffraction patterns (number of Kikuchi bands detected = 12).for each analysis point using HKL CHANNEL 5+ software with sampling steps ranging from 10 to 16 µm. Typical working conditions of the SEM were 17.50 kV for acceleration voltage, around 7 na for probe current and a working distance of 25.0 mm under low vacuum conditions (chamber pressure = 2 Pa).

2. Microprobe and Ti-in Ms Geothermometer

In this study, the microprobe analyses were aimed at determining the titanium content of muscovite so it could be used as a thermometer (Wu and Chen, 2015). Also, the combined Ti, Na and Mg contents of muscovite were measured to allow the determination of the magmatic or hydrothermal genetics of muscovite (Miller et al., 1981).

An Electron Micro Probe Analyser (EMPA) is an in-situ and non-destructive SEM-based technique that allows the determination of the chemical composition of mineral phases by detecting all the elements from Beryllium in a volume of about 1 μm^3, with a precision of about ± 100 ppm. The electron beam analyses the x-ray wave produced by incident electrons bombarding the analysed mineral.

Geochemical data were acquired using the microprobe EPMA CAMECA SX100 that is composed of 4 to 5 WDS (Wavelength Dispersion Spectrometer) spectrometers, which are composed of a crystal monochromator, a gas-flow proportional counter and a proportional counter. They analyse the X-rays emitted by the analysed mineral that are diffracted by the crystal following Bragg's law and collected by the proportional counter. Each crystal has a specific distance adapted for a range of wavelength characterising a limited number of elements. Therefore the EPMA CAMECA SX100 uses several WDS detectors with each of them being equipped with up to 3 crystals, which allow measuring X-ray emission of several elements simultaneously.

The mineral compositions presented in **Chapter IIII** (Armorican Massif) were measured at the Service Inter-régional Microsonde Sud of the University of Montpellier (France) using a Cameca SX100 electron probe microanalyzer (EPMA) operating at 20 kV accelerating voltage and 10 nA beam current for aluminium (Al), silicon (Si), titanium (Ti),

sodium (Na), magnesium (Mg), manganese (Mn), iron (Fe), potassium (K), calcium (Ca), chromium (Cr) and oxygen (O) X-ray point analysis. The elemental analysis of **Chapter IV** (Massif Central) was performed at the Ecole Nationale Supérieure de Chimie de Lille (France) using a Cameca SX-100 electron probe microanalyzer (EPMA) using wavelength dispersive X-ray spectrometers at 15 kV and 15 nA for backscattered electrons (BSE) images and at 15 kV 40 nA for the same above elements X-ray point analysis. The uncertainty of analysis is ± 0.01 ox. wt%.

The Titanium-in-Muscovite (Ti-in-Ms) geothermometer was developed to estimate metamorphic temperatures of muscovite coexisting with ilmenite and Al_2SiO_5 polymorphs using the titanium content of muscovite measured by electron microprobe for P-T conditions of 450–800 °C and 0.1–1.4 GPa (Wu and Chen, 2015). The temperature can be estimated using the following equation developed by Wu and Chen (2015):

$$\ln[\mathbf{T(°C)}] = 7.258 + 0.289\ln[\mathbf{Ti}] + 0.158\,[\mathbf{Mg/(Fe+Mg)}] + 0.031\,\ln(\mathbf{P})$$

The parameters that need to be input to calculate the temperature are highlighted in bold and are namely: (1) the estimated pressure P (kbar); (2) the Ti content (mol) and (3) the ratio Mg/(Fe+Mg) (mol). Parameters (2) and (3) are determined by electronic microbe analysis, but a significant unknown in the Ti-in-Ms geothermometer is the estimated pressure. The calibrations conditions of the Ti-in-Ms geothermometer and comparision with measurements form this study are summarized in **Table II-1**.

An input pressure error of ± 3 kbar may propagate to a tolerable temperature error of ± 4–20 °C (Wu and Chen, 2015). In chapters III and IV, the estimated pressure of 4 ±1 kbar gives an uncertainty of ± 5°C. The random error of this thermometer is estimated to be of ± 65 °C (Wu and Chen, 2015). In Chapters III and IV, the standard deviation of

temperatures estimated from point analysis of different muscovite in the same sample gives a maximum uncertainty of ± 57°C, in good agreement with the calibration of Wu and Chen (2015).

	Ti (mol)	Fe (mol)	Mg (mol)
Wu and Chen (2015)	0.01 – 0.07	0.03 – 0.16	0.01 – 0.32
Chapter III	0.02 - 0.05	0.11 - 0.15	0.08 - 0.11
Chapter IV	0.00 – 0.05	0.02 – 0.10	0.04 – 0.18

Table II-1: Comparison between the conditions to use the Ti-in-Ms geothermometer of Wu and Chen (2015) and the Ti, Fe and Mg contents measured in this study.

D. Hydrogen isotope geochemistry

1. Theoretical approach

a. Hydrogen and oxygen isotope ratios

The hydrogen and oxygen stable isotope composition of precipitation are commonly expressed by the δ-notation that expresses the relative abundance of the stable isotopes ($^{2}H/^{1}H$ (or $D/^{1}H$) or $^{18}O/^{16}O$), compared to the one of a reference standard in per mil (‰). For example, the δD expresses the isotopic ratio between D and ^{1}H through the following formula:

$$\delta D_{sample} = \left(\frac{D/\ ^{1}H_{sample}}{D/\ ^{1}H_{standard}} - 1\right) * 1000 \qquad \text{expressed in ‰.}$$

In this study, all δD and $\delta^{18}O$ values were reported to VSMOW (Vienna Standard Mean Ocean Water).

b. Hydrogen isotope ratios of fluids

Hydrogen is quite particular as its isotopes have a high relative mass difference amongst them that leads to a broad range of δD values in naturally occurring waters (Coplen et al., 2002). δD_{water} values of precipitation range from -495 ‰ in Antarctic ice to +129 ‰ in the Sahara (Fontes and Gonfiantini, 1967, Jouzel et al., 1987). The range of δD values of natural water is 10 times greater than the range of their $\delta^{18}O$ values (-63 ‰ to +31 ‰) (Aldaz and Deutsch, 1967; Fontes and Gonfiantini, 1967).

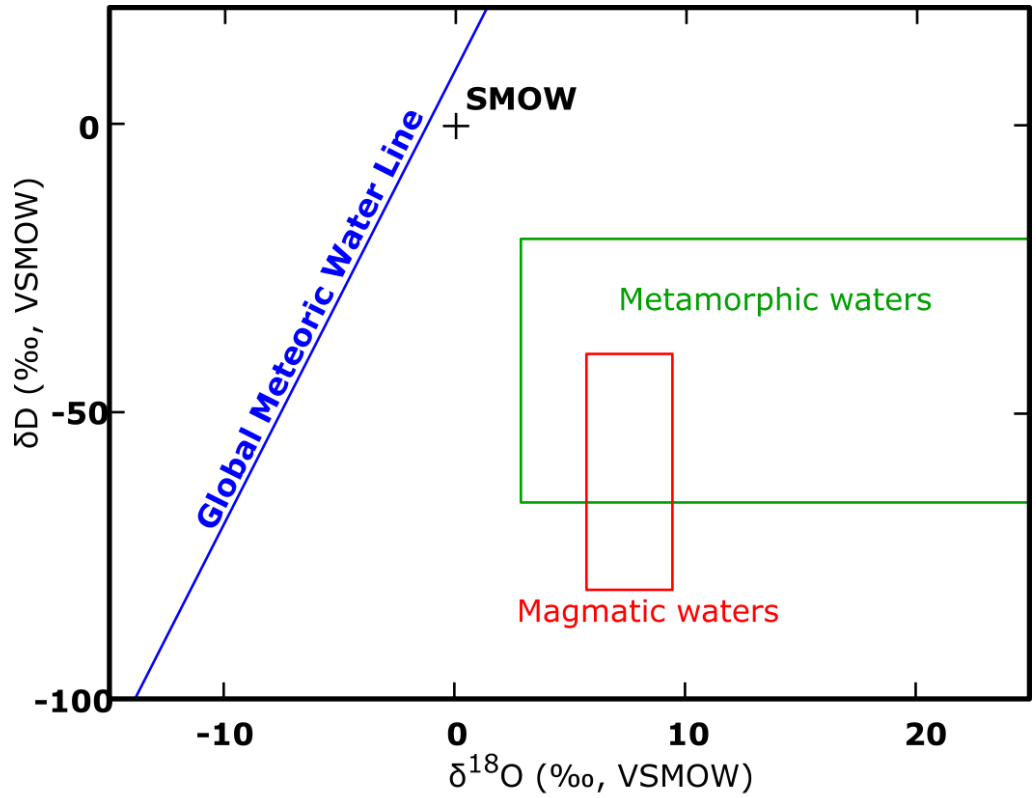

Figure II-7: Graph showing different oxygen and hydrogen isotopic ratios for different fluid sources (after Sheppard, 1986). VSMOW = Vienna Standard Mean Ocean Water.

Crustal fluids can be grouped in two main groups: (1) **Metamorphic fluids** yield δD values from -70 to -20 ‰ and (2) **Magmatic fluids** with δD values that range from -80 to -40‰ (Taylor, 1974; Rye et al., 1976; Field and Fifarek, 1985; Sheppard, 1986). This means that δD_{water} values lower than -80‰ reflect a composition of surface-derived fluids (e.g. Mulch et al., 2004a, 2006; Gébelin et al., 2011, 2015, 2017).

The hydrogen (δD) and oxygen ($\delta^{18}O$) isotopic ratios of meteoric water plot along the Global Meteoric Water Line (GMWL) following the equation from Craig (1961):

$$\delta D = 8 \times \delta^{18}O + 10 \ (‰)$$

Along a shear zone interface, the downward penetration of surface-derived low-δD fluids in the crust would lead to an increase in δD_{water} and $\delta^{18}O_{water}$ values as the fluid interacts with the host magmatic and metamorphic rocks. However, even with low water-rock ratio (W/R ≥ 1), the final δD_{water} value remains similar to the original δD_{water} value. Hence, deuterium-depleted δD_{water} values found at depth represents a maximum value that could have been even lower if it would have been extracted from the near-surface geological record (e.g. Gébelin et al., 2012), but provides a reasonable estimate of the δD_{water} value of the meteoric fluid originating from the earth's surface. On the opposite, $\delta^{18}O_{water}$ values shift to more positive values with very low water rock ratio (W/R ≤ 1). Water–rock reaction paths can be calculated at different water–rock ratios and temperatures using a closed system (Taylor, 1974, 1978; Field and Fifarek, 1985) where the final δ_{water} value after equilibrating with crustal rock (δ_{rock}) depends on the initial δ_{water} value, the water–rock ratio and the temperature of water–rock interactions (example in **Fig. II-8**).

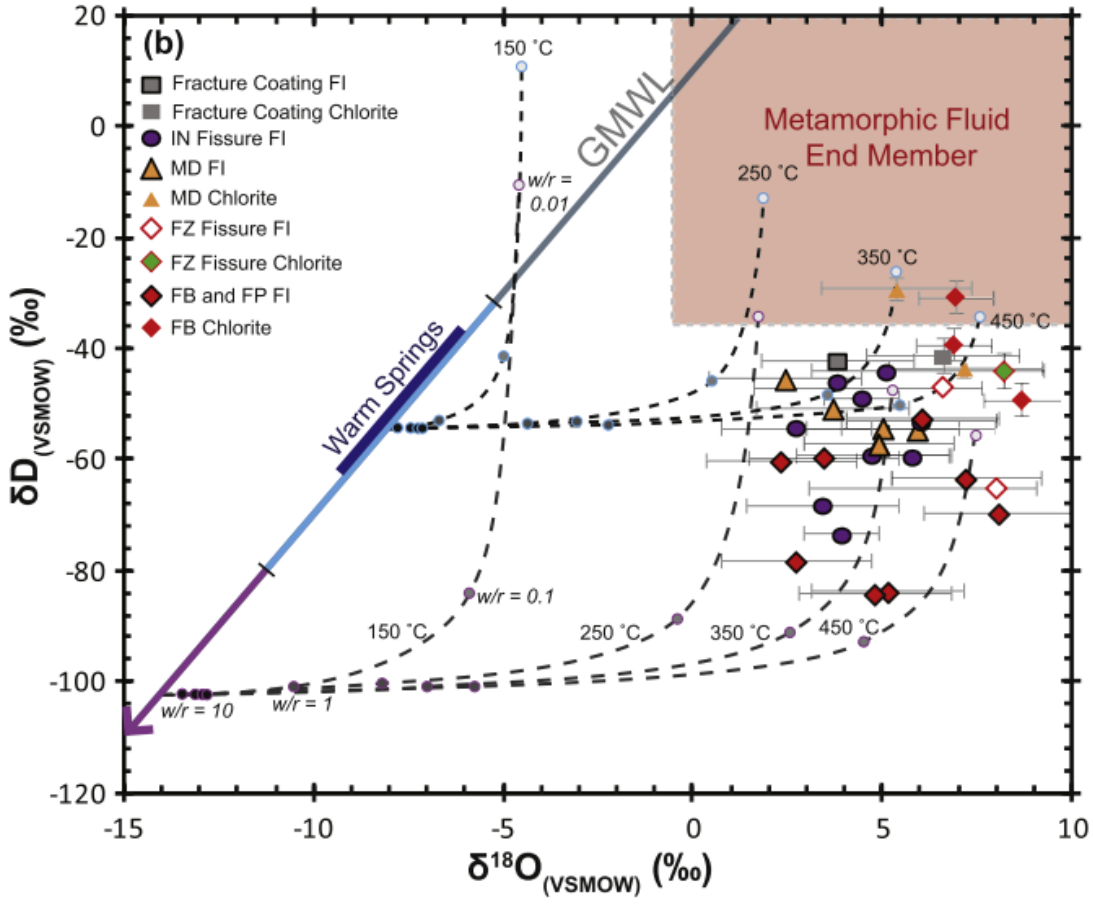

Figure II-8: Modelled closed system water-rock reaction paths (based on Taylor, 1974, 1978; Field and Fifarek, 1985) for fluids in equilibrium with Alpine schists at different water-rocks ratios and temperatures based on δD_{water} and $\delta^{18}O_{water}$ values measured from fluid inclusions and calculated from chlorite (Menzies et al., 2014)**.**

2. Analytical approach

a. Sample Preparation

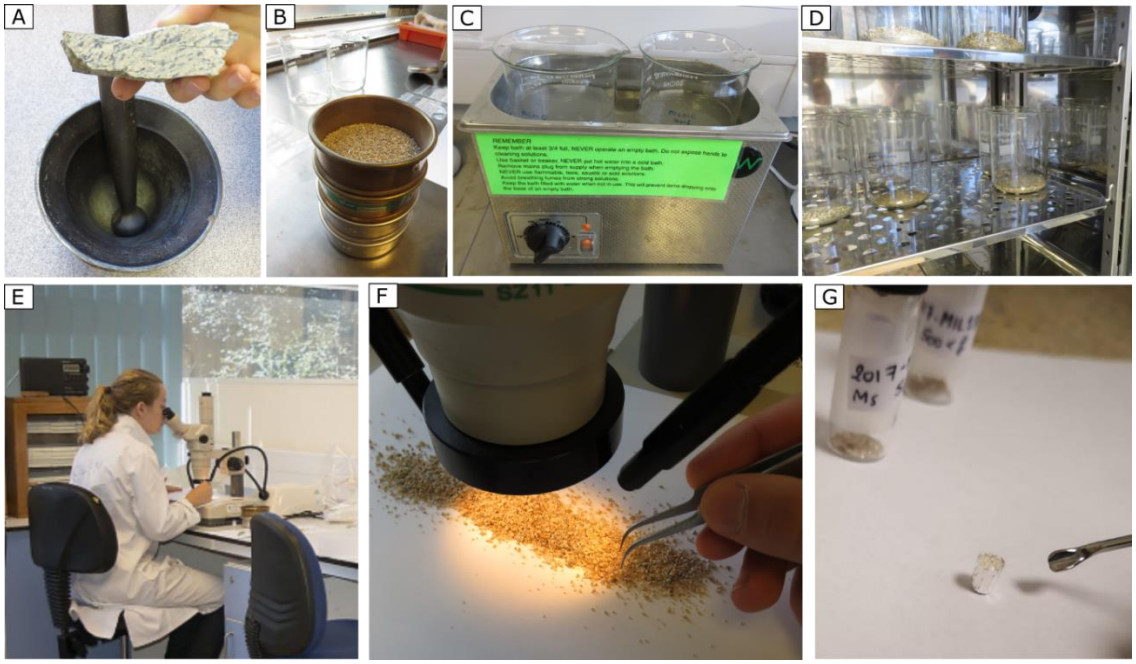

Figure II-9: Sample preparation at the University of Plymouth for hydrogen isotope measurements. (A) Sample crushing using a pestle and mortar; (B) Sample sieving; (C) Sample fractions washing in ultrasonic bath; (D) Sample drying in oven; (E) and (F) Hydrous silicates hand picking under binocular; (G) Hydrous silicate grains weighting and sealing in aluminium capsules.

Samples were crushed using a pestle and a mortar, and then separated in four different fractions using sieves (f > 500 µm, 500 < f < 250 µm, 250 < f < 180 µm, and f < 180 µm; **Fig. II-9 - A and B**). The fractions were washed using an ultrasonic bath to remove dust and split grains and dried at about 50°C for 24h (**Fig. II-9 – C and D**). Finally, pure and clean hydrous minerals present in the sample (e.g. muscovite, biotite, tourmaline, epidote, and chlorite) were hand-picked using a low-powered binocular (**Fig. II-9 – E and F**). The samples were weighed and sealed in aluminium capsules for hydrogen isotope measurements (**Fig. II-9 - G**). The sample size depends on the mineral water content that can attain up to ~10%: muscovite contains 4.07 wt% of water, biotite 3.64 wt%, tourmaline 3.42 wt% and chlorite 8.14 wt%. As a consequence, ~1.5 to 2.0 mg

was needed for muscovite, tourmaline and biotite that contain ~4‰ of water, whereas only 1 mg of chlorite was enough as chlorite contain twice as much water as muscovite.

b. Measurement of hydrogen isotope ratios of silicates

The hydrogen isotopic composition (δD) of silicates range from -429 ‰ to +5 ‰ (Wenner, 1979; Graham et al., 1980). Hydrous silicates are minerals that (re)crystallize in ductile shear zones at depth and interact and exchange isotopically with depth-sourced and/or surface-derived waters. Combined stable isotope ratios and geochronology of synkinematic micas that crystallised in detachment zones is therefore a powerful proxy for meteoric water and can be used as a paleoaltimeter (Mulch and Chamberlain, 2007).

Figure II-10: Thermo-Finnigan High Temperature Conversion Elemental Analyser coupled with a continuous flow mass spectrometer at the Geowissenschaften, Goethe Universitat, Frankfurt, Germany.

Hydrogen isotope measurements were performed in the joint Goethe University/-Senckenberg BiK-F Stable Isotope Facility, Frankfurt. δD values of muscovite (δD_{Ms}) were determined by continuous flow mass spectrometry using a high temperature elemental analyzer (Thermo Finnigan TC/EA) coupled to a Finnigan MAT 253 mass spectrometer in continuous flow mode (**Fig. II-10**).

A sample weight of 1.6 to 2.5 mg was used to obtain sufficient signal sizes, and measurements with low signal sizes (< 7 Vs) were rejected from further interpretation. Three internationally referenced standard materials and additional in-house working standards were run at the beginning, middle and at the end of each individual runs. After correction for mass bias, daily drift of the thermal combustion reactor, and offset from the certified reference values (δD_{NBS30} = -65.7‰, δD_{NBS22} = -117‰, and δD_{CH7} = -100.3‰), NBS30 (biotite), NBS22 (oil), CH7 (polyethylene foil) had δD values of -66‰, -117‰, and -101‰, respectively.

The raw δD values obtained by the instrument need three types of corrections: (1) size (i.e. weight), (2) drift and (3) standards. (1) The correction for size takes into account the fact that δD values can differ regarding the weight of the sample. This was corrected though the use the size correction factor that was determined experimentally using a standard material with a known δD value (in this study's case, kaolinite Kga1b) with weights ranging from 0.03 to 3.7 mg. (2) The drift correction consisted of taking into account the drift of δD values along the run due to the thermal combustion reactor. The slope of standard's values through time is applied to the δD value of the sample. (3) The standard correction consists of comparing standards' δD values corrected for size and drift to the certified reference δD values. The slope correction is then applied to the δD value of the sample. For this study, three internationally referenced standard materials were used: NBS30 (biotite), NBS22 (oil), and CH7 (polyethylene foil) as well as additional in-house working standards. After corrections for size, drift, and standards, NBS30 (biotite), NBS22 (oil), CH7 (polyethylene foil) had δD = -65.7‰, -117‰, and -100.3‰, respectively. Repeated measurements of various standards gave a precision of ± 2‰ for δD. All isotopic ratios are reported relative to standard mean ocean water (VSMOW).

E. Oxygen isotope geochemistry and thermometry

The oxygen stable isotope composition ($\delta^{18}O$) of quartz (Qz) and muscovite (Ms) were measured in the Stable Isotope Laboratory of the University of Lausanne, (Switzerland). About 1.00 to 2.00 mg of muscovite and quartz were heated using a CO_2 laser fluorination line coupled to a Finnigan MAT253 mass spectrometer. One in-house standard quartz sample was measured at the beginning and the end of each run. The average precision of measurements was ± 0.1 ‰.

If quartz and muscovite attained isotopic equilibrium during activity of the shear zone, the difference in their $\delta^{18}O$ values ($\Delta^{18}O_{Qz\text{-}Ms}$) permits the calculation of a temperature of isotope exchange equilibrium. The thermometer of Chacko et al. (1996) was calibrated for temperatures ranging from 123°C to 1227°C based on the following equation:

$$\Delta^{18}O_{Qz\text{-}Ms} = 1.350\ 10^6\ T^{-2} + 0.042\ (10^6\ T^{-2})^2 - 0.0086\ (10^6\ T^{-2})^3$$

F. Fluid inclusion analyses

Fluid inclusions (FIs) are 1 µm to 1 mm cavities containing fluids trapped inside minerals. The study of FIs allows the determination of the fluid composition and the pressure-temperature conditions of its entrapment. At room temperature, FIs are commonly composed of two phases: A liquid phase (mainly dominated by H_2O; sometimes oil) and a vapour phase (generally a mixture of CO_2, CH_4 and N_2). They sometimes contain one or several solid phases such as salt and/or minerals.

The study of FIs is based on three principles: (1) The fluid composition has not changed since it was trapped; (2) The inclusion volume has not changed since it formed; (3) The fluid composition was homogeneous at the time of trapping (Roedder, 1984).

FIs studies must be conducted with caution as 4 processes can modify the fluid properties:

1) Necking down: Fluid inclusions split into tinier inclusions after vapour nucleation
2) Recrystallization: The shape of the cavity changes to replicate the host mineral crystal architecture
3) Stretching: Fluid inclusion volume increases due to temperature or pressure changes. This process is called decrepitation if stretching leads to expose the cavity to the outside environment
4) Leakage: The fluid escapes through microcracks or cleavages due to chemical gradients

FI analysis is based on several methods that will be explained further in this section: (1) petrography, (2) microthermometry, (3) extraction and stable isotope analysis of the fluid, and (4) spectroscopic methods.

1. Petrography and typology

The optical methods consist of establishing the typology of FIs (evaluation of shape, size, and number of phases at room temperature), estimating the fluid/vapour ratio and defining the relative chronology between the different generations of fluid inclusions.

In this study, thick sections were made at the thin-section laboratory of the University of Lille (France) and have been specifically made following the X-Z plan in

order to allow structural observations. FIs were analysed in quartz grains on ~100 µm-thick rock sections to prevent FIs to be affected by sample preparation.

2. Microthermometry

Microthermometry is the observation of phase changes as a function of temperature. It is a statistical method performed on Fluid Inclusions Assemblages (FIAs) that are typically composed of 15 to 20 inclusions and represent the smaller formation time (Goldstein and Reynolds, 1994). According to the FIA approach, all inclusions of a given FIA must have the same composition and density. Therefore, a single composition and temperature of homogenisation can be attributed to each FIA corresponding to the average of individual FI measurements.

In this study, microthermometry measurements were performed at the University of Lille (France) using a Linkam MDS600 plate. The plate calibration was done using synthetic fluid inclusions: melt of pure CO_2 and pure H_2O provided by SynFlinc. The maximum uncertainty for measured temperatures was ± 0.1°C. In this study, fluid inclusions were all aqueous. As a consequence, the lower limit for cooling was about -50°C and heating never exceeded 400°C.

Two kinds of temperature paths are applied on FIs. Cryometry (T<25°C) allows the **temperature of ice melting** (T_{im}) to be measured. The T_{im} is obtained by freezing the FIs down to -200°C with liquid nitrogen, and observing at which temperature the last ice crystal melts during heating (typically around 0°C for aqueous inclusions). The T_{im} is related to salinity; in other words, the lower the T_{im} value, the higher the salinity. Salinities were calculated based on the temperature of ice melting using the equation of Bodnar (1993). A polynomial fit of the ice melting curve is generally used (Bodnar, 1993). Thermometry (T>25°C) consists of measuring the **temperature of**

homogenisation (T_h), that is obtained by heating the fluid inclusions up to +700°C using an electrical resistance and observe the homogenization of the FI. T_h relates to the minimum temperature of the inclusion formation.

The P-T conditions of entrapment can be estimated by calculating isochores that represent temperature evolution according to pressure assuming a constant volume. Considering that all of this study's fluid inclusions can be modelled in a water-salt system, the isochores are calculate using the empirical equation of state (EOS) of Zhang and Frantz (1987). The only required input data are T_{im} and T_h.

The thermobaric gradient at the time of inclusion entrapment is assumed to be based on a postulated geothermal gradient at the time of the geological process. Once a geothermal gradient (present day = 30°C/km in the crust) has been chosen, two possibilities can be considered: a hydrostatic gradient that allow water infiltration from the surface, or a lithostatic gradient (no circulation between the surface and the depth). The choice of a geothermal gradient and associated uncertainties, as well considering either a lithostatic or a hydrostatic gradient, must be carefully considered regarding the metamorphic and tectonic context from which the samples were collected.

3. Oxygen and hydrogen stable isotope measurements

Once the microthermometry analysis was done, the isotopic composition of the fluid contained in the FIs was determined using several techniques. The technique used in this study was the crush-leach technique. The rock sample was crushed in order to handpick quartz grains down to 0.1 g. The fluid contained in the inclusions was then extracted by decrepitation in a vacuumed line. T_h obtained from the microthermometry (section II-F2) helped to define the temperatures of decrepitation.

The isotopic composition of the fluid was measured at the Laboratoire de Géologie de Lyon, Terre, Planètes, Environnement (France) by Dr. Véronique Gardien during October 2018. Water trapped in quartz grains was extracted by thermal decrepitation (i.e. fluid inclusions opening due to internal overpressure resulting from the thermal expansion of fluids). 5 to 8 g of millimetre-scale quartz grains were dried overnight at 110°C in an oven, then loaded in a quartz tube and degassed at 80°C under vacuum for at least 90 min. Water was extracted by heating the samples up to 650°C for 20 min. Water blanks did not contribute for more than 1% of the total amount of water extracted from FIs over the complete set of experiments.

The 2 to 8 µL of water collected during the FI decrepitation was then transferred to a microequilibration vessel, to which 5–10 µmol of CO_2 of known isotopic composition was added. The vessel was placed at 25°C for 2 days where H_2O and CO_2 were able to exchange oxygen isotopes. Once the equilibration was complete, the equilibrated samples of H_2O and CO_2 were separated cryogenically. The water samples $\delta^{18}O$ values were calculated using the mass balance equation of Kishima and Sakai (1980):

$$\delta^{18}O_{H_2O} = (\delta^{18}O_{CO_{2f}} - \delta^{18}O_{CO_{2i}})(2\frac{[CO_2]}{[H_2O]}) + (1 + \frac{\delta^{18}O_{CO_{2f}}}{1000})\frac{1000}{\alpha_{CO_2-H_2O}} - 1000$$

With:

- $\alpha_{CO_2-H_2O}$ = 1.0412 at T = 25°C (O'Neil and Adami, 1969).
- $\delta^{18}O_{CO_{2i}}$= $\delta^{18}O$ value of CO_2 before equilibrium with H_2O = 15.3 ± 0.1‰ (SMOW).
- $\delta^{18}O_{CO_{2f}}$ = $\delta^{18}O$ value of CO_2 after 2 days of equilibration with H_2O.
- $[CO_2]$ and $[H_2O]$ are the amounts of the two gases in µmol.

Internal reproducibility obtained during the experiments for $\delta^{18}O$ values of water was ± 0.5‰. After equilibration, the same water was collected into a silica glass tube containing about 500 mg of fine-grained chromium metal. This water was reduced by Cr at 1000°C for 5 min to produce H_2 gas. The δD of this gas was then determined using a dual-inlet GV Prisme mass spectrometer. External reproducibility of δD measurements was estimated to be ± 3‰ by normalizing raw data to the VSMOW-SLAP scale. Aliquots of «Lyon water » were analysed along with water samples obtained from the fluid inclusions. Sample water amounts were determined by comparison with a series of water samples of known weights ranging from 0.5 to 3.5 µL. After expansion of H_2 into a constant volume in the mass spectrometer sample inlet, the amount of gas was estimated from the voltage on the mass 2 collector. Uncertainty associated with the determined amount of water was close to ± 0.05 µL. The internal reproducibility of δD analyses of reference waters was better than 1.5‰.

4. Spectroscopic method

Raman spectroscopy is used to identify molecules using low-frequency modes induced by Raman scattering of monochromatic light from a laser. It can therefore help to identify the phases contained in a fluid inclusion.

Raman analyses were performed at the University of Lille using a Horiba Jobin Yvon HR 800 UV Raman spectrometer. An Ar Lexel laser tuned at 532 nm was used to reach excitation and the time for integration ranged from 30 to 120 s. Raman was mainly used to check the absence of volatile components in the inclusions, allowing the interpretation to be confined to the H_2O-NaCl system only.

G. Calculation of δD_{water} values based on $\delta D_{mineral}$ values

In order to calculate the isotopic composition of water (δD_{water}) that interacted with minerals during deformation/recrystallization based on the $\delta D_{mineral}$ values, the temperature of hydrogen isotopic exchange between the fluid and the mineral is required. If hydrous minerals show evidence of synkinematic (re)crystallization (see **section II-C1**), the temperature of deformation is considered to represent the temperature of isotopic exchange between the fluid and the mineral during the shear zone activity. In this study, this temperature was estimated using complementary methods: (1) Microstructural study of quartz (including EBSD; **sections II-B2 and C1**); (2) Titanium-in-muscovite thermometry (**section II-C2**); (3) Oxygen isotope thermometry (**section II-E**); (4) Fluid inclusions microthermometry (**section II-F2**).

The temperature-dependent equations that allow the calculation of the fractionation factor between OH-bearing minerals and water were experimentally-calibrated by previous studies. The following equations were considered for mineral-water hydrogen isotopic exchange:

- **Muscovite**-water hydrogen isotopic exchange between 450 and 800°C (Suzuoki and Epstein, 1976): $10^3 \ln \alpha_{muscovite\text{-}water} = -22.1 (10^6 T^{-2}) + 19.1$
- **Biotite**-water hydrogen isotopic exchange between 450 and 800°C (Suzuoki and Epstein, 1976): $10^3 \ln \alpha_{biotite\text{-}water} = -21.3 (10^6 T^{-2}) + 2.8$
- **Tourmaline**-water hydrogen isotopic exchange between 350 and 600°C (Kotzer et al., 1993): $10^3 \ln \alpha_{tourmaline\text{-}water} = -27.2 (10^6 T^{-2}) + 28.1$

➢ $10^3 \ln \alpha_{mineral\text{-}water}$ is the stable isotope fractionation factor between the mineral and the fluid

- T is the temperature of stable isotope exchange in Kelvin.

The isotope composition of the fluid is calculated using the following equation:

$$\delta D_{water} = \delta D_{mineral} - 10^3 \ln \alpha_{mineral\text{-}water}$$

H. Geochronology

In order to unravel the thermal history of the studied fossil hydrothermal systems, radiometric dating of different minerals associated with different closure temperatures were used. The U/Pb system, which closes at about 700-800°C in zircon and monazite (e.g. Cherniak and Watson, 2001; Cocherie, 2005), allow the determination of the timing of granite emplacement. The closure temperature for Ar diffusion in muscovite is estimated at 425 ± 50°C (Villa, 1998). Muscovite $^{40}Ar/^{39}Ar$ ages can be interpreted as the age of cooling and/or mylonitisation. $^{40}Ar/^{39}Ar$ geochronology of muscovite was used in this study to determine the timing and duration of minerals (re)crystallization, i.e. timing of the isotopic exchange between the mineral and the fluid (e.g. Mulch and Cosca, 2004; Teyssier et al., 2004; Mulch et al., 2005).

1. $^{40}Ar/^{39}Ar$ geochronology on muscovite

$^{40}Ar/^{39}Ar$ geochronology is a radiometric method that compares the ^{40}Ar (naturally radioactive isotope) with the ^{39}Ar (decay product). As the rate of decay is known and constant, the $^{40}Ar/^{39}Ar$ ratio relates to the sample's age. In other words, the older the sample is, the more ^{40}Ar it contains. Samples were irradiated in a nuclear reactor to be able to produce ^{39}Ar from the stable potassium from ^{39}K. Samples were then heated in a furnace to release gases (including Argon) that were measured by a mass-spectrometer.

White micas used for $^{40}Ar/^{39}Ar$ laser probe step heating experiments were randomly extracted by handpicking them from the largest fraction (f > 500 µm) using a binocular microscope. The muscovite grains were analysed following the analytical procedure described by Ruffet et al. (1991, 1995) and Castonguay et al. (2001, 2007). Irradiation of samples was performed at Mac Master Nuclear Reactor (Hamilton, Ontario, Canada) in the 8F facility and lasted 250.067 h with a global efficiency (J/h) of 1.096×10^{-4} h^{-1}. The irradiation standard was the amphibole Hb3gr (Turner, 1971; Roddick, 1983; Jourdan et al., 2006; Jourdan and Renne, 2007) dated at 1081.0 ± 1.2 Ma according to Renne et al. (2010, 2011).

Apparent age errors were plotted at the 1σ level and do not include the errors on the $^{40}Ar^*/^{39}Ar_K$ ratio and age of the monitor and decay constant. Plateau ages were calculated if 70% or more of the $^{39}Ar_K$ was released in at least three or more contiguous steps, the apparent ages of which agreeing to within 1σ of the integrated age of the plateau segment. Pseudo-plateau ages (PPA) were defined when less than 70% of the $^{39}Ar_K$ was released and in less than three contiguous steps. The errors on the $^{40}Ar^*/^{39}Ar_K$ ratio and age of the monitor and decay constant are included in the final calculation of the error margins on the pseudo-plateau age (PPA) or on apparent ages individually cited.

Analytical data and parameters used for calculations (e.g. isotopic ratios measured on K, Ca and Cl pure salts; mass discrimination; atmospheric argon ratios; J parameter; decay constants) and reference sources are available in **Table II-2**.

Parameters	(^{36}Ar/^{37}Ar)Ca	0.000322	3	%
	(^{39}Ar/^{37}Ar)Ca	0.000788	4	%
	(^{38}Ar/^{37}Ar)Ca	0.000026	100	%
	(^{40}Ar/^{37}Ar)Ca	0.0006	100	%
	(^{40}Ar/^{39}Ar)K	0.00085	4	%
	(^{38}Ar/^{39}Ar)K	0.011	91	%
[3]	(^{36}Cl/^{38}Cl)	316	5	%
[1] and [1']	(^{40}Ar/^{36}Ar)Atm	298.56	0.104	%
[1] and [1']	(^{38}Ar/^{36}Ar)Atm	0.1885	0.159	%
[2]	Lambda 40	5.53E-10	1.35E-12	y-1
	Lambda 39	2.58E-03		y-1
	Lambda 37	1.98E-02		d-1
	Lambda ^{36}Cl	2.26E-06		y-1

Table II-2: Ar/Ar analytical parameters used for calculations and references. References: [1] Lee et al. (2006); [1'] Mark et al. (2011)); [2] Renne et al. (2011); [3] York, Personnal Communication, McMaster reactor. Regression method from York (1968). Ages and errors of Hb3gr and TCs monitors refers to Renne et al. (2011).

2. U-Th/Pb geochronology on monazite

Monazite is a phosphate mineral that contains Rare Earth Elements (REE). It is an accessory mineral found in granitic and metamorphic rocks. U-Th/Pb ages are generally interpreted in terms of metamorphism, deformation, melting and hydrothermal alterations.

In **section III-B**, monazite in migmatite were located and mapped in BSE using a ZEISS Evo MA 10 Scanning Electron Microscope at the University of Portsmouth (UK). In-situ monazite U-Pb and trace element analyses were performed in two separate sessions at the University of Portsmouth using a Jena PlasmaQuant Elite ICP-MS coupled to an ASI RESOlution 193 nm ArF excimer Laser system.

For U-Pb analyses, Trebilcock monazite (~272 Ma; Tomascak et al., 1996), was used as the primary reference material and Itambé (aka Moacyr, ^{207}Pb/^{235}U age 509.1 ± 1.2 Ma; Gonçalves et al., 2016) and Bananeira monazites (^{207}Pb/^{235}U age 503.3±1.2 Ma;

Gonçalves et al., 2016) were used as secondary reference materials and gave weighted average ages within 1.2% of reported values (**Table VI-2 in the appendix**). NIST610 glass was used as the primary reference material for trace element analysis. BHVO-2G, and Trebilcock monazite were used as secondary reference material. BHVO-2G gave an average reproducibility of 2.9%; Trebilcock reproduced less well due to non-matrix matched standard problems. Laser conditions for U-Pb analyses were 9 µm spot size, laser fluency of ~2.5 J.cm2 and repetition rate of 3 Hz. Laser conditions for trace element analysis in monazite were 3 µm spot size, laser fluency was ~2 J.cm2 and its repetition rate was 2 Hz. Glasses were ablated under the same conditions with a 60 µm spot size. There was 20 seconds of background measurement, followed by 30 seconds of ablation and 15 seconds of washout for each analysis. Four pulses of pre-ablation using 11 µm spot sizes were used to clean the area before each analysis. Full analytical details are shown in **Table VI-2**. Monazite data were processed, corrected for down-hole fractionation and instrumental drift using the Iolite 3.4 software (Paton et al., 2011). Data was presented using software Isoplot 4. Uncertainties include instrumental drift and were increased in quadrature to include 2% reproducibility of the secondary reference material.

III. THE SOUTHERN ARMORICAN DOMAIN

Introduction

This chapter focusses on the southern Armorican domain (Armorican Massif, France) that experienced crustal thickening and high-pressure metamorphism during the Carboniferous. The southern Armorican Massif has been intensively studied (see review in Ballèvre et al., 2013) due to the exceptional outcropping conditions on the coast of Britany which has allowed the eroded internal zones of the Variscan Belt of Western Europe to be revealed.

Part A is based upon a paper accepted for publication in Terra Nova. It focuses on late-Carboniferous ductile shear zones in the southern part of the Armorican Massif that represent sites of strong fluid-rock interaction. The hydrogen isotope composition of muscovite (δD_{Ms}) from syntectonic leucogranite allows the determination of the source of fluids that infiltrated the footwall of three detachment zones and the South Armorican Shear Zone. This study documents the infiltration of meteoric fluids with δD values as low as -74‰ in the upper part of detachment footwalls.

Part B is a paper in preparation. It presents structural, microstructural, stable isotope, and geochronological ($^{40}Ar/^{39}Ar$ and U-Th/Pb) data from the Quiberon detachment shear zone, where meteoric fluids interacted with muscovite (δD_{Ms} values down to -85‰) and tourmaline (δD_{To} values down to -87‰). Quartz microstructures and EBSD agree with high deformation temperatures (≥ 500°C), that are corroborated by the Ti-in-Ms geothermometer applied to synkinematic muscovite. Various dating techniques (U-Th/Pb, Ar/Ar and Fission Track) applied to different minerals (zircon, monazite and muscovite) that have different closure temperatures allow us to

reconstruct the thermochronological history of the Quiberon detachment zone. It reveals that surface-derived fluids (δD_{water} value ~ -75‰) penetrated the brittle-ductile transition the Quiberon detachment during the Late Carboniferous and interacted with white mica during extensional shearing and mylonitic fabric formation. The downward infiltration of rainfall was enhanced by a combination of brittle fault development in the upper crust, while migmatite sustained convection at depth. Therefore, the Quiberon detachment zone represents an important orogen-scale structure for fault-controlled hydrothermal activity.

Part C presents the fluid inclusions analysis performed on 5 samples from the footwall of Quiberon and Piriac detachment zones. The microstructural and petrological characterisation of fluids inclusions aims to understand better the relationship between the deformation history and fluid entrapment. Then, the microthermometry allows us to calculate the salinity of the fluid and infer the thermobarometric conditions of fluid entrapment. Finally, the oxygen and hydrogen isotope measurements of fluids inclusions acquired using the crush-leach method allow us to decipher the source of the fluid. This work will be submitted for publication once more isotope data has been acquired.

A. Meteoric fluid-rock interaction in Variscan detachment zones

This section is based upon a paper that was accepted for publication in the journal Terra Nova in March 2019 (**Chapter VII**).

1. Introduction

Crustal-scale shear zones are sites of significant fluid circulation and hydrothermal alteration (e.g. McCaig, 1988; Fricke et al., 1992; Mulch et al., 2006b; Gébelin et al., 2011; Menzies et al., 2014). They represent critical interfaces where metamorphic, magmatic and surface-derived fluids meet (e.g. Upton et al., 1995; Nesbitt and Muehlenbachs, 1995; Mulch et al., 2006b; Gébelin et al., 2015, 2017). Characterization of a meteoric component of crustal fluids is crucial to better understand ore deposition at the orogen scale (e.g. Boiron et al., 2003) or for paleoaltimetry reconstructions (e.g. Mulch et al., 2004, 2007; Gébelin et al., 2012, 2013).

Muscovite that crystallized at depth during deformation-related fluid flow provides a reliable record to track meteoric-derived fluids that circulated in ductile shear zones during high temperature deformation (~400-600°C; e.g. Gébelin et al., 2011, 2015; Methner et al., 2015). In particular, the hydrogen isotope ratio of the fluid (δD_{water}) can be estimated if muscovite-water hydrogen isotope equilibrium was attained during deformation and crystallization, and if the temperature of isotope exchange can be assessed independently (Fricke et al., 1992; Mulch and Cosca, 2004; Mulch et al., 2007). In addition, the high resistance of muscovite to post-deformational alteration and low-temperature isotopic exchange makes it an excellent tracer of water present during deformation (e.g. Guggenheim et al., 1987; Mariani et al., 2006).

This method has proven to be one of the cornerstones when recovering the isotopic composition of ancient rainfall that infiltrated the upper crust through a brittle deformation network down to 15 km depth in the footwall of detachment zones in the North American Cordillera (e.g. Fricke et al., 1992; Losh, 1997; Mulch et al., 2004, 2007; Gébelin et al., 2011, 2012, 2015), in the European Central Alps (Campani et al., 2012) but also in the Himalaya (Gébelin et al., 2013, 2017).

Here hydrogen isotope geochemistry of synkinematic muscovite (δD_{Ms}) from Variscan strike-slip and detachment footwalls of the Armorican Massif (**Fig. III-1**) is employed to identify and characterize ancient meteoric water that circulated along and across the brittle-ductile transition. Low δD_{Ms} values indicate that meteoric fluids infiltrated the upper part of detachment footwalls and strike-slip shear zones to variable degrees.

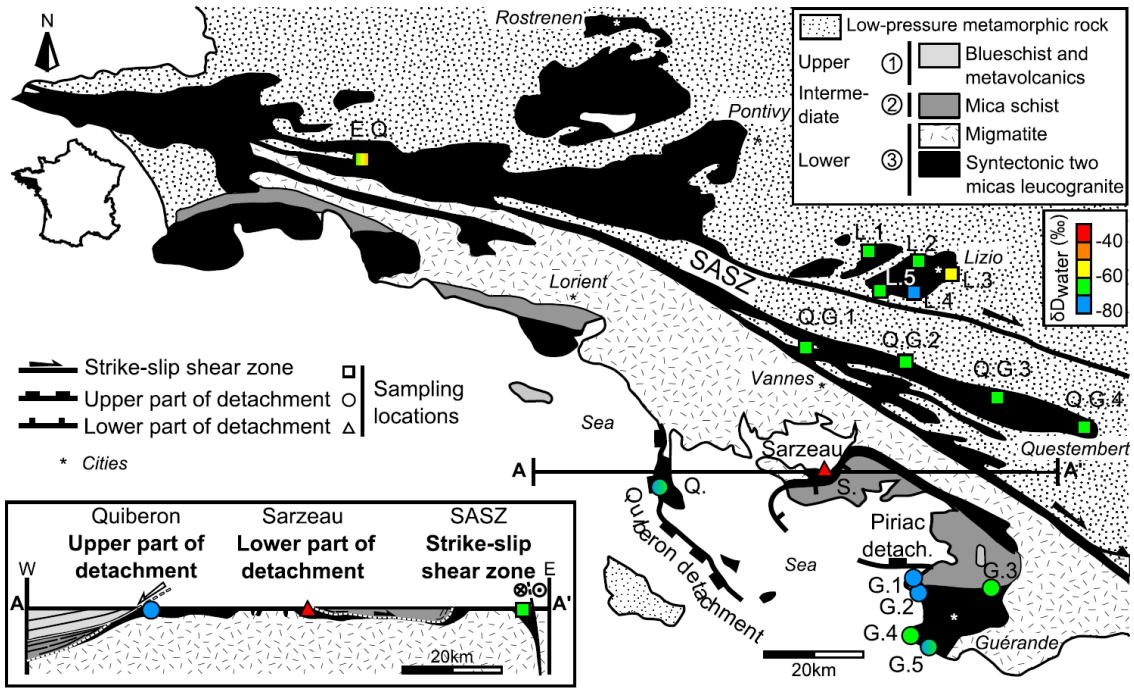

Figure III-1: General map of the southern Armorican domain and E-W cross-section (AA'). Samples sites colours indicate the calculated hydrogen isotope composition of fluids that interacted with muscovite in syntectonic granites. E.Q: Elliant quarry; Q.G.: Questembert granite; L.: Lizio leucogranite; S.: Sarzeau leucogranite; Q.: Quiberon leucogranite G.: Guérande leucogranite; modified after Gapais et al. (1993).

2. Geological framework

The southern Armorican domain represents the internal zone of the Variscan Belt that experienced crustal thickening and high-pressure metamorphism during the Carboniferous (e.g. Ballèvre et al., 2013). From top to bottom, three units can be distinguished (**Fig. I-1**): 1) Upper units (blueschists and greenschist facies metasediments and metavolcanics; Bosse et al., 2002; Le Hébel et al., 2002); 2) Intermediate units (mica schist; Barrovian metamorphism from greenschist to amphibolite facies conditions; Triboulet and Audren, 1988); 3) Lower units (migmatites; 750°C-1000MPa; Jones and Brown (1990) and syntectonic peraluminous leucogranites).

The entire region was affected by coeval WNW-ESE trending dextral strike-slip and E-W extensional faulting during the Late Carboniferous that provided effective pathways for melt migration and fluid infiltration (e.g. Gapais et al., 2015). Syntectonic two-mica leucogranites forming the footwall of detachment shear zones and spatially associated with the dextral South Armorican Shear Zone (SASZ) were emplaced between ~320 and 300 Ma (Ar/Ar on muscovite and U-Th-Pb on zircon and monazite; e.g. Jegouzo, 1980; Gapais, 1989; Brown and Dallmeyer, 1996; Turrillot et al., 2009, 2011a; Tartèse et al., 2012; Ballouard et al., 2015, 2017; Gapais et al., 2015).

3. Sampling strategy and sample description

To characterize the role of different types of active shear zones in controlling meteoric water infiltration in the Variscan crust, oriented samples of highly to weakly deformed leucogranites were collected along the SASZ and following transects from Quiberon and Piriac detachment shear zones into their underlying mylonitic footwalls (samples locations in **Table 1**). Some leucogranites display albitic and chloritic alteration that, together with the presence of quartz veins, point to the involvement of magmatic

and/or hydrothermal fluids (higher Sn and Cs content and lower K/Rb and Nb/Ta ratios; e.g. Ballouard et al., 2016). Also, the involvement of surface-derived fluids is suspected by oxygen isotope analysis ($\delta^{18}O_{Quartz}$ values as low as -2‰ in quartz veins formed at ~250-350°C; e.g. Lemarchand et al., 2012; Tartèse et al., 2012; Ballouard et al., 2017). Leucogranite samples from the Sarzeau detachment shear zone that allows the observation of a deeper structural level (e.g. Gapais et al., 2015) were also collected.

Sub-solidus deformation textures such as rectangular and castellate quartz grain boundaries indicate that grain boundary migration (≥550°C; e.g. Stipp et al., 2002; Bukovská et al., 2016) was the dominant dynamic recrystallization process that affected mylonitic syntectonic leucogranites from all three types of shear zones (**Fig. III-2**). These microstructural observations, together with EBSD data indicating prism <c> and <a> glide (Gapais and Boundi, 2014; Bukovská et al., 2016), support high deformation temperature (≥400°C, e.g. Langille et al., 2010).

C-S structures highlighted by muscovite fish along shear and schistosity planes indicate a syntectonic emplacement of leucogranites (e.g. Gapais, 1989; **Fig. III-3**, Supporting Information). Solution-precipitation mechanisms can explain the development of synkinematic lozenge-shaped muscovite grains (groups 1, 2 and 3 of ten Grotenhuis et al. (2003) classification; **Figs. III-3 and III-4**). Weakly deformed granite display euhedral muscovite grains and large primary quartz crystals and/or quartz grain boundary migration consistent with high-temperature deformation (**Fig. III-4**).

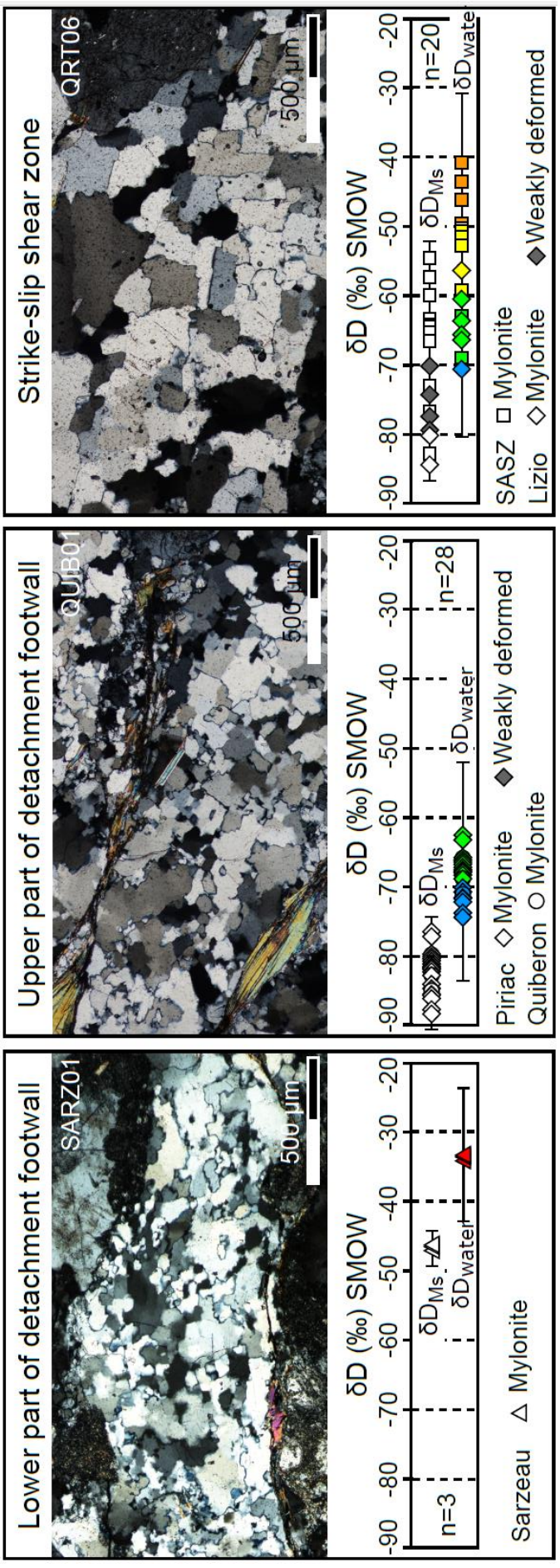

Figure III-2:

Representative quartz microstructure from the SASZ and detachment zones as well as associated measured δD_{Ms} values (± 2‰) and calculated δD_{water} values (± 10‰).

Hydrogen isotope ratios of water have been calculated from δD_{Ms} values using a deformation temperature of 550 ± 100˚C and temperature-dependent fractionation equations from Suzuoki and Epstein (1976).

4. Hydrogen isotope geochemistry

δD values of muscovite (δD_{Ms}) were measured in 51 syntectonic leucogranite samples from the different ductile shear zones (**Fig. III-2**; Methods in **Chapter II** and data in **Table III-1**). δD_{Ms} values from the Sarzeau detachment footwall (SARZ-) range from -47 to -46‰ (n=3). δD_{Ms} values from the Quiberon (QUIB-) and Piriac (PIR-, GUE-) transects are constant within the footwall from the top to the bottom and range from -88 to -76‰. Weakly deformed leucogranites located at larger distance from the hanging wall (GUEweakd-) have similar values (-84 to -80‰).

δD_{Ms} values from mylonitic samples from the SASZ (ELL-, QRT-, QUEST-, LRT-) vary from -84 to -54‰. The range of values allows to define a lateral trend from lower δD_{Ms} values (-84 to -79‰) obtained on highly deformed samples within the SASZ to higher δD_{Ms} values (-79 and -70‰) at increasing distance from the deformation zone where leucogranites are weakly deformed (GRTweakd-, LRTweakd-; **Figs. III-1 and III-2**).

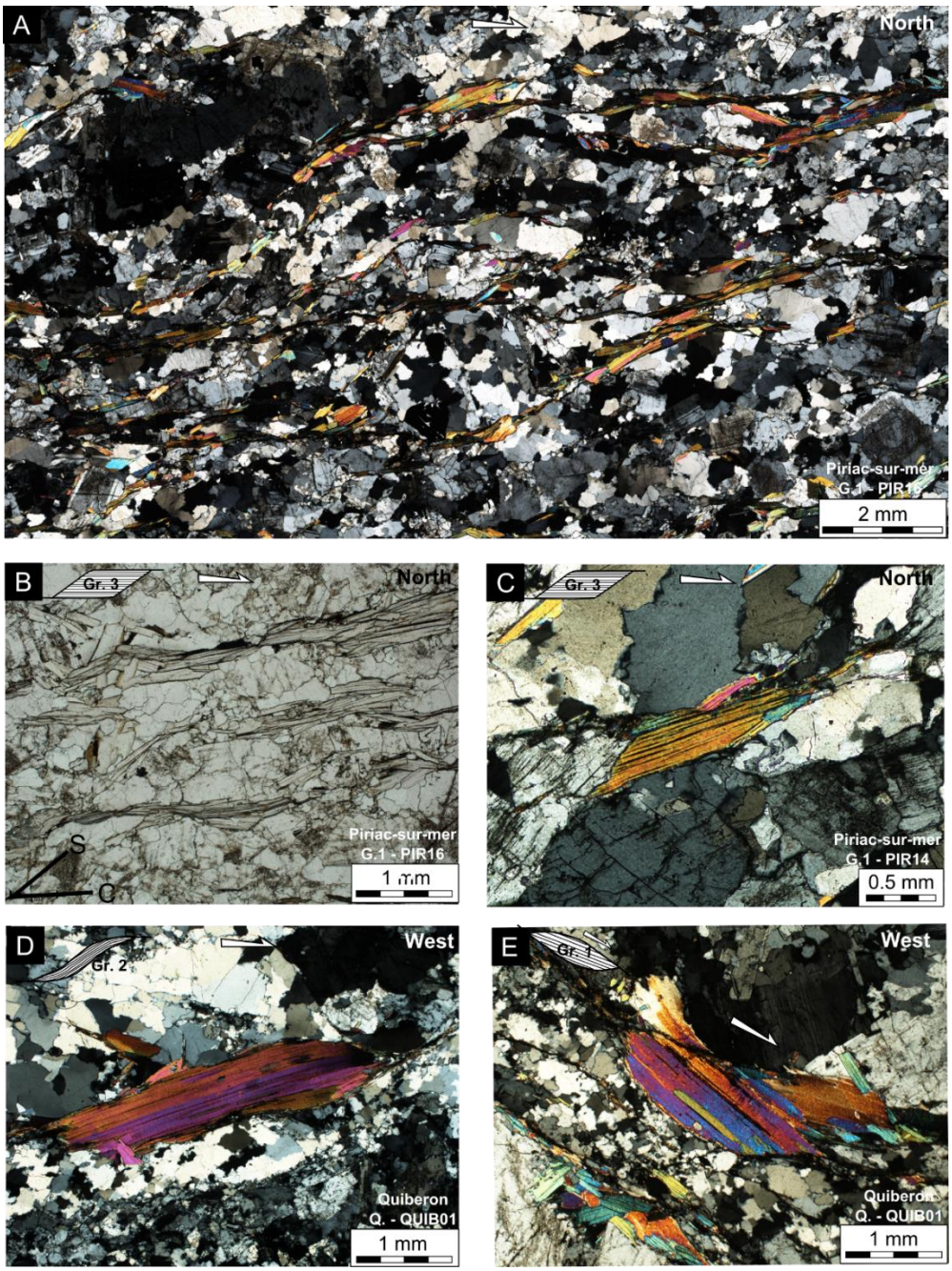

Figure III-3: Muscovite microstructures from the upper part of Quiberon and Piriac detachments footwall. Sections are cut perpendicular to foliation and parallel to lineation. Sub-solidus deformation textures such as rectangular and castellate quartz grain boundaries suggest that grain boundary migration (regime 3, Hirth and Tullis, 1992) was the dominant dynamic recrystallization process. (A) and (B) Muscovite fish (group 3 of ten Grotenhuis et al., 2003) from the Guérande mylonitic leucogranite forming C-S structures indicating a top-to-the-north sense of shear (Location G.1 on fig. DR1; sample PIR16 in table DR1); (C) Rhomboidal muscovite fish as observed in (A) and (B) (group 3) highlighting a cleavage parallel to the longest side of the fish that develops as a result of synthetic slip on (001) basal planes (G.1; PIR14); (D) Group 2 mica fish that forms from group 1 mica fish as a result of drag along micro shear planes that develop along the upper and lower sides of the grain, indicating a top-to-the-west sense of shear (Q.; QUIB01); (E) Lenticular muscovite fish (group 1) forming C-S structures that formed by rotation and then removal of the upper and lower part of the grain indicating a recrystallization process by solution-precipitation (QUIB01).

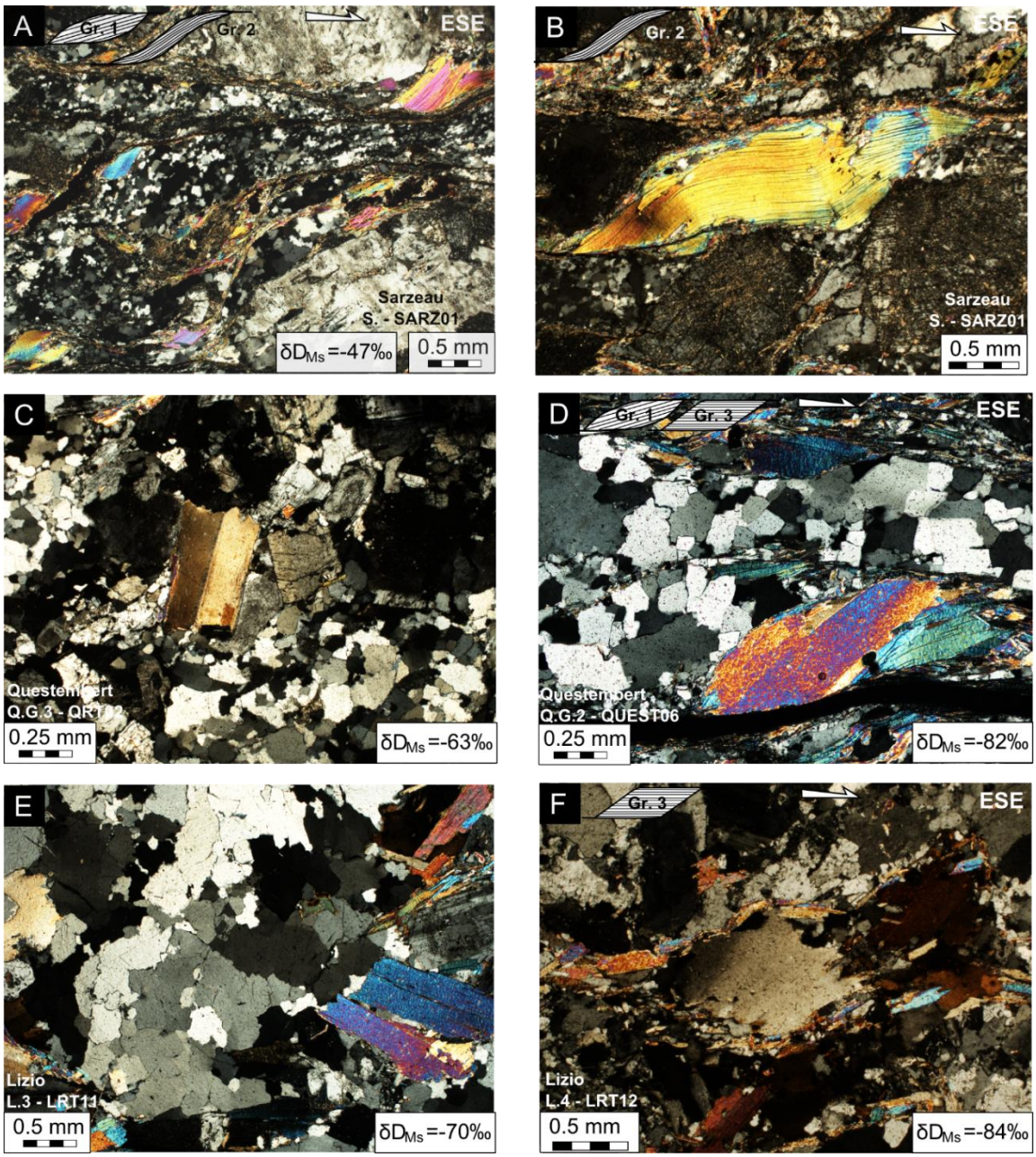

Figure III-4: : Muscovite microstructures from Sarzeau disclosing the lower part of the detachment footwall (A, B), and from the Questembert (C, D) and Lizio (E, F) leucogranites that emplaced within the active South Armorican Shear Zone (SASZ). Sections are cut perpendicular to foliation and parallel to lineation and quartz microstructures suggest that grain boundary migration was the dominant dynamic recrystallization process. (A) and (B) Muscovite fish (group 1 and 2 of ten Grotenhuis et al., 2003) from the Sarzeau mylonitic leucogranite forming C-S structures indicating a top-to-the-ESE sense of shearing. Group 1 mica fish show evidence of recrystallization by solution-precipitation and evolve into group 2 by drag along micro shear planes and folding; Within the Questembert leucogranite, (C) euhedral muscovite fish from the weakly deformed facies (see location G.3 on Fig. DR1) provide a higher δD_{Ms} value (-63‰) than (D) lenticular muscovite fish (G.2 on Fig. DR1) that give a lower δD_{Ms} value (-82‰) suggesting an interaction with meteoric fluids. (E) Euhedral muscovite (see location L3 on Fig. DR1) from the weakly deformed Lizio granite facies yielding a higher δD_{Ms} value (-70‰) than (F) muscovite fish (group 3) forming C-S structures in the high strain zone (L.4 on Fig. DR1) that provides δD_{Ms} value as low as -84‰.

Type	Area	Fig. 1	Sample	Rock type	δD_{Ms} (‰)	Structural distance from the detachment hanging wall (m)	Latitude (DD)	Longitude (DD)
Lower part of detachment footwall	Sarzeau	S.	2016-SARZ01	Mylonitic leucogranite	**-47**	6	47.527336	-2.755594
		S.	2016-SARZ02	Mylonitic leucogranite	**-46**	12	47.527597	-2.752014
		S.	2016-SARZ03	Mylonitic leucogranite	**-46**	140	47.544139	-2.724361
Strike-slip shear zone	Elliant quarry	E.Q.	2016-ELL01	Mylonitic leucogranite	**-65**	n/a.	47.975056	-3.894417
		E.Q.	2016-ELL03	Mylonitic leucogranite	**-60**	n/a.	47.976167	-3.894000
		E.Q.	2016-ELL05	Mylonitic leucogranite	**-64**	n/a.	47.976444	-3.894000
		E.Q.	2016-ELL06	Mylonitic leucogranite	**-57**	n/a.	47.976556	-3.893972
		E.Q.	2016-ELL07	Mylonitic leucogranite	**-54**	n/a.	47.976556	-3.893972
		E.Q.	ELL08	Mylonitic leucogranite	**-73**	n/a.	47.975686	-3.893881
		E.Q.	ELL09	Mylonitic leucogranite	**-76**	n/a.	47.975606	-3.892611
		E.Q.	ELL10	Mylonitic leucogranite	**-66**	n/a.	47.975456	-3.894297
		E.Q.	ELL11	Mylonitic leucogranite	**-64**	n/a.	47.975186	-3.891769
	Questembert granite	Q.G.1	Q-RT-08	Mylonitic leucogranite	**-74**	n/a.	47.728056	-2.617500
		Q.G.2	2016-QUEST04	Mylonitic leucogranite	**-80**	n/a.	47.709300	-2.551819
		Q.G.2	2016-QUEST06	Mylonitic leucogranite	**-82**	n/a.	47.709300	-2.551819
		Q.G.3	Q-RT-02	Mylonitic leucogranite	**-63**	n/a.	47.671667	-2.361944
		Q.G.4	Q-RT-01	Mylonitic leucogranite	**-74**	n/a.	47.648889	-2.160000
	Lizio granite	L.1	GRTweakd-16	*Weakly deformed leucogranite*	**-77**	n/a.	47.908333	-2.688889
		L.1	GRTweakd-17	*Weakly deformed leucogranite*	**-74**	n/a.	47.897500	-2.696667
		L.2	LRTweakd-10	*Weakly deformed leucogranite*	**-79**	n/a.	47.887222	-2.569444
		L.3	LRTweakd-11	*Weakly deformed leucogranite*	**-70**	n/a.	47.873333	-2.497500
		L.4	LRT-12	Mylonitic leucogranite	**-84**	n/a.	47.838056	-2.589722
		L.5	LRT-14	Mylonitic leucogranite	**-79**	n/a.	47.831944	-2.645000
Upper part of detachment footwall	Piriac-sur-mer (Guérande granite)	G.1	2016-PIR01	Mylonitic leucogranite	**-81**	500	47.383722	-2.547472
		G.1	2016-PIR02	Mylonitic leucogranite	**-82**	503.5	47.383722	-2.547444
		G.1	2016-PIR03	Mylonitic leucogranite	**-81**	507.5	47.383722	-2.547417
		G.1	2016-PIR04	Mylonitic leucogranite	**-79**	509	47.383667	-2.547389
		G.1	2016-PIR05	Mylonitic leucogranite	**-85**	512	47.383611	-2.547306
		G.1	2016-PIR06	Mylonitic leucogranite	**-76**	517	47.383528	-2.547389
		G.1	2016-PIR07	Mylonitic leucogranite	**-79**	521	47.383444	-2.547139
		G.1	2016-PIR08	Mylonitic leucogranite	**-80**	523	47.383333	-2.547166
		G.1	2016-PIR09	Mylonitic leucogranite	**-82**	526	47.383194	-2.547000
		G.1	2016-PIR10	Mylonitic leucogranite	**-85**	528	47.383083	-2.546972
		G.1	2016-PIR11	Mylonitic leucogranite	**-87**	531	47.382972	-2.546972
		G.1	2016-PIR12	Mylonitic leucogranite	**-77**	536	47.382806	-2.546889
		G.1	2016-PIR13	Mylonitic leucogranite	**-84**	540	47.382694	-2.546583
		G.1	2016-PIR14	Mylonitic leucogranite	**-81**	544	47.382472	-2.546417
		G.1	2016-PIR15	Mylonitic leucogranite	**-88**	550	47.382306	-2.546667
		G.1	2016-PIR16	Mylonitic leucogranite	**-88**	560	47.382111	-2.547083
		G.1	GUE12-09	Mylonitic leucogranite	**-85**	570	47.381192	-2.548596
		G.2	GUE12-06	Mylonitic leucogranite	**-85**	1900	47.370945	-2.515918
		G.2	GUE12-21	Mylonitic leucogranite	**-86**	2150	47.365750	-2.541317
		G.3	GUE12-07	Mylonitic leucogranite	**-80**	2000	47.380000	-2.346883
		G.4	GUEweakd12-14	*Weakly deformed leucogranite*	**-81**	8000	47.296217	-2.546383
		G.4	GUEweakd12-17	*Weakly deformed leucogranite*	**-80**	8100	47.286967	-2.526550
		G.5	GUEweakd12-11	*Weakly deformed leucogranite*	**-81**	10000	47.274183	-2.484200
		G.5	GUEweakd12-12	*Weakly deformed leucogranite*	**-84**	10000	47.274183	-2.484200
		G.5	GUEweakd12-13	*Weakly deformed leucogranite*	**-81**	10000	47.274367	-2.484533
	Quiberon (Quiberon granite)	Q.	2016-QUIB01	Mylonitic leucogranite	**-85**	300	47.484472	-3.143917
		Q.	2016-QUIB02	Mylonitic leucogranite	**-79**	305	47.484500	-3.143694
		Q.	2016-QUIB03	Mylonitic leucogranite	**-82**	322	47.484444	-3.143750

Table III-1: GPS location and hydrogen isotope composition of muscovite from syntectonic granite along the South Armorican Shear Zone, the mylonitic footwall of Quiberon and Piriac-sur-mer detachment zones and Sarzeau intra-crustal shear zone. ELL, LRT, GRT and QRT samples are the ones described in Tartèse and Boulvais (2010) and Tartèse et al. (2011, 2012, 2013). GUE samples are from Ballouard et al. (2015, 2017).

Type	Area	Fig. 1	Sample	**δD_{Ms} (‰)**	δD_{water} (‰) 450°C	**δD_{water} (‰) 550°C**	δD_{water}(‰) 650°C
Lower part of detachment footwall	Sarzeau	S.	2016-SARZ01	**-47**	-24	**-34**	-40
		S.	2016-SARZ02	**-46**	-23	**-33**	-40
		S.	2016-SARZ03	**-46**	-23	**-33**	-39
Strike-slip shear zone	Elliant quarry	E.Q.	2016-ELL01	**-65**	-42	**-52**	-58
		E.Q.	2016-ELL03	**-60**	-37	**-46**	-53
		E.Q.	2016-ELL05	**-64**	-41	**-51**	-57
		E.Q.	2016-ELL06	**-57**	-34	**-44**	-50
		E.Q.	2016-ELL07	**-54**	-31	**-41**	-48
		E.Q.	ELL08	**-73**	-50	**-59**	-66
		E.Q.	ELL09	**-76**	-53	**-63**	-70
		E.Q.	ELL10	**-66**	-43	**-53**	-60
		E.Q.	ELL11	**-64**	-41	**-50**	-57
	Questembert granite	Q.G.2	2016-QUEST04	**-80**	-57	**-66**	-73
		Q.G.2	2016-QUEST06	**-82**	-59	**-69**	-76
		Q.G.4	Q-RT-01	**-74**	-51	**-60**	-67
		Q.G.3	Q-RT-02	**-63**	-40	**-50**	-56
		Q.G.1	Q-RT-08	**-74**	-51	**-60**	-67
	Lizio granite	L.2	*LRTweakd-10*	**-79**	-56	**-66**	-72
		L.3	*LRTweakd-11*	**-70**	-47	**-57**	-63
		L.4	LRT-12	**-84**	-61	**-71**	-77
		L.5	LRT-14	**-79**	-56	**-66**	-72
		L.1	*GRweakdT-16*	**-77**	-54	**-64**	-70
		L.1	*GRTweakd-17*	**-74**	-51	**-61**	-67
Upper part of detachment footwall	Piriac-sur-mer (Guérande granite)	G.1	2016-PIR01	**-81**	-58	**-68**	-75
		G.1	2016-PIR02	**-82**	-59	**-69**	-76
		G.1	2016-PIR03	**-81**	-58	**-68**	-74
		G.1	2016-PIR04	**-79**	-56	**-66**	-73
		G.1	2016-PIR05	**-85**	-62	**-72**	-78
		G.1	2016-PIR06	**-76**	-53	**-63**	-69
		G.1	2016-PIR07	**-79**	-56	**-66**	-72
		G.1	2016-PIR08	**-80**	-57	**-66**	-73
		G.1	2016-PIR09	**-82**	-58	**-68**	-75
		G.1	2016-PIR10	**-85**	-62	**-72**	-78
		G.1	2016-PIR11	**-87**	-64	**-74**	-80
		G.1	2016-PIR12	**-77**	-54	**-63**	-70
		G.1	2016-PIR13	**-84**	-60	**-70**	-77
		G.1	2016-PIR14	**-81**	-58	**-68**	-74
		G.1	2016-PIR15	**-88**	-65	**-74**	-81
		G.1	2016-PIR16	**-88**	-65	**-74**	-81
		G.1	GUE12-06	**-85**	-61	**-71**	-78
		G.2	GUE12-07	**-80**	-56	**-66**	-73
		G.2	GUE12-09	**-85**	-62	**-72**	-78
		G.3	GUE12-21	**-86**	-62	**-72**	-79
		G.5	*GUEweakd12-11*	**-81**	-58	**-68**	-74
		G.5	*GUEweadkd12-12*	**-84**	-61	**-71**	-77
		G.5	*GUEweadkd12-13*	**-81**	-58	**-68**	-74
		G.4	*GUEweadkd12-14*	**-81**	-58	**-68**	-74
		G.4	*GUEweadkd12-17*	**-80**	-57	**-67**	-73
	Quiberon (Quiberon granite)	Q.	2016-QUIB01	**-85**	-61	**-71**	-78
		Q.	2016-QUIB02	**-79**	-56	**-66**	-73
		Q.	2016-QUIB03	**-82**	-59	**-69**	-76

Error calculation taking into account the precision on the isotopic analysis and the temperature isotopic exchange

	Error	Error in δD_{water}	Propagated error in δD_{water}
Isotopic analysis (δD_{Ms})	± 2‰	± 2‰	± 10.2‰
Deformation temperature	± 100°C	± 10‰	

Table III-2: Calculated δD_{water} values, with error taking into account the precision on isotopic analyses (δD_{Ms} ± 2‰) and the uncertainties linked to the temperature of recrystallization (550 ± 100˚C results in δD_{water} uncertainties of ± 10‰). δD_{water} values have been calculated by using the hydrogen isotope muscovite-water fractionation factor (α) of Suzuoki and Epstein (1976) with 10lnα varying from -23.2‰ at 450°C to -6.8‰ at 650°C.

Based on microstructural observations (e.g. C-S structures and quartz Grain Boundary Migration; ≥550°C; e.g. Stipp et al., 2002) and previous EBSD data (≥400°C; Gapais and Boundi, 2014; Bukovská et al., 2016), a temperature of deformation of 550 ± 100°C was used which corresponds to the temperature of hydrogen isotope exchange between the fluid and the mineral. Together with measured δD_{Ms} values and using the hydrogen isotope muscovite-water fractionation of Suzuoki and Epstein (1976), δD values of the fluid (δD_{water} ±10‰ taking into account analytical and temperature uncertainties) present during deformation and (re)crystallization were calculated and vary from –34 to −33‰ in the Sarzeau detachment zone, from –74 to −63‰ in the Quiberon and Piriac detachment zones, and from –71 to −41‰ in the SASZ (**Figs. III-1, III-2 and III-5**; **Table III-2**).

5. Discussion

a. Meteoric infiltration and mixing with deep crustal fluids

Samples from Sarzeau exposing the deepest part of a detachment footwall display calculated δD_{water} values of -34 to -33‰ which are significantly higher than those obtained from the Quiberon and Piriac detachments (δD_{water} values as low as -74‰; **Fig. III-5**). δD_{water} values calculated from samples collected in the SASZ vary from –71 to −41‰, covering the entire range of hydrogen isotope compositions found in Sarzeau and in Quiberon and Piriac.

Considering that the Sarzeau granite was emplaced at ~15 km depth (Turrillot et al., 2011b), the highest calculated δD_{water} value (~-33‰) is interpreted to reflect the hydrogen isotope composition of a deep crustal fluid (-70‰ < $\delta D_{metamorphic\ fluids}$ < -20‰ and/or -80‰ < $\delta D_{magmatic\ fluids}$ < -40‰; e.g. Field and Fifarek, 1985) present during deformation at such a depth. In contrast, the lower δD_{water} values obtained from

Quiberon and Piriac (-74‰ to −63‰) suggest that muscovite from these syntectonic leucogranites interacted with deuterium-depleted fluids during deformation. These lower δD_{water} values (41‰ lower than those obtained from Sarzeau) can most readily be explained by the involvement of meteoric fluids, in good agreement with the shallower depths of granite emplacement at Quiberon and Piriac (~ 3-6 km; Le Hébel et al., 2007; Ballouard et al., 2017).

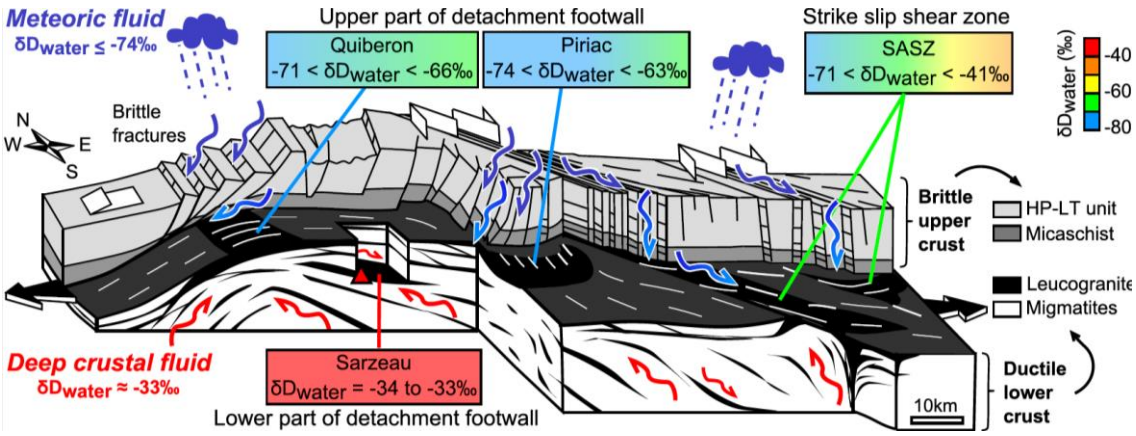

Figure III-5: 3D simplified sketch showing the crustal-scale ductile shear zones and associated δD_{water} values. Blue arrows: meteoric fluids infiltration. Red Arrows: deep crustal fluids. SASZ: South Armorican Shear Zone.

The range of δD_{water} values (-74‰ to -33‰) obtained from the Variscan shear zones of the southern Armorican domain indicates a mixing relationship between deep crustal fluids and meteoric fluids in the mylonitic detachment footwalls and along the SASZ. As shown in **Figs. 5 and 6**, two fluid end-members are defined: a crustal fluid that predominantly involves magmatic and/or metamorphic fluids (δD_{water} value = -33‰) and a surface-derived fluid that reflects a large percentage of mixing with low-δD meteoric water (δD_{water} value = -74‰).

The variability in the low δD_{water} values within the Quiberon and Piriac detachment zones (-74 to -63‰) and in the SASZ (-71 to -41‰) can be explained by 1) different degrees of mixing with meteoric water, and 2) a difference in the temperature controlling the hydrogen isotope exchange between the fluid and synkinematic muscovite (± 100°C gives an uncertainty of ±10‰ for the δD_{water} values).

In addition, this study suggests that the lowest δD_{water} value of -74‰ represents the hydrogen isotope composition which approximates most closely the value of surface-derived fluid that penetrated the crust at depth during detachments activity (**Fig. 5**). As the downward penetration of meteoric fluids in the crust generally leads to an increase in δD_{water} values due to fluid-rock interaction, this δD_{water} value represents a maximum value that may have been potentially lower than -74 ‰ if it would have been extracted from the near-surface geological record (e.g. Gébelin et al., 2012).

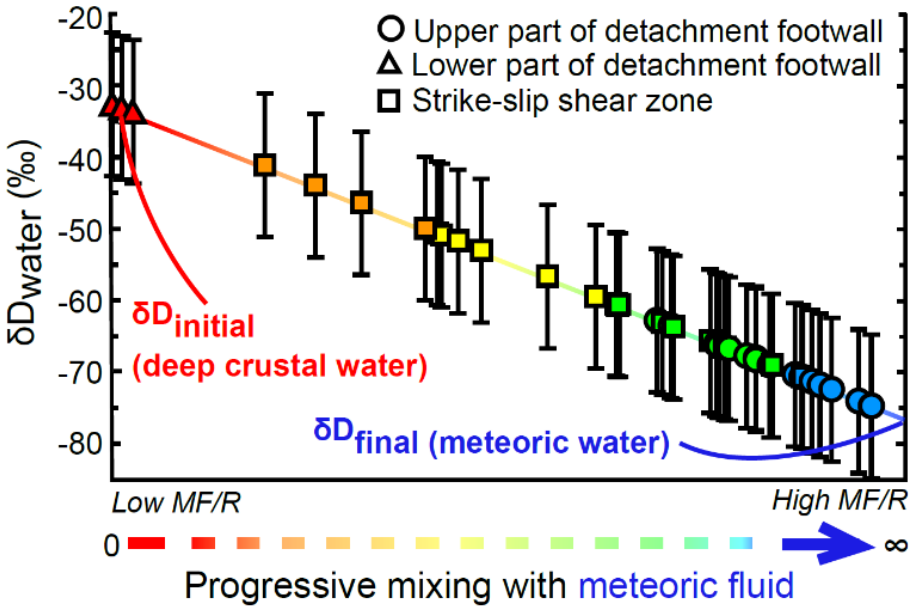

Figure III-6: Graph showing the δD_{water} values from detachments footwall and the SASZ calculated from measured δD values of synkinematic muscovite (this study). Note the progressive involvement of meteoric fluids from an unmixed deep crustal end-member fluid in the Sarzeau lower part of detachment footwall (δD_{water} value = -33‰) to greater

b. Timing, depth and mechanisms of meteoric fluid infiltration

The onset of meteoric fluid infiltration can be estimated at ~320 Ma based on U/Pb ages from syntectonic leucogranites emplaced in detachment footwalls or along strike-slip shear zones (e.g. Tartèse et al., 2012; Ballouard et al., 2015). Deformation and fluid infiltration likely ended at ~300 Ma with the cessation of the shear zones activity ($^{40}Ar/^{39}Ar$ muscovite ages from the same studied leucogranite intrusion; Turrillot et al., 2011a; Tartèse et al., 2012; Gapais et al., 2015; Ballouard et al., 2017, 2018).

Based on the depth at which leucogranites were emplaced at Quiberon and Piriac (~3 to 6 km) and along the SASZ (~3 to 12 km), a minimum depth of ~3 km is estimated for the infiltration of Carboniferous meteoric fluids. However, based on the depth of Sarzeau granite emplacement (~15 km) and on its deep crustal fluid signature, this study infers that the penetration of meteoric fluids in the crust did not exceed ~12 km corresponding to the deepest level of leucogranites emplacement in the SASZ (e.g. Le Hébel et al., 2007; Tartèse and Boulvais, 2010; Turrillot et al., 2011b; Ballouard et al., 2017).

These results are in good agreement with previous studies conducted on ductile shear zones in the Pyrenees, the New Zealand Alps, the North American Cordillera and the Himalaya that highlight the infiltration of meteoric fluids at similar depths (e.g. McCaig, 1988; Upton et al., 1995; Mulch et al., 2004, 2006; Person et al., 2007; Gébelin et al., 2011, 2017; Menzies et al., 2014). As proposed for detachment zones in Western USA and the South Tibetan Detachment (Mulch et al., 2004; Person et al., 2007, Gébelin et al., 2011, 2013; 2015, 2017), three main conditions are essential to explain the downward infiltration of meteoric fluids at depth and imply a combined effect of brittle normal faults in the upper crust, a high geothermal gradient and the presence of a

hydraulic head. These criteria were very likely met in the southern Armorican domain where brittle normal faults have been recognized and linked to the exhumation of high-grade metamorphic rocks at ~300 Ma, but also where the thickened crust would have provided the necessary hydraulic head (Fig. 3; e.g. Gapais et al., 2015; Brown and Dallmeyer, 1996).

Fault-valve rupture (fluid pressure builds up and results in periodically slip where a high volume of fluid can be released) could represent another mechanism for the downward flow of small volumes of meteoric fluids where quick episodes of fluid penetration are followed by protracted periods of fluid stagnation promoting fluid-rock interaction under lithostatic conditions (e.g. Sibson, 1981; McCaig, 1988; Sibson et al., 1988; Jenkin et al., 1994; Upton et al., 1995; Menzies et al., 2014), Fault sealing may enhance the buffering between the deuterium-depleted surface-derived fluids and the deuterium-enriched rocks (Famin et al., 2005), in good agreement with the rock-buffered meteoric fluid signatures found in this study.

c. Isotopic composition of ancient rainfall in the Armorican Massif

Low-δD meteoric precipitation typical of high-altitude regions (δD_{water} ~ -150‰ in the Himalayas; e.g. Quade et al., 2011) are expected in the thickened Armorican Massif. Although this study's data highlight the presence of meteoric fluids at depth, δD values of these surface waters (estimated at -74‰) remain relatively high if corresponding to the initial meteoric water (see above). Four main factors can explain these relatively high δD values for Carboniferous rainfall: 1) a moderate paleoelevation as hydrogen (δD) isotope ratios of rainfall scale with elevation on the windward side of a mountain range (e.g. Poage and Chamberlain, 2001); 2) the equatorial paleogeographic position of the Armorican Massif during the Late Carboniferous (e.g. Tait et al., 1996; Boucot et al., 2013)

would have yielded higher $\delta D_{rainfall}$ values as observed today due to the high global evaporation flux over the oceans at the equator (Rozanski et al., 1993); 3) the warm equatorial late-Carboniferous paleoclimate that characterized the Variscan belt of western Europe could lead to relatively high $\delta D_{meteoric\ water}$ values (e.g. Poulsen and Jeffery, 2011); 4) the presence of major ice sheets (40% more extensive than today) during the Late Carboniferous may have induced an increase of +1.5‰ in the $\delta^{18}O$ of ocean waters or +12‰ for the $\delta D_{ocean\ water}$ values (González-Bonorino and Eyles, 1995; Buggisch et al., 2008).

6. Conclusion

Fluid flow in ductile shear zones is investigated in the southern Armorican domain through muscovite hydrogen isotope ratios (δD_{Ms}) from syntectonic leucogranites emplaced within detachment footwalls and strike-slip fault systems. Mica fish from the lower part of detachment footwalls reveal a typical metamorphic and/or magmatic fluid source, whereas the top of detachment footwalls reveal low δD_{Ms} values indicative of meteoric fluids infiltration. Syntectonic leucogranites from the SASZ also interacted with surface-derived fluids, but varying degrees of mixing between deep-sourced and surface-derived fluids resulted in intermediate δD_{Ms} values. Penetration of surface-derived fluids in the crust occurred between ~320 and 300 Ma by the means of upper-crustal brittle fracture networks while active shear zones continuously exhumed lower-crustal rocks. Ancient rainfall δD values are relatively high compared to present-day major orogens and can be explained by moderate paleoelevation and/or warm paleoclimatic and equatorial paleogeographic conditions. Variscan shear zones in the Armorican Massif represented major orogen-scale structures where fluids from both the Earth's surface and the deep parts of the crust mixed.

B. Late-Carboniferous infiltration of meteoric fluid in the Quiberon detachment zone (Armorican Massif, France)

Publication in preparation for Tectonics by Dusséaux C., Gébelin A., Grimes S., Mulch A., Boulvais P., Ruffet G., Poujol M., Cogné N., Branquet Y., Mottram C., Barou F.

1. Introduction

Extensional shear zones play a major role during post-orogenic collapse as they control lateral and vertical displacements in the continental crust, that in turn affects the Earth's surface dynamics by shaping topography and controls mass transport in the middle and lower crust (e.g. Brun and van den Driessche, 1994; Teyssier and Whitney, 2002; Mulch et al., 2004; Whitney et al., 2013). Therefore, detachment zones that separate the cool upper crust from the hot middle crust are sites of strong fluid-rock interaction where meteoric, metamorphic and magmatic fluids meet (e.g. Fricke et al., 1992; Nesbitt and Muehlenbachs, 1995; Famin et al., 2004; Mulch et al., 2005, 2007; Person et al., 2007; Gébelin et al., 2011, 2015, 2017). Assessing the source of fluids in such hydrothermal systems can be used to better understand ore deposition and mineralization (e.g. Beaudoin et al., 1991; Boiron et al., 2003), but also for paleoaltimetry reconstructions if Earth's surface-derived fluids are present (e.g. Mulch et al., 2004, 2007; Campani et al., 2012; Gébelin et al., 2012, 2013).

Meteoric water infiltration has been documented in the footwall of detachment zones in the North American Cordillera (e.g. Mulch et al., 2004, 2006; Person et al., 2007; Gébelin et al., 2011, 2015) and in the Himalayas (Gébelin et al., 2013, 2017; Webster et al., 2018). These pioneering studies highlight three main conditions for the downward infiltration of meteoric fluids: (1) brittle normal faults and fracture development in the

upper crust which enhances the porosity and permeability, (2) a high geothermal gradient with advection of partially molten material in the footwall that maintains an active convection system for fluids, and (3) a minimum topography that provides the necessary hydraulic head.

This study documents meteoric fluid infiltration in one of the best-exposed Variscan extensional shear zones, the Quiberon detachment zone in the south Armorican Massif (France), that developed as a result of post-orogenic extension of the Variscan belt of Western Europe. The Quiberon detachment (QD) represents an excellent target to better understand the fluid-rock-deformation interaction in the crust and the timing of fluid flow during the Variscan post-orogenic extension because: 1) the structural, metamorphic, and geochronological record of the region is well established (e.g. Gapais et al., 1993, 2015; Turrillot, 2010); 2) brittle normal faults have been identified in the hanging wall of the QD (Gapais et al., 2015); 3) the QD is considered to have played a major role in the exhumation of high-grade metamorphic rocks (Brown and Dallmeyer, 1996), and 4) the region was characterized by a high geothermal gradient in part generated by the emplacement of peraluminous syntectonic leucogranites and migmatites (e.g. Brown and Dallmeyer, 1996; Gapais et al., 2015).

This study presents structural, microstructural, electron backscatter diffraction (EBSD) petrofabrics, Ti-in-muscovite thermometry, hydrogen isotope (δD) and geochronology data ($^{40}Ar/^{39}Ar$ and U-Th/Pb) from mylonitic leucogranites exposed in the QD footwall and associated high-grade metamorphic rocks. These data indicate that surface derived-fluids penetrated the ductile segment of the QD during high temperature deformation and that intense fluid-rock interaction started at ~320 Ma. The QD can be compared, from at least a crustal permeability point of view, to

extensional detachments observed in the western part of the U.S. where tertiary meteoric fluid infiltration was enhanced by the combined effect of steep brittle normal faults development in the upper plate and advection of partially molten rocks in the lower crust.

2. Geological setting and previous works in the southern Armorican domain

a. General tectonic context and timing of metamorphism

The Armorican Massif (Western France) is part of the Ibero-Armorican arc, which forms the western part of the Variscan belt of Western Europe. Three main domains, characterized by contrasted tectonic, geochronological and metamorphic features, are delimited by two major dextral strike-slip shear zones, the North Armorican Shear Zone (NASZ) to the north and the South Armorican Shear Zone (SASZ) to the south. In contrast to the southern domain where substantial Carboniferous crustal thickening and high-pressure metamorphism have been recognized, the northern and central compartments are characterized by moderate crustal thickening and metamorphism (e.g. Ballèvre et al., 2013) (**Fig. III-7A**). In the southern domain, three main units can be identified from top to bottom (**Fig. III-7 A and B**): 1) The upper units formed by blueschists (1.4-1.8 GPa, 550°C) and metavolcanics (0.8 GPa, 350-400°C) (Bosse et al., 2002; Le Hébel et al., 2002, 2007); 2) The intermediate units represented by micaschists characterized by greenschist to amphibolite-facies metamorphism (Bossière, 1988; Triboulet and Audren, 1988; Goujou, 1992); and 3) The lower units marked by the presence of syntectonic leucogranites and high grade metamorphic rocks (0.8 GPa, 700-750°C; Jones and Brown, 1990).

The whole region was affected by active late-Carboniferous strike-slip and coeval extensional shear zones that served as conduits for aqueous fluids and / or melt migration (e.g. Gapais et al., 2015). Syntectonic two-mica leucogranites, resulting from the partial melting of pelitic sediments, emplaced along the South Armorican dextral strike-slip Shear Zone (SASZ) as well as in the footwall of detachment zones (e.g. Jegouzo, 1980; Bernard-Griffiths et al., 1985; Gapais et al., 1993, 2015; Turrillot et al., 2009; Tartèse and Boulvais, 2010; Tartèse et al., 2012; **Fig. III-7 - A and B**). These extensional shear zones separate high pressure-low temperature rocks (blueschist and metavolcanics) from leucogranites and migmatites below (**Fig. III-7**; e.g. Gapais et al., 2015).

The peak of high pressure metamorphism in the upper and intermediate units has been dated between ~370 Ma and ~345 Ma (U/Pb, $^{40}Ar/^{39}Ar$ and Rb/Sr, eg. Bosse et al., 2002, 2005; Le Hébel, 2002; El Korh et al., 2011). Following this episode, activity on ductile shear zones at ~350-345 Ma allowed the exhumation of blueschist, porphyroid and micaschist ($^{40}Ar/^{39}Ar$ and Rb/Sr dates; e.g. Bosse et al., 2002, 2005; Le Hébel, 2002; El Korh et al., 2011; Ballèvre et al., 2012). Migmatites from the lower crust were brought to the surface much later during the Late Carboniferous by the activity on detachment zones that developed as a consequence of post-orogenic extension (e.g. Goujou, 1992; Gapais et al., 1993, 2015; Brown and Dallmeyer, 1996; Cagnard et al., 2004; Turrillot et al., 2011).

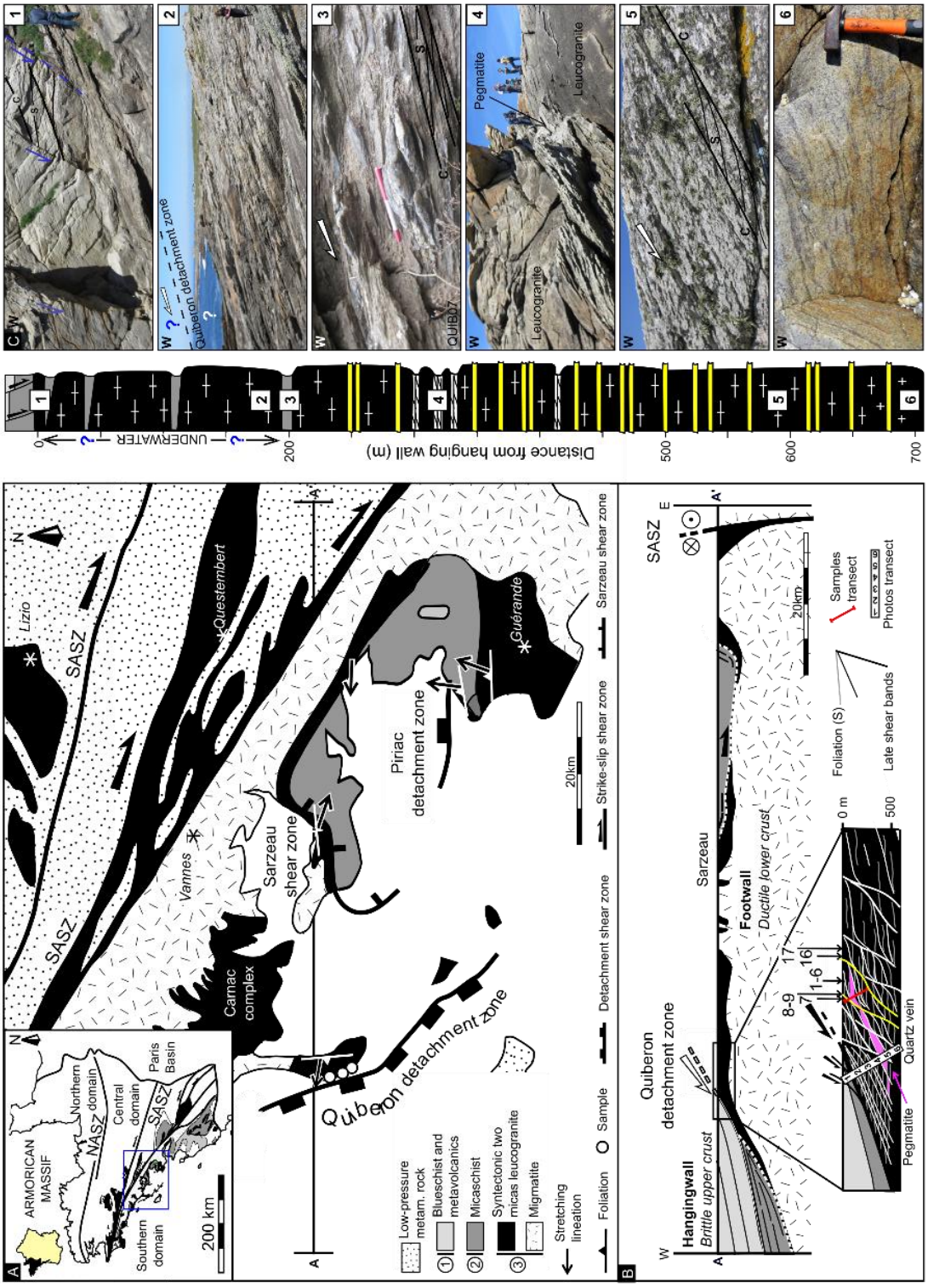

Figure III-7: (A) Map of the southern Armorican domain. SASZ: South Armorican Shear zone; (B) W-E cross-section across the Quiberon detachment and the SASZ with focus on the main structures and rock types found in the Quiberon footwall; (C) Stratigraphic column and associated field pictures: (1) Late brittle normal faults, (2) General view of the Quiberon detachment zone, (3) Micaschist enclave (sample QUIB07), (4) High-strain zone made of ultramylonitic pegmatite and mylonitic leucogranite (samples QUIB03-06), (5) Mylonitic leucogranite with C-S structures highlighting a top-to-the-West sense of shear, (6) Magmatic foliation in weakly deformed leucogranite. Modified after Gapais et al (1993, 2015) and Turillot (2010).

b. The Quiberon detachment zone

The Quiberon detachment footwall exposes two-mica leucogranites that contain a shallow (10-30°) southwest-dipping foliation and ESE-WNW trending stretching lineation (**Fig. III-7**). Kinematic criteria (including C-S structures) indicate a dominant top-to-the-WNW sense of shear (Gapais et al., 1993). Using U/Pb on monazite and zircon from synkinematic leucogranites and $^{40}Ar/^{39}Ar$ thermochronology, the activity of this representative Variscan detachment zone has been bracketed between ~320 Ma and 298 Ma (Turrillot, 2010; Gapais et al., 2015).

Low hydrogen isotope ratios (δD) of synkinematic muscovite from similar syntectonic leucogranite samples indicate that meteoric water interacted with these hydrous silicates during high temperature deformation (Dusséaux et al., 2019). However, the timing of surface-derived fluid infiltration and the duration of isotopic exchange is still elusive. Here, new hydrogen isotope, thermometry and geochronology data on syntectonic leucogranites emplaced in the footwall of the QD and migmatites below are presented. They indicate that the QD represented a major hydrothermal system during the Late Carboniferous, especially at ~300 Ma where syntectonic hydrothermal muscovite and apatite crystallized during partial melting and coeval migmatization. The analytical methods employed are presented in **Chapter II**.

3. Results

a. Structural study

(1) Macrostructures

Quiberon Island provides exceptional outcrop conditions to study a late-Variscan detachment zone (**Fig. III-7 - C2**). It is mainly composed of mylonitic two-mica leucogranite emplaced within the footwall of the Quiberon detachment zone (**Fig. III-7**). Foliation planes (S) dip shallowly to the west and exhibit a strong lineation plunging to the WNW (~N280). S-planes are affected by C-planes that dip to the WSW at 30° (**Figs. III-7 - B, C2 and C5**). The C-planes are parallel to the shear zone boundary and together with the S-planes form shear bands that indicates a top-to-the-WNW sense of shear (**Fig. III-7 – C5**). The ductile shear bands form an heterogeneous and anastomosing network that isolate sigmoidal quartz veins and micaschist lenses (**Fig. III-7-C3**). In some areas, leucogranites are moderately crosscut by pegmatite dykes that display different amount of strain. In high-strain zones, ultramylonitic pegmatite forms a 1 to 2-meter-thick layer, whereas coarser mylonitic leucogranite displays pervasive deformation with more spaced shear planes (**Fig. III-7 - C4**). Down section, away from localized deformation zones, weakly deformed leucogranites outcrop and exhibit a more magmatic foliation (**Fig. III-7 - C6**). Near the contact with the hanging-wall, mylonitic foliation is affected by steep brittle and late normal faults (**Fig. III-7 - C1**).

(2) Microstructures

As observed at the mesoscopic scale, coeval development of muscovite fish along shear and schistosity planes displaying a top-to-the-WNW sense of shear (**Fig. III-8 - A**) strengthens the idea that the Quiberon leucogranite was emplaced at the same time as shear zone activity (e.g. Gapais, 1989). The majority of mica fish are truncated in their upper and lower parts, suggesting that they form by rotation and then process of

solution-precipitation (Group 1, Ten Grotenhuis et al., 2003) (**Fig. III-8 - B and D**). Some of these group 1 muscovite fish evolve into group 2 by drag along micro shear planes that develop along the upper and lower sides of the grain, resulting in bent tips, comparable to the deflection of the S-planes in shear bands (**Fig. III-8 - C**; Passchier and Simpson, 1986). Shear planes also affect the tourmaline grains that display sigmoidal shapes within the shear bands (**Fig. III-8 - A**).

Sub-solidus deformation textures such as rectangular and castellate quartz grain boundaries indicate that grain boundary migration (regime 3, Hirth and Tullis, 1992) was the dominant dynamic recrystallization process that affected the mylonitic syntectonic leucogranite (**Figs. III-8 - E and F**; 500-700°C; e.g. Stipp et al., 2002).

(3) <u>EBSD on quartz grains</u>

The crystallographic-preferred orientation (CPO) of quartz grains is used here as a mean to assess the temperature of quartz (re)crystallization in mylonitic granite from the QD footwall (**Fig. III-8 - G**; analytical procedure in **Chapter II**). Sample QUIB01 is representative of the section and located structurally 300 m below the QD detachment interface, contains ~35% of quartz, 35% of plagioclase, 15% of K-feldspar, 5% of muscovite and less than 1% of biotite. Sigmoidal quartz ribbons **(Fig. III-8 - G)** contain grains affected by grain boundary migration **(Figs. III-8 - E and F)** that indicate high-temperature recrystallization processes. The quartz CPO of a representative quartz ribbon is shown on **Fig. III-8 - G**.

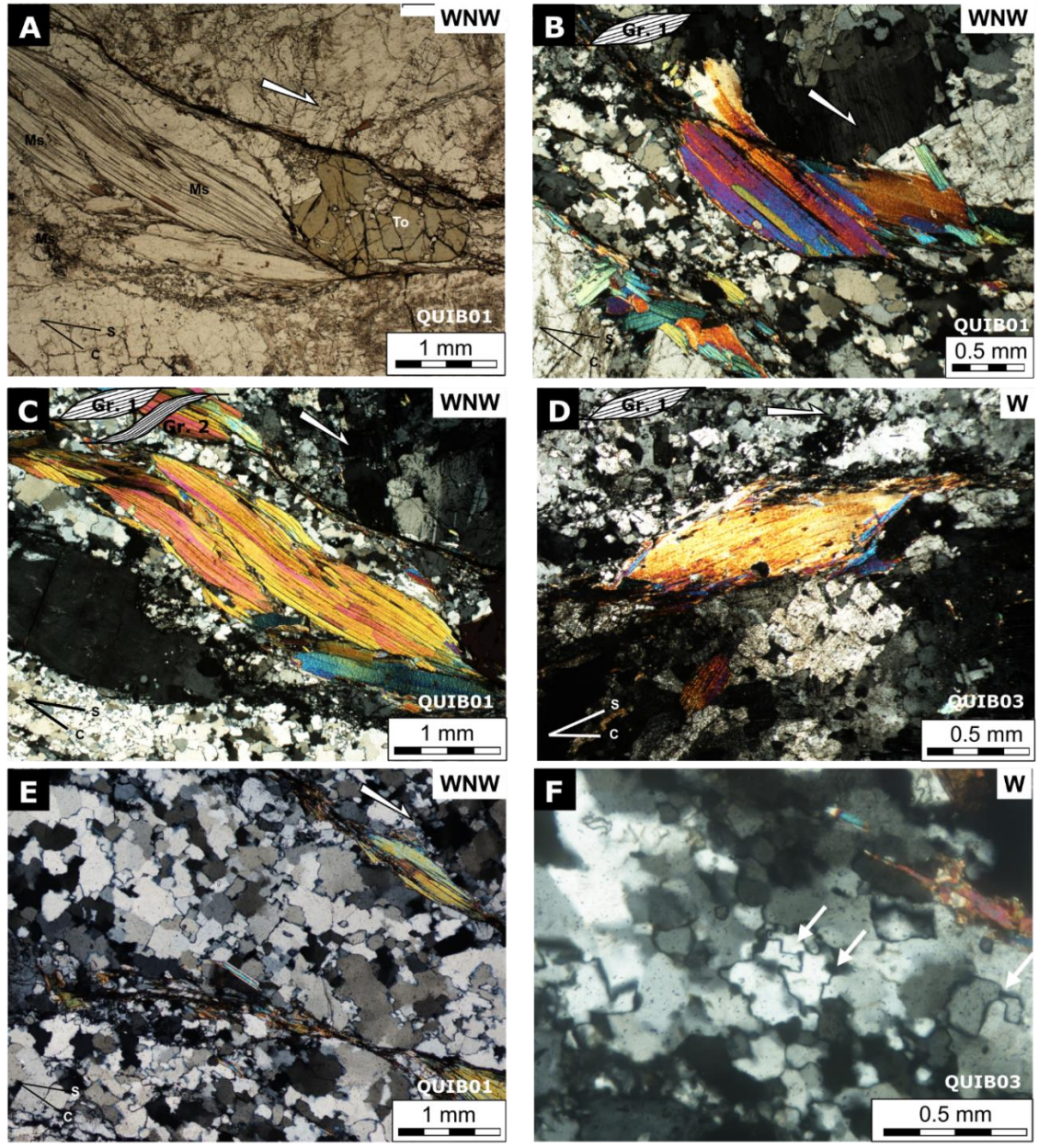
A
WNW
Ms
Ms
Ms
To
S
C
QUIB01
1 mm
B
WNW
Gr. 1
S
C
QUIB01
0.5 mm
C
WNW
Gr. 1
Gr. 2
S
C
QUIB01
1 mm
D
W
Gr. 1
S
C
QUIB03
0.5 mm
E
WNW
S
C
QUIB01
1 mm
F
W
QUIB03
0.5 mm

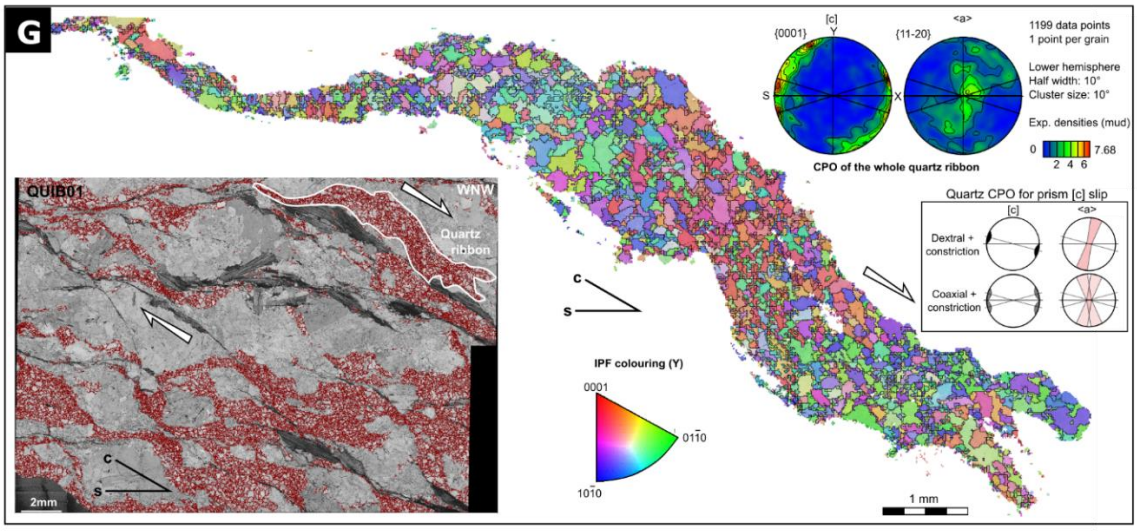
G
QUIB01
WNW
Quartz ribbon
C
S
2mm
{0001}
[c]
Y
S
X
{11-20}
<a>
CPO of the whole quartz ribbon
1199 data points
1 point per grain
Lower hemisphere
Half width: 10°
Cluster size: 10°
Exp. densities (mud)
0
7.68
2 4 6
Quartz CPO for prism [c] slip
[c]
<a>
Dextral + constriction
Coaxial + constriction
IPF colouring (Y)
0001
0110
1010
C
S
1 mm

Figure III-8 (last page): Microstructures from the Quiberon detachment footwall. Sections are cut perpendicular to foliation and parallel to lineation. In mylonitic leucogranite, (A) Muscovite fish are associated with tourmaline sigma clast in shear band; (B) and (D) Lenticular muscovite fish (group 1 of Ten Grotenhuis et al., 2003); (C) Group 2 mica fish that form C-S structures indicating a top-to-the-west sense of shear; (E) and (F) Sub-solidus deformation textures such as rectangular and castellate quartz grain boundaries suggest that grain boundary migration (regime 3, Hirth and Tullis, 1992) was the dominant dynamic recrystallization process; (G) Microstructure and Crystallographic Preferred Orientation (CPO) of quartz grains measured using EBSD. Equal-area projection, Lower hemisphere. Foliation (XY plane) is vertical, and lineation (X) is horizontal in this plane. (1) Band contrast map with quartz grain boundary highlighted in red, (2) Map of a quartz ribbon quartz grain boundary with Inverse Pole Figure (IPF) coloring (Y represents the lineation direction) and (3) corresponding CPO.

Quartz c-axis pole figures exhibits 4 maxima symmetrically distributed at ~25° around the foliation plane (S) and the lineation direction (**Fig. III-8 - G3**) that suggest plastic deformation dominated by prismatic ‹c› glide system in a coaxial context with constriction (see framed model on **Fig. III-8 - G** from Barth et al., 2010). The c-axis also show 2 maxima located at ~70° asymmetrically to the direction of the lineation which can be interpreted as the activation of basal [a] slip. However, Kilian and Heilbronner (2017) have shown that peripheral [c]-axis maxima can occur due to different texture forming processes, especially during the nucleation of new grains at high differential stress levels, but with no relation to the activity of slip systems related to temperature.

Quartz a-axes form a single asymmetric girdle indicating a dextral sense of shear combined with constriction (see framed model on **Fig. III-8 - G** from Barth et al., 2010). Both quartz c- and a-axes points to the activation of prism <c> that typically occurs around 550-600°C (e.g. Okudaira et al., 1995; Stipp et al., 2002). A m.u.d. (multiples of a uniform density) of 7.68 suggests a weak quartz CPO that can be explained by the presence of well-connected mica layers that localize the deformation and that in turn can decrease the amount of strain in the stronger quartz matrix (Hunter et al., 2016).

b. Hydrogen Isotope Geochemistry

The hydrogen isotope compositions (δD values) of muscovite (Ms) and tourmaline (To) were measured in 11 samples of sheared leucogranite, pegmatite, micaschist and quartz veins collected across 300m of structural section into the underlying mylonitic footwall of the Quiberon detachment zone (**Fig. III-9** and **Table III-3**; analytical procedures are summarized in **Chapter II**). The location of the Quiberon detachment shear zone was estimated based on the geological map of France to 1/1000000 (BRGM, 2003). The structural distance of the samples below the Quiberon detachment was estimated based on samples coordinates and assuming an angle of dip of ~38° to the WNW for the detachment. This dataset includes δD values of muscovite previously reported in Dusséaux et al. (2019).

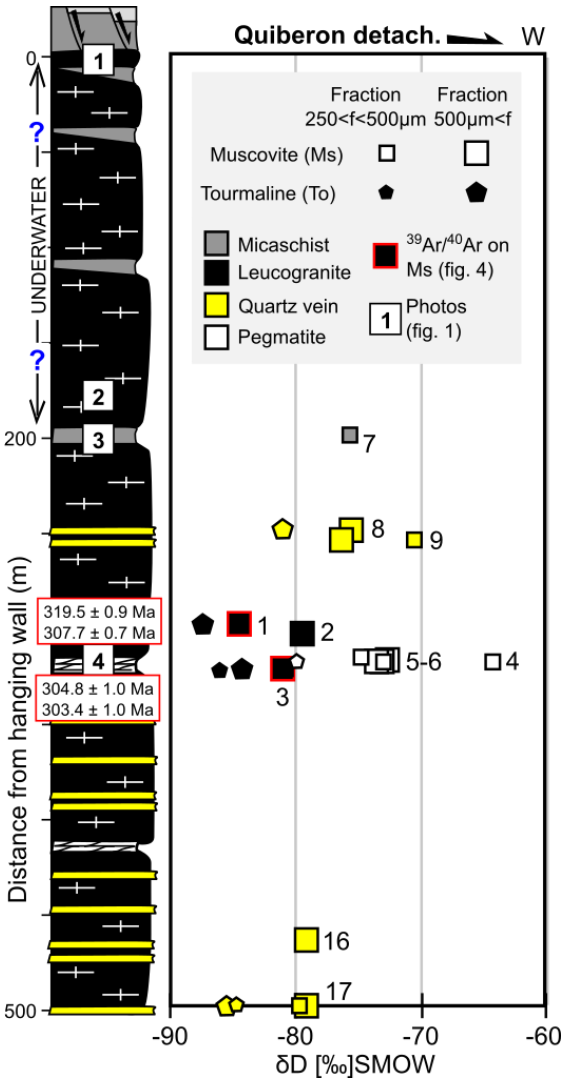

Figure III-9: Hydrogen isotope analysis (δD [‰]) of hydrous silicates (muscovite and tourmaline) from micaschist, leucogranite, quartz veins and pegmatite located in the footwall of Quiberon detachment zone with respect to the distance from the hanging wall (200 to 500m).

Muscovite from leucogranite samples yields δD_{Ms} values from -85 to -79‰, which are 4 to 22‰ lower than those from the pegmatite with δD_{Ms} values between -75 and -63‰. Muscovite from quartz veins and micaschist yields intermediate δD_{Ms} values that range from -80 to -70‰. As observed for the muscovite, tourmaline from leucogranite samples yield lower δD_{To} values ($-87 \leq \delta D_{To} \leq -84$‰) than those from pegmatite (δD_{To} = -80‰). Tourmaline from quartz veins have intermediate δD_{To} values that vary between -85 and -81‰.

c. Muscovite geochemistry and Ti-in-Ms geothermometry

To determine the origin (e.g. hydrothermal or magmatic) of muscovite and check if a link exists between their Mg, Ti, and Na content and their hydrogen isotope values, their chemical composition was tested using EPMA (**Table III-4;** analytical procedure described in **Chapter II**). Most muscovite grains have a high titanium content and plot essentially in the primary field of magmatic muscovite (**Fig. III-10**). However, some muscovite point analysis plot in the secondary muscovite field indicating a more hydrothermal origin (**Fig. III-10**).

Results from QUIB01 sample with low δD_{Ms} and δD_{To} of -85‰ and -87‰ respectively are heterogeneous with $0.02 < Ti < 0.05$ mol, $0.08 < Mg < 0.10$ mol and $0.02 < Na < 0.03$ mol. In contrast, QUIB03 sample with slightly higher δD_{Ms} and δD_{To} of -82‰ and -86‰, respectively, provides a more homogeneous composition with a lower Ti content ($0.02 < Ti < 0.03$ mol), higher Mg content ($0.09 < Mg < 0.11$ mol) and similar Na content ($0.02 < Na < 0.03$ mol) when compared to sample QUIB01. As a consequence, muscovites displaying heterogeneous chemical compositions (QUIB01-type sample) predominantly plot in the primary (magmatic) field of the Miller diagram (1981), whereas those which are more homogeneous (QUIB03-type sample), and characterized

by low titanium and high magnesium contents, have a tendency to plot in the hydrothermal field. The heterogeneity of sample QUIB01 muscovites is also strengthened at the grain scale where transects along the long axis of the grain show a decrease of the titanium content from the tip to the core (i.e. muscovite 11; **Table III-4**).

To determine the temperature of isotopic exchange between the fluid and the mineral, the titanium-in-muscovite thermometer (Wu & Chen, 2015) was used on two representative samples of mylonitic leucogranite (QUIB01 and QUIB03). A pressure of 4 ± 1 kbar at which the leucogranite has been emplaced was used (e.g. Gapais et al., 1993; Turrillot, 2010) to define the Ti-in-Ms geothermometer of Wu and Chen (2015). Results indicate a temperature of 569 ± 42°C for QUIB01 and 546 ± 41°C for QUIB03 (**Table III-4**).

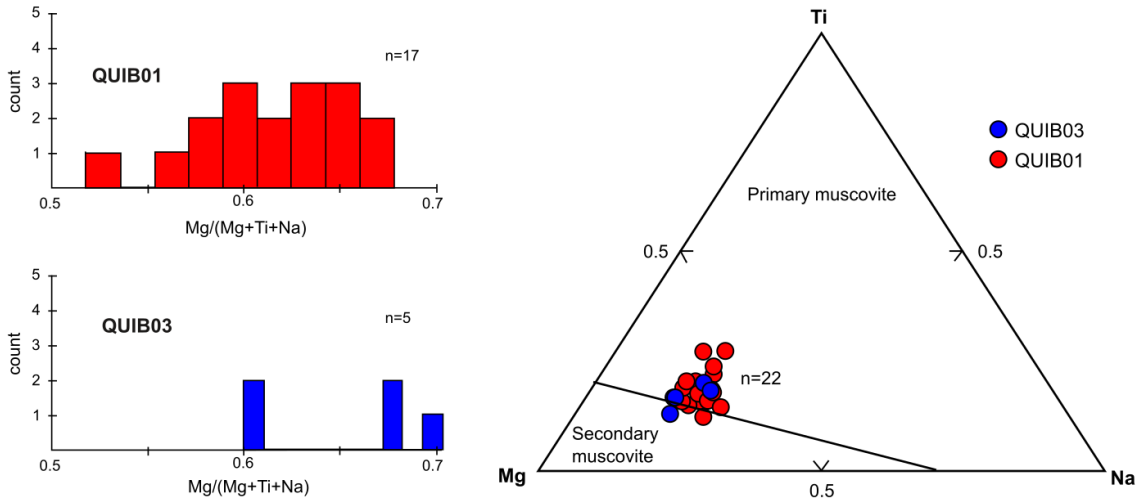

Figure III-10: Muscovite chemical composition of Quiberon mylonitic leucogranite plotted in the terciary Mg–Ti–Na diagram of Miller et al. (1981) with associated Mg/(Mg + Ti + Na) molar ratios that illustrates the shift from the primary (magmatic) to the secondary (hydrothermal) muscovite fields. See Figure III-11 for corresponding $^{40}Ar/^{39}Ar$ ages.

Name	Rock type	Structural distance (m)	$\delta D_{Muscovite}$ (‰)		$\delta D_{Tourmaline}$ (‰)		δD_{Ms} - δD_{To}	Quartz microstructure thermometry								Ti-in-Muscovite thermometry					Location	
			250 < f < 500 µm	500 µm < f	250 < f < 500 µm	500 µm < f		T (°C)	± (°C)	δD_{water} (‰) [δD_{Ms}]	-	+	δD_{water} (‰) [δD_{To}]	-	+	T (°C)	± (°C)	δD_{water} (‰) [δD_{Ms}]	-	+	Latitude (DD)	Longitude (DD)
QUIB 07	Micaschist	200	-76					550	150	-62	9	16									47°30'21.94''N	03°09'37.87''W
QUIB 08	Quarz vein	250		-76		-81	5	550	150	-62	9	16	-69	11	20						47°30'26.2''N	03°08'58.6''W
QUIB 09	Quarz vein	255	-70	-76				550	150	-63	9	16									47°30'26.1''N	03°08'58.6''W
QUIB 01	Mylonitic leucogranite	300		-85		-87	3	550	150	-71	9	16	-75	11	20	569	42	-72	3	3	47°29'04.1''N	03°08'38.1''W
QUIB 02	Mylonitic leucogranite	305	-79	-79				550	150	-66	9	16									47°29'04.2''N	03°08'37.3''W
QUIB 06	Ultramylonitic pegmatite	320	-75					550	150	-61	9	16									47°29'04.5''N	03°08'37.9''W
QUIB 04	Ultramylonitic pegmatite	321	-64	-73				550	150	-50	9	16									47°29'04.0''N	03°08'37.6''W
QUIB 05	Ultramylonitic pegmatite	321.5	-73	-73	-80		7	550	150	-60	9	16	-68	11	20						47°29'03.9''N	03°08'37.6''W
QUIB 03	Mylonitic leucogranite	322	-82	-81	-84	-86	3	550	150	-69	9	16	-74	11	20	546	41	-69	3	4	47°29'04.0''N	03°08'37.5''W
QUIB 16	Quarz vein	465		-79				550	150	-66	9	16									47°28'54.5''N	03°08'11.0''W
QUIB 17	Quarz vein	500	-80	-79	-85	-85		550	150	-66	9	16	-73	11	20						47°28'54.3''N	03°08'07.8''W

Propagated uncertainties	Error	Error (‰)	Propagated error in δD_{water}
Isotopic analysis (δD)	± 2‰	± 2‰	± 16.2‰
Temperature deduced from quartz microstructure	± 150°C	± 16‰	
Temperature deduced from Ti-in-Ms geothermometry	± 42°C	± 5‰	± 5.2‰

Table III-3: GPS localization, hydrogen isotope composition of muscovite (Ms) and tourmaline (To) from leucogranite, micaschist, quartz vein and pegmatite granite found in the mylonitic footwall of Quiberon detachment zone. δD_{water} values have been calculated by using the hydrogen isotope muscovite-water and tourmaline-water fractionation factors (α) of Suzuoki and Epstein (1976) and Kotzer et al. (1993), respectively, and using temperatures indicated by quartz microstructures (550 ± 150°C) and by the Ti-in-Ms thermometer (546 to 569 ± 42°C). Calculated δD_{water} values have a propagated uncertainties of ± 16.2‰ and ± 5.2‰, taking into account the precision of isotopic analyses ($\delta D_{hydrous\ silicate}$ ± 2‰) and the uncertainties linked to the temperature of recrystallization (550 ± 150˚C results in δD_{water} uncertainties of ± 16‰ and T ± 42˚C results in δD_{water} uncertainties of ± 5.2‰).

Sample		QUIB01																	QUIB03				
Muscovite		2	3	4	5	6	7	8	9	10	11			12	13				2		3	4	8
Point											a	b	c		a	b	c	d	a	b			
Oxide (Wt.%)	Al2O3	33.93	33.91	33.50	33.36	33.65	33.63	33.66	33.91	33.78	33.56	33.96	33.61	34.17	33.30	33.71	33.89	33.81	33.89	33.68	33.36	34.28	33.26
	SiO2	46.68	46.46	46.24	47.23	47.42	47.02	46.46	46.92	46.93	46.45	46.52	46.35	46.87	46.71	46.91	46.67	46.43	46.50	46.33	45.67	46.35	46.57
	TiO2	0.35	0.72	0.50	0.58	0.57	0.89	0.48	0.65	0.46	0.74	0.57	0.91	0.38	0.66	0.56	0.49	0.54	0.58	0.63	0.45	0.32	0.52
	Na2O	0.50	0.50	0.51	0.38	0.38	0.39	0.51	0.43	0.44	0.45	0.51	0.49	0.52	0.40	0.48	0.42	0.51	0.50	0.45	0.33	0.31	0.38
	MgO	0.92	0.96	1.01	1.01	1.00	0.94	0.94	0.99	1.02	0.89	0.93	0.89	0.82	1.03	1.01	1.05	0.91	0.95	0.94	0.92	0.86	1.07
	MnO	0.01	0.03	0.03	0.04	0.03	0.04	0.03	0.02	0.02	0.02	0.04	0.04	0.02	0.04	0.04	0.00	0.02	0.01	0.01	0.03	0.03	0.01
	FeO	2.22	2.24	2.36	2.36	2.26	2.39	2.35	2.39	2.20	2.15	2.19	2.26	2.06	2.60	2.60	2.27	2.19	2.09	2.14	2.07	1.97	2.17
	K2O	11.40	11.22	11.20	11.00	11.32	11.33	11.12	11.45	11.42	11.22	11.30	11.25	10.82	11.29	11.17	11.20	11.27	11.21	11.18	11.20	9.62	11.36
	CaO	0.00	0.00	0.02	0.00	0.01	0.00	0.00	0.00	0.00	0.01	0.00	0.00	0.03	0.00	0.00	0.02	0.01	0.00	0.01	0.02	0.03	0.00
	Cr2O3	0.02	0.01	0.01	0.00	0.00	0.00	0.00	0.02	0.00	0.02	0.03	0.00	0.00	0.00	0.00	0.00	0.03	0.01	0.05	0.01	0.00	0.04
	Sum	96.04	96.04	95.38	95.96	96.66	96.63	95.55	96.79	96.27	95.51	96.04	95.81	95.69	96.03	96.47	96.03	95.73	95.76	95.40	94.05	93.76	95.38
Conversion Factor		4.01	4.01	4.04	4.00	3.98	3.98	4.03	3.98	4.00	4.03	4.01	4.02	4.00	4.02	3.99	4.00	4.02	4.01	4.03	4.09	4.05	4.03
Mol (normalised to 11 oxygens)	Al	2.67	2.67	2.65	2.62	2.62	2.63	2.66	2.65	2.65	2.65	2.67	2.65	2.68	2.62	2.64	2.66	2.67	2.67	2.66	2.68	2.72	2.63
	Si	3.11	3.10	3.11	3.14	3.14	3.12	3.11	3.11	3.12	3.11	3.10	3.10	3.12	3.12	3.12	3.11	3.11	3.11	3.11	3.11	3.12	3.13
	Ti	**0.02**	**0.04**	**0.03**	**0.03**	**0.03**	**0.04**	**0.02**	**0.03**	**0.02**	**0.04**	**0.03**	**0.05**	**0.02**	**0.03**	**0.03**	**0.02**	**0.03**	**0.03**	**0.03**	**0.02**	**0.02**	**0.03**
	Na	0.03	0.03	0.03	0.02	0.02	0.03	0.03	0.03	0.03	0.03	0.03	0.03	0.03	0.03	0.03	0.03	0.03	0.03	0.03	0.02	0.02	0.02
	Mg	0.09	0.10	0.10	0.10	0.10	0.09	0.09	0.10	0.10	0.09	0.09	0.09	0.08	0.10	0.10	0.10	0.09	0.09	0.09	0.09	0.09	0.11
	Mn	0.00	0.00	0.00	0.00	0.00	0.00	0.00	0.00	0.00	0.00	0.00	0.00	0.00	0.00	0.00	0.00	0.00	0.00	0.00	0.00	0.00	0.00
	Fe	0.12	0.12	0.13	0.13	0.13	0.13	0.13	0.13	0.12	0.12	0.12	0.13	0.11	0.15	0.14	0.13	0.12	0.12	0.12	0.12	0.11	0.12
	K	0.49	0.48	0.48	0.47	0.48	0.48	0.48	0.48	0.48	0.48	0.48	0.48	0.46	0.48	0.47	0.48	0.48	0.48	0.48	0.49	0.41	0.49
	Ca	0.00	0.00	0.00	0.00	0.00	0.00	0.00	0.00	0.00	0.00	0.00	0.00	0.00	0.00	0.00	0.00	0.00	0.00	0.00	0.00	0.00	0.00
	Cr	0.00	0.00	0.00	0.00	0.00	0.00	0.00	0.00	0.00	0.00	0.00	0.00	0.00	0.00	0.00	0.00	0.00	0.00	0.01	0.00	0.00	0.00
[Mg/(Fe+Mg)]		**0.43**	**0.43**	**0.43**	**0.43**	**0.44**	**0.41**	**0.42**	**0.43**	**0.45**	**0.42**	**0.43**	**0.41**	**0.41**	**0.42**	**0.41**	**0.45**	**0.43**	**0.45**	**0.44**	**0.44**	**0.44**	**0.47**
T(°C) at 4 Kbar		**494**	**607**	**546**	**571**	**567**	**643**	**539**	**587**	**536**	**611**	**567**	**648**	**505**	**590**	**563**	**546**	**559**	**572**	**585**	**534**	**482**	**557**
SD (°C) (for P ± 1 kbar)		4	5	4	5	4	5	4	5	4	5	4	5	4	5	4	4	4	5	5	4	4	4
Average T(°C) at 4 Kbar		**569**																	**546**				
SD (°C) on average		42																	41				

Table III-4: Microprobe analysis of muscovite grains (transects across grains are shaded) and Ti-in-Ms geothermometry (Wu and Chen, 2015).

d. Geochronology

(1) $^{40}Ar/^{39}Ar$ on muscovite from mylonitic leucogranite

Two samples of mylonitic leucogranite (QUIB01 and QUIB03, highlighted by red squares on **Fig. III-9**) were dated using $^{40}Ar/^{39}Ar$ laser probe step-heating geochronology on single grains (**Table VI-1** in the appendix; **Fig. III-11**; procedure described in Ruffet et al., 1991, 1995 and method in **Chapter II**). Apparent age errors are plotted at the 1σ level.

Two single grains from QUIB01 provide plateau ages of 319.5 ± 0.9 Ma and 307.7 ± 0.7 Ma. Two muscovite grains from QUIB03 give constant plateau ages of 304.8 ± 1.0 Ma and 303.4 ± 1.0 Ma. The two different ages obtained in sample QUIB01 are consistent with the heterogeneous composition of muscovite but also with the magmatic and hydrothermal signatures emphasized in the ternary diagram of Miller et al. (1981). The constant age of ~304 Ma provided by sample QUIB03 is also reflected in muscovite composition.

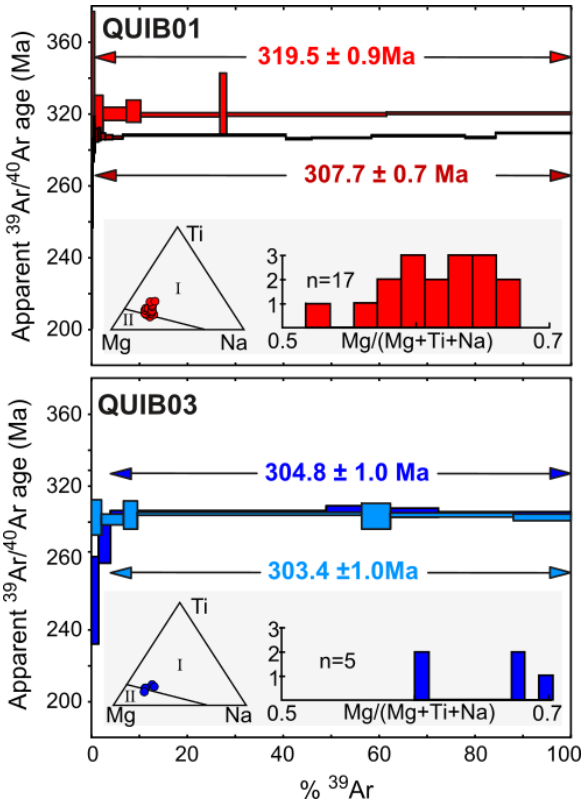

Figure III-11: $^{40}Ar/^{39}Ar$ step-heating spectra of muscovite from mylonitic leucogranite (QUIB01 and QUIB03) with associated Mg/(Mg + Ti + Na) for each analyzed muscovite grain that illustrates the shift from (I) the primary to (II) the secondary muscovite fields in the tertiary Mg–Ti–Na diagram (e.g. Miller et al., 1981).

(2) U-Th/Pb and Fission Track dating in leucogranite

Two samples of weakly deformed and mylonitic leucogranite from the Quiberon footwall were dated by U-Th/Pb (**Table III-5**; **Fig. III-12**; Géosciences Rennes, France). The weakly deformed leucogranite (sample 15-12) gives an age of 318 ± 2.2 Ma on monazite, and of 312.8 ± 3.0 Ma on magmatic apatite (compact REE spectra). The more deformed sample (15-1) yields an age of 316 ± 4.3 Ma on zircon and of 303 ± 3.6 Ma on hydrothermal apatite (spread REE spectra).

Sample	Description	U-Th/Pb Zircon	U-Th/Pb Monazite	U-Th/Pb Apatite	Fission track Apatite	REE spectra Apatite
15-12	Weakly deformed leucogranite	Non conclusive	318 ± 2.2 Ma	312.8 ± 3.0 Ma	160 Ma	Compact
15-1	Mylonitic leucogranite	316 ± 4.3 Ma	Non conclusive	303.0 ± 3.6 Ma	160 Ma	Spread

Table III-5: Summary of zircon, monazite and apatite U-Th/Pb and apatite fission track dates, with associated apatite REE spectra.

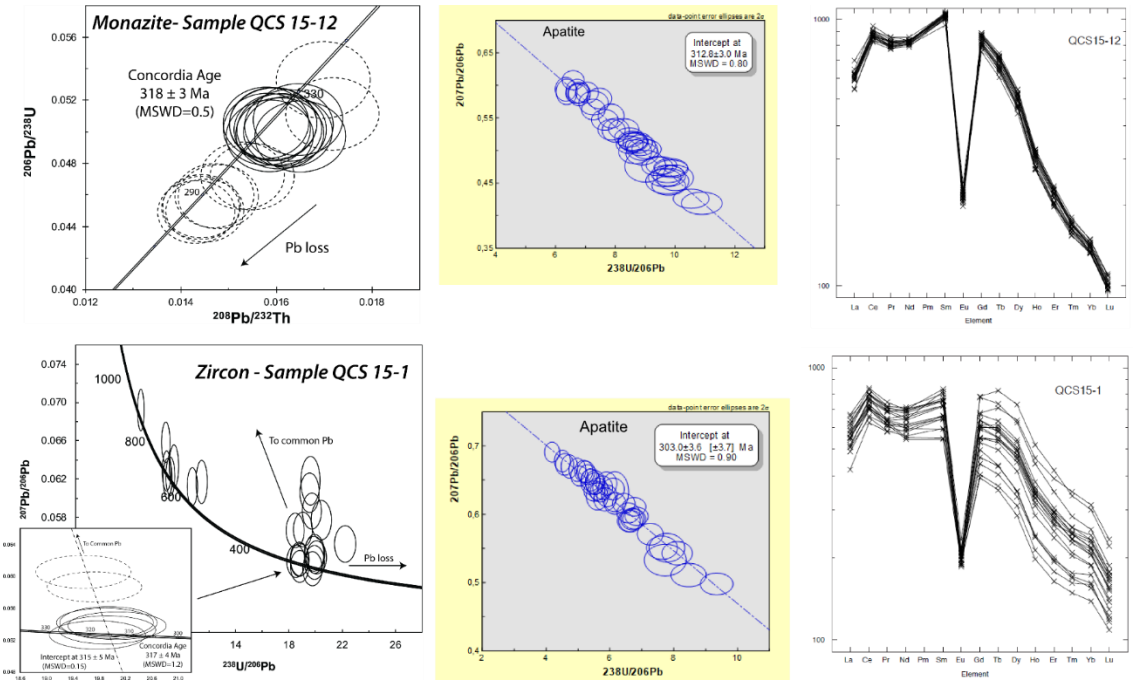

Figure III-12: Summary of the U-Th/Pb results on monazite, zircon and apatite obtained on weakly deformed (QSC 15-12) and mylonitic (QSC 15-1) Quiberon leucogranite. Note the compact REE spectra that reflect a magmatic signature in apatite of the weakly deformed sample (QSC 15-12) compared to the hydrothermal apatite with spread REE spectra in the mylonitic leucogranite sample (QSC 15-1).

(3) U-Th/Pb (LA-ICPMS) on monazite from migmatites

Sample NAV04 yields a spread of concordant U-Pb analyses that range from ~320 to ~290 Ma (n = 35; **Fig. III-13; Table VI-2** in the appendix). A weighted average of $^{207}Pb/^{236}U$ age provides a result of 308.4 ± 2.3 Ma (MSWD = 1.2, n = 35; **Fig. III-13**). Monazite is relatively enriched in LREE, and is characterized by a significant Eu anomaly and yields a slight range in HREE (**Fig. III-13F**), consistent with peritectic crystallisation with feldspar from (partial) melt. This is consistent with observations of selvages of quartz and feldspar (myrmekite) and lobate grain boundaries (grain boundary migration) in thin section that are textures indicative of partial melting within the migmatitic host rock. Monazites show some faint zoning in BSE (**Fig. III-13A**) and show differences in Y concentration (**Table VI-2** in the appendix). This can be interpreted as growth zoning, demonstrating that monazite grew during reactions with another phase. The relative differences in Y and HREE concentrations may indicate reactions with garnet. The difference in age zoning was however within uncertainty and therefore non-resolvable. As monazites that yield relatively older ages within the spread are generally elongate and oriented within the fabric (**Fig. III-13A**), it could be postulated that continued crystallization of monazite occurred during a fabric-forming event, potentially as the rock began to exhume.

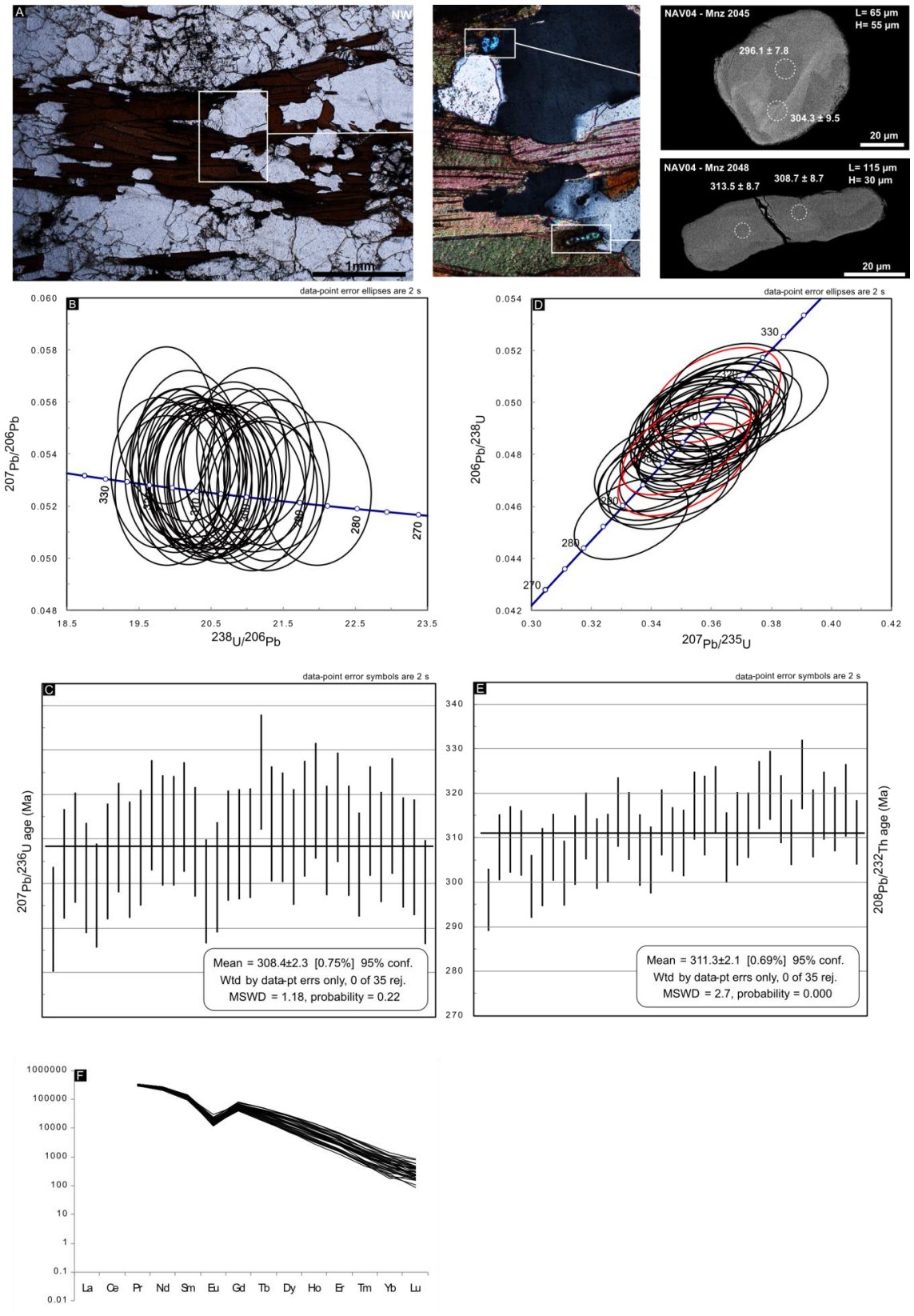

Figure III-13: Summary of the U-Th/Pb on monazite results obtained in Port-Navalo migmatite. (A) Microtextural aspect of monazite grains; (B) ; (D) $^{207}Pb/^{236}U$ and (E) $^{208}Pb/^{232}Th$ dates obtained in this study; (F) Monazite REE spectrum highlighting the magmatic signature of apatite.

4. Discussion

a. Meteoric fluid infiltration during high-temperature deformation

(1) Fluid-rock interaction during high-temperature deformation

The microstructural analysis of quartz showing grain boundary migration together with EBSD data indicating prism <c> glide (**Fig. III-8**) is compatible with high temperature deformation (500 ± 150°C, e.g. Hirth and Tullis, 1992; Okudaira et al., 1995; Stipp et al., 2002). The Ti-in-Ms geothermometer applied to synkinematic mica fish also indicates temperatures above 500°C (546 to 569 ± 42°C; **Table III-4**).

Synkinematic muscovite and tourmaline have reached hydrogen isotope equilibrium as: (1) the microstructures contain tourmaline and muscovite associated in C/S structures (**Fig. III-8B**), and (2) the δD_{To} values are 3 to 7‰ lower than the δD_{Ms} values (**Fig. III-9**), in agreement with the difference of 5‰ between those two minerals shown by the isotope fractionation of Blamart et al. (1989) at 550°C and 3 kbar.

Two main observations indicate that hydrogen isotope exchange between fluids and hydrous minerals likely occurred during high-temperature grain-scale deformation: (1) elongate lenticular muscovite fish formed by recrystallization involving solution-precipitation (ten Grotenhuis et al., 2003) and tourmaline grains form shear bands that indicate a top-to-WNW sense of shear (**Fig. III-8**); (2) consistent high deformation temperatures are indicated by quartz microstructures and the Ti-in-Ms geothermometer.

(2) Calculation of the δD_{water} values of syntectonic fluids

The isotope composition of the fluid present in the Quiberon detachment footwall was calculated based on the hydrogen isotope composition of synkinematic muscovite and tourmaline, the hydrogen water-muscovite isotope fractionation factor of Suzuoki

and Epstein (1976) and the hydrogen water-tourmaline isotope fractionation factor of Kotzer et al. (1993) and estimated temperature of isotope exchange between the fluid and the mineral (**Table III-3**).

- **Deformation temperatures of 550 ± 150°C deduced from quartz microstructures,** coupled with the **δD_{Ms} values** and the muscovite-water hydrogen isotope fractionation factor of Suzuoki and Epstein (1976), allow us to calculate δD_{water} values ranging from **-71 to -50 ± 16‰.**

- The same temperature estimates (550 ± 150°C), combined with the **δD_{To} values** and the tourmaline-water hydrogen isotope fractionation factor of Kotzer et al. (1993), allow us to calculate δD_{water} values ranging from **-75 to -69 ± 20‰.**

- The **Ti-in-Ms thermometer** (569 ± 42°C for sample QUIB01), coupled with the **δD_{Ms} values** and the muscovite-water hydrogen isotope fractionation factor of Suzuoki and Epstein (1976), allows us to calculate a δD_{water} value of **-72 ± 3‰** for QUIB01.

- The **Ti-in-Ms thermometer** (546 ± 41°C for sample QUIB03) coupled with the **δD_{Ms} values** and the muscovite-water hydrogen isotope fractionation factor of Suzuoki and Epstein (1976) allows us to calculate a δD_{water} value of **-69 ± 4‰** for QUIB03.

The δD_{water} value calculations based on muscovite are similar to those calculated from tourmaline within uncertainty. The δD_{water} values calculated based on Ti-in-Ms geothermometry exhibit a maximum difference of 1% with the δD_{water} calculated based on quartz microstructure thermometry (**Table III-1**).

(3) Meteoric fluid infiltration and mixing with deep crustal fluids

The lowest δD_{water} values were measured in mylonitic leucogranite (-75‰) whereas the ultramylonitic pegmatite yielded the highest δD_{water} (-50‰). This 25‰ difference can be explained by: (1) predominant interaction with magmatic fluids - pegmatite developed during syntectonic crystallization of late magmatic fluids (Gapais and Boundi, 2014); (2) flow partitioning in high strain zones; (3) duration of meteoric fluid-rock interaction - shorter in late pegmatite dykes than in leucogranite; (3) rock permeability - the ultramylonitic small-grained pegmatite was less porous and permeable than the surrounding coarser-grained leucogranite. In contrast, the low δD values of muscovite and tourmaline ($-87 < \delta D_{hydrous\ silicate} < -73$‰) are obtained in leucogranite, pegmatite, quartz veins and micaschist in the Quiberon footwall. They are interpreted as indicating interaction with deuterium-depleted meteoric fluids, in good agreement with the hydrogen isotope data published in Dusséaux et al. (2019), where strong meteoric fluid-rock interaction has been identified in the upper part of the detachment footwalls, including the Quiberon detachment (**Fig. III-9 and Table III-3**).

The calculated δD_{water} values in the Quiberon detachment footwall range from -75 to -50‰. This 25‰ difference in δD_{water} values from leucogranite, micaschist, quartz veins and pegmatite are interpreted as indicating different fluid sources that interacted with muscovite during deformation. This interpretation agrees with the mixing relationship defined between two end-member fluids in the Armorican shear zones, with high-δD deep crustal (magmatic and/or metamorphic) fluids (δD_{water} value ~ -35‰) and low-δD meteoric fluids (δD_{water} value ~ -75‰) (Dusséaux et al., 2019).

The variability in the low δD_{water} values calculated from muscovite and tourmaline in leucogranite (from -72 to -50‰ and -75 to -69‰, respectively) within the Quiberon

detachment footwall can be explained either by variable temperatures of fluid-rock interaction and/or prevalent interaction with either metamorphic or meteoric fluids; the lowermost δD_{water} value of -75‰ reflecting the greatest interaction with surface-derived fluids and the uppermost δD_{water} value of -50‰ involving predominantly metamorphic fluids (see discussion in **part III-A**; Dusséaux et al., 2019).

(4) Hydrogen isotope composition of meteoric fluids

The lowermost δD_{water} value of -75‰ provides a reasonable estimate of the δD_{water} value of the invading meteoric fluid in the crust. However, the downward penetration of surface-derived fluids in the crust leads to an increase in δD_{water} values due to fluid-rock interaction. Therefore the lower δD_{water} value of -75‰ estimated from synkinematic minerals that crystallized at depth represents a maximum value that could have been even lower if this fluid was extracted from the near-surface geological environment (e.g. Gébelin et al., 2012). As discussed in **section III-A** (Dusséaux et al., 2019)**,** this δD_{water} value remains relatively high and could be explained by the paleogeographic framework during the Late Carboniferous. Indeed, many parameters could have induced an increase of the δD_{water} values of precipitation in the southern Armorican domain, such as its low-latitude position, a warm paleoclimate, the presence of an extensive ice sheet cover, and/or a medium elevation.

b. Geochronology

(1) Thermochronological history of the Quiberon detachment shear zone

Various dating techniques (U-Th/Pb, Ar/Ar and fission track) applied to different minerals (zircon, monazite and muscovite) that have different closure temperatures allow us to reconstruct the thermochronological history of the Quiberon leucogranite (**Fig. III-14**).

- Zircon from weakly deformed leucogranite yields an U-Th/Pb age of 316 ± 4.3 Ma with a closure temperature estimated at 800 ± 50°C (Cherniak and Watson, 2001).
- Monazite from mylonitic granite yields an U-Th/Pb age of 318 ± 2.2 Ma with a closure temperature estimated at 700 ± 50°C (Cocherie, 2005).
- Monazite from the Port Navalo migmatite, below the footwall of Quiberon detachment, gave U-Th/Pb ages ranging from ~320 to 290 Ma.

These ages are interpreted as reflecting the emplacement of the Quiberon granite and the onset of partial melting at ~320 Ma. Similar ages have been reported for Varican partial melting events in the southern Armorican domain at ~320 Ma (e.g. Peucat, 1983; Turrillot et al., 2009; Turrillot, 2010; Tartèse et al., 2012). Similarly, the onset of migmatization was dated at ~315 Ma, based on zircon and monazite U-Th/Pb ages of migmatites in the French Massif Central that constitute the eastern continuation of the Armorican Massif (Gébelin et al., 2009).

- Apatite has a closure temperature of 325 to 550°C for the diffusion of Pb (e.g. Watson et al., 1985; McDougall and Harrison, 1988; Cherniak et al., 1991) and yields an U-Th/Pb age of 312.8 ± 3.0 Ma for weakly deformed leucogranite and 303.0 ± 3.6 Ma for mylonitic leucogranite.

- Muscovite from mylonitic leucogranite yields $^{40}Ar/^{39}Ar$ ages that range from 319.5 ± 0.9 to 303.4 ± 1.0 Ma, with a closure temperature for Ar diffusion estimated at 425 ± 50°C (Villa, 1998).

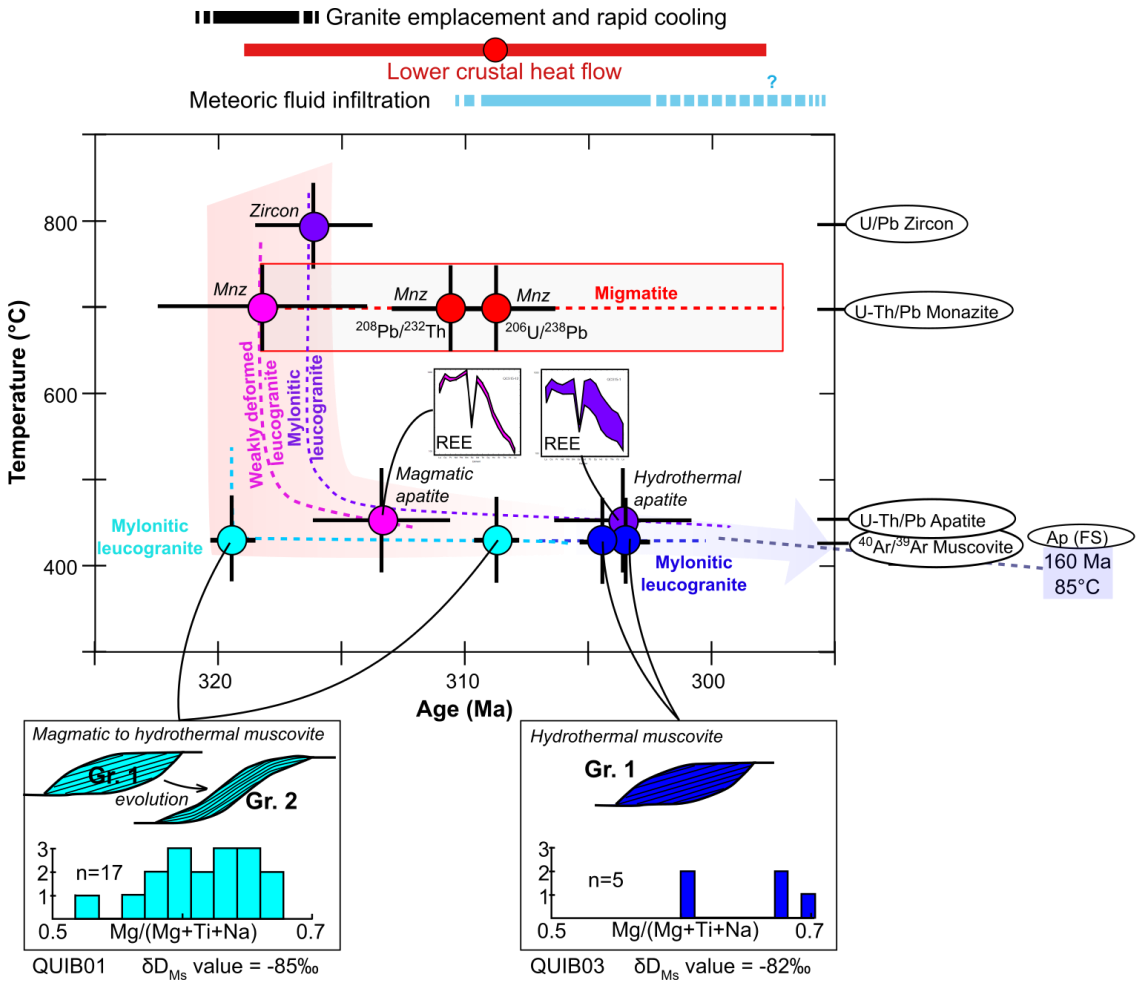

Figure III-14: Temperature (°C) – time (Ma) plot summarizing the geochronology results obtained in the Quiberon footwall weakly deformed to mylonitic leucogranite and the Port-Navalo migmatite (Monazite: Mnz; Apatite: Ap; Fission Track; FS). Note the associated frames with REE spectras associated with magmatic orhydrothermal apatite and the microstructure and chemical composition associated with magmatic to hydrothermal muscovite.

- Apatite from weakly deformed to undeformed leucogranites yields fission track ages of ~160 Ma with an estimated closure temperature of 85 ± 50°C (Gunnell, 2000).

The oldest $^{40}Ar/^{39}Ar$ age of ~320 Ma obtained on muscovite is comparable to the U-Th/Pb ages on monazite and zircon that were interpreted to reflect leucogranite emplacement (**Fig. III-14**). Therefore, the oldest muscovite $^{40}Ar/^{39}Ar$ age is interpreted to show a rapid cooling of the leucogranite from ~800 to 400°C at ~320 Ma.

The ages obtained using various dating techniques on muscovite and apatite with closure temperatures estimated from ~500 to 85°C range from ~320 to 160 Ma (**Fig. III-14**). Therefore, the Quiberon leucogranite cooled very slowly from the Late Carboniferous to the Middle Jurassic.

The $^{40}Ar/^{39}Ar$ ages obtained on synkinematic muscovite allow us to bracket activity on the QD between ~320 Ma and 303 Ma. These results are consistent with previous U/Pb on monazite and zircons and $^{40}Ar/^{39}Ar$ thermochronology of the Quiberon leucogranite that support activity on the QD between ~320 Ma and 298 Ma (Turrillot, 2010; Gapais et al., 2015).

(2) <u>Timing of meteoric fluid infiltration</u>

- Magmatic apatite (less variable REE spectra) from weakly deformed leucogranite yields the oldest U-Th/Pb age (312.8 ± 3.0)

- Hydrothermal apatite (spread REE spectra) for mylonitic leucogranite yields the younger U-Th/Pb age (303.0 ± 3.6 Ma)

- Muscovite in mylonitic leucogranite with heterogeneous compositions (i.e. magmatic to hydrothermal; 0.02 < Ti < 0.05 mol) yields the older $^{40}Ar/^{39}Ar$ ages that range from 319.5 ± 0.9 Ma to 307.7 ± 0.7 Ma

- Muscovite in mylonitic leucogranite with homogeneous hydrothermal compositions (0.02 < Ti < 0.03 mol) yields the younger $^{40}Ar/^{39}Ar$ ages that range from 304.8 ± 1.0 Ma to 303.4 ± 1.0 Ma

- However, muscovite from both dated leucogranite samples yield low δD values that are similar within uncertainty (± 2‰) with δD_{Ms} values ranging from -85 to 81‰ and δD_{To} value from -87 to 84‰. The $\delta D_{mineral}$ values allow

us to calculate δD_{water} values ranging from -75 to -69 ± 5‰ in mylonitic leucogranite that are interpreted as a signature of deuterium-depleted meteoric fluids.

- The weighted average of $^{207}Pb/^{235}U$ ages of monazite from migmatite below the footwall is 308.4 ± 2.3 Ma.

The minerals with a magmatic composition yield ages between ~320 and 308 Ma (**Fig. III-14**). The magmatic monazites of the undeformed granite have an age of ~313 Ma and the youngest muscovite from mylonitic leucogranite with an heterogeneous (magmato-hydrothermal) composition is dated at ~308 Ma. However, monazite and muscovite grains are getting younger as their chemistry tends towards a more hydrothermal signature. Indeed, both hydrothermal monazite and muscovite only yield young ages between ~305 and 303 Ma. It is therefore very likely that infiltration of meteoric fluids was intensified between ~308 and 303 Ma. The youngest Ar/Ar age obtained on a deuterium-depleted muscovite fish is interpreted to record the infiltration of meteoric fluids until ~303 Ma (**Fig. III-14**). Meteoric fluids could continue infiltrating the crust after the closing of the argon and hydrogen systems during exhumation of the samples.

However, the more evolved muscovite fish (group 1 micafish of **Fig. III-8B**, and bent tips of group 2 micafish (**Fig. III-8C**) in QUIB01) from mylonitic leucogranite have lower δD values and Ar/Ar ages that cover a large time span from ~320 to 308 Ma. Moreover, they display a heterogeneous composition at the grain scale with a decrease of the titanium content from the tip to the core, in good agreement with microstructural observation that show recrystallization processes by solution-precipitation. In contrast, the less evolved muscovite fish (group 1 only in QUIB03) which are homogeneous at the

grain scale have higher δD values and Ar/Ar ages from ~305 to 303 Ma. One interpretation is that the QUIB01 mylonitic leucogranite sheet was susceptible to deformation-induced recrystallization and meteoric-fluid rock exchange for a longer time compared to the QUIB03 mylonitic leucogranite.

Finally, the migmatite below the footwall yield a spread of concordant U-Pb analyses varying from ~320–290 Ma, but the weighted average of ages records an important partial melting event at ~308 Ma that could have provided the necessary heat at depth to enhance and intensify the hydrothermal system in the QD footwall.

c. Mechanisms of meteoric fluid infiltration

As developed in the introduction, previous studies conducted on detachment zones have found 3 main conditions for explaining the infiltration of meteoric fluids down to the brittle-ductile transition (e.g. Mulch et al., 2004, 2006; Person et al., 2007; Gébelin et al., 2011, 2015, 2017): 1) brittle normal faults and fracture development in the upper crust 2) a high geothermal gradient and 3) the presence of a hydraulic head.

1) In Quiberon Island, brittle normal faults have been recognized anchoring in the micaschists (**Figs. III-7 – A and B**). These brittle structures may have enhanced the porosity in the upper crust and served as conduits for surface-derived fluids to penetrate the crust.

2) At the same time, emplacement of syntectonic leucogranites (Ar/Ar and U/Pb) and important partial melting events in the lower crust (U/Pb) could have provided the necessary high heat flow to sustain the convection of fluids at depth (**Fig. III-14**). In addition, the anastomosing C-S structures made of well-connected mica layers that have localized the strain and weakened the rock may have promoted an

enhanced permeability of mylonitic leucogranite in the QD footwall (e.g. McCaig, 1988; Bauer et al., 2000; Tartèse et al., 2013; Hunter et al., 2016).

3) The fact that previous studies have shown that a regional hydraulic head would be needed to allow surface fluids to migrate downwards is in good agreement with the fact that the southern Armorican domain is part of the internal thickened zones of the Variscan Belt (e.g. Ballèvre et al., 2013).

5. Conclusion

The late-Variscan Quiberon detachment zone juxtaposes high pressure-low temperature rocks over high-grade leucogranite and migmatite in the southern Armorican domain (France). This study documents the infiltration of meteoric fluids into the footwall of the Quiberon detachment at ~305 Ma, when recrystallized hydrous minerals (muscovite and tourmaline) equilibrated with low-δD (meteoric) water at depth during high temperature deformation. The downward flow of meteoric fluid at depth is coeval with the emplacement of migmatite. Migration of fluids from the Earth's surface down to the active mylonitic detachment footwall was achieved by fluid flow along normal faults that developed during post-orogenic extension. The high heat flow from migmatization helped sustain buoyancy-driven fluid convection over the timescale of detachment tectonics. Low δD values in synkinematic fluids are indicative of precipitation-derived fluids sourced at high elevation and document that the ground surface above this section of the Variscan Belt attained a certain elevation at the end of the Carboniferous.

C. Fluid inclusions analysis in Quiberon and Piriac detachment zones

1. Introduction

Detachment zones are extensional structures that favour the downward penetration of meteoric fluids (e.g. Fricke et al., 1992; Nesbitt and Muehlenbachs, 1995; Mulch et al., 2005, 2007; Gébelin et al., 2011, 2015, 2017). As explained in the parts A and B of Chapter III , deciphering the meteoric component of fluids present at depth allows a better understanding of fluid circulation in the crust and mineralisation processes at the orogen scale, as well as being used for paleoaltimetry reconstruction (e.g. Boiron et al., 2003; Mulch et al., 2004).

During the crystallisation of minerals, microscopic amounts of fluids are trapped in cavities and form fluid inclusions (FIs). Their study allows the distinguishing of different types of fluids and help to recover the P-T conditions at the time of trapping (Roedder, 1984). These fluids can originate from dehydration reactions of metamorphic rocks, segregation of magmatic fluids during magma crystallisation, downward infiltration of surface-derived fluids into the crust, in addition to devolatilizing of the mantle.

The aim of this study was to analyse the fluid inclusions trapped in deformed metamorphic and magmatic rocks in the footwall of the Quiberon and Piriac detachment zones (Armorican Massif, France) where meteoric fluids have been identified through low δD values of hydrous minerals (δD_{Ms} down to -88‰, see **sections III-A and III-B**).

2. Structural and microstructural description of samples

Fluid inclusions were analysed on oriented thick sections of two samples from the Quiberon detachment zone (QUIB03 and QUIB07) and one sample from Piriac-sur-Mer

detachment zone (PIR16). QUIB03 is a mylonitic leucogranite found in a high-strain zone (field picture on **Fig. III-7 - C4**) and QUIB07 is a sigmoidal quartz vein in a micaschist enclave (**Fig. III-7 - C3**), both located in the footwall of the Quiberon detachment. PIR16 is a mylonitic leucogranite in the footwall of the Piriac detachment (**fig. III-3 - A**). QUIB03 yield a δD_{Ms} value of -82% and QUIB07 yield a δD_{Ms} value of -76‰. PIR16 yielded the lowest δD_{Ms} value (-88‰, i.e. the most "meteoric" value) found in the southern Armorican domain (δD_{Ms} values are detailed in **section III-A**).

FIs were analysed in quartz grains and have a typical diameter of ~10 µm. They are all biphasic and composed of a vapour and a liquid phase (**Fig. III-15**). Raman microspectrometry does not reveal any volatile species in the vapour phase. This means that the only phase transitions that will be observable when conducting microthermometry are the temperature of ice melting (T_{im}) and the bulk homogenisation temperature (T_h).

The microstructural analysis shows that most secondary fluid inclusions define structural planes that are interpreted as conjugate plans or relay structures (**Fig. III-15 - A**). Some FIs seem aligned (**Fig. III-15 - B**) on planes as if they may have been trapped along an initial crack plane. They could correspond to "healed fractures" described in Lambrecht and Diamond (2014). In sample QUIB03, some FIs display a fish shape that reflects dextral shearing (**Fig. III-15 - C and D**). The brittle planes and deformed shapes of the inclusions globally appear in good agreement with the sense of shearing of the detachment zones (top-to-W for Quiberon and top-to-N for Piriac). The structural observations highlight a syntectonic entrapment of the fluid inclusions during the activity of the detachment zones.

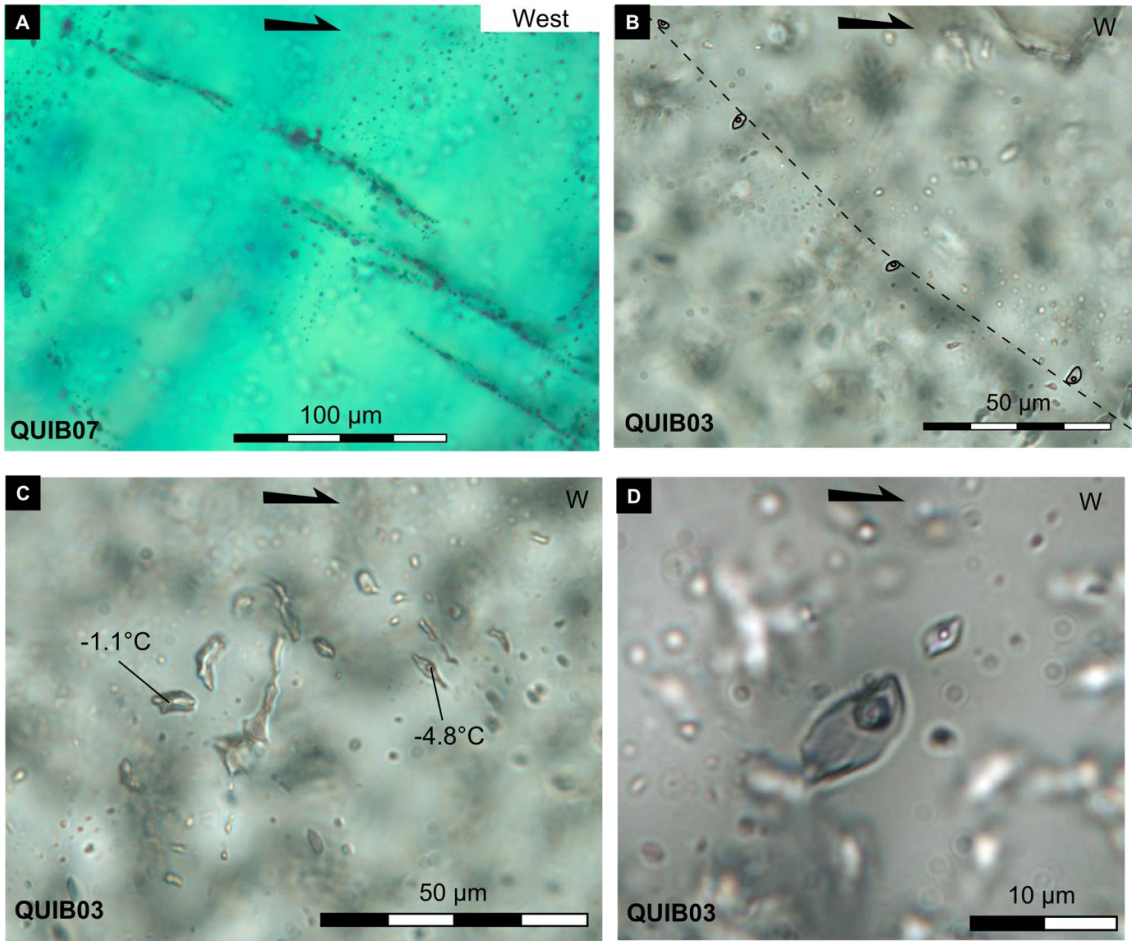

Figure III-15: (A) Fluid inclusions in structural planes interpreted as a relay structure; (B) Biphasic aqueous inclusions defining a plane; (C) Biphasic aqueous inclusions with different shapes and ice melting temperatures; (D) Biphasic aqueous inclusions appearing sheared with a top-to-the-west sense of shearing or changed by the process of necking-down.

After preliminary study of the three samples described above, Théo Piantoni performed the microthermometric study of two leucogranite samples sent by C. Dusséaux as part of an internship at the University of Lille (France) under the supervision of Pr. Michel Dubois. The data were analysed and interpreted by C. Dusséaux and M. Dubois. Both samples are Guérande-type mylonitic leucogranite emplaced in the footwall of the Piriac detachment. Sample PIR01 is the closest to the detachment (~500m) and yield a low δD_{Ms} value (-81‰). Sample PIR06 is situated at 517m beneath the detachment and yielded the higher δD_{Ms} found in Guérande granite (-76‰). The

optical analysis coupled with Raman microspectrometry, showed that the inclusions in PIR01 and PIR06 were all biphasic, volatile-free, therefore similar to samples QUIB03, QUIB07 and PIR16.

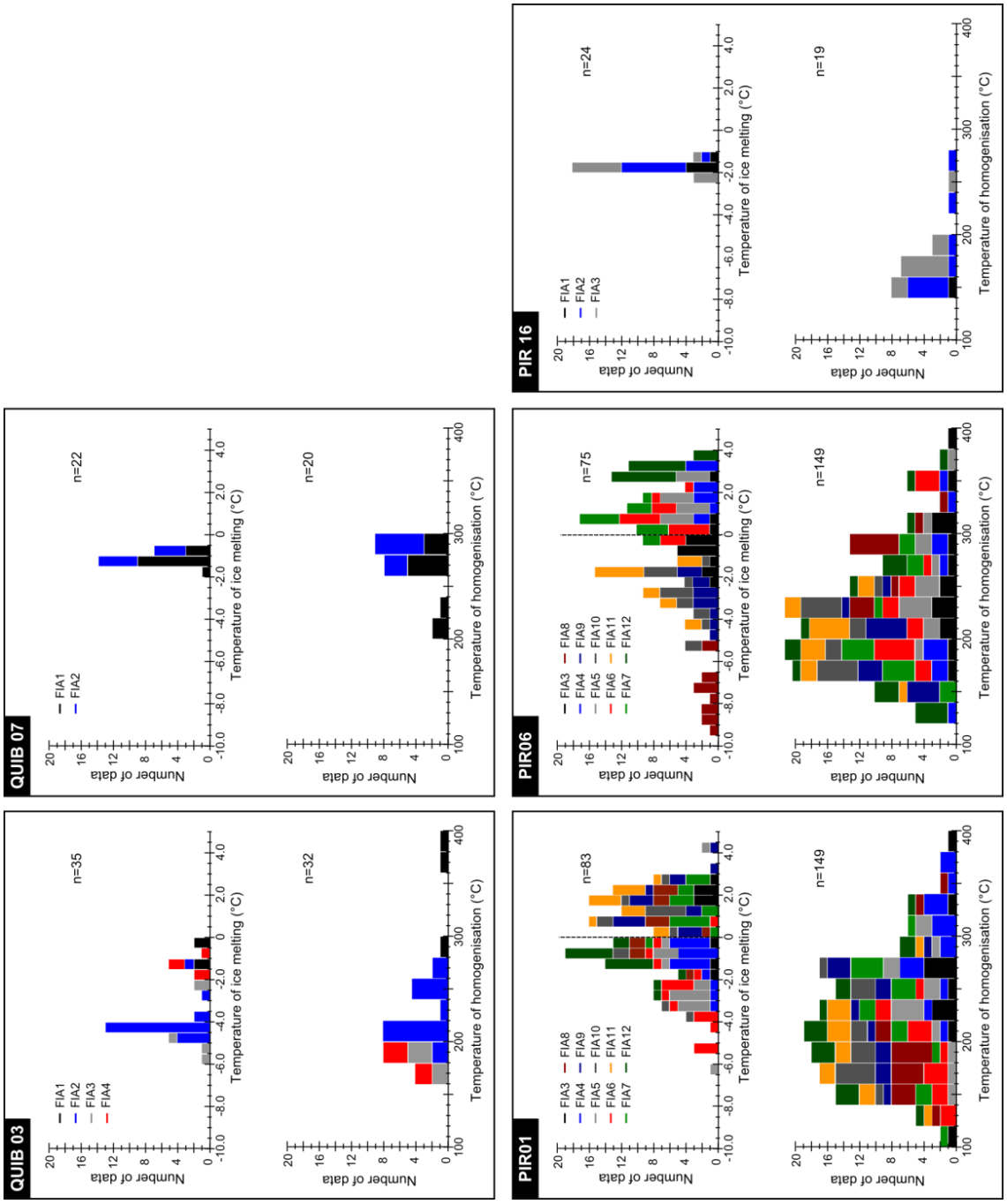

Figure III-16: Histograms reporting the ice melting and homogenisation temperatures acquired on samples QUIB and PIR from the Quiberon and the Piriac detachment footwalls, respectively.

3. Results

a. Microthermometry results

Accumulated microthermometry data are shown in histogram format for each analysed sample on **Fig. III-16**). Salinity calculated from measured ice melting temperature (T_{im}) and homogenisation temperature (T_h) are summarised in **Table III-6**. Detailed data can be found in **Table VI-3** in the appendix. Microthermometry data distribution is shown within individual FIAs (a Fluid Inclusion Assemblage is a finely discriminated, petrographically associated, group of inclusions, see **Chapter II** for methodology) as microthermometric data of individual fluid inclusion should not be included via histograms summarizing data for the whole sample (Goldstein and Reynolds, 1994; Goldstein et al., 2003; Chi and Lu, 2008)**.** For this preliminary study, 20 to 35 inclusions were analysed per sample.

T_{im} values range from -5.7 to -0.3°C in sample QUIB03, depicting salinities from 0.6 up to 8.8 wt% eq. NaCl. In sample QUIB07, T_{im} values (-1.8 to -1.0°C) indicate low salinities (1.4 to 2.7 wt% eq. Nacl). In sample PIR16, T_{im} values (-2.3 to -1.2°C) allow us to calculate salinities from 2.2 to 4.0 wt% eq. NaCl. Most of the T_{im} plot around -1.5°C, depicting salinities of ~2.5 to 3.0 wt% eq. NaCl.

The follow-up study by T. Piantoni and M. Dubois allowed acquiring more than 150 T_h and T_{im} values in samples PIR01 and PIR06 (**Fig. III-16; Tables III-6 and VI-3**). T_{im} values range from -6.1 to 5.0°C in sample PIR01 and from -9.4 to 4.0°C in sample PIR06. In both samples, the majority of the T_{im} plot above -2°C. However, about 50% of the T_{im} measured in samples PIR01 and PIR06 are above or equal to 0°C (i.e. 84 inclusions in PIR01, 76 in PIR06). These positive T_{im} values can be explained by: (1) an incorrect interpretation of phase transitions (ice melting instead of hydrate melting), but Raman

analysis confirm the absence of volatile compounds in the fluid inclusion vapour bubble and therefore negates this hypothesis; (2) a change in the microthermometric plate calibration, but the thermocouple (although it had to be changed) was carefully checked and did not show any signs of abrupt "jump" or drift during the set of measurements; (3) The liquid-vapour equilibrium (ice + liquid + vapour) was not reached during the ice melting. The vapour bubble that is compressed during ice solidification sometimes does not reappear at the beginning of the eutectic melting, particularly in the case of FIs with small vapour filling. This phenomenon leads to ice metastable melting, which in turn significantly increases the melting temperature at steady state (up to 6°C). The T_{im} values above 0°C are therefore not directly interpretable, but the approximate correction of metastable T_{im} give values between -6 and 0°C, similar to the range of negative T_{im} obtained in the same samples. Maximum calculated salinities are 9.4 wt% eq. NaCl in PIR01 and 13.3 wt% eq. NaCl in PIR06. Regarding the temperature of homogenisation, T_h values range from 160 to 400°C in sample QUIB03, from 260 to 300°C in QUIB07, from 140 to 280°C in PIR16, from 113 to 381°C in PIR01 and from 128 to 393°C in PIR06. Most of the T_h plot between 150 and 250°C.

a. Hydrogen and oxygen stable isotope geochemistry

The oxygen ($\delta^{18}O$) and hydrogen (δD) isotopic composition of fluid inclusions in quartz grains from samples PIR16 and QUIB07 were measured by Dr Véronique Gardien at the University of Lyon (France) using the crush-leach method (**Table III-7,** see **Chapter II** for methodology). PIR16 yields a $\delta^{18}O_{water}$ value of -68‰ and a δD_{water} value of -1.0‰. QUIB07 yields a $\delta^{18}O_{water}$ value of -76‰ and a δD_{water} value of 3.1‰.

Sample	**QUIB 03**	QUIB 03	QUIB 03	QUIB 03	QUIB 03	**QUIB 07**	QUIB 07	QUIB 07	**PIR 16**	PIR 16	PIR 16	PIR 16
FIA	**Total**	1	2	3	4	**Total**	1	2	**Total**	1	2	3
number of data	35	4	21	5	5	22	13	9	24	5	9	10
Average Salinity (wt% eq. Nacl)	**5.4**	1.5	6.6	6.5	2.1	**1.9**	1.9	1.9	**2.9**	2.9	2.8	3.1
SD	2.5	1.0	1.2	2.5	0.7	0.3	0.4	0.3	0.4	0.4	0.2	0.5
Min	0.6	0.6	2.3	3.6	0.9	1.4	1.4	1.6	2.1	2.3	2.4	2.1
Max	8.8	2.4	7.4	8.8	2.6	2.8	2.8	2.4	3.9	3.3	3.1	3.9
number of data	32	3	19	5	5	20	11	9	19	1	8	10
Average Th (°C)	**223**	345	226	179	184	**272**	260	287	**181**	149	186	180
SD	51	53	26	4	11	27	31	10	36	0	45	28
Min	172	284	190	173	172	203	203	274	149	149	149	153
Max	384	384	275	183	198	297	287	297	278	149	278	250

Sample	**PIR06**	PIR06	PIR06	PIR06	PIR06	PIR06	PIR06	PIR06	PIR06	PIR06	PIR06
FIA	**Total**	3	4	5	6	7	8	9	10	11	12
number of data	75	13			3	2	13	14	15	15	
Average Salinity (wt% eq. Nacl)	**4.6**	1.4			0	0	11.0	4.7	4.4	3.7	
SD	3.5	1.2	$T_{im} > 0°C$	$T_{im} > 0°C$	0	0	1.6	1.4	1.5	1.7	$T_{im} > 0°C$
Min	0.0	0.0			0	0	8.1	3.1	2.2	1.7	
Max	13.3	3.6			0	0	13.3	7.3	7.0	7.0	
number of data	149	15	13	15	17	15	12	14	15	15	18
Average Th (°C)	**227**	251	258	252	236	206	273	186	201	207	213
SD	59	49	89	47	61	49	35	34	28	28	78
Min	128	174	134	190	175	141	220	142	163	154	128
Max	393	342	393	374	356	286	324	242	247	253	364

Sample	**PIR01**	PIR01	PIR01	PIR01	PIR01	PIR01	PIR01	PIR01	PIR01	PIR01	PIR01
FIA	**Total**	3	4	5	6	7	8	9	10	11	12
number of data	83	3	19	17	17	1	5		4		17
Average Salinity (wt% eq. Nacl)	**2.8**	1.8	1.8	3.8	4.7	0.0	1.4		3.2		1.9
SD	2.1	0.9	1.4	2.2	2.6	0.0	0.8	$T_{im} > 0°C$	1.9	$T_{im} > 0°C$	1.1
Min	0.0	0.7	0.0	0.0	0.0	0.0	0.7		0.9		0.0
Max	9.3	2.7	5.3	9.3	8.4	0.0	2.7		5.9		4.6
number of data	149	12	17	15	14	16	17	13	15	14	16
Average Th (°C)	**223**	255	297	236	185	225	194	223	200	196	211
SD	58	65	44	46	40	54	58	45	38	43	56
Min	113	113	216	142	123	114	129	158	145	127	139
Max	381	381	362	302	259	302	349	286	267	290	331

Table III-6: Statistical analysis of studied Fluid Inclusion Assemblages (FIA) in samples QUIB03, QUIB0, PIR16, PIR06 and PIR01. T_h: Homogenisation Temperature; SD: Standard Deviation; T_{im}: Temperature of ice melting.

Sample	δD_{water} (‰) Fluid Inclusion	$\delta^{18}O_{water}$ (‰) Fluid Inclusion	H_20 (µL)	δD_{water} (‰) Muscovite
Lyon water	-87	-9.6		
	-87	-10.0		
	-86	-9.7		
PIR16	**-68**	**-1.0**	**$2.8\ 10^{16}$**	-74 ± 16‰
Lyon water	-91	-9.9	$3.4\ 10^{16}$	
	-83	-9.1	$3.3\ 10^{16}$	
	-84	-9.4	$3.3\ 10^{16}$	
QUIB07	**-76**	**3.1**	**$6.4\ 10^{15}$**	-62 ± 16‰
Lyon water	-91	-9.4	$3.3\ 10^{16}$	
	-89	-9.9	$3.2\ 10^{16}$	
Lyon water + air				
100%	-85.68	-9.43	$3.2\ 10^{16}$	
80% water + 20% air	-86.28	-8.46	$2.6\ 10^{16}$	
70% water + 30% air	-87.01	-7.84	$2.2\ 10^{16}$	

Table III-7: Hydrogen (δD) and oxygen ($\delta^{18}O$) stable isotope compositions obtained from crush leach analyses of aqueous fluid inclusions in quartz grains, with δD_{water} values calculated from muscovite from the same samples for comparison.

4. Discussion

a. Composition of the fluid

Cryometric data showing only the ice melting phase transition and Raman analyses confirming the absence of gas suggest that all the fluid inclusions are composed of a salty aqueous fluid. The eutectic melting is not observable due to the inclusions size (<10 µm). Without any further information, the fluid can be assumed to belong to the H_2O-NaCl system. This choice does not affect the estimation of the salt charge, as calculated salinities are low.

The estimated salinities range from 0 to 13.3 wt% eq. NaCl in samples QUIB03, QUIB07, PIR01, PIR06 and PIR16. It can be observed that most of the salinity estimates fall in the range of ~1 to 7 wt% eq. NaCl (**Fig. III-17**). However, FIA8 of sample PIR06 exhibits high salinity (11 wt% eq. NaCl).

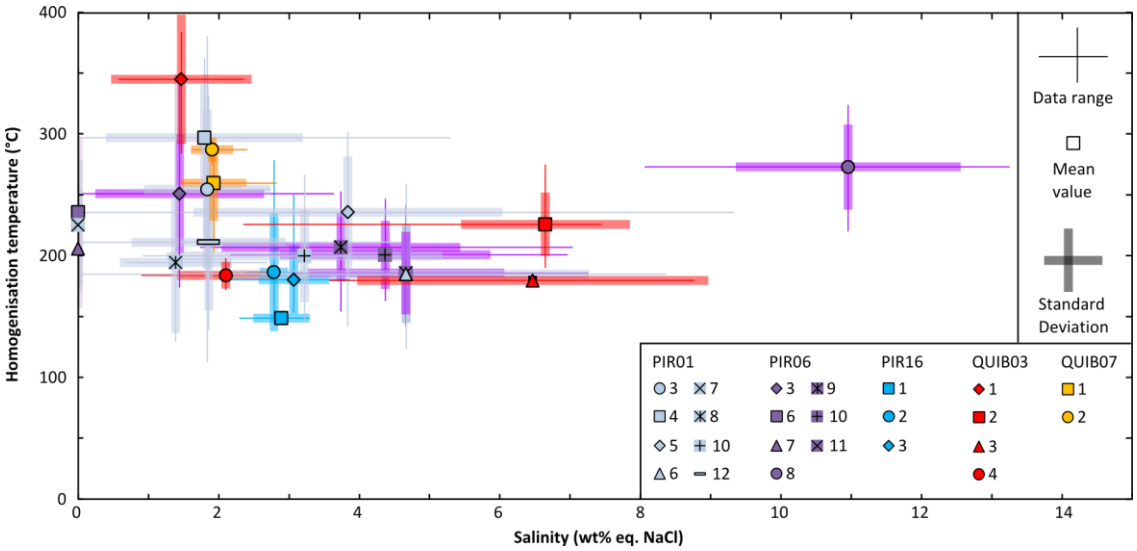

Figure III-17: Measured homogenisation temperature – calculated salinity plot summarizing microthermometry data from Piriac and Quiberon detachments footwall. Data representation respects the Fluid Inclusion Assemblage concept.

The salinity variation in a given FIA can be due to: (1) heterogeneous trapping of a boiling saline fluid; (2) refilling of previous cavities by a later fluid of different salinity; (3) water diffusion out of the inclusions (Bakker, 2017). The first two options are very unlikely as: (1) the heterogeneous trapping of a boiling fluid would result in a much greater salinity variation (up to 26wt% eq. NaCl; Sourirajan and Kennedy, 1962), and (2) refilling is generally observed at plane intersections which were rejected in the FIA selection. Therefore, salinity variations are assumed to be due to water diffusion outside inclusions (Bakker, 2017).

The hydrogen and oxygen isotopic values of water extracted from fluid inclusions allow more information about the source of the fluid to be determined. QUIB07 and PIR16 plot between the deep crustal fluids (metamorphic and/or magmatic) and the Meteoric Water Line, suggesting a mixing of two end members as shown on **Fig. III-18**.

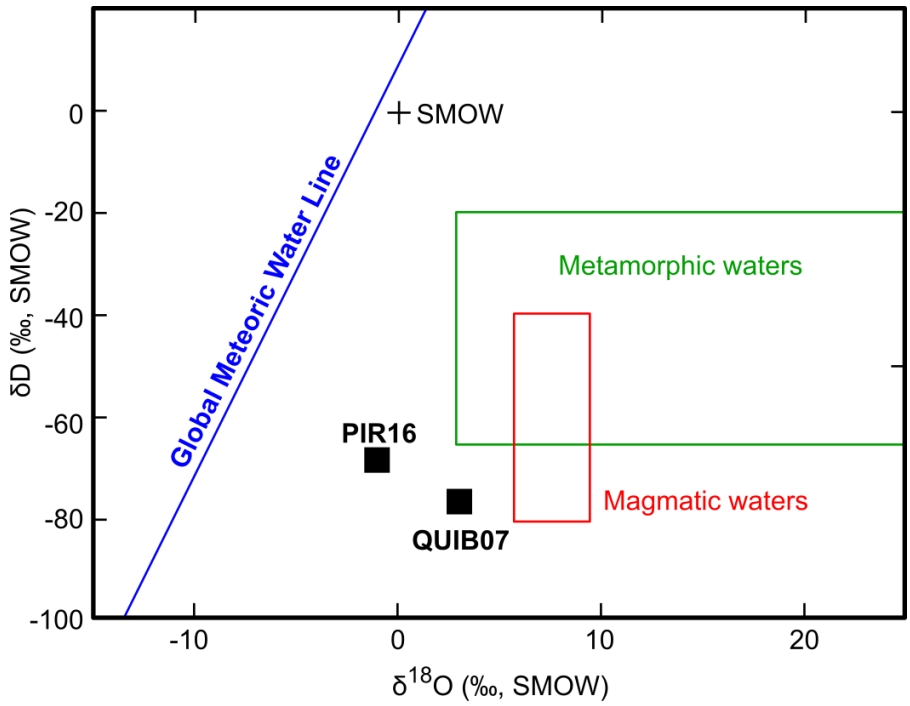

Figure III-18: Oxygen ($\delta^{18}O$) and hydrogen (δD) isotopic ratios of samples PIR16 and QUIB07 compared to different fluid sources (after Sheppard, 1986). SMOW = Standard Mean Ocean Water.

This is not surprising as a mixing of deep crustal fluids (magmatic and/or metamorphic) and surface-derived fluids is often observed in FIs found within ductile shear zones (Templeton et al., 1998; Siebenaller et al., 2013; Menzies et al., 2014; Quilichini et al., 2016). In the Variscan Belt, this mixing process between surface-derived and deep-sourced fluids is known to have led to the concentration of economic elements creating ore deposits (e.g. Boiron et al., 2003).

The low-salinity secondary fluid inclusions found in most of the samples define structural planes (**Fig. III-15 - A and B**) showing their synkinematic entrapment during activity on the shear zone. It is in good agreement with the synkinematic infiltration of meteoric fluids highlighted by low-salinity aqueous fluid inclusion in the Guérande granite in the footwall of Piriac detachment (1–6 wt.% NaCl eq.; Ballouard et al., 2017). It also agrees with low δD values of synkinematic hydrous silicates (δD_{Ms} down to -88%)

in both the Piriac and the Quiberon detachment footwalls (Dusséaux et al., 2019; **Chapter III - A and B**). The low-salinity fluid likely represents a surface-derived fluid that could have infiltrated during a more brittle phase of deformation during the exhumation of the sample.

All the samples were taken in the apical zone of the Quiberon and Guérande granitic intrusions emplaced in the footwall of detachment zones. These hydrothermal systems typically enhance fluid circulation, from both the Earth's surface and the underlying crust. **Chapter III - A and B** acknowledges the channelization of surface-derived fluids through brittle normal faults in the hanging wall, while the exhumation of migmatite sustained fluid convection at depth between 320 and 300 Ma.

b. Temperature of the fluid

The spread of T_h is significant in a given FIA (up to 100°C, **Fig. III-16**). Different processes can be evoked to explain such scattering: (1) the necking down process is the split of an inclusion when the vapour bubble has already nucleated, leading to two drastically distinct T_h values of both sub-cavities; (2) the stretching process is a partial increase of the inclusion volume leading to a density drop and subsequent T_h increase; (3) damage can be produced by rock section making and/or by experiment-induced heating; (4) the initial trapping of an heterogeneous fluid (i.e. water + gas).

Stretching (process 2) generally results in the presence of two modes, the lower one corresponding to unaffected FIs, the higher one to reequilibrated FIs (Goldstein and Reynolds, 1994); this is not observed in this study. The enlargement of fluid inclusions during thin section making and heating experiments (process 3) is excluded as quartz is very resistant to heating, and laboratory drawings allow checking of the consistency of the vapour filling during heating runs. Finally, a heterogeneous fluid entrapment

(process 4) would lead to the coexistence of vapour-rich and liquid-rich end members (Sourirajan and Kennedy, 1962). With this in mind, the data distribution would suggest the **necking-down process** (process 1) as being responsible for the observed T_h heterogeneity.

As it has been assumed that the process of necking down is responsible for the spread of T_h values, the average of all homogenisation temperatures is the most representative of the fluid.

The average temperatures of the five samples are as follow:

- PIR16: 181 ± 36 °C
- PIR01: 223 ± 58 °C
- PIR06: 227 ± 59° C.
- QUIB03: 223 ± 51 °C
- QUIB07: 285 ± 11 °C

c. Entrapment conditions of the fluid

Conditions of fluid entrapment are determined based on microthermometry properties of fluid inclusions:

- The average salinity is **3.7 ± 2.9 wt% eq. NaCl** for the five samples
- The average homogenisation temperature is **225 ± 62 °C** for the five samples.

Isochores are shown on **Fig. III-19**. The present-day gradient of 30°C/km includes two possibilities: a hydrostatic gradient (implying water infiltration from the surface) and a lithostatic gradient (no circulation between the surface and the depth). A higher

gradient of 40°C/km was also considered as the studied syntectonic leucogranites were emplaced in detachment footwalls within a hot late-orogenic crust (e.g. Vigneresse and Burg, 2003).

The average salinity and homogenisation temperature isochores allow the determination of the following conditions for a gradient of 30°C/km:

- 3950 bar and 480°C (16 km) under a lithostatic gradient
- 950 bar and 280°C (9.3 km) under a hydrostatic gradient.

For a higher gradient of 40°C/km, the isochores indicates P-T conditions of 2300 bar and 380°C (9.5 km) under a lithostatic gradient, and of 600 bar and 260°C (6.5 km) under a hydrostatic gradient.

Considering a lithostatic gradient seems more realistic as the samples: (1) belong to the footwall of two detachment systems, (2) are deformed in the ductile regime and (3) the aqueous fluids have a composition close to the metamorphic/magmatic composition (**Fig. III-18**). Therefore the microthermometry properties allow the determination of a pressure of ~4 kbar and a temperature of ~500°C when considering a lithostatic gradient. This is in good agreement with temperatures of 550 ± 50°C highlighted by quartz microstructures (grain boundary migration and prism <c> slip) and the Ti-in-MS geothermometer (see **section III-B**). Indeed, the Quiberon and Guérande granites were emplaced in the lower to middle crust that experienced Barrovian metamorphism and reached P-T conditions of 8 kbar and 700–750 °C (Jones and Brown, 1990).

However, the mechanism of fault-valve rupture could lead to intermittent slips along the fault: protracted periods of fluid stagnation and subsequent interaction with the rock under lithostatic pressure could be interrupted by short periods of fluid pressure release under lithostatic conditions (e.g. Sibson, 1981; McCaig, 1988; Sibson et al., 1988; Jenkin et al., 1994; Upton et al., 1995; Menzies et al., 2014).

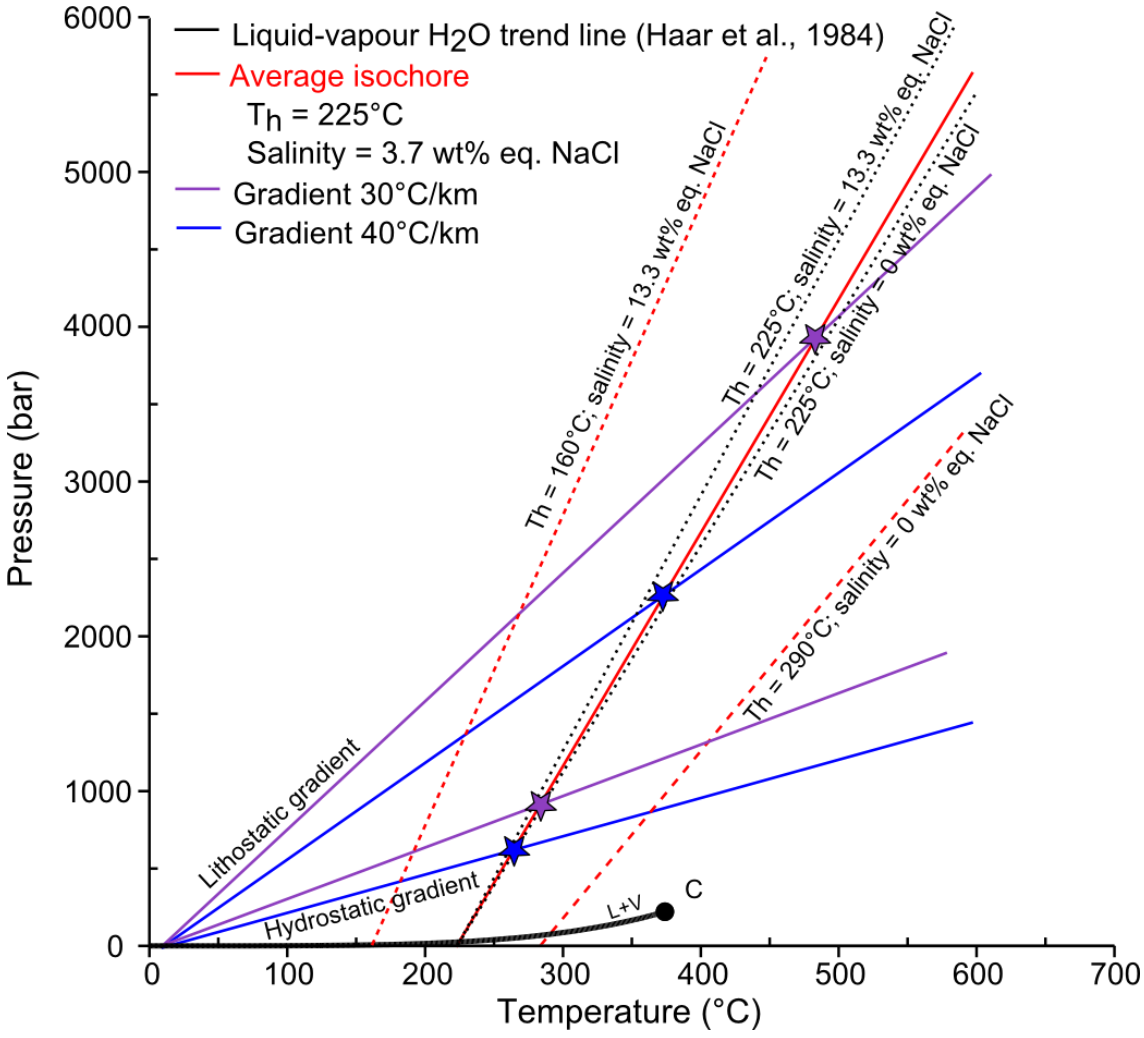

Figure III-19: Isochores of fluids trapped in inclusions of samples from Quiberon and Piriac detachment zones. The data have been produced using the equation of state of Zhang and Frantz (1987). L+V is the liquid-vapour curve of water; C is the critical point of pure water (Haar et al., 1984).

5. Conclusion

Detachment zones are the site of enhanced fluid circulation where meteoric fluids mix with magmatic and/or metamorphic fluids. Fluid inclusions were analysed in five samples from the mylonitic footwall of Variscan detachment zones. Most samples display biphasic aqueous fluids inclusions that appear secondary and synkinematic as they define structural planes. Synkinematic fluid inclusions are associated with microthermometry data depicting low-salinity water (~4 wt% eq. NaCl) trapped at ~4 kbar and ~500°C. The fluid inclusions hydrogen and oxygen isotopic compositions highlight a mixed signature between deep-sourced and surface-derived fluids. These results are in good agreement with the infiltration of meteoric water during high-temperature deformation documented by deuterium-depleted synkinematic muscovite in the same samples. Microstructural and microthermometry data of fluid inclusions point to the infiltration of surface-derived waters channelized via brittle fractures during the activity of Quiberon and Piriac detachment zones.

Conclusions of Chapter III

Chapter III aimed at investigating fluid-rock interactions in late-Variscan ductile shear zones in the southern Armorican domain, with a focus on the Quiberon and Piriac detachment zones that were invaded by surface-derived fluids during post-orogenic extension. A multidisciplinary study including structural, microstructural, hydrogen isotope geochemistry, geochronology and microthermometry data of fluid inclusions allows us to recover a range of information about the meteoric fluid infiltration:

1) The hydrogen isotopic composition of late-Carboniferous precipitation ($\delta D_{water} \leq$ -75‰) is revealed by hydrogen isotopic ratios of muscovite down to -88‰ and hydrogen and oxygen isotopic ratios of fluid inclusions down to -76‰ and -1‰, respectively.
2) The infiltration of meteoric fluids and associated fluid-rock interaction were synchronous with activity on the shear zone as shown by synkinematic mica fish and fluid inclusion microstructures.
3) The pressure-temperature conditions of meteoric fluid-rock interactions (~500-600°C and 4 kbar) are recorded by quartz microstructures, titanium content of muscovite and fluid inclusion microthermometry.
4) The timing of isotopic exchange between the fluid and the muscovite at ca. 305 Ma is highlighted by combined U-Th/Pb and Ar/Ar geochronology.
5) Meteoric fluid infiltration was made possible by a combined effect of brittle normal faulting in the upper crust, as shown by field evidence, helped by a sustained convection of fluids at depth highlighted by geochronology of leucogranite and migmatite.

IV. THE FRENCH MASSIF CENTRAL

A. Introduction

The western part of the French Massif Central (Limousin) represents the south-eastern extension of the southern Armorican domain. Both areas are characterized by syntectonic peraluminous granites closely associated with strike-slip and low-angle normal-sense shear zones (e.g. Virlogeux et al., 1999; Le Carlier de Veslud et al., 2004; Gébelin et al., 2007). In the previous chapter, it was shown that late-Variscan shear zones in south Brittany represent zones of intense meteoric fluid-rock interactions (**Chapter III;** Dusséaux et al., 2019).

In this chapter, the aim is to study the thermomechanical behaviour and associated fluid flow of crustal-scale shear zones in the Limousin to see if they can be compared from that perspective to those that affect the southern Armorican domain. This involved the use of hydrogen isotopes as tracers of meteoric fluids. The hydrogen isotope composition of muscovite (δD_{Ms}) from syntectonic leucogranites collected at the regional scale were measured and compared with previous structural, microstructural, geochronology and gravity data (e.g. Faure, 1995; Roig et al., 2002; Faure et al., 2002; Gébelin, 2004; Gébelin et al., 2004, 2006, 2007, 2009, Bellot, 2007, 2008; Cartannaz et al., 2007; Rolin et al., 2009, 2014). Based on the preliminary hydrogen isotope data, this study focused on the NE corner of the Millevaches massif near Felletin where low δD_{Ms} values (-116‰) from mylonitic leucogranite indicated a signature of meteoric fluids found at depth. Follow-up oxygen isotope analyses, combined with chemical and geochronological data allowed the characterisation of the mechanisms of deformation

during high temperature deformation and fluid flow, as well as the determination of the timing of meteoric fluid infiltration.

B. Geological background

The western part of the French Massif Central is characterized by syntectonic leucogranites that were emplaced within crustal-scale shear zones in the form of a horse-tail structure that represent the continuation of the Armorican shear zones (e.g. Virlogeux et al., 1999; Le Carlier de Veslud et al., 2004; Gébelin et al., 2007, 2009). The French Massif Central exposes allochthonous units involved in a south-verging stack of metamorphic nappes built from the Devonian to the Carboniferous over autochthonous units (e.g. Ledru et al., 1989; Faure et al., 2009).

In the Limousin region, three main tectono-metamorphic units can be described (**Fig. IV-1**): (1) the Upper Gneiss Unit (paragneiss hosting eclogite); (2) the Lower Gneiss Unit (orthogneiss and biotite-sillimanite paragneiss); and (3) the Para-autochthonous Unit (micaschist) (Fig. IV-1; e.g. Ledru et al., 1989; Faure et al., 2009). Two types of granite intruded these units: 1) granodiorite-monzogranite emplaced at ~360-350 Ma derived from the mixing of mantle and crustal magmas ("Guéret type"; e.g. Downes et al., 1997) and, 2) two-mica leucogranites formed from the partial melting of metasediments only (e.g. Turpin et al., 1990; Williamson et al., 1996). Gravity data indicate that the leucogranites are laccoliths that do no exceed a 4-km vertical thickness and were emplaced as horizontal layers in the flat-lying micaschist foliation between ~330 and 300 Ma (e.g. Cuney et al., 1990; Williamson et al., 1996; Gébelin et al., 2004, 2006).

This region is characterized by three main strike-slip shear zones cut by low-angle detachment zones (**Fig. IV-1**). To the north, the E-W-trending La Marche fault system separates the Aigurande Plateau to the north from the Guéret Massif to the south. This major shear zone is broken into two sections: the West and the East Marche shear zones indicating a northeastward sinistral reverse sense of shear and sinistral strike-slip movement, respectively (e.g. Gébelin et al., 2007). To the south of the La Marche shear zone is the NW-SE-trending dextral strike-slip fault system of Ouzilly - St Michel de Veisse - La Courtine. This major dextral fault system is crosscut by two main granitic laccolith intrusions that are the focus of this study: the Brâme Massif to the west and the Millevaches Massif to the east. Finally, the third major fault system is defined by the NNW-SSE Pradines dextral strike-slip shear zone that parallels the Millevaches Massif in its core.

The Brâme granite is bounded by NNE-SSW-trending low-angle detachment zones: the top-to-the-NW Nantiat shear zone to the west and the top-to-the-SE Bussières-Madeleine shear zone to the east. The Brâme syntectonic two-mica leucogranites was emplaced at ~324 $\pm$ 4 Ma (U-Pb on zircon; (Holliger et al., 1986) and was progressively exhumed along the detachments zones between ~320 to 305 Ma (Scaillet et al., 1996; Gébelin et al., 2007, 2009).

The 150 km-long N-S-trending Millevaches Massif is bounded to the west by the Argentat detachment zone and to the east by the Felletin detachment zone (e.g. Ledru and Autran, 1987; Roig et al., 2002; Gébelin, 2004; Gébelin et al., 2004, 2007, 2009; Cartannaz et al., 2007; Bellot, 2008; Rolin et al., 2009, 2014). The Pradines NNW-SSE-striking dextral strike-slip shear-zone controlled the syntectonic emplacement of two-mica leucogranite in the centre of the Millevaches massif at 313 $\pm$ 4 Ma, coeval with

high-grade metamorphism and migmatization (Gébelin et al., 2009). To the east of the Millevaches massif, the 180 km-long and NWN-SES-trending Argentat shear zone was active as a westward-dipping normal to dextral movement between ~340 and 330 Ma (Ar/Ar on muscovite; Roig et al., 2002). It was later reactivated at vertical sinistral fault zone where hydrothermal fluids circulation associated with brittle fracturing that occurred between ~300 and 295 Ma and led to As ± Au mineralization (e.g. Roig et al., 2002; Boiron et al., 2003; Bellot, 2008).

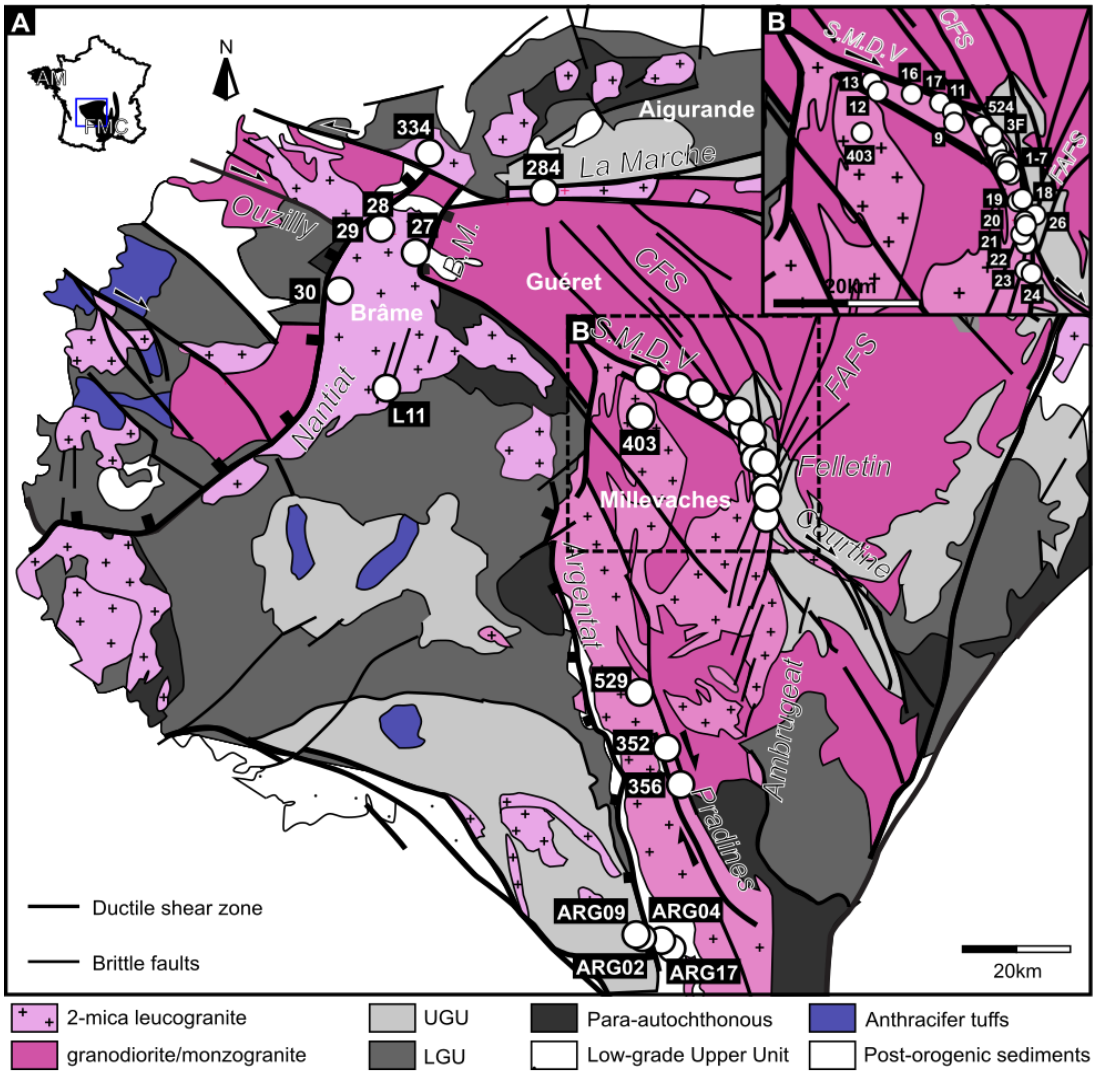

Figure IV-1: (A) Simplified geological map of the western part of the French Massif Central modified after BRGM (2003), Gébelin et al. (2007) and Rolin et al. (2014) with (B) a zoom on the Felletin area. B.M.: Bussières-Madeleine fault; S.M.D.V.; St Michel de Veisse fault; CFS: Creuse Fault System; FAFS: Felletin-Ambrugeat Fault System; UGU: Upper Gneiss Unit; LGU: Lower Gneiss Unit.

In the NE part of the massif, the WNW-ESE-striking Saint Michel de Veisse and Courtine dextral shear zones separate the Guéret granite emplaced at ~360 Ma from the Millevaches Massif made of syntectonic two-mica leucogranite that was emplaced continuously between ~340 and 305 Ma (U/Pb on monazite and Ar/Ar on muscovite; e.g. Gébelin, 2004; Cartannaz et al., 2007). The NW-SE-trending dextral Creuse brittle fault system cross-cuts both the Guéret massif to the north and the Millevaches leucogranite to the south. This brittle fault system is interpreted to have been active during the middle-upper Visean (~338 – 325 Ma; Rolin et al., 2014). The NW-SE-trending dextral Felletin-Ambrugeat brittle fault system affected the eastern flank of the Millevaches massif between ~325 and 320 Ma (Rolin et al., 2014).

C. Sampling strategy at the regional scale

The description and location of samples collected in the Limousin region can be found on **Fig. IV-1** and in **Tables IV-1, 2, 3 and 4**. Mylonitic leucogranite emplaced along the W-E trending near-vertical strike-slip La Marche shear zone that borders the Brâme granite to the North was sampled (**Fig. IV-1**). The western part of the Brâme granite in the mylonitic footwall of the Nantiat detachment shear zone was also sampled, where it displays foliations that dips 20° to the NW and supports ~WNW-ESE trends lineations (**Fig. IV-2 – A and B**). In the eastern part, into the footwall of the Bussières-Madeleine detachment shear zone, mylonitic granite displays foliations that dip ~50° to the east and bear ~E-W lineations (**Figs. IV-2 – C, D and E**).

Samples from the Millevaches leucogranite were collected along the Saint Michel de Veisse shear zone, especially in the NE part where the leucogranites are dissected by the Creuse and Felletin-Ambrugeat fault systems (**Figs. IV-2 – F and G; Fig. IV-4**).

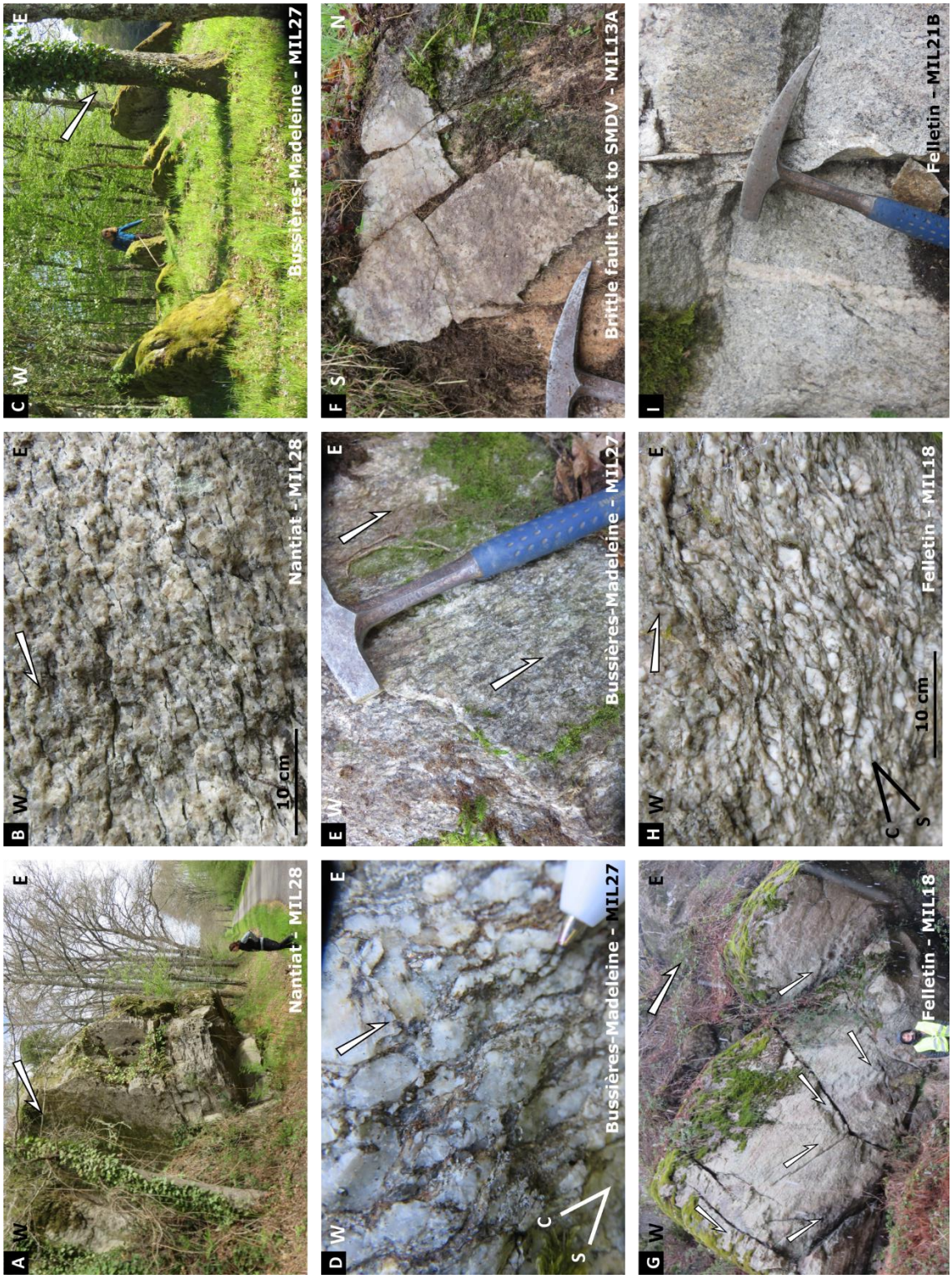

Figure IV-2: Field pictures from the Western part of the French Massif Central shear zones. (A) and (B) Leucogranite in the footwall of the Nantiat detachment zone dipping to the W (MIL28); (C), (D) and (E) Moderately-dipping leucogranite in the footwall of Bussières-Madeleine shear zone (MIL27; Foliation N010; 50E; Lineation N080); (F) Brittle fault filled with quartz representative of the Creuse fault system (MIL13A); (G) Leucogranite affected by conjugate brittle normal faults in the footwall of the Felletin detachment zone; (H) Mylonitic leucogranite in the Felletin detachment footwall; (I) Undeformed leucogranite granite (MIL21B).

In addition, some leucogranite samples were also collected along the Courtine shear zone (**Fig. IV-1**). Samples were also collected in the vicinity of the massif along the dextral Pradines shear zone (**Fig. IV-1**). Finally, samples were collected in the footwall and the hanging-wall of the Argentat detachment zone (**Fig. IV-1**; samples from Courtnadge, 2016).

For all sampling sites, mylonitic (**Fig. IV-2 – H**) to weakly deformed (**Fig. IV-2 – I**) two-mica leucogranites were collected within strike-slip ductile shear zones, and also along transects from detachment zones into the mylonitic footwall. As mentioned in **Chapter III**, samples were collected as close to the detachment interface as possible. The distance of the samples was estimated into the outcropping footwall with respect to the supposed contact between the upper plate and the lower plate or at least the highest point that is outcropping. In addition, samples in the host rocks (e.g. micaschist and biotite-sillimanite paragneiss), pegmatite, and quartz veins parallel to the granitic foliation (**Fig. IV-4**) or filling brittle fractures (**Fig. IV-2 - F**) were also collected. Some outcrops show evidence of intense brittle fracturing (**Fig. IV-2 – G**).

D. Results of hydrogen isotope geochemistry at the regional scale

The hydrogen isotope ratios (δD) of hydrous silicates (Muscovite: Ms; Biotite: Bt; Tourmaline: To; Chlorite: Chl) was measured on 73 different samples of leucogranite, pegmatite, quartz vein, micaschist, and gneiss from ductile shear zones (**Fig. IV-3 and Tables IV-1, IV-2, IV-4, IV-4**). Hydrogen isotope ratios of muscovite range from -116 to -40‰ (see coloured dots on **Fig. IV-3**). Bt and Chl yield δD values within a similar range ($-104 \leq \delta D_{Bt} \leq -59‰$ and $-118 \leq \delta D_{Chl} \leq -67‰$). In contrast, tourmaline indicates a smaller range of δD values (-74 to -69‰). The fractions $250 < f < 500$ µm and 500 µm $< f$ yield comparable δD values for all measured minerals as their difference never exceed ± 6‰.

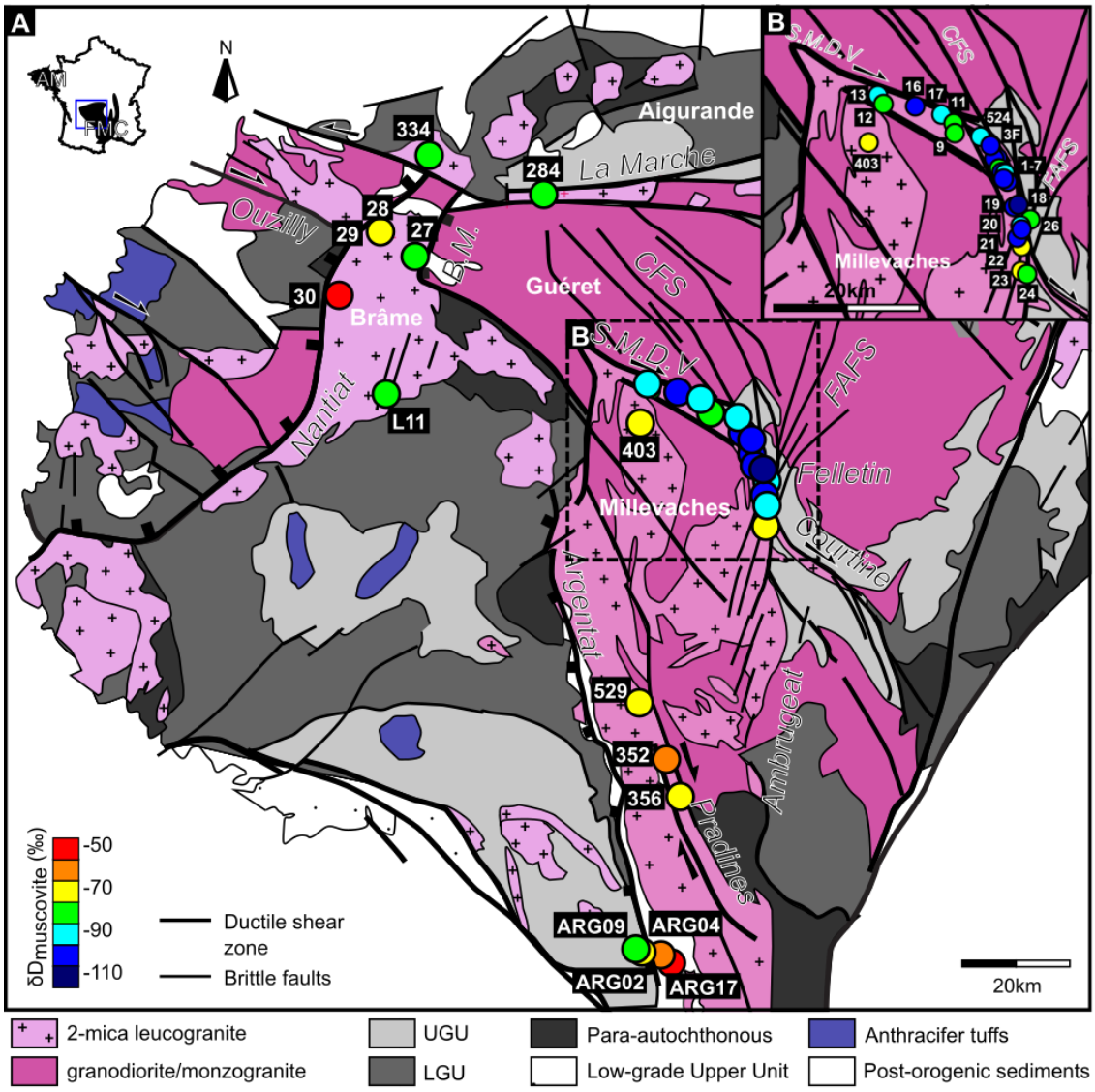

Figure IV-3: Hydrogen isotope ratios (δD) of muscovite in the Limousin region. (A) Simplified geological map of the western part of the French Massif Central modified after BRGM (2003), Gébelin et al. (2007) and Rolin et al. (2014) with (B) a zoom on the Felletin area. Samples sites colours indicate the measured hydrogen isotope composition of synkinematic muscovite. B.M.: Bussières-Madeleine fault; S.M.D.V.; St Michel de Veisse fault; CFS: Creuse Fault System; FAFS: Felletin-Ambrugeat Fault System; UGU: Upper Gneiss Unit; LGU: Lower Gneiss Unit.

1. The Brâme Massif

a. Strike-slip shear zone

Two mylonitic leucogranite samples along the Marche strike-slip shear zone yield δD_{Ms} values from -87 to -80‰ and δD_{Bt} values from -89 to -62‰ (**Fig. IV-3 and Tables IV-1 and 2**).

b. Detachment footwalls

In the footwall of the Nantiat detachment that bounds the Brâme massif to the west, 3 mylonitic leucogranite samples yield δD_{Ms} values that range from -73 to -55‰ and δD_{Bt} values from -77 to -59‰. In contrast, 3 mylonitic leucogranite samples from the western part of the Brâme granite, in the footwall of the Bussières-Madeleine detachment show lower δD_{Ms} values (-84 to -74‰), as well as lower δD_{Bt} values (-89 to -81‰) and δD_{To} values (-73 to -69‰; **Fig. IV-3; Tables IV-1 and 2**).

2. The Millevaches Massif

a. Strike-slip shear zones

Along the dextral strike-slip Pradines shear zone in the heart of the Millevaches massif, 3 mylonitic leucogranite samples yielded relatively high δD_{Ms} values (-79 to -66‰) and δD_{Bt} values (-79 to -73‰). These values are similar to the ones obtained in one sample of the Grand Janon migmatite ($-77 \leq \delta D_{Ms}$ values ≤ -74‰) that represent granulite that have been exhumed in the north-western extension of the Pradines shear zone. Along the dextral strike-slip St Michel de Veisse shear zone that bound the Millevaches massif to the North, δD_{Ms} values range from -107 to -64‰, δD_{Bt} values from -94 to -81‰, and δD_{Chl} from -108 to -67‰ in mylonitic leucogranite, pegmatite, quartz vein and granodiorite samples. The dextral Courtine shear zone, located at the east of the massif, have δD_{Ms} values from -84 to -72‰ and δD_{Bt} values from -86 to -82‰ in mylonitic and undeformed leucogranite and gneiss (LGU; **Fig. IV-3** and **Tables IV-1 and IV-2**).

b. Detachment footwall

In the footwall of the Felletin detachment shear zone, where the Creuse and the Felletin-Ambrugeat brittle fault systems and both the St Michel de Veisse and the

Name	Description	Shear zone/Granite	δD Silicates (‰)				Longitude	Latitude	Ar/Ar on muscovite (Gébelin, 2004)
			δD Muscovite (‰)		δD Biotite (‰)				
			250<f<500µm	500µm<f	250<f<500µm	500µm<f			
L11	Mylonitic leucogranite	Buissières-Madeleine/Brâme		-84		-82	1.393083	45.937189	
227	Mylonitic leucogranite	Felletin/Millevaches	-96	-98			2.109872	45.915478	
417	Mylonitic leucogranite	Felletin/Millevaches	-97	-99			2.156508	45.844781	
427	Mylonitic leucogranite	Felletin/Millevaches			-99	-99	2.163814	45.761736	
468	Mylonitic leucogranite	Felletin/Millevaches	-97	-98			2.156669	45.823317	
3F	Mylonitic leucogranite	Felletin/Millevaches		-101			2.134536	45.884153	306.5 ± 1.6 Ma to 325.0 ± 1.4 Ma
524	Mylonitic leucogranite	Felletin/Millevaches	-90	-89			1.777725	45.926136	303.8 ± 6.7 Ma to 318.3 ± 2.6 Ma
334	Mylonitic leucogranite	La Marche (East)		-87		-89	1.284694	46.344920	324.9 ± 3.0 Ma
284	Mylonitic leucogranite	La Marche (West)		-80		-62	1.541364	46.268381	314 to 329 Ma
403	Migmatite	Le Grand Janon/Millevaches	-74	-77			1.886467	45.929303	
352	Mylonitic leucogranite	Les Pradines/Millevaches		-66			1.931464	45.398783	
356	Mylonitic leucogranite	Les Pradines/Millevaches		-78			1.977808	45.345939	310.2 ± 2.9 Ma
529	Mylonitic leucogranite	Les Pradines/Millevaches	-79	-75	-79	-73	1.853478	45.507547	

Table IV-1: Hydrogen isotopic composition of hydrous silicates (this study) of samples described and dated by Ar/Ar on muscovite by Gébelin (2004)

Name	Description	Shear zone/Granite	δD Silicates (‰)								Longitude	Latitude
			δD Muscovite (‰)		δD Biotite (‰)		δD Tourmaline (‰)		δD Chlorite (‰)			
			250<f<500µm	500µm<f	250<f<500µm	500µm<f	250<f<500µm	500µm<f	250<f<500µm	500µm<f		
MIL09A	Weakly deformed pegmatite	Saint Michel de Veisse/Millevaches	-76	-76	-81	-82					2.031640	45.946785
MIL09B	Mylonitic granite	Saint Michel de Veisse/Millevaches		-88		-94					2.031640	45.946785
MIL11B	Quartz vein	Saint Michel de Veisse/Millevaches	-86						-94		2.041021	45.962696
MIL11C	Mylonitic leucogranite	Saint Michel de Veisse/Millevaches	-64								2.041021	45.962696
MIL12B	Quartz vein	Saint Michel de Veisse/Millevaches	-82								1.896550	45.985193
MIL13A	Brittle quartz vein	Saint Michel de Veisse/Millevaches	-85	-87							1.891688	45.997039
MIL13B	Mylonitic leucogranite	Saint Michel de Veisse/Millevaches		-81						-67	1.891688	45.997039
MIL13C	Pegmatite	Saint Michel de Veisse/Millevaches	-92	-94							1.891688	45.997039
MIL13D	Coarse-grained pegmatite	Saint Michel de Veisse/Millevaches		-71				-74			1.891688	45.997039
MIL16	Mylonitic granodiorite (Guêret)	Saint Michel de Veisse/Millevaches	-107						-108		1.959138	45.987788
MIL17	Mylonitic leucogranite	Saint Michel de Veisse/Millevaches	-92	-92							2.008264	45.970600
MIL22	Undeformed leucogranite	Courtine/Millevaches		-72		-82					2.152208	45.802480
MIL23	Mylonitic leucogranite	Courtine/Millevaches	-78	-76							2.153440	45.771458
MIL24	Gneiss (LGU)	Courtine/Millevaches	-84		-86						2.171693	45.759292
MIL27A	Mylonitic leucogranite	Buissières-Madeleine/Brâme	-81		-88	-89					1.399592	46.169060
MIL27B	Mylonitic leucogranite	Buissières-Madeleine/Brâme	-75	-74	-84	-81	-69	-73			1.399592	46.169060
MIL28	Mylonitic leucogranite	Nantiat/Brâme			-59						1.303564	46.218760
MIL29	Mylonitic leucogranite	Nantiat/Brâme	-73	-71	-77	-76					1.316316	46.221588
MIL30	Mylonitic leucogranite	Nantiat/Brâme	-55								1.190938	46.127146

Table IV-2: Hydrogen isotopic composition of hydrous silicates in the western part of the French Massif Central.

Name	Description	Shear zone/Granite	δD Silicates (‰)						δDwater (‰) [Ms;550°C]	δDwater (‰) [Ms;550°C]	δDwater (‰) [Bt;550°C]	δDwater (‰) [Chl;550°C]	Longitude	Latitude
			δD Muscovite (‰)		δD Biotite (‰)		δD Chlorite (‰)							
			250<f<500µm	500µm<f	250<f<500µm	500µm<f	250<f<500µm	500µm<f						
MIL01A	Mylonitic micaschist	Felletin/Millevaches	-96	-94		-98			-83	-81	-64		2.130371	45.885831
MIL01B	Weakly deformed pegmatite	Felletin/Millevaches	-100	-97					-87	-84			2.130371	45.885831
MIL01C	Mylonitic pegmatite	Felletin/Millevaches	-94	-91	-101				-81	-78	-67		2.130371	45.885831
MIL02A	Mylonitic leucogranite	Felletin/Millevaches	-101	-101		-98			-88	-88	-64		2.137289	45.883394
MIL02B	Undeformed pegmatite	Felletin/Millevaches	-101	-101					-88	-88			2.137289	45.883394
MIL03A	Mylonitic pegmatite	Felletin/Millevaches		-84		-81				-71	-47		2.122216	45.901330
MIL03B	Mylonitic micaschist	Felletin/Millevaches		-80						-67			2.122216	45.901330
MIL04A	Mylonitic pegmatite	Felletin/Millevaches		-100		-99				-87	-65		2.127975	45.895808
MIL04B	Weakly deformed pegmatite	Felletin/Millevaches	-97	-100					-84	-87			2.127975	45.895808
MIL05	Mylonitic pegmatite	Felletin/Millevaches		-93		-89				-80	-55		2.129432	45.894498
MIL06A	Mylonitic pegmatite	Felletin/Millevaches	-102	-101		-85		-115	-89	-88	-51	-86	2.111130	45.916198
MIL06C	Pegmatite vein (synfoliation)	Felletin/Millevaches	-101	-103					-88	-90			2.111130	45.916198
MIL06D	Mylonitic pegmatite	Felletin/Millevaches	-86	-87			-76	-75	-73	-74		-47	2.111130	45.916198
MIL07	Weakly deformed pegmatite	Felletin/Millevaches		-101						-88			2.105976	45.913867
MIL18A	**Mylonitic leucogranite**	**Felletin/Millevaches**	**-94**	**-96**					**-81**	**-83**			**2.148242**	**45.852764**
MIL18B	**Mylonitic leucogranite**	**Felletin/Millevaches**	**-102**	**-102**	**-96**				**-89**	**-89**			**2.148242**	**45.852764**
MIL18C	**Mylonitic leucogranite**	**Felletin/Millevaches**	**-102**	**-104**	**-104**				**-89**	**-91**	**-70**		**2.148242**	**45.852764**
MIL18D	**Mylonitic leucogranite**	**Felletin/Millevaches**		**-105**						**-92**			**2.148242**	**45.852764**
MIL18E	**Mylonitic leucogranite**	**Felletin/Millevaches**	**-102**	**-104**			**-107**		**-89**	**-91**		**-78**	**2.148242**	**45.852764**
MIL18F	**Quartz vein**	**Felletin/Millevaches**	**-99**	**-99**				**-104**	**-86**	**-86**		**-75**	**2.148242**	**45.852764**
MIL18G	**Mylonitic leucogranite**	**Felletin/Millevaches**	**-99**	**-96**			**-98**		**-86**	**-83**		**-69**	**2.145043**	**45.850982**
MIL18H	**Mylonitic coarse-grained leucogranite**	**Felletin/Millevaches**		**-116**				**-112**		**-103**		**-83**	**2.144694**	**45.850847**
MIL18I	**Undeformed leucogranite**	**Felletin/Millevaches**	**-95**	**-96**		**-93**			**-82**	**-83**	**-59**		**2.142585**	**45.849840**
MIL19	**Mylonitic leugranite**	**Felletin/Millevaches**		**-109**						**-96**			**2.147190**	**45.853884**
MIL20A	Mylonitic leucogranite	Felletin/Millevaches	-106				-118		-93			-89	2.158887	45.821669
MIL20D	Mylonitic leucogranite	Felletin/Millevaches		-99						-86			2.155482	45.825732
MIL21A	Mylonitic leucogranite	Felletin/Millevaches	-103	-102	-98				-90	-89	-64		2.149093	45.811931
MIL21B	Undeformed leucogranite	Felletin/Millevaches		-74		-77				-61	-43		2.146578	45.812753
MIL26A	Quartz vein	Felletin/Millevaches		-87						-74			2.170876	45.836544
MIL26B	Micaschist	Felletin/Millevaches			-98						-64		2.170876	45.836544

Table IV-3: Hydrogen isotopic composition of hydrous silicates in the Felletin area. δD_{water} are calculated from Ms (muscovite). Bt (biotite) and Chl (chlorite) at 550°C following the water-mineral fractionation factors of Suzuoki and Epstein (1976) and Graham et al. (1984). Data in gray are from the detailed section in the Felletin detachment footwall (part IV. E).

Name	Description	Shear zone/Granite	δD Silicates (‰)				Longitude	Latitude
			δD Muscovite (‰)		δD Biotite (‰)			
			250<f<500µm	500µm<f	250<f<500µm	500µm<f		
ARG1	Ordovician orthogneiss (LGU)	Hanging wall Argentat	-81	-83			E1°54'41.9"	N45°06'09.6"
ARG2b	Ordovician orthogneiss (LGU)	Hanging wall Argentat	-78	-78			E1°55'13.8"	N45°05'48.1"
ARG3	Micaschist	Hanging wall Argentat	-60	-58			E1°56'40.4"	N45°05'40.9"
ARG4	Micaschist	Hanging wall Argentat	-70	-67			E1°56'34.9"	N45°05'38.3"
ARG9	Ordovician orthogneiss (LGU)	Hanging wall Argentat	-80	-82			E1°53'53.6"	N45°08'48.0"
ARG10	Ordovician orthogneiss (LGU)	Hanging wall Argentat	-76	-80			E1°53'57.2"	N45°08'54.8"
ARG11c	Ordovician orthogneiss (LGU)	Hanging wall Argentat	-78	-77			E1°53'52.2"	N45°08'56.8"
ARG13	Leptynite	Hanging wall Argentat	-51	-49			E1°52'10.3"	N45°10'15.8"
ARG17a	Mylonitic leucogranite	Footwall Argentat	-53	-47			E1°57'46.3"	N45°05'12.9"
ARG17c	Micaschist	Footwall Argentat			-63		E1°57'48.9"	N45°05'15.1"
ARG17f	Micaschist	Footwall Argentat	-44	-40			E1°57'26.0"	N45°05'06.3"

Table IV-4: Hydrogen isotopic composition of hydrous silicates in Argentat detachment zone (Courtnadge, 2016).

Courtine ductile shear zones meet, δD of hydrous minerals are typically the most negative with δD_{Ms} values ranging from -116 to -74‰, δD_{Bt} values from -104 to -77‰, and δD_{Chl} values from -118 to -75‰ in 18 samples of mylonitic leucogranite, 2 of undeformed leucogranite, 11 of pegmatite, 2 of quartz veins and 3 of micaschists (**Fig. IV-3; Table IV-4**).

A preliminary study by Courtnadge (2016) measured lower δD_{Ms} values in 8 samples of the orthogneiss (LGU) and micaschist of the hanging wall of Argentat detachment (-83 to -49‰) compared to the higher δD_{Ms} values (-49 to -40‰) obtained on 2 samples of micaschist and 1 mylonitic leucogranite in the footwall. A micaschist sample in the footwall of Argentat yielded a δD_{Bt} value of -63‰ (**Fig. IV-3; Table IV-4**).

E. The NE corner of the Millevaches granite (Felletin)

The pilot study based on the hydrogen isotope geochemistry of the western part of the French Massif Central allowed the identification of the presence of meteoric fluids in the footwall of the Felletin detachment footwall (δD_{Ms} values of -116‰, sample MIL18H; **Table IV-3**). In an attempt to better characterise the mechanisms during deformation-related fluid flow, 10 samples were collected along a detailed section in the footwall of the Felletin detachment (see location of samples MIL18-19 on **Fig. IV-1** and associated field pictures on **Fig. IV-4**). This detailed study includes structural (see **section IV-E1**), microstructural (**E2**), hydrogen (**E3**) and oxygen (**E4**) isotope analyses coupled with the chemical composition of muscovite (**E5**). This allowed us to: (1) see if the infiltration of meteoric fluids affected the oxygen system of muscovite as much as the hydrogen system in the eastern part of the French Massif Central, and (2) acquire thermometry data using three different techniques (quartz microstructure, quartz-muscovite oxygen isotope exchange and Ti-in-muscovite thermometry) in order to calculate the hydrogen isotope composition of fluids present during deformation using experimentally-calibrated hydrogen isotope exchange parameters.

1. Macrostructures

The leucogranite was sampled along a transect into the mylonitic footwall of the top-to-the-E Felletin detachment shear zone at the NE edge of the Millevaches massif (**Fig. IV-4**). This zone allowed a continuous section from mylonitic leucogranite at the top of the section (MIL19) to anisotropic leucogranite towards the bottom (MIL18I) to be investigated (**Figs. IV-4 and 5**). Within the top 100m of section, the foliation dips from 20° to 70° to the east and displays shear bands orientated parallel to the lineation indicating a top-to-E sense of shear (**Figs. IV-4 and 5**). However, some samples contain

asymmetric feldspar grains with pressure shadows indicating a contradictory top-to-W sense of shear (**Fig. IV-5** - MIL18A). Moreover, some outcrops show intense folding of the mylonitic foliation (**Fig. IV-4**). This observation agrees with previous studies on the Millevaches massif that describe the magma rising towards the roof the laccolith being accommodated by low-angle detachment shear zones, leading to a strong coaxial deformation (Gébelin et al., 2006). Quartz veins (MIL18F) and coarser-grained leucogranite (MIL18H) are observed orientated parallel to the foliation (**Fig. IV-4**). In addition, numerous brittle conjugate faults and fractures affect the whole outcrop (**Fig. IV-4**).

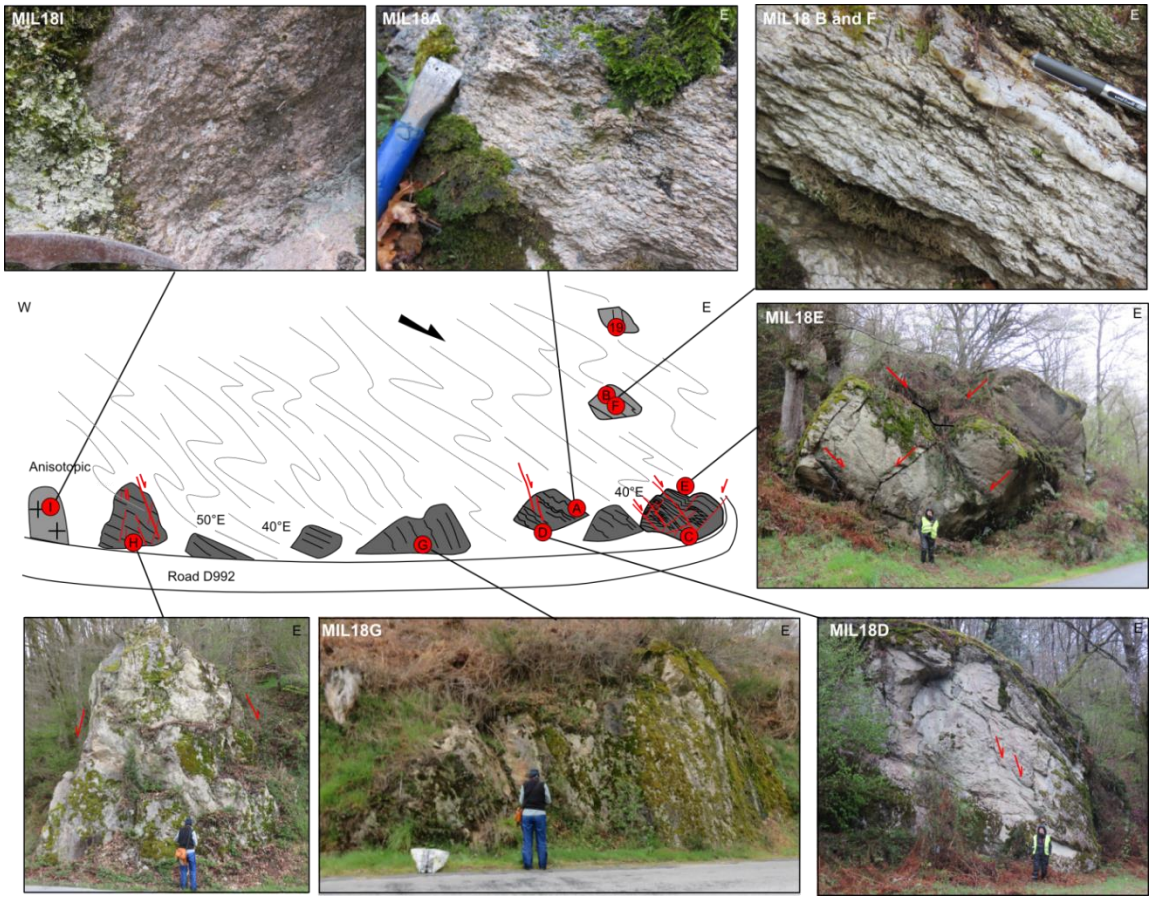

Figure IV-4: Cross-section and field pictures of the NE part of the Millevaches granite from anisotropic granite (MIL18I) to highly deformed granite (MIL19). Note the presence of brittle normal faults (red arrows).

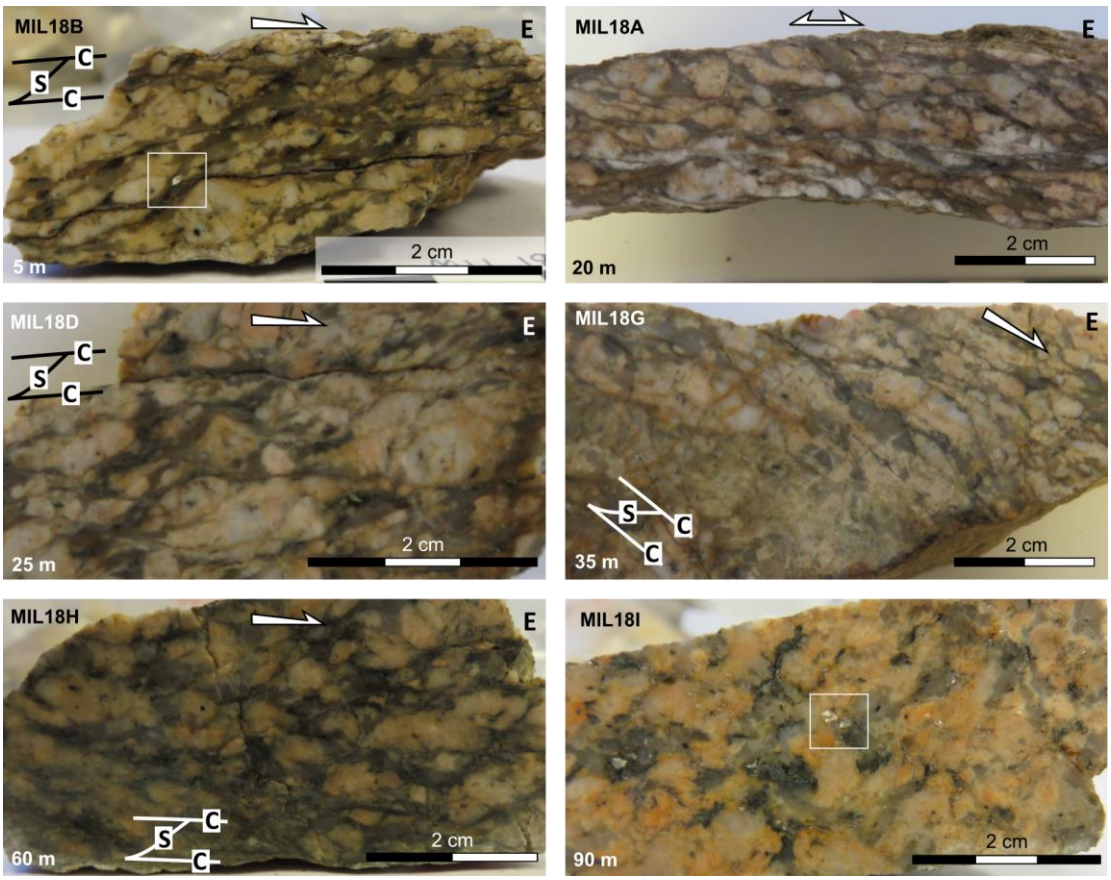

Figure IV-5: Hand samples collected in the NE part of the Millevaches granite from highly deformed granite (MIL18B) at the top of the section to anisotropic granite (MIL18I) at the bottom. Muscovite fish (MIL18B) and euhedral muscovite (MIL18I) are shown in white squares. The distance (m) to the top of the section is indicated at the bottom left.

2. Microstructures

Sub-solidus deformation textures such as rectangular and castellate quartz grain boundaries indicate that grain boundary migration (~500 to 700°C; e.g. Jessell, 1987; Hirth and Tullis, 1992; Stipp et al., 2002) was the dominant dynamic recrystallization process that affected syntectonic leucogranites of the NE corner of the Millevaches Massif (**Figs. IV-6 – A and B**). Quartz grains often exhibit chessboard-like texture indicative of both <a> and <c> dislocation slip that highlight high temperature deformation (>650°C) under hydrous conditions (**Fig. IV-6 – C**; Blumenfeld et al., 1986; Mainprice et al., 1986). Dynamic recrystallization of quartz-feldspar boundaries is

common (**Fig. IV-6 – D**) and indicates deformation at elevated temperatures (650–750°C; Gower and Simpson, 1992). Orthoclase is sometimes inverted to microcline (**Fig. IV-6 – E**) indicating solid-state deformation (Eggleton and Buseck, 1980). Coarser-grained sample MIL18H exhibits quartz grain boundary migration (500-700°C) but also sub-grain rotation that typically occur between 400 and 500°C (**Fig. IV-6 – F and G**; e.g. Stipp et al., 2002). Myrmerkite (intergrowth of quartz and plagioclase) are typical of deformation temperature above 500°C (**Fig. IV-6 - H**; e.g. Wirth and Voll, 1987). They occur asymmetrically in shortening quarters on sigmoidal K-feldspar grain rim and confirm the top-to-NE sense of shear (**Fig. IV-6 - H**; Simpson and Wintsch, 1989). These observations are in agreement with previous EBSD data obtained on quartz grains from similar samples (Gébelin et al., 2007) that revealed plastic deformation dominated by prismatic <a> glide, which occurs between 400°C and 700°C (Tullis et al., 1973; Mainprice and Paterson, 1984).

Sample MIL18H contains evidence of brittle fracturing as feldspar grains are affected by conjugated normal faults (**Fig. IV-4 - G**) or antithetic rotation leading to the formation of domino structures (**Fig. IV-4 - F**). This is good agreement with field observations of brittle fractures (**Figs. IV-2 and IV-4**).

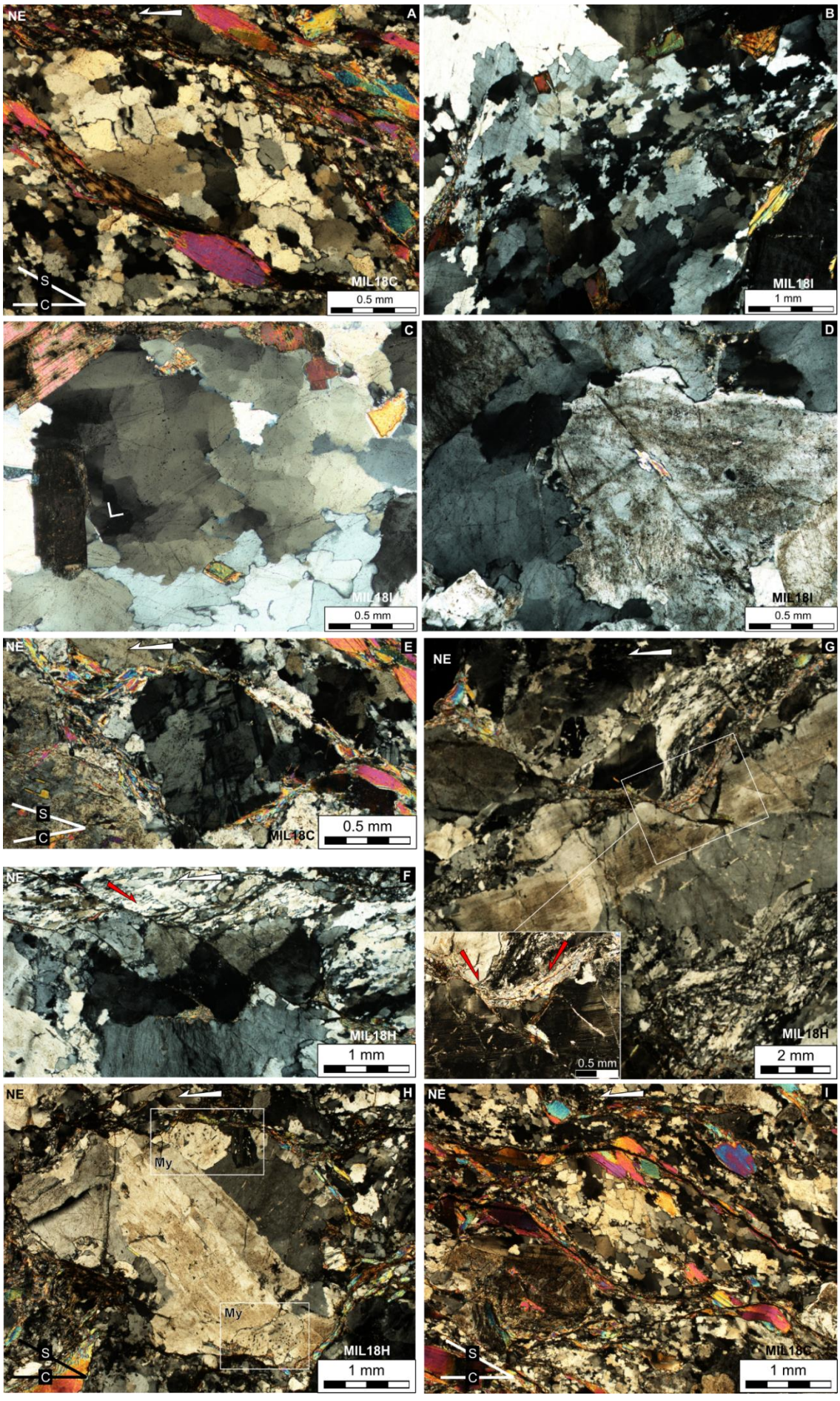
NE
A
S
C
MIL18C
0.5 mm
B
MIL18I
1 mm
C
MIL18I
0.5 mm
D
MIL18I
0.5 mm
NE
E
S
C
MIL18C
0.5 mm
NE
F
MIL18H
1 mm
NE
G
0.5 mm
MIL18H
2 mm
NE
H
My
My
S
C
MIL18H
1 mm
NE
I
S
C
MIL18C
1 mm

Figure IV-6 (last page): Quartz microstructures under cross-polarised light in the footwall of the Felletin detachment typical of high temperature deformation. (A) and (B) Grain boundary migration of a polycrystalline quartz aggregate; (C) Quartz with chess- board pattern; (D) Grain boundary migration between quartz and feldspar grains; (E) Orthoclase inversion to microcline and muscovite defining shear bands; (F) Domino-style rotation with antithetic shear; (G) Micro conjugated normal faults affecting a feldspar grain; (H) Assymetric distribution of myrmekite on sigmoidal felpar grain; (I) Top-to-E shear bands highlighted by muscovite grains.

Shear bands highlighted by muscovite fish along shear (C) and foliation (S) planes support a syntectonic emplacement of leucogranite (e.g. **Fig. IV-6 - I;** Gapais and Barbarin, 1986). Lozenge-shaped muscovite grains can be explained to have formed by solution precipitation and/or in strain shadows during deformation. Indeed, muscovite grains were sheared by slip on their (001) planes to form mica fish of the group 3 (**Fig. IV-7 – B**) of the classification of ten Grotenhuis et al. (2003). Some muscovite fish that fall into the group 1 (**Fig. IV-7 – C**) of the classification of ten Grotenhuis et al. (2003) formed by simultaneous grain rotation and reduction of their upper and lower sides. Group 1 mica fish were transformed into group 2 mica fish (**Fig. IV-7 – A**) by drag along micro shear zones (ten Grotenhuis et al., 2003). In the coarser-grained leucogranite MIL18H, muscovite fish show evidence of intense recrystallization (**Fig. IV-7 – D and E**) while some muscovite grains are folded (**Fig. IV-7 – F**).

The weakly deformed granite sample MIL18I displays euhedral muscovite grains **Fig. IV-7 – G and H**) and large primary quartz crystals and/or quartz grain boundary migration (**Fig. IV-6 – A, B, C, D**) consistent with high temperature deformation.

3. Hydrogen isotope results

The hydrogen isotope ratios of muscovite (δD_{Ms}), biotite (δD_{Bt}) and chlorite (δD_{Chl}) have been analysed in mylonitic to undeformed leucogranite along a transect into the Felletin detachment footwall. Sample MIL19 collected at the top of the section was

considered to represent the closest point to the eroded detachment interface (at 0m; **Fig. IV-7, Table IV-3**). The δD_{Ms} values range from -116 to -95‰. The difference between the δD values of the largest muscovite size fraction (500µm < f) and the smallest size one (250 < f < 500µm) does not exceed ± 3‰. The lowest δD_{Ms} values (from -116 to -100‰) occur within the 0-25 m and 60 m depth intervals. The δD_{Ms} values decrease along the 100m-long section, from lower δD_{Ms} values at the top in mylonitic leucogranite (MIL19; δD_{Ms} = -109‰) down to higher values at the bottom where leucogranite are undeformed (MIL18I; δD_{Ms} = -95‰; **Fig. IV-7**). The coarser-grained leucogranite sample MIL18H at 60m yields the lowest δD_{Ms} value (δD_{Ms} = -116‰) found in this study.

The δD_{Bt} values vary from -104 to -93‰. The difference between the δD_{Ms} and the δD_{Bt} values range from -2 to +7‰. Considering that biotite and muscovite show a ~20 ‰ difference in hydrogen isotope fractionation (21‰ at 550°C, Suzuoki and Epstein, 1976; lower for biotite), it can be deduced that these 2 minerals did not reach hydrogen isotopic equilibrium.

The δD_{Chl} values vary from -112 to -98‰. The difference between the δD_{Ms} and the δD_{Chl} values range from -5‰ at the top of the section to +4‰ at the bottom. This difference has been interpreted as demonstrating that muscovite and chlorite have not reached isotopic equilibrium as the isotopic fractionation between muscovite and chlorite is -16‰ at 550°C (Suzuoki and Epstein, 1976; Graham et al., 1984). It is interesting to note that biotite and chlorite were rarely found together in the same sample.

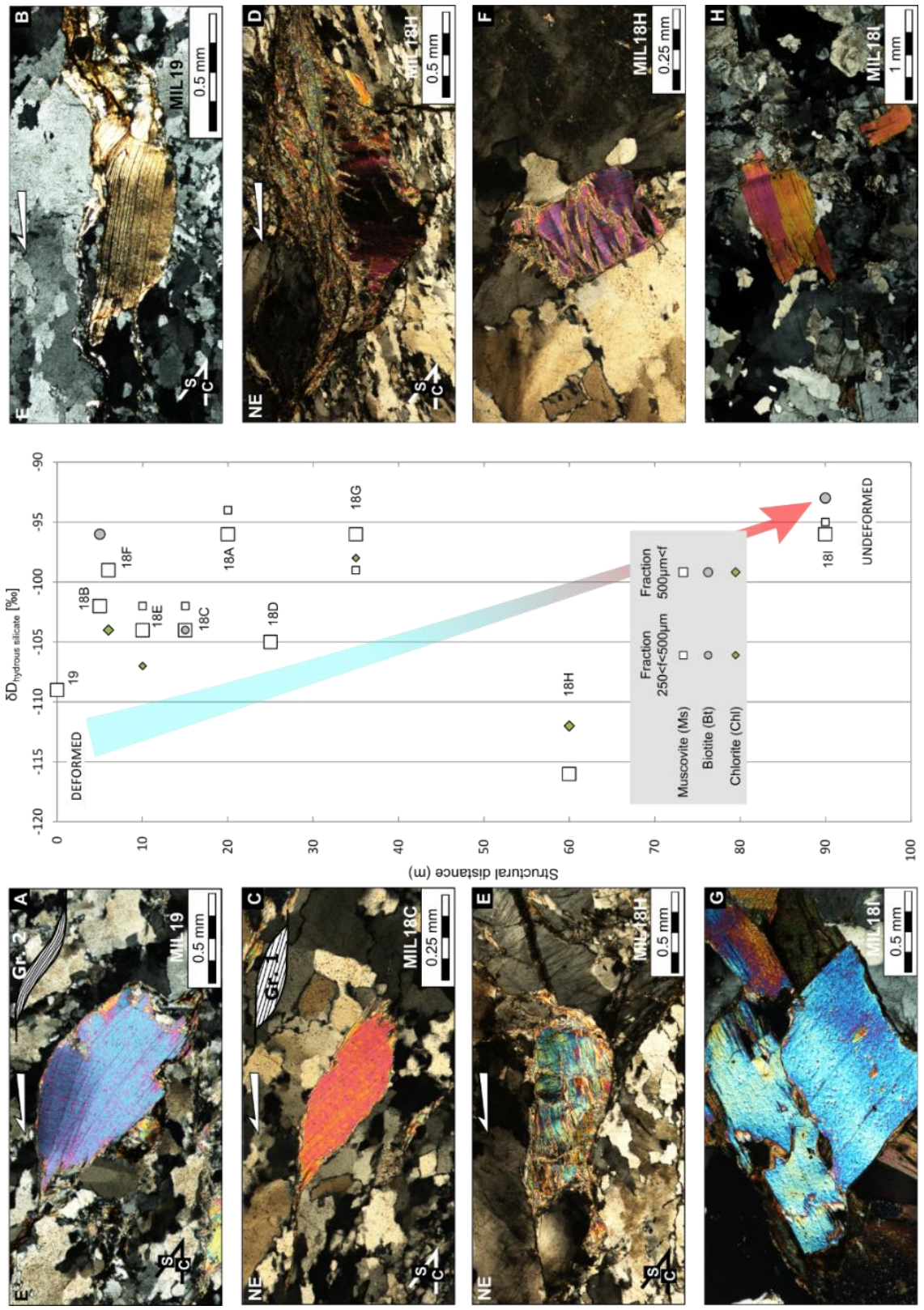

Figure IV-7: Muscovite microstructures and hydrogen isotope analysis of muscovite, biotite and chlorite in the footwall of the Felletin detachment with respect to the distance to the hanging-wall (0 to 100m). See text for description of photographs. Note the sketches in A, B and C that describe the different mica fish groups from the classification of ten Grotenhuis et al. (2003).

4. Oxygen isotope results

The oxygen isotope ratios ($\delta^{18}O$) of muscovite and quartz were measured on 4 samples of leucogranite (MIL19, MIL18C, MIL18H and MIL18I) in the Felletin section using laser-fluorination mass spectrometry at the University of Lausanne, Switzerland. The average precision of measured $\delta^{18}O$ values is ± 0.1 ‰ (detailed methods in **Chapter II**).

The $\delta^{18}O_{Ms}$ values range from 8.4 to 9.0‰ (**Fig. IV-8 - A; Table IV-5**) and are in good agreement with the trend defined by the δD_{Ms} values as they also decrease from the top to the bottom of the section (**Fig. IV-8 - A**). Indeed, the undeformed leucogranite (MIL18I) yields the highest $\delta^{18}O_{Ms}$ value of 9.0‰ corresponding to a high δD_{Ms} value of -95‰ whereas the coarse-grained sample (MIL18H) has the lowest $\delta^{18}O_{Ms}$ value of 8.4‰ with the lowest δD_{Ms} value of -116‰ (**Fig. IV-8 - B**).

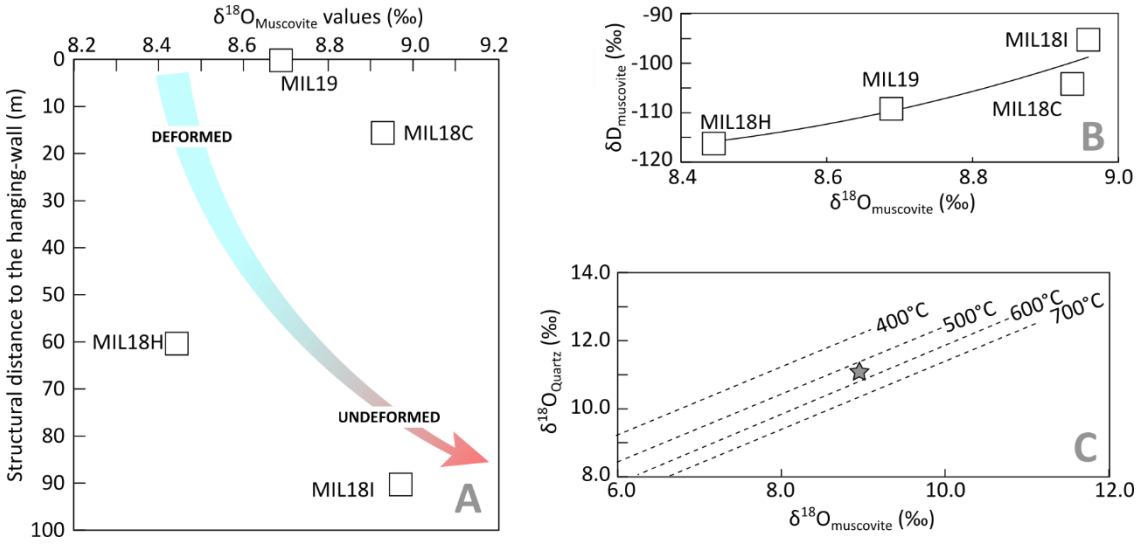

Figure IV-8: Oxygen isotope geochemistry. (A) Oxygen isotope composition of muscovite (Ms) according to the structural distance; (B) $\delta^{18}O$ values versus δD values of muscovite; (C) $\delta^{18}O_{Qz}$ versus $\delta^{18}O_{Ms}$ from sample MIL18C. Isotherms are based on the Qz-Ms thermometer from Chacko et al. (1996).

Isotope exchange equilibrium temperatures can be calculated based on the difference in $\delta^{18}O$ values of muscovite and quartz, given that the minerals reached isotopic equilibrium (e.g. Chacko et al., 1996). Sample MIL18C has a $\delta^{18}O_{Ms}$ value of 8.9‰ and a $\delta^{18}O_{Qz}$ value of 11.1‰. Assuming oxygen isotope equilibrium during deformation and recrystallization in sample MIL18C and using the calibration of Chacko et al. (1996), a $\Delta^{18}O_{Qz\text{-}Ms}$ value of 2.15 ‰ is consistent with a deformation temperature of 538 ± 41°C (**Fig. IV-8 - C**). Indeed, the uncertainty on the isotopic analysis ± 0.1‰ gives an uncertainty of ± 41°C for the geothermometer. This temperature is in good agreement with those deduced from quartz microstructures (T > 400°C). However, this quartz sample showed some minor contamination with another phase, so this temperature has to be carefully interpreted and coupled with other thermometry techniques.

Sample	Distance [m]	Mineral	Weight [mg]	$\delta^{18}O$ [‰]	δD_{Ms} [‰]	$\Delta^{18}O_{Qz\text{-}Ms}$ [‰]	Temperature [°C]
MIL19	0	Muscovite	1.46	8.7	-109		
MIL18C	15	Muscovite	1.67	8.9	-104	2.15	538
MIL18C	15	Quartz	1.35	11.1			
MIL18H	60	Muscovite	1.74	8.4	-116		
MIL18I	90	Muscovite	1.73	9.0	-95		

Table IV-5: Oxygen isotope data and associated quartz-muscovite oxygen isotope exchange temperatures (Chacko et al., 1996).

5. Muscovite geochemistry and Ti-in-Ms geothermometer

The chemical composition of muscovite was measured using CAMECA SX100 microprobe at the University of Lille (France) in order to check the homogeneity of muscovite grains and use the Ti-in-Ms geothermometer of Wu and Chen (2015). Three polished thin-sections were made (MIL18C. MIL18H and MIL18I) in order to obtain muscovite major elements contents via the electronic microprobe (analytical procedure described in **Chapter II**). Muscovite compositions are heterogeneous in the studied

samples with 0.00 < Ti < 0.05 mol, 0.02 < Na < 0.10 mol and 0.04 < Mg < 0.18 mol (**Table VI-4 in the appendix**). Muscovite grains plot essentially in the primary field in a tertiary diagram (**Fig. IV-9**). However, the chemical composition of recrystallized tips of muscovite fish tend towards the secondary muscovite field compared to cores that plot in the primary field (see zooms and associated BSE pictures of **Fig. IV-9**).

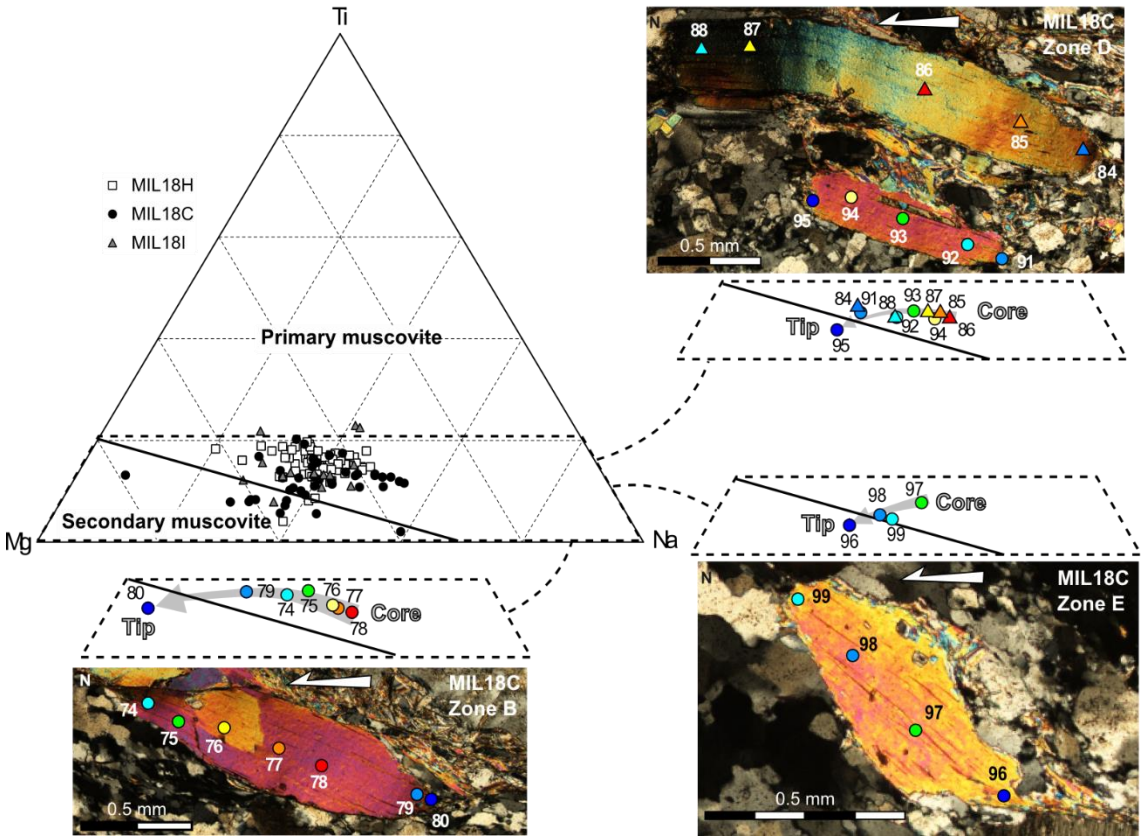

Figure IV-9: Ternary Mg–Ti–Na diagram (Miller et al., 1981) for muscovite from the NE corner of the Millevaches granite (Massif Central, France). Zooms on specific analysed points and associated oriented photographs under cross-polarised light (Zones B, D and E of sample MIL18C) show that grain cores plot in the primary field of the tertiary diagram whereas recrystallized tips of muscovite fish tend towards the field of secondary muscovite. Data can be found in Table VI-4 in the appendix..

The titanium-in-muscovite thermometer (Wu & Chen, 2015) has been applied to the three samples considering a pressure of 4 ± 1kbar (Gébelin et al., 2009). The mylonitic leucogranite sample (MIL18C) yields average temperatures of 493 ± 57°C, the pegmatite sample (MIL18H) an average temperature of 568 ± 42°C and the anisotropic granite (MIL18I) 559 ± 55°C (**Table VI-4 in the appendix)**. The Ti-in-Ms allows us to estimate a temperature of 540 ± 51°C for the Felletin section.

6. Isotopic composition of the fluids in the Felletin detachment footwall

The isotope composition of the fluid present in the Felletin detachment footwall was calculated using the hydrogen isotope composition of muscovite, the hydrogen water-muscovite isotope fractionation factor of Suzuoki and Epstein (1976) and the temperature of isotope exchange between the fluid and the mineral estimated by 1) quartz microstructure; 2) Ti-in-Ms geothermometry and 3) oxygen isotope thermometry (**Table IV-6**):

1) Deformation temperatures of 550 ± 150°C deduced from **quartz microstructures** (this study, e.g. Hirth and Tullis, 1992; Stipp et al., 2002; Langille et al., 2010) allow the calculation of δD_{water} values ranging from -103 to -83 ± 16‰.

2) The **Ti-in-Ms thermometer** (Wu and Chen, 2015) yielded an average temperature of 540 ± 51°C for the section that allows the calculation of δD_{water} values ranging from -104 to -89 ± 5‰.

3) The temperature of 538 ± 41°C estimated by **quartz-muscovite oxygen isotope exchange thermometry** allows allow the calculation of δD_{water} values ranging from -104 to -89 ± 4‰.

			Muscovite			Quartz microstructures thermometry					Titanium-in-Ms thermometry					Quartz-muscovite oxygen isotope exchange thermometry				
Sample	Distance (m)	Rock type	δD Ms (‰)	Fraction Ms (µm)	± (‰)	**T (°C)**	± (°C)	**δD water (‰)**	-	+	**T (°C)**	Uncertainty (°C)	**δD water (‰)**	-	+	**T (°C)**	Uncertainty (°C)	**δD water (‰)**	-	+
MIL19	0	Mylonitic leugranite	-109	500<f	2	550	150	**-96**	-9	16	540	51	**-95**	-4	5	538	41	**-95**	-3	4
MIL18B	5	Mylonitic leucogranite	-102	500<f	2	550	150	**-89**	-9	16	540	51	**-88**	-4	5	538	41	**-88**	-3	4
MIL18F	6	Quartz vein	-99	500<f	2	550	150	**-86**	-9	16	540	51	**-85**	-4	5	538	41	**-85**	-3	4
MIL18E	10	Mylonitic leucogranite	-104	500<f	2	550	150	**-91**	-9	16	540	51	**-90**	-4	5	538	41	**-90**	-3	4
MIL18C	15	Mylonitic leucogranite	-104	500<f	2	550	150	**-91**	-9	16	**493**	**57**	**-86**	-5	8	**538**	**41**	**-90**	-3	4
MIL18A	20	Mylonitic leucogranite	-96	500<f	2	550	150	**-83**	-9	16	540	51	**-82**	-4	5	538	41	**-82**	-3	4
MIL18D	25	Mylonitic leucogranite	-105	500<f	2	550	150	**-92**	-9	16	540	51	**-91**	-4	5	538	41	**-91**	-3	4
MIL18G	35	Mylonitic leucogranite	-99	250<f<500	2	550	150	**-86**	-9	16	540	51	**-85**	-4	5	538	41	**-85**	-3	4
MIL18H	60	Mylonitic pegmatite	-116	500<f	2	550	150	**-103**	-9	16	**568**	**42**	**-104**	-3	3	538	41	**-102**	-3	4
MIL18I	90	Undeformed leucogranite	-96	500<f	2	550	150	**-83**	-9	16	**559**	**55**	**-83**	-4	5	538	41	**-82**	-3	4
		AVERAGE	-103			550		**-90**	-9	16	540	51	**-89**	-4	5	538	41	**-89**	-3	4
		SD	6			0		**6**	0	0	19	4	**7**	0	1	0	0	**6**	0	0
		Min	-116			550		**-103**	-9	16	493	42	**-104**	-5	3	538	41	**-102**	-3	4
		Max	-96			550		**-83**	-9	16	568	57	**-82**	-3	8	538	41	**-82**	-3	4

Table IV-6: Stable isotope data from the Felletin detachment footwall (Limousin, Massif Central, France). δD_{water} values are calculated based on temperatures deduced from quartz microstructures (Hirth and Tullis, 1992; Stipp et al., 2002; Langille et al., 2010), the Ti-in-Ms geothermeter (Wu and Chen, 2015) and the quartz-muscovite oxygen isotope exchange thermometer (Chacko et al., 1996), combined with the hydrogen and oxygen isotope fractionation factors of Suzuoki and Epstein (1976) and the measured hydrogen isotope composition (δD) of muscovite (Ms).

F. Discussion

1. Hydrogen isotope geochemistry in the Limousin shear zones

The 76‰ difference in δD_{Ms} values measured in all mylonitic leucogranites collected at the regional scale in the Limousin indicates the presence of fluids from different sources that interacted with muscovite during high temperature deformation (**Fig. IV-10**; **Tables IV-1 to 4**).

In the Brâme massif, leucogranite emplaced along the strike-slip La Marche shear zone and in the footwall of the Bussières-Madeleine detachment are characterised by low δD values of muscovite, biotite and tourmaline. In comparison, leucogranite from the western part of the Brâme massif in the Nantiat detachment footwall yield higher δD values of muscovite and biotite (**Fig. IV-10**; **Tables IV-1 to 4**).

In the Millevaches massif, higher δD values of muscovite and biotite (comparable to those found in Nantiat) are found in the Grand Janon migmatite in the NW part of the massif and in the leucogranite emplaced along the dextral strike-slip Pradine shear zone in the heart of the massif. High to low δD values of muscovite and biotite are found in the leucogranite collected along the La Courtine dextral strike-slip shear zone and St Michel de Veisse. In contrast, δD values of muscovite, biotite and chlorite are the most negative in the footwall of the Felletin detachment shear zone, with δD_{Ms} values ranging from -116 to -74‰, δD_{Bt} values from -104 to -77‰, and δD_{Chl} values from -118 to -75‰. A similar pattern is observed from high δD_{Ms} and δD_{Bt} values in the micaschist of the Argentat footwall down to low δD_{Ms} values in the orthogneiss of the hanging wall of Argentat detachment as pointed out by Courtnadge (2016) (**Fig. IV-10**; **Tables IV-1 to 4**).

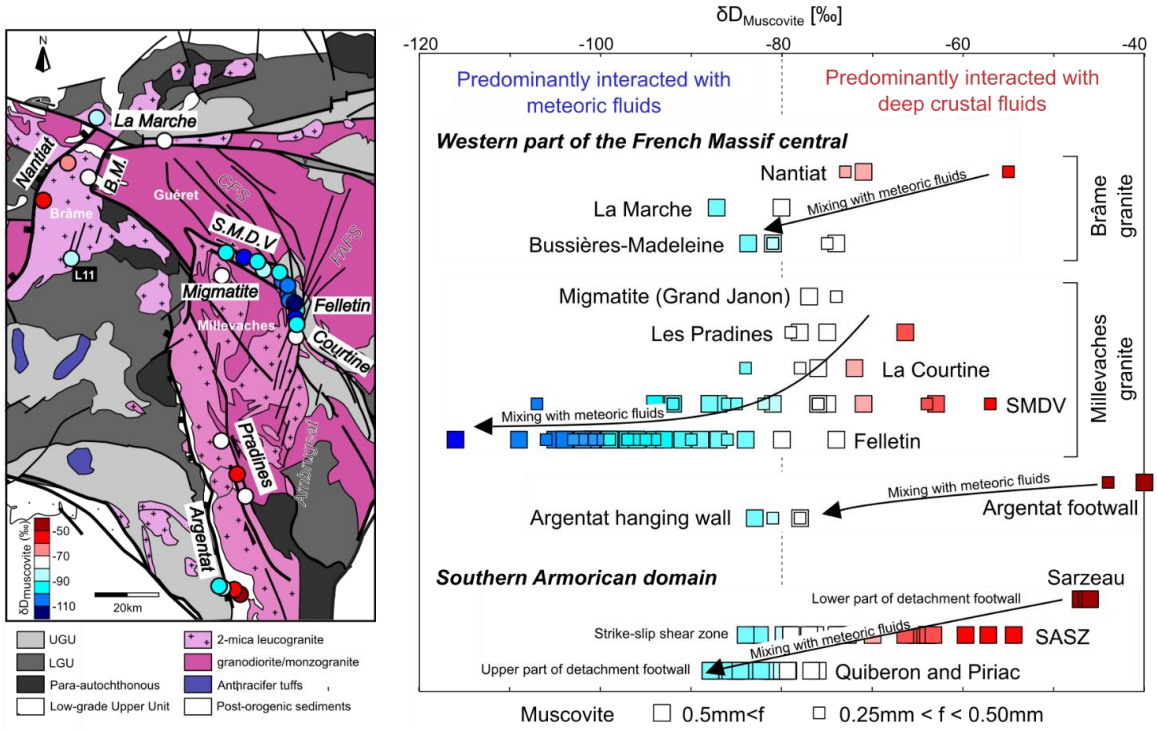

Figure IV-10: Graph showing the measured $\delta D_{Muscovite}$ values from strike-slip shear zones and detachment footwalls in the Western part of the French Massif Central (locations shown on map on the left), and in the southern Armorican domain for comparison. Note the progressive involvement of meteoric fluids from unmixed deep crustal (metamorphic and/or magmatic) fluids in the lower part of detachment footwall (-80 < $\delta D_{Muscovite}$ values < -40‰) to greater mixing with D-depleted meteoric fluids in the upper part of detachment footwalls (-116 < $\delta D_{Muscovite}$ values < -80‰). SMDV – Saint Michel de Veisse; SASZ – South Armorican Shear Zone.

The highest δD values of hydrous silicates (i.e. δD_{Ms} > -80‰; **Fig. IV-10**) in the leucogranite collected within the main Limousin shear zones indicate a signature dominated by deep crustal (metamorphic or magmatic) fluids. In contrast, the most negative δD values of hydrous silicates (i.e. δD_{Ms} < -80‰) reflect interaction with low-δD meteoric water during high temperature deformation (**Fig. IV-10**). In addition, as indicated by the large range of δD_{Ms} values in the footwall of the Felletin detachment (-116 ≤ δD_{Ms} ≤ -74‰) or in the St Michel de Veisse strike-slip shear zone (-107 ≤ δD_{Ms} ≤ -64‰), it can be suggested that hydrous minerals interacted to various degrees with surface-derived fluids. However, δD_{Ms} values lower than -100‰ indicate an incontestable signature of meteoric fluids.

Considering a large range of temperatures (550 ± 150°C) estimated from quartz microstructures and the muscovite-water isotopic fractionation factor of Suzuoki and Epstein (1976), the high δD_{Ms} values that range from -80 to -40‰ allow the calculation of δD_{water} values that range from –66 to -26 ± 16‰. These δD_{water} values correspond to the classic range of deep crustal fluids (-70‰ < $\delta D_{metamorphic\ fluids}$ < -20‰ and/or -80‰ < $\delta D_{magmatic\ fluids}$ < -40‰; e.g. Field and Fifarek, 1985). In contrast, the lowest δD_{Ms} (-116 to -80‰) combined with the same temperature range and fractionation factor gives δD_{water} values ranging from –103 to -66 ± 16‰ that can only be interpreted at best as deuterium-depleted meteoric water.

2. Comparison between the δD_{Ms} values in the Limousin (Massif Central) and southern Brittany (Armorican Massif)

In the syntectonic leucogranite of the southern Armorican domain, a mixing relationship between deep crustal fluids in the lower part of Sarzeau detachment footwall (-47 ≤ δD_{Ms} ≤ -46‰) and D-depleted meteoric fluids in the upper part of Piriac and Quiberon detachment footwalls (-88 ≤ δD_{Ms} ≤ -76‰) has been proposed (**Fig. IV-10** and **Chapter III.A**; Dusséaux et al., 2019). Intermediate δD_{Ms} values in the dextral strike-slip South Armorican Shear Zone (-84 ≤ δD_{Ms} ≤ -54‰) were also measured.

The highest δD_{Ms} values in the Limousin (-80 ≤ δD_{Ms} ≤ -40‰) are comparable to the high values obtained in the southern Armorican domain (δD_{Ms} up to -46‰ in Sarzeau) that represent deep crustal (metamorphic and/or magmatic) fluids (**Fig. IV-10**). In both the southerm Armorican domain and the Limousin, the highest δD values (-80‰ ≤ δD_{Ms}) are found in the lower part of detachment or in strike-slip shear zones. In contrast, the lowest δD_{Ms} values in the Limousin (-116 to -80‰) in the Bussières-Madeleine and Felletin detachment footwalls and in the Argentat detachment hanging-wall) are similar

but even lower than the δD_{Ms} values down to -88‰ that were measured in the southern Armorican domain that were interpreted in terms of interaction with D-depleted meteoric fluids (Dusséaux et al., 2019). Indeed, the lowest δD_{Ms} value in the Limousin (-116‰) is 28‰ lower than the lowest δD_{Ms} value in the southern Armorican domain (-88‰). Such a depletion in deuterium in the Felletin leucogranite establishes the evidence for D-depleted meteoric fluid infiltration in the Variscan detachment shear zones during the Late Carboniferous.

3. Isotopic composition of meteoric water in the NE corner of the Millevaches

Using the hydrogen isotope composition of muscovite, the hydrogen water-muscovite isotope fractionation factor of Suzuoki and Epstein (1976) and the average temperature of 540 ± 51°C given by the Ti-in-Ms thermometer (Wu and Chen, 2015), **δD_{water} values** ranging from **-104 to -89 ± 5‰** were calculated (**Table IV-6**). It should be noted that different thermometry methods such as the observation of quartz microstructures (550 ± 150°C) or quartz-muscovite oxygen isotope exchange (538 ± 41°C) give similar temperatures, and consequently allow consistent δD_{water} and $\delta^{18}O_{water}$ values to be calculated (**Table IV-6**).

The calculated δD_{water} values in the Felletin footwall (-104 to -89 ± 5‰) can only be interpreted as a signature of D-depleted meteoric fluids as they are way below the typical hydrogen isotope composition of deep crustal fluids ($-70 < \delta D_{metamorphic\ fluids} < -20$‰ and/or $-80 < \delta D_{magmatic\ fluids} < -40$‰; e.g. Field and Fifarek, 1985). As the downward penetration of meteoric fluids in the crust generally leads to an increase in δD_{water} values due to fluid-rock interaction, these δD_{water} values represents a maximum value that could have been lower than -104‰ if they were extracted from the near-surface geological record (**Fig. IV-11**; e.g. Gébelin et al., 2012).

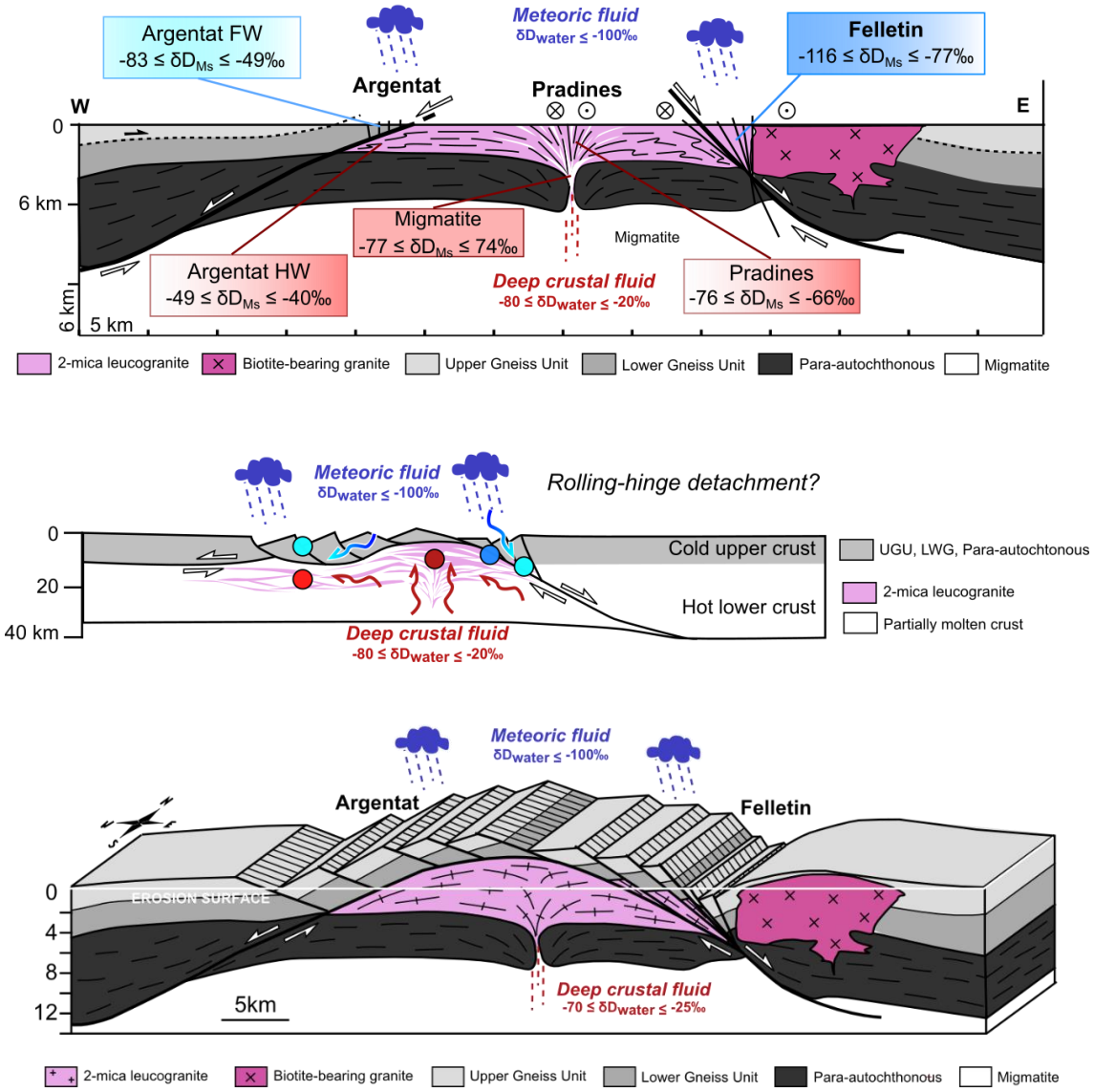

Figure IV-11: *Top* - 2D simplified cross-section showing the emplacement of the Millevaches granite between the Argentat and the Felletin detachment shear zones and associated fluid circulation that led to different hydrogen isotope ratios of muscovite (δD_{Ms}) (adapted from Gébelin et al., 2004). *Middle* - Proposal of a rolling-hinge detachment model for the Millevaches massif with sustained meteoric fluid-rock interaction along the main top-to-right detachment shear zone (adapted from Teyssier and Whitney (2002)). *Bottom* – 3D diagram integrating the true cross-section with the rolling-hinge detachment model.

It is established that the δD values of these surface waters (estimated at -104‰) remain relatively high. As discussed in **Chapter III** for the Armorican Massif (Dusséaux et al., 2019), this could be explained by different factors that characterised the French Massif Central during the Late Carboniferous: its equatorial position (Rozanski et al., 1993; Tait et al., 1996a; Boucot et al., 2013) and subsequent warm paleoclimate (e.g.

Poulsen and Jeffery, 2011), and/or the presence of extensive ice sheets in southern Gondwana (e.g. González-Bonorino and Eyles, 1995; Buggisch et al., 2008). Lastly, it could be due to a moderate to high paleoelevation (e.g. Poage and Chamberlain, 2001). However, the calculated $\delta D_{meteoric\ water}$ values (~-105‰), that are ~30‰ lower compared to age-equivalent $\delta D_{meteoric\ water}$ values in the Armorican Massif (~-75‰; Dusséaux et al., 2019), likely reflect a higher elevation in the French Massif Central.

4. Mechanisms and timing of meteoric fluid infiltration

Previous studies have proposed a model to explain the infiltration of surface-derived fluids down to the brittle-ductile transition in detachment shear zones (Mulch et al., 2004, 2006; Person et al., 2007; Gébelin et al., 2011, 2015, 2017). Brittle normal faults, recognized at the field scale (**Fig. IV-2 and 4**) as well as at microscopic scale (Fig. IV-6), participated in increasing the porosity and permeability by dissecting the upper crust (**Fig. IV-11**). At the same time, high-grade metamorphic rocks (migmatite and leucogranite) sustained the convection of fluids at depth (**Fig. IV-11**). In addition, as the western part of the French Massif Central is part of the internal thickened zones of the Variscan Belt, a hydraulic head probably played a role in helping the fluids to migrate downwards.

The timing of meteoric fluid infiltration can be estimated to have started at ~315 Ma based on U/Pb ages from syntectonic leucogranites that were emplaced in the footwall of the Felletin detachment zone (Gébelin et al., 2009). Deformation and fluid infiltration likely ended at ~304 Ma with the cessation of shear zone activity (muscovite $^{40}Ar/^{39}Ar$ ages from the same studied leucogranite outcrop; Gébelin, 2004). Microprobe analyses showed that the cores of muscovite grains plot in the magmatic field whereas the muscovite tips predominantly plot in the hydrothermal field (Fig. IV-6). Gébelin

(2004) found older ages (~315 Ma) in muscovite clasts compared with muscovite along shear planes (~305 Ma). These 2 observations argue for late recrystallization of muscovite grains during deformation-related meteoric fluid flow.

A rolling-hinge detachment is proposed based on the geometry and the stable isotope data acquired across the Argentat and Felletin detachment zones (**Fig. IV-11**). The consistency of low δD_{Ms} values in the Felletin detachment footwall (δD_{Ms} < -80‰) suggest that D-depleted surface-derived fluid continued to permeate the top-to-east rolling-hinge detachment footwall. In contrast, meteoric fluid infiltration and interaction with rocks may have ceased in the Argentat section during the rolling-hinge development (e.g. Brun and van den Driessche, 1994; Gébelin et al., 2015)

Six samples were sent to the University of Rennes (France) for Ar/Ar dating on single grains (collaboration with G. Ruffet) that will be analysed during the year 2019. Five samples are extracted from the detailed cross-section of the NE corner of the Millevaches granite for which δD_{Ms} values as low as -116‰ have been obtained (MIL19, MIL18C, MIL18D, MIL18H, MIL18I). These five samples will allow us to define the timing of fluid-rock interaction from undeformed granite with high δD_{Ms} values at the base of the section (MIL18H) to mylonitic granite at the top of the section (MIL19) with low δD_{Ms} values. One last sample represents a muscovite veneer (MIL13, δD_{Ms} value = -87‰) on a brittle fault plane that corresponds to the Felletin-Ambrugeat Fault System in the hanging-wall of the Felletin detachment. This last sample will allow us to better characterise the timing of brittle faulting that likely played a major role in routing the meteoric fluids downwards in the crust.

G. Conclusions

Chapter IV aimed to decipher the source of fluids that circulated into ductile shear zones of the western part of the French Massif Central using structural and microstructural data, different geothermometry techniques and hydrogen and oxygen isotope geochemistry. Syntectonic leucogranites from the Millevaches massif yield $\delta D_{muscovite}$ values as low as -116‰ coupled with low $\delta^{18}O_{Ms}$ values (8.4‰) that indicate an incontestable signature of meteoric fluids. The infiltration of fluids was synchronous with the shear zones activity, as shown by muscovite fish in syntectonic leucogranite. The quartz microstructures, the oxygen isotope composition of quartz and muscovite and the titanium content of muscovite agree on a similar temperature of syntectonic fluid infiltration (~500-600°C). The isotopic composition of meteoric water is estimated at ~ -105‰. The infiltration of surface-derived fluids is estimated to have occurred between ~315 and 305 Ma, through brittle normal faults that dissected the upper crust while leucogranite emplacement sustained fluid convection in the lower crust.

V. PALEOALTIMETRY RECONSTRUCTIONS OF THE VARISCAN BELT OF WESTERN EUROPE

A. Introduction

This chapter aims at reconstructing the Late-Palaeozoic elevation of the Variscan Belt of Western Europe using stable isotope paleoaltimetry (e.g. Garzione et al., 2000; Poage and Chamberlain, 2001; Rowley et al., 2001; Mulch et al., 2004; Mulch and Chamberlain, 2007; Campani et al., 2012; Gébelin et al., 2012, 2013). Stable isotope geochemistry (δD and $\delta^{18}O$ values) of hydrous silicates coupled with thermometry and geochronology techniques allowed us to determine the isotope composition of meteoric water that infiltrated the ductile segment of detachment zones in the internal zones of the orogen at the end of the Carboniferous (**Fig. V-1; Chapters III and IV**). Because single-site paleoaltimetry estimates frequently suffer of lack of knowledge of paleoclimatic and paleoenvironmental conditions, the objective of this study is to reference the hinterland precipitation records to age-equivalent records obtained in the foreland near sea level (e.g. Campani et al., 2012; Gébelin et al., 2012, 2013). Comparing multiple proxies from different levels that have preserved the rainfalls composition in the same paleogeographic conditions such the latitude or the source of precipitation allow us to minimize some of the uncertainties related to the past climate change.

In the external zones of the highly eroded Variscan Belt, it is hard to find geological material that could have preserved the stable isotope composition of late-Palaeozoic precipitation. Hydrated carbonates and volcanic glasses have reset their primary isotope composition due to later diagenetic processes. To recover the precipitation conditions near sea level, the oxygen isotope composition of phosphate ($\delta^{18}O_p$) from teeth and

spines from sharks that evolved in lacustrine or fluvial environments in the Permo-Carboniferous foreland basins was used. The hydrogen isotope composition (δD) of hydrous silicates from the Espinouse detachment footwall in the Montagne Noire was also investigated.

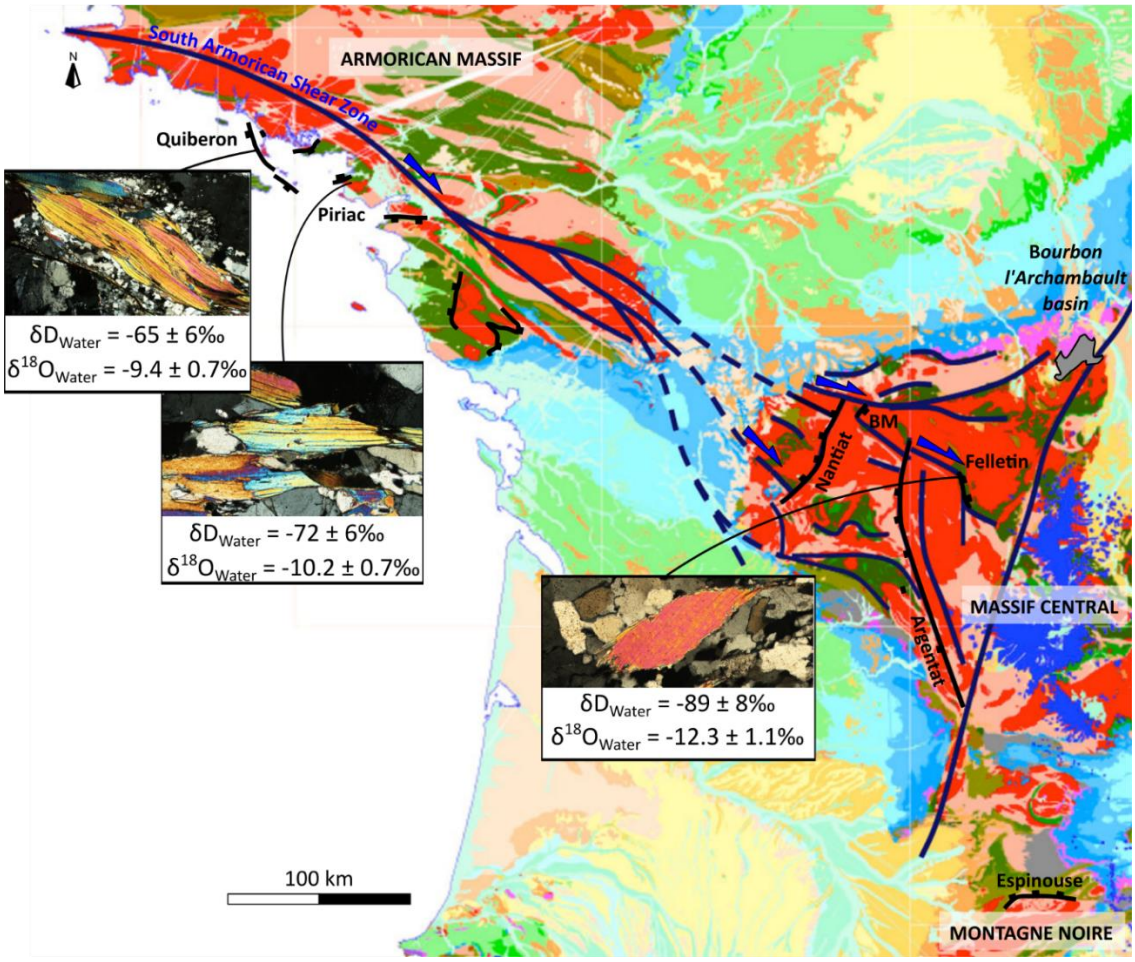

Figure V-1: Geological map of the Armorican Massif, the French Massif Central and the Montagne Noire (France). Note the average calculated δDwater and δ18Owater values based on the isotope composition of muscovite in the footwalls of Quiberon, Piriac and Felletin detachment zone in the hinterland of the Variscan Belt (France). Black line: strike-slip shear zone. Purple line: detachment shear zone. Red: Variscan granite; Pink: Variscan terranes; Grey: Permo-Carboniferous basins.

B. Isotope record of meteoric water from the hinterland

1. Isotope record of meteoric water in the Armorican Massif

In the southern Armorican domain, the hydrogen isotope ratios of muscovite (δD_{Ms}) and tourmaline (δD_{To}) were measured in the mylonitic footwalls of Piriac and Quiberon detachment shear zones (**Fig. V-1; Chapter III**). The δD_{Ms} values range from -88 to -73 ± 2‰ and the δD_{To} values from -87 to -57 ± 2‰ (**Table V-2 - A and B**). Two different thermometry techniques allow the calculation of the isotope composition of the fluids that were present in the Piriac and Quiberon detachment footwalls:

(1) Using deformation **temperatures of 550 ± 150°C deduced from quartz microstructures** (Hirth and Tullis, 1992; Stipp et al., 2002; Langille et al., 2010), the hydrogen isotope fractionation factors of Suzuoki and Epstein (1976) and Kotzer et al. (1993) and the measured δD_{Ms} and δD_{To} values, the calculated δD_{water} values range from -74 to -59 ±16‰ and from -75 to -49 ± 20‰, respectively (**Table V-2A; Chapter III**).

(2) Using **temperatures deduced from the Ti-content of muscovite** of 587 ± 34°C for Piriac and 563 ± 41°C for Quiberon, the hydrogen isotope fractionation factors of Suzuoki and Epstein (1976) and Kotzer et al. (1993), and the measured δD_{Ms} and δD_{To} values, the calculated δD_{water} values in both detachment zones range from -77 to -60 ± 3‰ and from -77 to -49 ± 10‰, respectively (**Table V-2B; Chapter III**).

An average δD_{water} value of **-70 ± 5‰** (n=36) can be calculated for the meteoric water that penetrated the footwall of the two Armorican detachments and was used to reconstruct the paleoaltitude of the Variscan Belt. The uncertainty on this δD_{water} value (± 5‰) takes into account the isotope analysis (± 2‰), the temperature of isotope

exchange given by the Ti-in-Ms geothermometer (± 41°C equivalent to ± 3‰) and the average of δD_{Ms} values (± 4‰) (**Table V-1A; Chapter III**).

Based on Ar/Ar ages acquired on synkinematic muscovite, the timing of deformation and meteoric fluid infiltration along the Quiberon and Piriac detachment zones has been estimated between ca. 320 Ma and 300 Ma (e.g. Ballouard et al., 2015, 2017; Gapais et al., 2015, Dusséaux et al., 2019; **Table V-2B; Chapter III**).

A

	Measure/Estimate	Uncertainty	Uncertainty (‰)	**δD water (‰)**	Propagated uncertainty (‰)	**$\delta^{18}O$ water (‰)**	Propagated uncertainty (‰)
	Isotope analysis ($\delta D_{mineral}$)	2‰	2				
Muscovite	Temperature from quartz microstructure	150°C	16				
	Average of δD_{Ms} values	4‰	4	**-67**	17	-9.7	2.1
Tourmaline	Temperature from quartz microstructure	150°C	20				
	Average of δD_{To} values	9‰	9	**-67**	22	-9.6	2.8
Muscovite	Temperature from Ti-in-Ms	41°C	3				
	Average of δD_{Ms} values	4‰	4	**-70**	5	**-9.9**	0.7
Tourmaline	Temperature from Ti-in-Ms	41°C	10				
	Average of δD_{To} values	9‰	9	**-69**	14	-9.9	1.7

B

Measure/Estimate	Uncertainty	Uncertainty (‰)	**δD water (‰)**	Propagated uncertainty (‰	**$\delta^{18}O$ water (‰)**	Propagated uncertainty (‰)
Isotope analysis (δ_{Ms})	2‰	2				
Temperature from quartz microstructure	150°C	16				
Average of δD_{Ms} values	6‰	6	**-90**	17	-12.4	2.2
Temperature from Ti-in-Ms	51°C	5				
Average of δD_{Ms} values	7‰	7	**-89**	8	-12.3	1.1
Temperature from Quartz-muscovite oxygen isotope exchange	41°C	4				
Average of δD_{Ms} values	6‰	6	**-89**	7	-12.3	0.9

Table V-1: Average δD_{water} values and uncertainties calculated in (A) the Armorican Massif and (B) the Massif Central. The average δD_{water} values are calculated based on the measured hydrogen isotope composition (δD) of muscovite (Ms) and Tourmaline (To) from Quiberon and Piriac detachment footwalls, combined with estimated temperature using quartz microstructures (Hirth and Tullis, 1992; Stipp et al., 2002; Langille et al., 2010) and the Ti-in-muscovite geothermometer (Wu and Chen, 2015), together with the isotope fractionation factors of Suzuoki and Epstein (1976) and Kotzer et al. (1993). The final uncertainty includes the isotope analysis, the temperature of isotope exchange (deduced from quartz microstructures or Ti-in-Ms thermometry) and the average of stable isotope ratios in the area. The δD_{water} value is converted in $\delta^{18}O$ value using the meteoric water line of Craig (1961). Shaded data are used for paleoaltitude reconstructions.

			Muscovite		Tourmaline			Quartz microstructures thermometer		Muscovite			Tourmaline		
Sample	Distance (m)	Rock type	δD Ms (‰)	Fraction Ms (µm)	δD To (‰)	Fraction To (µm)	Uncertainty (‰)	**Temperature (°C)**	Uncertainty (°C)	**δD water (‰)**	-	+	**δD water (‰)**	-	+
PIR01	500	Mylonitic leucogranite	**-81**	500<f			2	**550**	150	**-68**	-9	16			
PIR02	503,5	Mylonitic leucogranite	**-82**	500<f			2	**550**	150	**-69**	-9	16			
PIR03	507,5	Mylonitic leucogranite	**-81**	500<f	**-75**	250<f<500	2	**550**	150	**-68**	-9	16	**-63**	-11	20
PIR04	509	Mylonitic leucogranite	**-79**	500<f			2	**550**	150	**-66**	-9	16			
PIR05	512	Mylonitic leucogranite	**-85**	500<f	**-57**	250<f<500	2	**550**	150	**-72**	-9	16	**-45**	-11	20
PIR06	517	Mylonitic leucogranite	**-76**	500<f			2	**550**	150	**-63**	-9	16			
PIR07	521	Mylonitic leucogranite	**-79**	250<f<500	**-75**	250<f<500	2	**550**	150	**-66**	-9	16	**-63**	-11	20
PIR08	523	Mylonitic leucogranite	**-80**	500<f			2	**550**	150	**-66**	-9	16			
PIR09	526	Mylonitic leucogranite	**-82**	500<f			2	**550**	150	**-68**	-9	16			
PIR10	528	Mylonitic leucogranite	**-85**	500<f			2	**550**	150	**-72**	-9	16			
PIR11	531	Mylonitic leucogranite	**-87**	500<f			2	**550**	150	**-74**	-9	16			
PIR12	536	Mylonitic leucogranite	**-77**	500<f			2	**550**	150	**-63**	-9	16			
PIR13	540	Mylonitic leucogranite	**-84**	500<f			2	**550**	150	**-70**	-9	16			
PIR14	544	Mylonitic leucogranite	**-81**	500<f			2	**550**	150	**-68**	-9	16			
PIR15	550	Mylonitic leucogranite	**-88**	500<f			2	**550**	150	**-74**	-9	16			
PIR16	560	Mylonitic leucogranite	**-88**	500<f			2	**550**	150	**-74**	-9	16			
GUE6	570	Mylonitic leucogranite	**-85**	500<f			2	**550**	150	**-71**	-9	16			
GUE7	1900	Mylonitic leucogranite	**-80**	500<f			2	**550**	150	**-66**	-9	16			
GUE9	2000	Mylonitic leucogranite	**-85**	500<f			2	**550**	150	**-72**	-9	16			
GUE21	2150	Mylonitic leucogranite	**-86**	500<f	**-85**	250<f<500	2	**550**	150	**-72**	-9	16	**-73**	-11	20
GUE14	8000	Weakly deformed leucogranite	**-81**	500<f			2	**550**	150	**-68**	-9	16			
GUE17	8100	Weakly deformed leucogranite	**-80**	500<f			2	**550**	150	**-67**	-9	16			
GUE11	10000	Weakly deformed leucogranite	**-81**	500<f			2	**550**	150	**-68**	-9	16			
GUE12	10000	Weakly deformed leucogranite	**-84**	500<f			2	**550**	150	**-71**	-9	16			
GUE13	10000	Weakly deformed leucogranite	**-81**	500<f			2	**550**	150	**-68**	-9	16			
QUIB01	300	Mylonitic leucogranite	**-85**	500<f	**-87**	500<f	2	**550**	150	**-71**	-9	16	**-75**	-11	20
QUIB02	305	Mylonitic leucogranite	**-79**	250<f<500			2	**550**	150	**-66**	-9	16			
QUIB03	322	Mylonitic leucogranite	**-82**	250<f<500	**-86**	500<f	2	**550**	150	**-69**	-9	16	**-74**	-11	20
QUIB04	321	Ultramylonitic pegmatite	**-73**	500<f			2	**550**	150	**-59**	-9	16			
QUIB05	321,5	Ultramylonitic pegmatite	**-73**	500<f	**-80**	250<f<500	2	**550**	150	**-60**	-9	16	**-68**	-11	20
QUIB06	320	Ultramylonitic pegmatite	**-75**	250<f<500			2	**550**	150	**-61**	-9	16			
QUIB07	200	Micaschist	**-76**	250<f<500			2	**550**	150	**-62**	-9	16			
QUIB08	250	Quartz vein	**-76**	500<f	**-81**	500<f	2	**550**	150	**-62**	-9	16	**-69**	-11	20
QUIB09	255	Quartz vein	**-76**	500<f			2	**550**	150	**-63**	-9	16			
QUIB16	465	Quartz vein	**-79**	500<f			2	**550**	150	**-66**	-9	16			
QUIB17	500	Quartz vein	**-80**	250<f<500	**-85**	250<f<500	2	**550**	150	**-66**	-9	16	**-73**	-11	20
		AVERAGE	**-81**		**-79**					**-67**	-9	16	**-67**	-11	20
		SD	**4**		**9**					**4**	0	0	**9**	0	0
		Min	**-88**		**-87**					**-74**	-9	16	**-75**	-11	20
		Max	**-73**		**-57**					**-59**	-9	16	**-45**	-11	20

Table V-2A: Stable isotope data from Quiberon and Piriac detachment footwalls (Armorican Massif). δD_{water} values are calculated based on deformation temperatures of 400-700°C deduced from quartz microstructures (Hirth and Tullis, 1992; Stipp et al., 2002; Langille et al., 2010), the hydrogen isotope fractionation factors of Suzuoki and Epstein (1976) and Kotzer et al. (1993) and measured hydrogen isotope composition (δD) of muscovite (Ms) and tourmaline (To) from Quiberon and Piriac detachment footwalls (Armorican Massif).

			Muscovite		Tourmaline			Ti-in-Ms thermometry		Muscovite			Tourmaline			$^{39}Ar/^{40}Ar$ on Muscovite			
Sample	Distance (m)	Rock type	δD Ms (‰)	Fraction Ms (µm)	δD To (‰)	Fraction To (µm)	± (‰)	T (°C)	± (°C)	δD water (‰)	-	+	δD water	-	+	Age (Ma)	± (Ma)	Age (Ma)	± (Ma)
PIR01	500	Mylonitic leucogranite	**-81**	500<f			2	**587**	34	**-71**	-2	3				322.4	1.0	306.2	0.5
PIR02	503,5	Mylonitic leucogranite	**-82**	500<f			2	**587**	34	**-72**	-2	3							
PIR03	507,5	Mylonitic leucogranite	**-81**	500<f	**-75**	250<f<500	2	**587**	34	**-70**	-2	3	**-67**	-3	3				
PIR04	509	Mylonitic leucogranite	**-79**	500<f			2	**587**	34	**-69**	-2	3							
PIR05	512	Mylonitic leucogranite	**-85**	500<f	**-57**	250<f<500	2	**587**	34	**-74**	-2	3	**-49**	-3	3				
PIR06	517	Mylonitic leucogranite	**-76**	500<f			2	**587**	34	**-65**	-2	3				318.5	0.9	312.8	0.5
PIR07	521	Mylonitic leucogranite	**-79**	250<f<500	**-75**	250<f<500	2	**587**	34	**-68**	-2	3	**-66**	-3	3				
PIR08	523	Mylonitic leucogranite	**-80**	500<f			2	**587**	34	**-69**	-2	3							
PIR09	526	Mylonitic leucogranite	**-82**	500<f			2	**587**	34	**-71**	-2	3							
PIR10	528	Mylonitic leucogranite	**-85**	500<f			2	**587**	34	**-74**	-2	3							
PIR11	531	Mylonitic leucogranite	**-87**	500<f			2	**587**	34	**-76**	-2	3				318.6	0.7		
PIR12	536	Mylonitic leucogranite	**-77**	500<f			2	**587**	34	**-66**	-2	3							
PIR13	540	Mylonitic leucogranite	**-84**	500<f			2	**587**	34	**-73**	-2	3							
PIR14	544	Mylonitic leucogranite	**-81**	500<f			2	**587**	34	**-70**	-2	3							
PIR15	550	Mylonitic leucogranite	**-88**	500<f			2	**587**	34	**-77**	-2	3							
PIR16	560	Mylonitic leucogranite	**-88**	500<f			2	**587**	34	**-77**	-2	3				308.5	0.6	305.4	0.7
GUE6	570	Mylonitic leucogranite	**-85**	500<f			2	**587**	34	**-74**	-2	3							
GUE7	1900	Mylonitic leucogranite	**-80**	500<f			2	**587**	34	**-69**	-2	3							
GUE9	2000	Mylonitic leucogranite	**-85**	500<f			2	**587**	34	**-74**	-2	3							
GUE21	2150	Mylonitic leucogranite	**-86**	500<f	**-85**	250<f<500	2	**587**	34	**-75**	-2	3	**-77**	-3	3				
GUE14	8000	Weakly deformed leucogranite	**-81**	500<f			2	**587**	34	**-70**	-2	3							
GUE17	8100	Weakly deformed leucogranite	**-80**	500<f			2	**587**	34	**-69**	-2	3							
GUE11	10000	Weakly deformed leucogranite	**-81**	500<f			2	**587**	34	**-70**	-2	3							
GUE12	10000	Weakly deformed leucogranite	**-84**	500<f			2	**587**	34	**-73**	-2	3							
GUE13	10000	Weakly deformed leucogranite	**-81**	500<f			2	**587**	34	**-70**	-2	3							
QUIB01	300	Mylonitic leucogranite	**-85**	500<f	**-87**	500<f	2	**563**	41	**-72**	-6	3	**-76**	-4	16	319.5	0.9	307.7	0.7
QUIB02	305	Mylonitic leucogranite	**-79**	250<f<500			2	**563**	41	**-67**	-6	3							
QUIB03	322	Mylonitic leucogranite	**-82**	250<f<500	**-86**	500<f	2	**563**	41	**-70**	-6	3	**-75**	-4	16	304.8	1.0	303.4	1.0
QUIB04	321	Ultramylonitic pegmatite	**-73**	500<f			2	**563**	41	**-60**	-6	3							
QUIB05	321,5	Ultramylonitic pegmatite	**-73**	500<f	**-80**	250<f<500	2	**563**	41	**-61**	-6	3	**-69**	-4	16				
QUIB06	320	Ultramylonitic pegmatite	**-75**	250<f<500			2	**563**	41	**-62**	-6	3							
QUIB07	200	Micaschist	**-76**	250<f<500			2	**563**	41	**-63**	-6	3							
QUIB08	250	Quartz vein	**-76**	500<f	**-81**	500<f	2	**563**	41	**-63**	-6	3	**-70**	-4	16				
QUIB09	255	Quartz vein	**-76**	500<f			2	**563**	41	**-64**	-6	3							
QUIB16	465	Quartz vein	**-79**	500<f			2	**563**	41	**-67**	-6	3							
QUIB17	500	Quartz vein	**-80**	250<f<500	**-85**	250<f<500	2	**563**	41	**-67**	-6	3	**-74**	-4	16				
		AVERAGE	**-81**		**-79**					**-70**	-3	3	**-69**	-3	10				
		SD	**4**		**9**					**5**	2	0	**9**	0	7				
		Min	**-88**		**-87**					**-77**	-6	3	**-77**	-4	3				
		Max	**-73**		**-57**					**-60**	-2	3	**-49**	-3	16				

Table V-2B: Stable isotope and geochronology data from Quiberon and Piriac detachment footwalls (Armorican Massif). δD_{water} values are calculated based on the Ti-in-Ms geothermometer (Wu and Chen, 2015), the hydrogen isotope fractionation factors of Suzuoki and Epstein (1976) and Kotzer et al. (1993) and measured hydrogen isotope composition (δD) of muscovite (Ms) and Tourmaline (To).

			Muscovite			Quartz microstructures thermometry					Titanium-in-Ms thermometry					Quartz-muscovite oxygen isotope exchange thermometry				
Sample	Distance (m)	Rock type	δD Ms (‰)	Fraction Ms (µm)	± (‰)	**T (°C)**	± (°C)	**δD water (‰)**	-	+	**T (°C)**	Uncertainty (°C)	**δD water (‰)**	-	+	**T (°C)**	Uncertainty (°C)	**δD water (‰)**	-	+
MIL19	0	Mylonitic leugranite	-109	500<f	2	550	150	**-96**	-9	16	540	51	**-95**	-4	5	538	41	**-95**	-3	4
MIL18B	5	Mylonitic leucogranite	-102	500<f	2	550	150	**-89**	-9	16	540	51	**-88**	-4	5	538	41	**-88**	-3	4
MIL18F	6	Quartz vein	-99	500<f	2	550	150	**-86**	-9	16	540	51	**-85**	-4	5	538	41	**-85**	-3	4
MIL18E	10	Mylonitic leucogranite	-104	500<f	2	550	150	**-91**	-9	16	540	51	**-90**	-4	5	538	41	**-90**	-3	4
MIL18C	15	Mylonitic leucogranite	-104	500<f	2	550	150	**-91**	-9	16	**493**	**57**	**-86**	-5	8	**538**	**41**	**-90**	-3	4
MIL18A	20	Mylonitic leucogranite	-96	500<f	2	550	150	**-83**	-9	16	540	51	**-82**	-4	5	538	41	**-82**	-3	4
MIL18D	25	Mylonitic leucogranite	-105	500<f	2	550	150	**-92**	-9	16	540	51	**-91**	-4	5	538	41	**-91**	-3	4
MIL18G	35	Mylonitic leucogranite	-99	250<f<500	2	550	150	**-86**	-9	16	540	51	**-85**	-4	5	538	41	**-85**	-3	4
MIL18H	60	Mylonitic pegmatite	-116	500<f	2	550	150	**-103**	-9	16	**568**	**42**	**-104**	-3	3	538	41	**-102**	-3	4
MIL18I	90	Undeformed leucogranite	-96	500<f	2	550	150	**-83**	-9	16	**559**	**55**	**-83**	-4	5	538	41	**-82**	-3	4
		AVERAGE	-103		2	550	150	**-90**	-9	16	540	51	**-89**	-4	5	538	41	**-89**	-3	4
		SD	6		0	0	0	**6**	0	0	19	4	**7**	0	1	0	0	**6**	0	0
		Min	-116		2	550	150	**-103**	-9	16	493	42	**-104**	-5	3	538	41	**-102**	-3	4
		Max	-96		2	550	150	**-83**	-9	16	568	57	**-82**	-3	8	538	41	**-82**	-3	4

Table V-2C: δD_{water} values calculated based on deformation temperatures of 400-700°C deduced from quartz microstructures (Hirth and Tullis, 1992; Stipp et al., 2002; Langille et al., 2010), the Ti-in-Ms geothermeter (Wu and Chen, 2015), the hydrogen isotope fractionation factors of Suzuoki and Epstein (1976) and the measured hydrogen isotope composition (δD) of muscovite (Ms) from the NE corner of the Millevaches (Massif Central).

2. Isotope record of meteoric water in the Massif Central

In the western part of the French Massif Central, the hydrogen isotope composition of muscovite (δD_{Ms}) was measured into the Felletin detachment footwall at the NE corner of the Millevaches Massif (**Fig. V-1; Chapter IV**). The δD_{Ms} values range from -116 to -90 ± 2‰ (**Table V-2C**). Three different thermometry techniques allow the calculation of the isotope composition of the fluids that were present in the Felletin detachment footwall (**Table V-2C; Chapter IV**):

(1) Using **deformation temperatures of 550 ± 150°C deduced from quartz microstructures**, the hydrogen isotope fractionation factor of Suzuoki and Epstein (1976) and the measured δD_{Ms} values, calculated δD_{water} values range from -103 to -83 ± 16‰;

(2) Using **temperatures deduced from the Ti-content of muscovite** of 493 ± 57°C for MIL18C, 568 ± 42°C for MIL18H, 559 ± 55°C for MIL18H, and an average temperature of 540 ± 51°C for the other samples, the hydrogen isotope fractionation factor of Suzuoki and Epstein (1976) and the measured δD_{Ms} values, calculated δD_{water} values range from -104 to -82 ± 5‰;

(3) Using **temperatures from muscovite-quartz oxygen isotope exchange thermometry** of 538 ± 41°C (n=1), the hydrogen isotope fractionation factor of Suzuoki and Epstein (1976) and the measured δD_{Ms} values, calculated δD_{water} values range from -102 to -82 ± 4‰.

An average δD_{water} value of **-89 ± 8‰** was calculated for the Felletin detachment in the French Massif Central, taking into account the uncertainty on the isotope analysis(± 2‰), the temperature of isotope exchange given by the Ti-in-Ms

geothermometer (± 41°C equivalent to ± 5‰) and the average of δD_{Ms} values (± 7‰) (**Fig. 1; Table V-1B; Chapter IV**).

Ar/Ar on synkinematic muscovite allow us to estimate the timing of deformation and fluid flow along the Quiberon and Piriac detachment zones was between ca. 325 Ma and 305 Ma (e.g. Gébelin, 2004).

C. Isotope record of meteoric water from the foreland

1. Oxygen isotope geochemistry of shark remains in foreland basins

a. Introduction

Fossil shark tooth enameloid represents an excellent proxy to recover the oxygen isotope composition of ambient water at the time of tooth formation due to its resistance to diagenetic alteration (e.g. Longinelli and Nuti, 1973; Kolodny et al., 1983; Kolodny and Raab, 1988; Schmitz et al., 1991; Koch et al., 1992; Kolodny and Luz, 1992; Vennemann and Hegner, 1998; Vennemann et al., 2001; Kohn and Cerling, 2002; Lécuyer et al., 2003; Kocsis et al., 2007, 2009; Zacke et al., 2009; Tütken et al., 2011). Also, the high crystallinity and low organic content of bioapatite ensure the preservation of its primary isotope composition (e.g. Kolodny and Raab, 1988; Sharp et al., 2000; Kohn and Dettman, 2007; Koch, 2008; Enax et al., 2012).

Shark teeth are recognized to represent valuable paleoenvironmental archives because: (1) the bioapatite in shark teeth can be used to reconstruct water paleotemperatures as $\delta^{18}O_P$ values depends on the temperature and the oxygen isotope composition of ambient water ($\delta^{18}O_{water}$) (e.g. Longinelli and Nuti, 1973; Kolodny et al., 1983), (2) they are the most common and widespread phosphate vertebrate from the

Devonian (e.g. Capetta, 1987; Ginter et al., 2010), (3) the isotope equilibrium between the shark teeth (and others remains) and the ambient water is maintained due to shark ectothermy (e.g. Amiot et al., 2007; Speers-Roesch and Treberg, 2010; Bernard et al., 2010), (4) the $\delta^{18}O_{Phosphate}$ of the tooth enameloid seems to be independent from metabolic fractionation effects (Kolodny et al., 1983), (5) the fractionation is independent of the sharks' taxon (Vennemann et al., 2001), and (6) shark enameloid consists mainly of stable fluorapatite ($Ca_5(PO_4)F$) with minor amounts of hydroxyl and carbonate apatite when compared to the bones (Vennemann et al., 2001; Enax et al., 2012).

Fossil sharks represented by teeth and spine are commonly found in Late Carboniferous and Early Permian continental basins in Western Europe (**Fig. V-2;** e.g. Soler-Gijón, 1997; Fischer et al., 2010, 2013). In this study, the phosphate oxygen ($\delta^{18}O_P$) isotope composition of biogenic fluorapatite of shark teeth from the foreland basins measured by Fischer et al. (2013) is being analysed for a paleoaltimetry purpose. A particular focus was applied to the Bourbon l'Archambault foreland basin (northern part of the French Massif Central) located near the studied areas (**Fig. V-2**). The shark remains in this basin represent exceptional proxies for referencing to the hydrogen isotope records obtained in the internal zones of the orogen for the following reasons: (1) they have a similar age as they have been biostratigraphically and isotopically dated at ~295 to 290 Ma (Sakmarian; Werneburg, 2003; Roscher and Schneider, 2005; Schneider and Werneburg, 2006), (2) sedimentological, paleogeographical, ecological and geochemistry ($\delta^{18}O_P$ and $^{87}Sr/^{86}Sr$) studies indicate that the sharks evolved in a freshwater environment (lacustrine to fluvial; e.g. (Soler-Gijon, 1997; Soler-Gijón, 1997; Schneider et al., 2000; Schultze and Soler-Gijón, 2004; Fischer et al., 2010, 2013), (3)

shark teeth have not been affected by diagenetic alteration resulting in a well preserved bioapatite (Fischer et al., 2013).

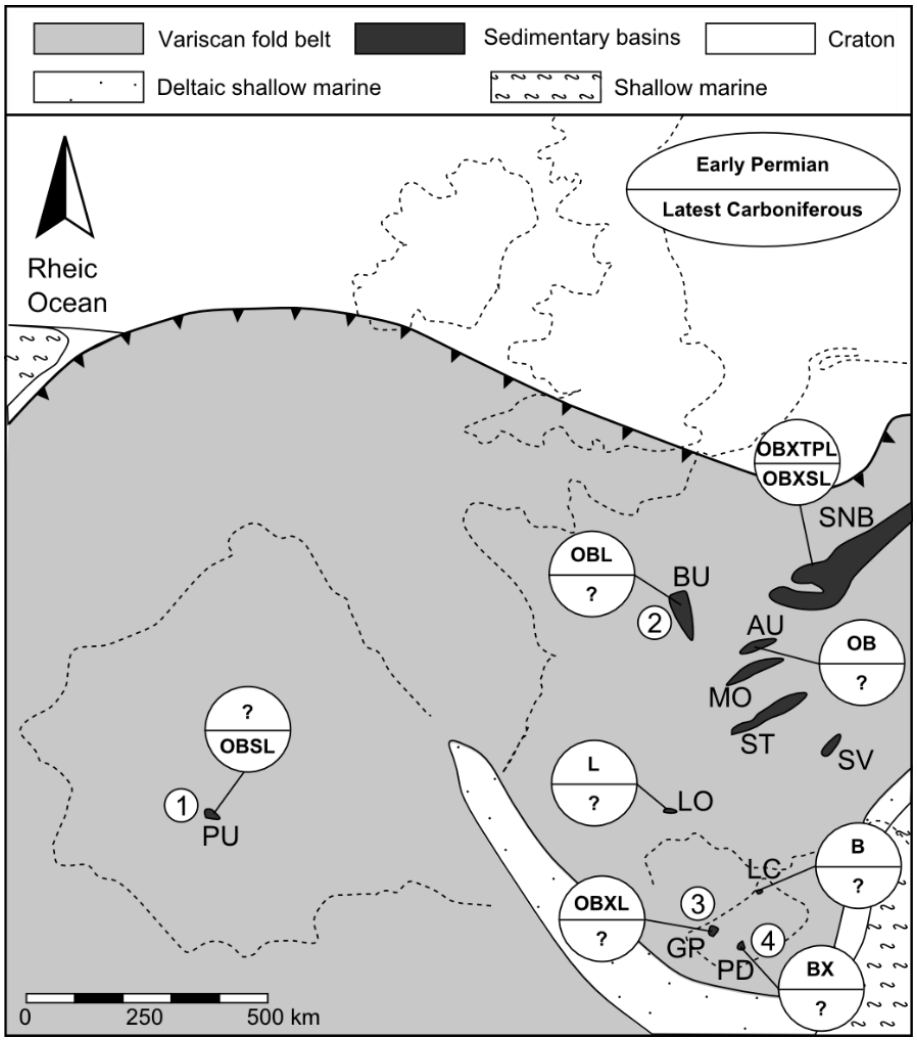

Figure V-2: Palaeogeographic map of the main late-Carboniferous and early-Permian basins with the palaeobiogeography of xenacanthiformes, hybodontids, sphenacanthids (modified from Schneider and Zajíc, 1994; Roscher and Schneider, 2006 and Fischer et al., 2010, 2013). Shark taxa: B — Bohemiacanthus, L — Lissodus, O — Orthacanthus, P — Plicatodus, S — Sphenacanthus, T — Triodus, and X — Xenacanthus; below the horizontal line — occurrences during Stephanian C (late Gzhelian 303.7 to 298.9 Ma – early Asselian 298.9 to 295 Ma), and above the horizontal line — occurrences during Rotliegend (middle Asselian 298.9 to 295 Ma – early Artinskian 290,1 to 283,5 Ma). Basins: AU — Autun basin, BU — Bourbon l'Archambault basin, GP — Guardia Pisano basin, LC — Lu Caparoni basin, LO — Lodève basin, MO — Montceau les Mines basin, PD — Perdasdefogu basin, PU — Puertollano basin, SNB — Saar–Nahe basin, ST — St. Etienne basin and SV — Salvan-Dorénaz basin.

b. The Bourbon l'Archambault basin: Geological context and previous isotope analyses

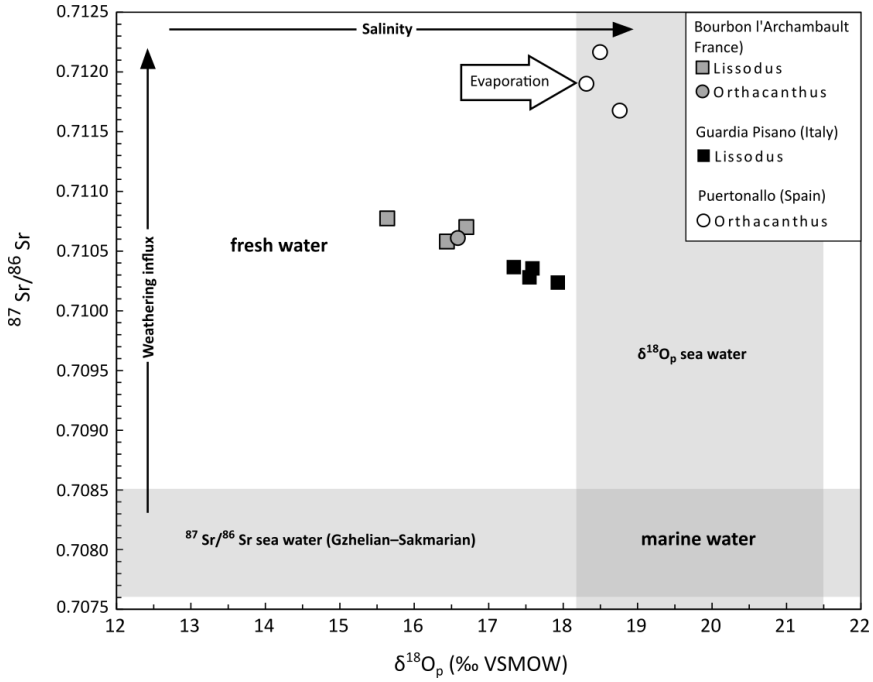

Figure V-3: $\delta^{18}O_P$ vs $^{87}Sr/^{86}Sr$ plot of shark teeth displaying the environmental conditions (i.e. the isotope composition of the ambient water in the shark habitat) at the time of tooth formation. The horizontal grey bar represents the range of the seawater strontium isotope composition (Denison et al., 1994; Veizer et al., 1999; Korte et al., 2006) while the vertical grey bar shows the proposed marine $\delta^{18}O$ range (Fischer et al., 2013). The intersection between both bars characterises bioapatite values expected for unequivocal fully marine conditions.

The shark remains were derived from black shales of the Buxières Formation in the former coal mine of Buxières-les-Mines (Bourbon l'Archambault basin, French Massif Central; **Figs. V-1 and V-2**). The basin has been dated at ~295 to 290 Ma and is filled with conglomerates, alluvial arkoses, palustrine deposits with coal seams, followed by bituminous black shales and fluvial sandstones, both intercalated with thin horizons of intermediary pyroclastics (Werneburg, 2003; Roscher and Schneider, 2005, 2006; Schneider and Werneburg, 2006). Even though the comparisons of aquatic faunas led to the hypothesis of a marine influence for this basin (e.g. Schultze and Soler-Gijón, 2004), sedimentology analysis and isotope studies of shark remains (teeth, scale and spine) and

sediments clearly point to freshwater lacustrine environmental conditions (Steyer et al., 2000; Roscher and Schneider, 2006; Fischer et al., 2013).

In the Bourbon l'Archambault basin, the $\delta^{18}O_P$ values of shark remains vary from 15.5 to 17.6‰ (n = 17) and the $^{87}Sr/^{86}Sr$ ratios from 0.71058 to 0.71077 (n=4) (**Fig. V-3; Table V-3;** (Fischer et al., 2013). The results are consistent for the two different shark species (Orthacanthus and Lissodus, **Fig. V-4**). Moreover, the lifelong proxies (9 Lissodus fine spines and 7 Orthacanthus dorsal spines) yield similar values ($15.5 \leq \delta^{18}O_P \leq 17.6$‰ and $0.71058 \leq {}^{87}Sr/^{86}Sr \leq 0.71077$) to the short-term proxies as one Orthacanthus tooth enameloid sample yielded a $\delta^{18}O_P$ value of 16.6‰ and a $^{87}Sr/^{86}Sr$ ratio of 0.71061 (Fischer et al., 2013).

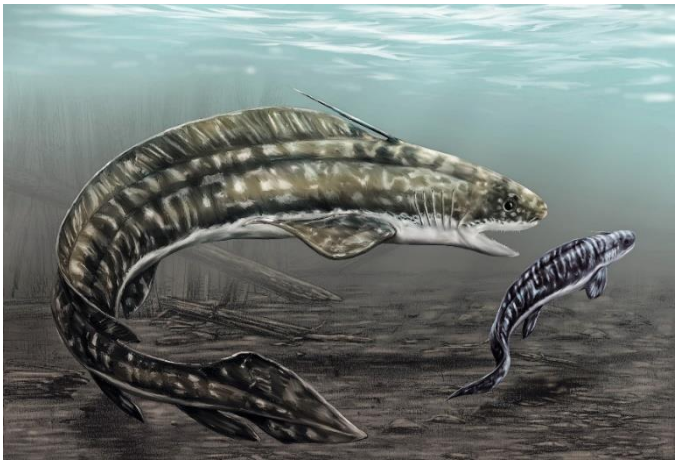

Figure V-4: Illustration of the late-Carboniferous freshwater xenacanthiform shark *Orthacanthus* (~3m-long) along with the smaller shark *Triodus*.

© Alain Bénéteau

Using the revised phosphate-water fractionation equation of Pucéat et al. (2010), the $\delta^{18}O_P$ values of shark remains and a typical seawater $\delta^{18}O_{water}$ value of −1‰ (Kolodny and Luz, 1991; Kocsis et al., 2009), Fisher et al. (2013) calculated paleotemperatures that exceed the biological tolerance limit for modern and Jurassic euryhaline sharks (26 to 32°C; Dera et al., 2009; Carlson et al., 2010; Fischer et al., 2012, 2013). As a consequence, these authors consider that the isotope composition of sea water that they used for their paleotemperature calculations is inappropriate. Hence, in order to fit the suitable

water paleotemperatures in which these animals have evolved, $\delta^{18}O_{water}$ values lower than the typical sea water range are required ($\delta^{18}O_{freshwater} \leq -1‰$). Therefore, the following section aims at calculating the oxygen isotope ratio of the ambient water using water temperatures that would be adequate for the freshwater sharks.

c. Calculation of the $\delta^{18}O_{water}$ values

The aim of this section is to calculate the isotope composition of water in which these sharks lived from the isotope composition of sharks remains phosphate ($\delta^{18}O_P$) measured by Fisher et al. (2013). Based on the study of modern and Jurassic euryhaline sharks (Dera et al., 2009; Carlson et al., 2010; Fischer et al., 2012, 2013) and to be consistent with Fischer et al. (2013) results, a temperature of phosphate-water isotope exchange of 29 ± 7°C was chosen. Using this temperature, the $\delta^{18}O_P$ values of Fischer et al. (2013) and the phosphate-water oxygen fractionation equation of Lécuyer et al. (2013), $\delta^{18}O_{water}$ values between **-4.1 and -2.1 ± 1.6‰** were calculated in the Bourbon l'Archambault basin. When compared to the ones obtained using the newer fractionation equation of Lécuyer et al. (2013), the phosphate-water fractionation equation of Pucéat et al. (2010) provides consistent $\delta^{18}O_{water}$ values that range from -4.8 to -2.8 ± 1.6‰ (**Table V-3**).

d. Discussion

The preserved original isotope composition of bioapatite from fossil shark remains from the Bourbon l'Archambault basin allows the estimation of an isotope composition of late-Carboniferous to early-Permian meteoric water of **-3.1 ± 1.7 ‰**, corresponding to the average of the calculated $\delta^{18}O_{water}$ values based on the fractionation equation of Lécuyer et al. (2013) and a temperature of 29 ± 7°C.

$\delta^{18}O_{Phosphate}$ data measured on other sharks from the Permo-Carboniferous basins in Spain and Italy provide similar values. Sharks from the Puertollano basin (Spain) yield $\delta^{18}O_P$ values that range from 18.0 to 20.2‰ falling into the marine water domain or at the boundary between the marine domain/ fresh water domain (**Figs. V-2 and V-3**; **Table V-3**; Fischer et al., 2013). The associated $^{87}Sr/^{86}Sr$ ratios indicate that the shark teeth formed in a fresh water environment. Fisher et al. (2013) interpret the ^{18}O-enriched $\delta^{18}O_P$ values by a strong evaporation effect that would have shifted the original $\delta^{18}O_P$ to higher values, which is in good agreement with a lacustrine basin environment (**Fig. V-3**; Fischer et al., 2013). Results from sharks teeth in the Guardia Pisano basin in Italy support the idea that late-Carboniferous to early-Permian sharks lived in rivers / lakes as both $\delta^{18}O_{Phosphate}$ (16.7 to 18.2‰) and $^{87}Sr/^{86}Sr$ values (0.71024 to 0.71036) fall into the freshwater environment domain (**Figs. V-2 and V-3**; **Table V-3**; Fischer et al., 2013).

These results strengthen the hypothesis that these sharks are comparable to modern diadromous shark that can migrate between salt and fresh waters (e.g. Soler-Gijon, 1997, 1999; Schneider et al., 2000; Schultze and Soler-Gijón, 2004; Fischer et al., 2010, 2013).

e. Conclusion

An average $\delta^{18}O_{water}$ value of **-3.1 ± 1.7‰** (n=17) was calculated for the meteoric water that exchanged with sharks teeth and spines in the Bourbon l'Archambault basin. This value will be used to reconstruct the paleoaltitude of the Variscan Belt during the Late Carboniferous. The uncertainty takes into account the isotope analysis (± 0.2‰), the temperature of isotope exchange (± 7°C equivalent to ± 1.6‰ in δD_{water} values) and the average of the $\delta^{18}O_P$ values (± 0.5‰).

Locality name	Number on map	Formation	Age	Taxon	Sample	Material	$\delta^{18}O_P$ (‰ VSMOW)	$^{87}Sr/^{86}Sr$	$\delta^{18}O_{water}$ (29 ± 7°C) Lécuyer et al. (2013)	$\delta^{18}O_{water}$ (29 ± 7°C) Pucéat et al. (2010)
Puertollano (Southern Spain)	1	Emma Quarry, bituminous bed 'Emma', above coal seam III	Gzehlian-Asselian, Stephanian C (304 - 300 Ma)	*Lissodus*	LP1	40 tooth crowns	18.0		-1.7	-2.4
				Triodus	TP1	2 tooth tips	18.3		-1.4	-2.1
				Orthacanthus meridonalis	OP1	tooth enameloid	18.8	0.71167	-0.9	-1.6
					OP2	tooth enameloid	18.5	0.71216	-1.1	-1.9
					OP3	tooth enameloid	18.3	0.71190	-1.3	-2.0
					OP4	tooth enameloid	18.6		-1.1	-1.8
					OP5	tooth enameloid	20.2		0.6	-0.2
						Average	18.7	0.71191	-1.0	-1.7
						SD	0.7	0.00025	0.7	0.7
						Min	18.0	0.71167	-1.7	-2.4
						Max	20.2	0.71216	0.6	-0.2
Buxiéres-les-Mines, Buxiéres lake, Bourbon l'Archambault Basin (France)	2	Buxiéres Fm	Early Permian, Sakmarian (295 - 290 Ma)	*Lissodus*	LBS 1A	fin spine	16.7	0.71070	-2.9	-3.7
					LBS 1B	fin spine	16.9		-2.8	-3.5
					LBS 2	fin spine	16.4	0.71058	-3.2	-3.9
					LBS 2A	fin spine	16.6		-3.1	-3.8
					LBS 2B	fin spine	16.7		-2.9	-3.6
					LBS 2C	fin spine	16.7		-3.0	-3.7
					LBS 3	fin spine	15.6	0.71077	-4.0	-4.7
					LBS 3A	fin spine	16.0		-3.7	-4.4
					LBS 3B	fin spine	15.5		-4.1	-4.8
				Orthacanthus buxieri	OB1	tooth enameloid	16.6	0.71061	-3.1	-3.8
					OBS 1a	dorsal spine	16.6		-3.0	-3.7
					OBS 2a	dorsal spine	16.3		-3.4	-4.1
					OBS 1b	dorsal spine	16.0		-3.6	-4.4
					OBS 2b	dorsal spine	16.7		-2.9	-3.6
					OBS 3b	dorsal spine	17.6		-2.1	-2.8
					OBS 4b	dorsal spine	17.4		-2.2	-2.9
					OBS 5b	dorsal spine	16.4		-3.3	-4.0
						Average	16.5	0.71066	**-3.1**	-3.8
						SD	0.5	0.00009	**0.5**	0.5
						Min	15.5	0.71058	**-4.1**	-4.8
						Max	17.6	0.71077	**-2.1**	-2.8

Table V-3 A: $\delta^{18}O_P$ values (‰ VSMOW) and $^{87}Sr/^{86}Sr$ ratios of tooth apatite from specific shark taxa in Western European Palaeozoic basins. Locality numbers refer to basin numbers in Figure V-2. Palaeotemperature estimates from Fischer et al. (2012) and phosphate-water fractionation factor from Lécuyer et al. (2013) and Pucéat et al. (2010).

Locality name	Number on map	Formation	Age	Taxon	Sample	Material	$\delta^{18}O_P$ (‰ VSMOW)	$^{87}Sr/^{86}Sr$	$\delta^{18}O_{water}$ (29 ± 7°C) Lécuyer et al. (2013)	$\delta^{18}O_{water}$ (29 ± 7°C) Pucéat et al. (2010)
Guardia Pisano basin, southwestern Sardinia, Italy	3	Member B	Early Permian, early Asselian (299 - 295 Ma)	Lissodus sardiniensis	LS 1	21 tooth crowns	17.55	0.710280	-2.1	-2.8
					LS 2	30 tooth crowns	18.19		-1.5	-2.2
					LS 3	30 tooth crowns	17.98		-1.7	-2.4
					LS 4	30 tooth crowns	17.93	0.710236	-1.7	-2.4
					LS 5	30 tooth crowns	17.97		-1.7	-2.4
					LS 6	28 tooth crowns	18.18		-1.5	-2.2
					LS 7	fin spine fragment	16.97		-2.7	-3.4
					LS 8	fin spine fragment	17.69		-2.0	-2.7
					LS 9	fin spine fragment	17.64		-2.0	-2.7
					LS 10	fin spine fragment	17.54		-2.1	-2.8
					LS 11	fin spine fragment	17.22		-2.4	-3.1
					LS 12	fin spine fragment	17.28		-2.4	-3.1
					LS 13	fin spine fragment	17.21		-2.4	-3.1
					LS 14	fin spine fragment	17.34	0.710364	-2.3	-3.0
					LS 15	fin spine fragment	18.04		-1.6	-2.3
					LS 16	fin spine fragment	17.84		-1.8	-2.5
					LS 17	fin spine fragment	17.79		-1.9	-2.6
					LS 18	fin spine fragment	17.76		-1.9	-2.6
					LS 19	fin spine fragment	17.59	0.710354	-2.1	-2.8
					LS 20	fin spine fragment	17.03		-2.6	-3.3
					LS 21	30 scales	17.37		-2.3	-3.0
					LS 22	30 scales	17.15		-2.5	-3.2
					LS 23	26 scales	16.67		-3.0	-3.7
						Average	17.6	0.71031	-2.1	-2.8
						SD	0.4	0.00006	0.4	0.4
						Min	16.7	0.71024	-3.0	-3.7
						Max	18.2	0.71036	-1.5	-2.2

Table V-3 B: $\delta^{18}O_P$ values (‰ VSMOW) and $^{87}Sr/^{86}Sr$ ratios of tooth apatite from specific shark taxa in Western European Palaeozoic basins. Locality numbers refer to basin numbers in Figure V-2. Palaeotemperature estimates from Fischer et al. (2012) and phosphate-water fractionation factor from Lécuyer et al. (2013) and Pucéat et al. (2010).

2. Hydrogen isotope geochemistry of hydrous silicates from the Montagne Noire

a. Introduction

In order to reference the hydrogen isotope records obtained from the south Armorican and Limousin detachments (**Chapters III and IV**), the hydrogen isotope composition (δD) of hydrous silicates that crystallized during high temperature deformation were measured in the footwall of the Montagne Noire Espinouse detachment (southern part of the French Massif Central) that separates the migmatitic orthogneiss (footwall) from the Graissessac-Lodève supra-detachment basin to the north (hanging-wall, **Fig. V-5**).

b. Geological settings

Located at the southern edge of the French Massif Central, the Metamorphic Core Complex of Montagne Noire (MN) is considered to have developed in the foreland of the Variscan belt (e.g. Ledru et al., 1989; Franke et al., 2011). It consists of a 20 km-wide and 80 km-long ENE-WSW trending high-grade metamorphic dome made of migmatitic orthogneiss and granite surrounded by a sequence of Palaeozoic metasediments (e.g. Geze et al., 1952; Van Den Driessche and Brun, 1992, **Fig. V-5)**. The axial zone is overlain by metamorphosed sediments that are involved in large scale southwards recumbent folds (e.g. Arthaud, 1970; Echtler, 1990; Van Den Driessche and Brun, 1992).

Although the Espinouse detachment shear zone might have acted as a thrust during the early stage of compression, the last increment of deformation is widely considered to be normal with a top-to-the-north sense of shearing (e.g. Malavieille et al., 1990; Pitra et al., 2012; Poujol et al., 2017). It is accepted that this detachment zone

developed as a result of post-orogenic extension during the Late Carboniferous (e.g. Malavieille et al., 1990; Pitra et al., 2012; Poujol et al., 2017).

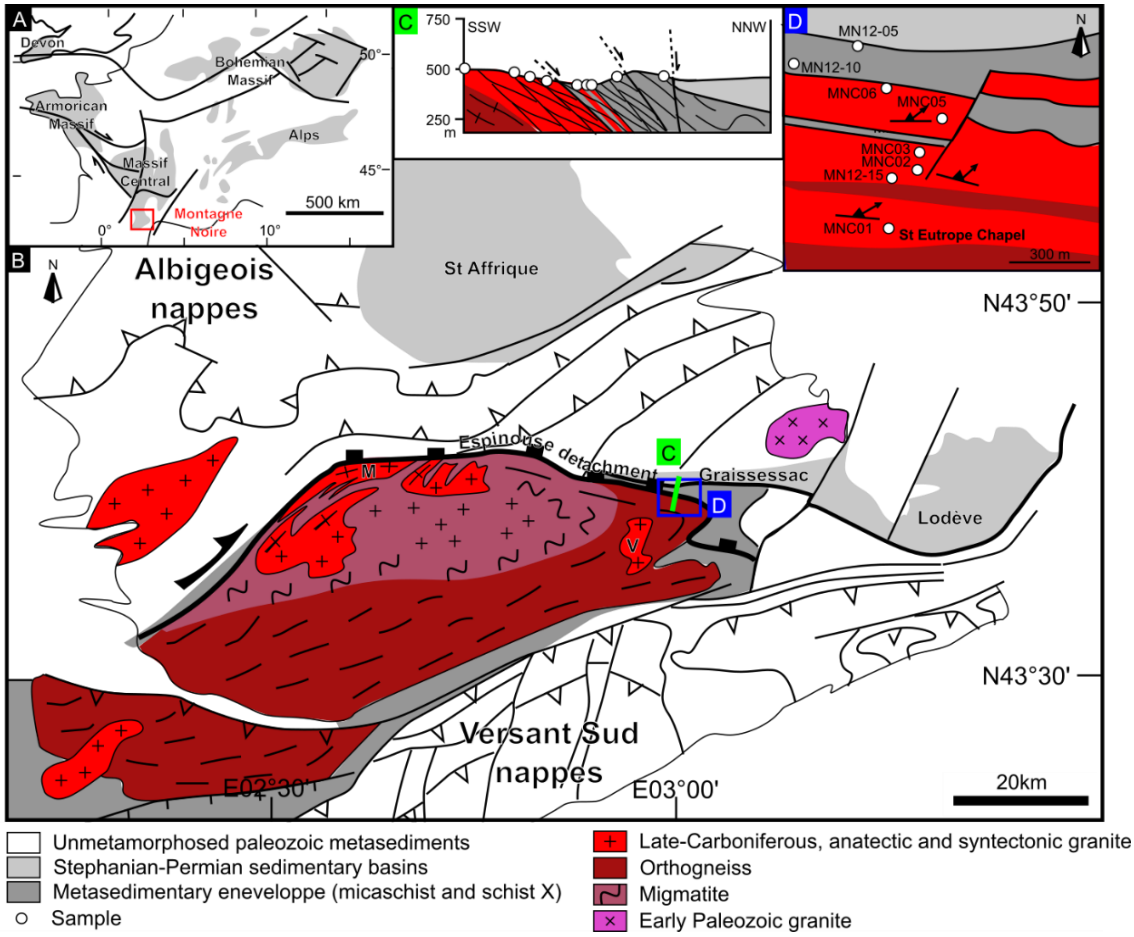

Figure V-5: (A) Location of the study area within the European Variscan belt; (B) Structural map of the Montagne Noire gneiss dome bounded by the Espinouse detachment, with relationship with Variscan thrusts and nappes and late-Carboniferous to early-Permian basins (modified after Brun and van den Driessche, 1994). (C) Cross section (see transect location on B) and (D) zoomed map showing location of sampling section (modified from Pitra et al., 2012 and Fréville et al., 2016). M – Montalet granite; V – Vialais granite.

The mylonitic footwall is represented by a highly deformed orthogneiss whose protolith is thought to represent a relic of an Ordovician magmatism episode dated at ~456-450 Ma (e.g. Roger et al., 2004, 2015; Pitra et al., 2012). These orthogneiss underwent high-temperature deformation and metamorphism during the Variscan orogeny between ~320 and 300 Ma (U-Th-Pb on monazite and zircon; Roger et al., 2015; Poujol et al., 2017) that postdates the Barrovian metamorphism and nappe

emplacement (>320 Ma; e.g. Feist and Galtier, 1985). The activity along the Espinouse detachment shear zone is thought to be coeval with migmatization (e.g. Maluski et al., 1991; Pitra et al., 2012; Roger et al., 2015), and its cessation has been estimated at 294.4 ± 4 Ma (LA-ICP-MS U-Pb-Th data on monazite on the Saint-Eutrope migmatitic orthogneiss, Pitra et al., 2012). These ages are similar with those at 294 ± 1 Ma obtained on monazite and zircon using U-Th-Pb on the syntectonic Montalet granite that outcrops further west in the Espinouse detachment footwall (Poilvet et al., 2011). In addition, the age of 295.3 ± 4.8 Ma obtained on a volcanic ash layer from the Graissessac-Lodève supra-detachment basin (north of the axial zone) confirms the late-Carboniferous activity on the Espinouse detachment (Bruguier et al., 2003).

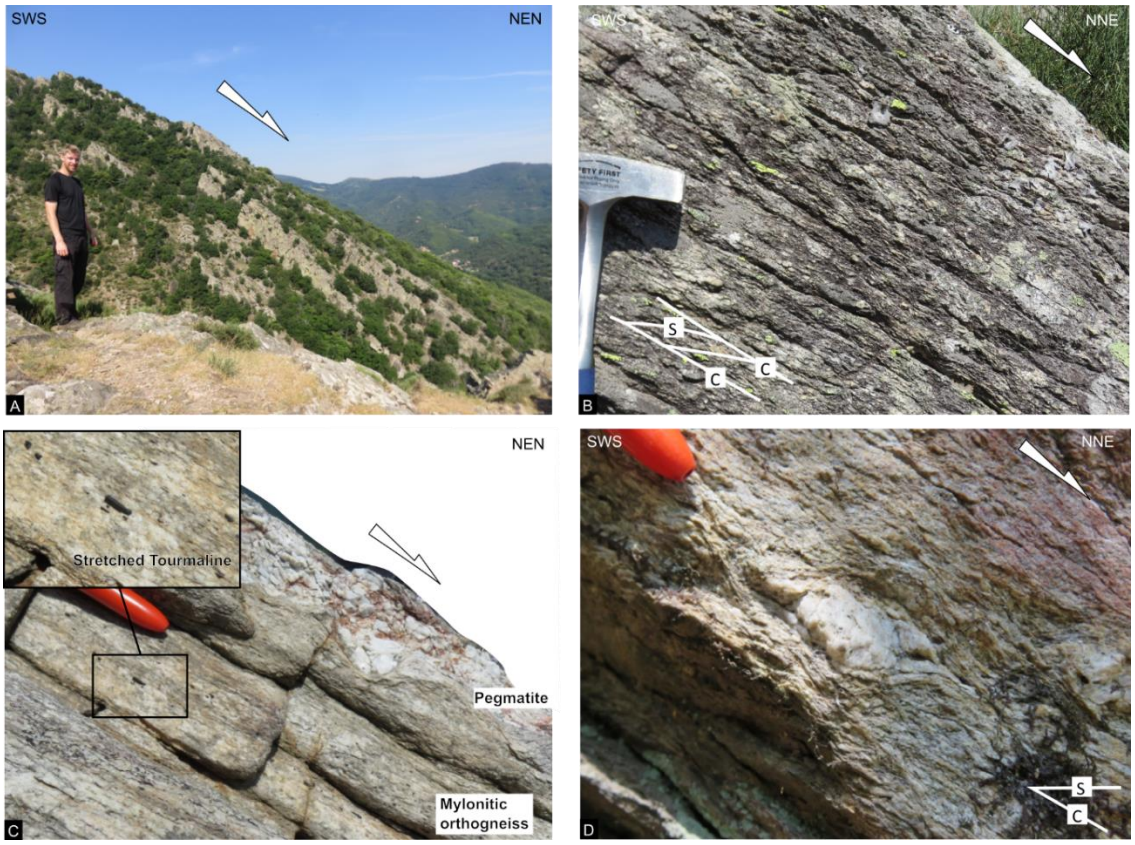

Figure V-6: Field pictures of the Espinouse detachment footwall at the NE of the Montagne Noire. (A) General view of the Espinouse detachment zone; (B) Mylonitic orthogneiss with shear bands highlighting a top-to-the-NE sense of shear; (C) Sheared pegmatite and mylonitic orthogneiss exhibiting stretched tourmaline parallel to the lineation; (D) Delta type clast of feldspar.

c. Structure and internal deformation

At the northern edge of the Montagne Noire, the sheared orthogneiss exhibits an E-W-striking foliation that dips shallowly to the N (**Fig. V-6 - A**). This foliation (S-planes) is overprinted by pervasive shear planes (C-planes) that dip moderately to the north (**Fig. V-6 - B**), giving rise to shear bands indicating a top-to-the north normal sense of shear when looking parallel to the ENE-trending lineation. The leucocratic migmatitic orthogneiss is intruded by syntectonic pegmatite (**Fig. V-6 - C**). Stretched tourmaline (**Fig. 6-C**) and asymmetric feldspar porphyroclasts (**Fig. V-6 - D**) confirms the normal kinematics to the ENE (e.g. Pitra et al., 2012).

At the microscopic scale, muscovite, tourmaline and biotite grains (**Fig. V-7 - A and B**) are predominantly located along shear planes (C) but also foliation planes (S) that form together shear bands. Large muscovite and tourmaline porphyroclasts grains (> 0.5mm) are surrounded by small biotite that developed along shear planes (**Fig. V-7 - D and E**). Micaschist samples collected in the orthogneiss "carapace" are affected by brittle normal faults where biotite crystallised on the walls of the fracture (**Fig. V-7 - F and G**).

Sub-solidus deformation textures, such as rectangular and castellate quartz grain boundaries, indicate that grain boundary migration (regime 3, Hirth and Tullis, 1992) was the dominant dynamic recrystallization process (**Fig. V-7 - C**). These microstructural observations are compatible with ductile shearing of the orthogneiss during high-temperature deformation (>500°C, Stipp et al., 2002). This is in good agreement with thermometry estimates of 566 ± 38°C conducted on a similar section using Raman Spectroscopy on Carbonaceous Matter (Fréville et al., 2016).

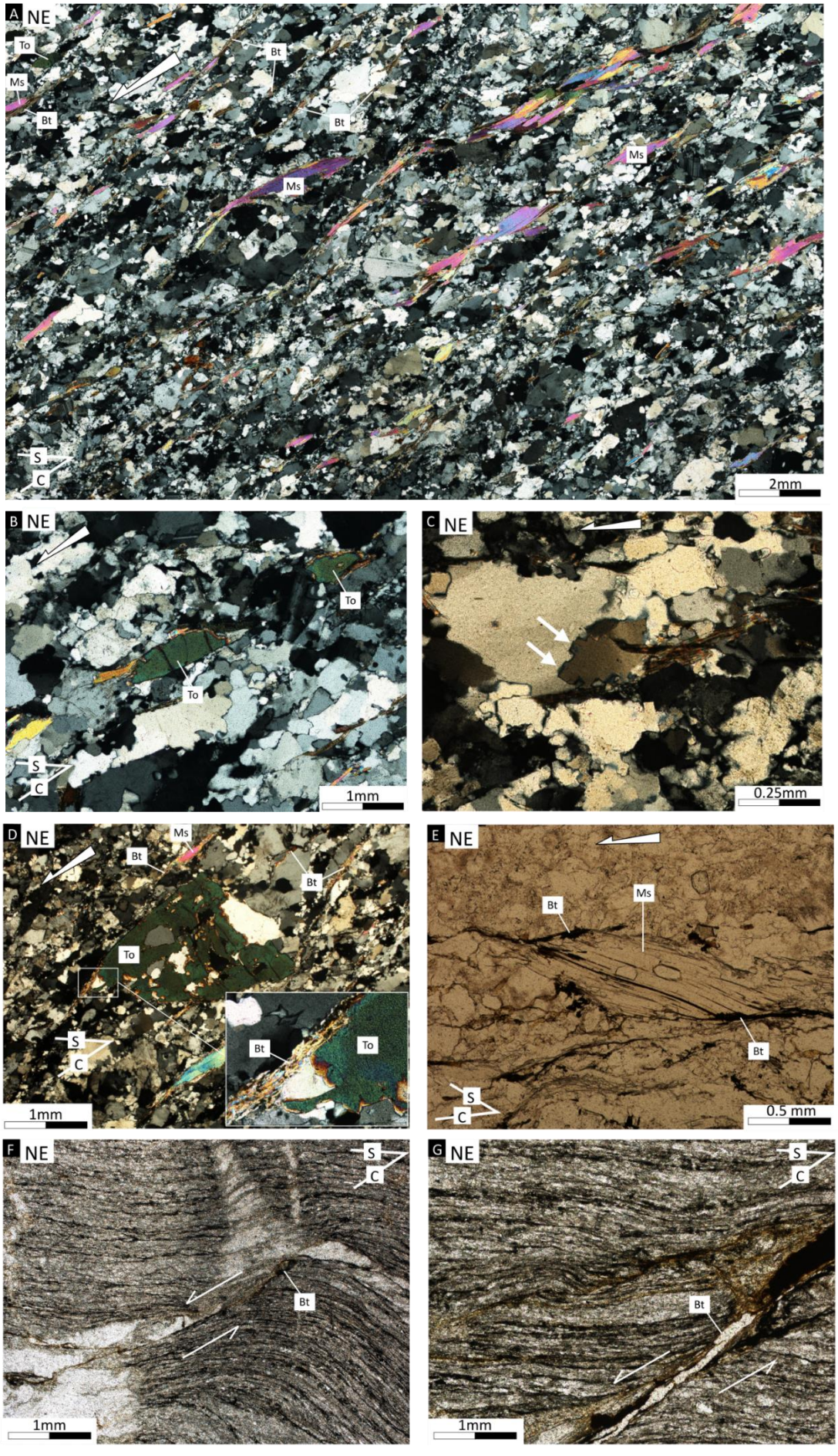
A NE
To
Ms
Bt
Bt
Bt
Ms
Ms
S
C
2mm
B NE
To
To
S
C
1mm
C NE
0.25mm
D NE
Ms
Bt
Bt
To
S
C
Bt
To
1mm
E NE
Bt
Ms
Bt
S
C
0.5 mm
F NE
S
C
Bt
1mm
G NE
S
C
Bt
1mm

Figure V-7 (last page): Microstructures from the footwall of the Espinouse detachment. Sections are cut perpendicular to foliation and parallel to lineation. Mylonitic orthogneiss (sample MNC03) (A) Shear bands highlighted by muscovite, tourmaline and biotite; (B) Stretched tourmaline along shear planes; (C) Quartz grain boundary migration (white arrows) and biotite on C plane; (D) Deformed tourmaline and muscovite porphyroclasts taped by biotite fish along shear planes; (E) Lenticular muscovite fish reduced on the upper and lower side by shear planes filled with biotite; Micaschist (sample MN12-10): (F) and (G) Normal faults with biotite on the walls

d. Hydrogen and oxygen isotope geochemistry

Hydrogen isotope measurements of muscovite (Ms), tourmaline (To), and biotite (Bt) were conducted on 7 samples of mylonitic orthogneiss, 2 samples of sheared pegmatite and 2 samples of micaschist ($\delta D_{mineral}$ ± 2‰; **Table V-4 and Fig. V-8**). δD_{Ms} values from orthogneiss range from -59 to -47‰. Pegmatite samples have similar δD_{Ms} values between -54 and -48‰. In contrast, tourmaline provides lower δD_{To} values that vary between -72 and -62‰ for the mylonitic orthogneiss and from -67 to -63‰ for the pegmatite. Biotite yield δD_{Bt} values between -76 and -56‰ in mylonitic orthogneiss, -64‰ in pegmatite and from -60 to -58‰ in micaschist.

δD_{Ms} values remain constant from the top to the bottom of the section and range from -59 to -47‰ (**Table V-4 and Fig. V-8**). In contrast, tourmaline have δD values that are lower at the bottom of the section (-72‰) compared to those at the top (-62‰). The δD_{To} values are systematically ~15‰ lower than those provided by muscovite, indicating these two minerals reached their hydrogen isotope equilibrium based on the fractionation factors of Suzuoki and Epstein, (1976) for muscovite-water and Jibao and Yaqian (1997) for tourmaline-water using a temperature of 566°C estimated by Fréville et al. (2016).

Similarly to tourmaline, hydrogen isotope ratios of biotite shows a decrease from the top (-56‰) to the bottom of the section (-76‰). When compared to the δD_{Ms} values, the δD_{Bt} values are 22‰ lower than those provided by muscovite at the bottom, and up

to 8‰ lower at the top of the section (**Table V-4**). This 22‰ difference between the two minerals at the bottom has been interpreted to reflect isotope equilibrium based on the difference in fractionation factors of ~21‰ between muscovite and biotite calculated by Suzuoki and Epstein (1976) at 566°C (Fréville et al., 2016). In contrast, the 8‰ difference between the δD values of biotite and muscovite at the top indicates a disequilibrium and suggests that biotite interacted with a different fluid at the top compared to the bottom of the section.

The oxygen isotope composition ($\delta^{18}O \pm 0.1‰$) of muscovite from sample MNC03 was also measured and a $\delta^{18}O_{Ms}$ value of 8.8‰ was obtained (**Table V-4**).

e. Hydrogen isotope composition of the fluids

The isotope composition of the fluid present in the Espinouse detachment footwall has been calculated based on the hydrogen isotope composition of hydrous minerals (Muscovite: Ms; Tourmaline: To and Biotite: Bt), the hydrogen isotope fractionation factors of Suzuoki and Epstein (1976) for muscovite and biotite and the one of Jibao and Yaqian (1997) for tourmaline, as well as the estimated temperature of isotope exchange between the fluid and the mineral (**Fig. V-8; Table V-5**). Two different temperatures estimates that lead to sensibly similar δD_{water} values have been considered:

- Deformation temperatures of 550 ± 150°C deduced from quartz microstructures (this study, e.g. Hirth and Tullis, 1992; Stipp et al., 2002; Langille et al., 2010) allow us to calculate δD_{water} values ranging from -42 to -33 ± 16‰ from δD_{Ms} values, -41 to -22 ± 16‰ from δD_{Bt} values and from -33 to -23 ± 20‰ from δD_{To} values.

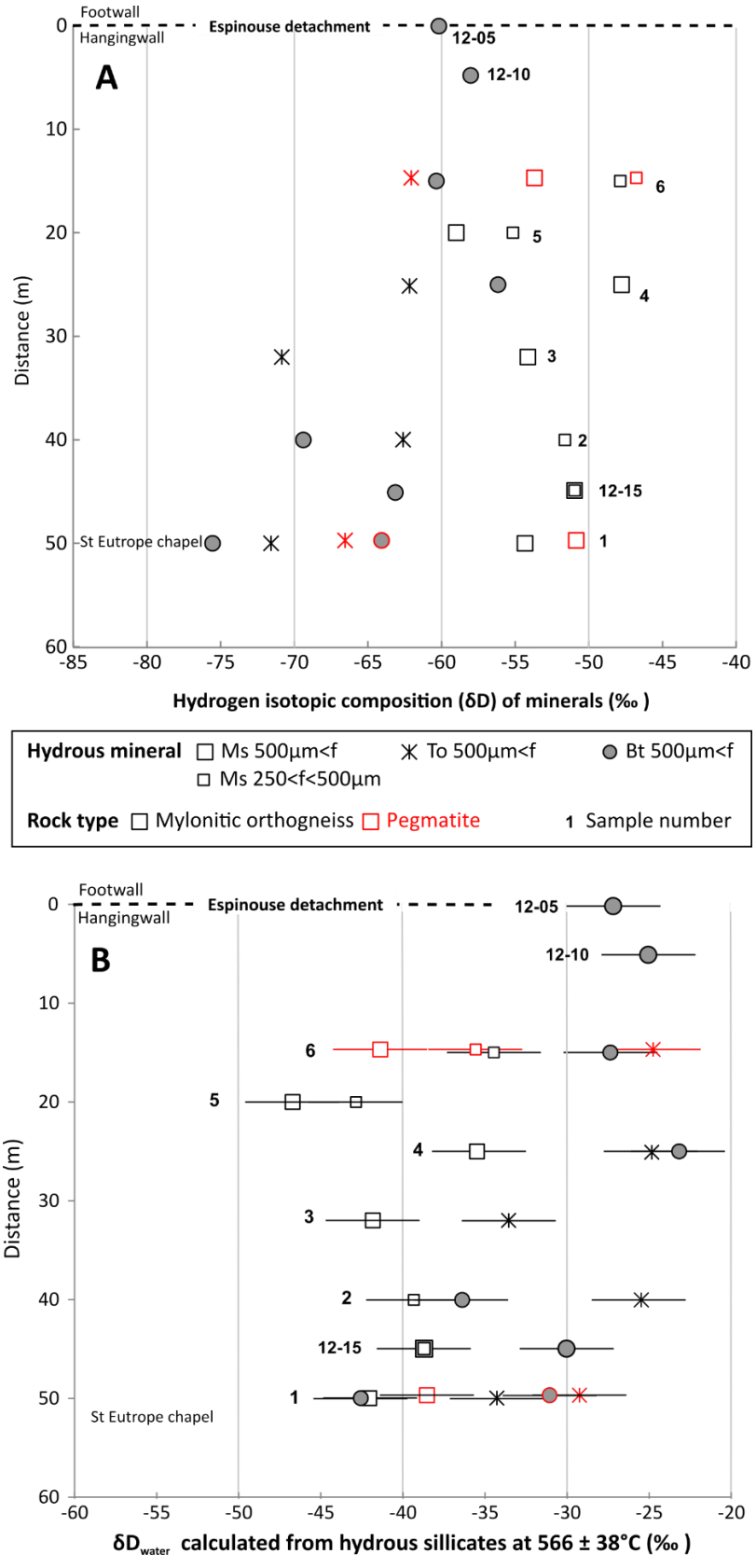

Figure V-8: Hydrogen isotope analysis of mylonitic orthogneiss and pegmatite samples from the Espinouse detachment footwall with respect to the estimated distance from the Espinouse detachment zone from 15m to 50m (St Eutrope chapel). (A) δD values [‰] of muscovite (Ms), tourmaline (To) and biotite (Bt); (B) δDwater [‰] calculated based on the δD values of hydrous silicates, a temperature of isotope exchange of 566°C and the hydrogen isotope fractionation factors of Suzuoki and Epstein (1976) and Jibao and Yaqian (1997).

	Name	Description	Distance (m)	Foliation	Lineation	Longitude	Latitude	δD_{Ms} (‰) (500µm<f)	δD_{Ms} (‰) (250<f<500µm)	δD_{Bt} (‰) (500µm<f)	δD_{Ms} - δD_{Bt} (‰)	δD_{To} (‰) (500µm<f)	δD_{Ms} - δD_{To} (‰)	$\delta^{18}O_{Ms}$ (‰) (500µm<f)
BOTTOM	MNC01A	Mylonitic orthogneiss	50	N095;50N	N060	43°39'41.04"N	2°59'21.39"E	-54		-76	22	-72	18	
	MNC01B	Pegmatite	50	N095;50N	N060	43°39'41.04"N	2°59'21.39"E	-51		-64	13	-67	16	
	MN12-15	Mylonitic orthogneiss	45	N103;45N	N070	43°39'45.60"N	2°59'21.15"E	-51	-51	-63	12			
	MNC02	Mylonitic orthogneiss	40	N285;60N	N048	N43˚39'47.0''	E02˚59'25.7''		-52	-69	17	-63	11	
	MNC03	Pegmatite + Mylonitic orthogneiss	32	N074;45N	N060	N43˚39'49.0''	E02˚59'26.0''	-54				-71	17	8.8
TOP	MNC04	Mylonitic orthogneiss	25	N090;38N	N072	N43˚39'51.8''	E02˚59'28.8''	-48		-56	8	-62	14	
	MNC05	Mylonitic orthogneiss	20	N093;30N	N052	N43˚39'52.6''	E02˚59'29.3''	-59	-55					
	MNC06A	Pegmatite	15	N082;50N	N040	N43˚39'56.2''	E02˚59'20.6''	-54	-48			-62	14	
	MNC06B	Mylonitic orthogneiss	15	N082;50N	N040	N43˚39'56.2''	E02˚59'20.6''		-47	-60	13			
	MN12-10	Micaschist	5			43°40'3.90"N	2°58'32.61"E			-58				
	MN12-05	Micaschist	0		N056	43°40'6.11"N	2°58'55.61"E			-60				

Table V-4: Location, description, hydrogen and oxygen isotope composition of samples from the NE edge of the Montagne Noire in the footwall of the Espinouse detachment shear zone. The estimated distance from the hanging wall/footwall interface is indicated in m. Ms: muscovite; Bt: biotite; To: tourmaline.

- Raman Spectroscopy on Carbonaceous Matter thermometry estimates of 566 ± 38°C obtained on similar samples (Fréville et al., 2016), allow us to calculate δD_{water} values ranging from -43 to -34 ± 3‰ from muscovite, -43 to -23 ± 3‰ from biotite and from -34 to -25 ± 4‰ from tourmaline.

The oxygen isotope ratio of muscovite ($\delta^{18}O_{Ms}$ = 8.8 ± 0.1‰) from a mylonitic orthogneiss, combined with the oxygen isotope fractionation factor of Zheng (1993) and the Raman Spectroscopy on Carbonaceous Matter thermometry estimates of 566 ± 38°C (Fréville et al., 2016), allows the calculation of a $\delta^{18}O_{water}$ value of 9.8 ± 0.1‰.

f. Discussion

The homogeneous lower δD_{water} values (-43 to -34‰) calculated from muscovite along the section can be interpreted to reflect the hydrogen isotope composition of a deep crustal fluid (-70‰ < $\delta D_{metamorphic\ fluids}$ < -20‰ and/or -80‰ < $\delta D_{magmatic\ fluids}$ < -40‰; 5‰ < $\delta^{18}O_{metamorphic\ fluids}$ < 25‰ and 5‰ < $\delta^{18}O_{magmatic\ fluids}$ < 10‰; e.g. Field and Fifarek, 1985). The δD_{water} values calculated from biotite (-43 to -36‰) and from tourmaline (-34 to -25‰) collected at the bottom (32 to 50m) of the section are consistent and reflect a signature of a deep crustal fluid.

In contrast, the δD_{water} values calculated from biotite and tourmaline at the top of the section (0 to 25m) range from -27 to - 23‰, interpreted to reflect a mixing relationship between deuterium-depleted (δD_{water} ~ -43‰) and deuterium-enriched (δD_{water} ~ -23‰) fluids.

Observations at the scale of the thin-section indicates that biotite crystallized along shear planes (C) affecting the orthogneiss during deformation in the footwall, and along brittle normal faults in micaschist in the hanging-wall (Fig. 7). It has been

demonstrated that the orthogneiss experienced an episode of intense ductile shearing along the Espinouse detachment at ~300-295 Ma (LA-ICP-MS U-Pb-Th on monazite and Ar/Ar on muscovite, Maluski et al., 1991; Pitra et al., 2012). This episode of shearing was coeval with intense fluid circulation as shown by patchy zoning of younger monazite gains (Pitra et al., 2012; Poujol et al., 2017). Consequently, the isotope composition of syntectonic biotite is interpreted to reflect the composition of the fluid that circulated during activity on the Espinouse detachment zone.

The high δD_{water} values (~-23‰) calculated from biotite can reflect: 1) a metamorphic fluid signature (-70‰ < $\delta D_{metamorphic\ fluids}$ < -20‰; e.g. Field and Fifarek, 1985) or 2) a meteoric fluid signature sourced at low elevation (e.g. Poage and Chamberlain, 2006). The Montagne Noire being located in the foreland of the Variscan Belt, the δD_{water} values of precipitation at the surface at low altitude can be assumed to be high in agreement with those obtained near sea level ($\delta D_{sea\ water}$ value = 0 ± 1-2‰, Hoefs, 2004). As a consequence, the δD_{Bt} values at the top of the detachment footwall could reflect interaction with deuterium-enriched meteoric fluids during high temperature deformation. However, the downward infiltration of surface-derived fluids with high δD_{water} values would result in lowering the δD_{water} values by progressive interaction with metamorphic and/or magmatic fluids. Therefore, the highest δD_{water} value of -23‰ obtained at the top of the section is considered to approximate most closely the δD_{water} value of precipitation at that time.

As proposed by previous studies, the infiltration of surface-derived fluids at depth can occur by percolating along fractures and normal faults that increase the permeability of the detachment zones (e.g. Mulch et al., 2004, 2007; Person et al., 2007; Gébelin et al., 2011, 2015, 2017). In the Montagne Noire, brittle normal faults in the

micaschists could have enhanced the permeability of the upper crust, while the emplacement of syntectonic granite and exhumation of high-grade metamorphic rocks would have provided the necessary heat to sustain the convection of fluids at depth.

g. Further work to be conducted in the Montagne Noire

The Montalet syntectonic leucogranite that was emplaced during late-orogenic extension along the Espinouse detachment at the NW corner of the Montagne Noire has also been sampled (see location on **Fig. V-5**). It was dated at 294 Ma ± 3 Ma by U–Th–Pb on zircon (Poujol et al., 2017) and at 294 ± 1 Ma on monazite (Poilvet et al., 2011). Combining the study of the orthogneiss of St Eutrope that experienced a late episode of shearing (NE of the Montagne Noire; see above) and this new study on the Montalet syntectonic granite, future work will be able to characterise the fluids that circulated along the Espinouse detachment during post-orogenic extension.

In order to determine the source of fluids that infiltrated the Montalet granite, this future study will measure the hydrogen isotope composition (δD) of muscovite and biotite from 9 leucogranite samples in the Stable Isotopes lab (Joint Goethe University and BIK-F) in Frankfurt (Germany) in 2019. As the hydrogen isotopic composition of muscovite from the foreland area is likely to fall into the range of metamorphic/magmatic muscovite the oxygen isotope ratios ($\delta^{18}O$ values) of two muscovite samples from the Montalet granite will also measured at the University of Lausanne (Switzerland). The temperature of isotope exchange between the fluid and the muscovite estimated using the Ti-in-Ms thermometer (Wu and Chen, 2015) combined with the stable isotope data acquired on synkinematic muscovite will allow us to decipher the source of fluids that were present in the detachment footwall during deformation. The chemical composition of muscovite from the Montalet granite will be

measured using the microprobe CAMECA SX100 at the University of Lille (France) in order to detect potential grain-scale chemical variations.

h. Conclusion

In the Montagne Noire, mylonitic orthogneiss samples were collected in the footwall of the Espinouse detachment. Muscovite porphyroclasts yielded δD_{Ms} values that reflect interaction with deep crustal fluids. Biotite and tourmaline located along shear planes yield δD values that progressively increase towards the top of the section. This increase has been interpreted to reflect a progressive interaction with a deuterium-enriched fluid. Using a temperature of isotope exchange of 566 ± 38°C deduced from Raman Spectroscopy on Carbonaceous Matter thermometry (Fréville et al., 2016), which is in agreement with quartz microstructure typical of high temperature deformation (>500°C), the hydrogen isotope composition of the fluids that exchanged with muscovite, tourmaline and biotite during high temperature deformation was calculated.

The results from this study indicate a 20‰ difference in δD_{water} values that are interpreted in terms of mixing between metamorphic fluids with lower δD values (-43‰) and deuterium-enriched metamorphic and/or meteoric fluids with higher δD values (-23‰). Postulating that all the conditions were met to allow low-altitude meteoric water to infiltrate the footwall of the Espinouse detachment during post-orogenic extension, a potential δD_{water} value of precipitation that penetrated during the detachment activity was calculated. The δD values of synkinematic biotite (± 2‰) combined with the temperature of isotope exchange given by the Raman Spectroscopy on Carbonaceous Matter thermometry (± 38°C equivalent to ± 3‰) allowed the calculation of an average δD_{water} value of **-30 ± 8‰** (n=8) for the precipitation that will be tested to reconstruct the paleoaltitude of the Variscan Belt (**Table 6**).

				Muscovite		Biotite		Tourmaline			Quartz microstructures thermometer									Raman Spectroscopy on Carbonaceous Matter thermometry								
	Sample	Distance (m)	Rock type	δD Ms (‰)	Fraction Ms (µm)	δD Bt (‰)	Fraction Bt (µm)	δD To (‰)	Fraction To (µm)	± ± (‰)	Temperature (°C)	± (°C)	δD water (‰) from Ms	δD water (‰) from Bt	-	+	δD water (‰) from To	-	+	Temperature (°C)	± (°C)	δD water (‰) from Ms	δD water (‰) from Bt	-	+	δD water (‰) from To	-	+
BOTTOM	MNC01A	50	Leucogranite	-54	500<f	-76	500<f	-72	500<f	2	550	150	-41	-41	-9	16	-33	-12	20	566	38	-42	-43	-3	3	-34	-3	4
	MNC01B	50	Pegmatite	-51	500<f	-64	500<f	-67	500<f	2	550	150	-37	-30	-9	16	-28	-12	20	566	38	-39	-31	-3	3	-29	-3	4
	MN12-15	45	Leucogranite	-51	500<f	-63	500<f			2	550	150	-38	-29	-9	16				566	38	-39	-30	-3	3			
	MNC02	40	Leucogranite	-52	250<f<500	-69	500<f	-63	500<f	2	550	150	-38	-35	-9	16	-24	-12	20	566	38	-39	-36	-3	3	-25	-3	4
	MNC03	32	Pegmatite + leucogranite	-54	500<f			-71	500<f	2	550	150	-41		-9	16	-32	-12	20	566	38	-42		-3	3	-34		
TOP	MNC04	25	Leucogranite	-48	500<f	-56	500<f	-62	500<f	2	550	150	-34	-22	-9	16	-23	-12	20	566	38	-35	-23	-3	3	-25	-3	4
	MNC05	20	Leucogranite	-55	250<f<500					2	550	150	-42		-9	16				566	38	-43		-3	3			
	MNC06A	15	Pegmatite	-48	250<f<500			-62	500<f	2	550	150	-34		-9	16	-23	-12	20	566	38	-36		-3	3	-25		
	MNC06B	15	Leucogranite	-47	250<f<500	-60	500<f			2	550	150	-33	-26	-9	16				566	38	-34	-27	-3	3			
	MN12-10	5	Micaschist			-58	500<f			2	550	150		-24	-9	16				566	38		-25	-3	3			
	MN12-05	0	Micaschist			-60	500<f			2	550	150		-26	-9	16				566	38		-27	-3	3			
			AVERAGE	-51		-64		-66		2	550	150	-38	-29	-9	16	-27	-12	20	566	38	-39	-30	-3	3	-29	-3	4
			SD	3		7		4		0	0	0	3	7	0	0	4	0	0	0	0	3	7	0	0	4	0	0
			Min	-55		-76		-72		2	550	150	-42	-41	-9	16	-33	-12	20	566	38	-43	-43	-3	3	-34	-3	4
			Max	-47		-56		-62		2	550	150	-33	-22	-9	16	-23	-12	20	566	38	-34	-23	-3	3	-25	-3	4

Table V-5: Measured hydrogen isotope composition (δD) of muscovite, biotite and tourmaline from the Espinouse detachment footwall (Montagne Noire, France), that, together with estimated temperature of hydrogen isotope exchange deduced from quartz microstructures (this study) and Raman Spectroscopy on Carbonaceous Matter thermometry (Fréville et al., 2016), and the isotope fractionation factors of Suzuoki and Epstein (1976) for muscovite and biotite and from Jibao and Yaqian (1997) for tourmaline, allow usto calculate the hydrogen isotope composition (δD) of water that exchanged with hydrous silicates.

A	Uncertainty	Uncertainty (‰)	**δD water (‰)**	Propagated uncertainty (‰)	**$\delta^{18}O$ water (‰)**	Propagated uncertainty (‰)
Isotope analysis ($\delta^{18}O_P$)	0.2‰	0.2				
Estimated temperature	7°C	1.6				
Average of $\delta^{18}O_P$ values	0.5‰	0.5	-15	14	**-3.1**	**1.7**

B	Uncertainty	Uncertainty (‰)	δD water (‰)	Propagated uncertainty (‰	$\delta^{18}O$ water (‰)	Propagated uncertainty (‰
Isotope analysis ($\delta D_{mineral}$)	2‰	2				
Temperature from quartz microstructures	150°C	16				
Average of δD_{Ms} values	3‰	3	-38	17	-5.9	2.1
Temperature from quartz microstructures	150°C	16				
Average of δD_{Bt} values	7‰	7	-29	17	-4.9	2.1
Temperature from quartz microstructures	150°C	20				
Average of δD_{To} values	4‰	4	-27	21	-4.6	2.6
Temperature from Raman Spectroscopy on Carbonaceous Matter	38°C	3				
Average of δD_{Ms} values	4‰	3	-39	5	-6.1	0.6
Temperature from Raman Spectroscopy on Carbonaceous Matter	38°C	3				
Average of δD_{Bt} values	7‰	7	-30	8	-5.0	1.0
Temperature from Raman Spectroscopy on Carbonaceous Matter	38°C	4				
Average of δD_{To} values	4‰	4	-29	7	-4.8	0.8

Table V-6: Average δD_{water} and $\delta^{18}O_{water}$ values and uncertainties calculated in the external zones of the Variscan Belt for (A) the Bourbon l'Archambault basin and (B) the Montagne Noire. (A) The calculated $\delta^{18}O_{water}$ values are calculated based on the $\delta^{18}O_P$ values of sharks remains (Fischer et al., 2013), water temperatures for modern and Jurassic euryhaline sharks (Dera et al., 2009; Carlson et al., 2010; Fischer et al., 2012) and the isotope fractionation factor of Lécuyer et al. (2013). (B) The average δD_{water} are calculated based on the measured hydrogen isotope composition (δD) of muscovite (Ms), biotite (Bt) and tourmaline (To) from the Espinouse detachment footwall, combined with estimated temperature using quartz microstructures (e.g. Stipp et al., 2002) and Raman Spectroscopy on Carbonaceous Matter thermometry estimates (Fréville et al., 2016), together with the isotope fractionation factors of Suzuoki and Epstein (1976). The final uncertainty includes the isotope analysis, the temperature of isotope exchange and the average. The δD_{water} value is converted in $\delta^{18}O$ value and vice-versa using the meteoric water line of Craig (1961).

D. Stable isotope paleoaltimetry of the Variscan Belt of Western Europe

1. Isotope records of precipitation in the hinterland and the foreland

To recover the isotope composition of meteoric water in the hinterland of the Variscan Belt of Western Europe, the hydrogen isotope composition of muscovite (δD_{Ms}) was measured in the detachment shear zones of the Armorican Massif and the French Massif Central (**Fig. V-9; Tables V-1 and V-2**). Using temperatures of isotope exchange based on the Ti-in-Ms geothermometer (Wu and Chen, 2015), combined with the calibration of muscovite-water hydrogen isotope exchange (Suzuoki and Epstein, 1976), the δD_{Ms} values from the Piriac and Quiberon detachment footwalls allowed the calculation of δD_{water} values as low as -77‰ with an average value of -70 ± 5‰ in the southern Armorican domain. Similarly, the δD_{Ms} values from the Felletin detachment footwall allowed the calculation of δD_{water} values as low as -104‰ with an average value of -89 ± 8‰ (western part of the French Massif Central). The uncertainty on both δD_{water} values takes into account the hydrogen isotope analysis, the temperature of isotope exchange and the average of the lower δD_{Ms} values found at the top of the detachment footwalls.

In order to reduce the uncertainty linked to the lack of knowledge in atmospheric circulation patterns, paleoclimate, and paleoenvironmental conditions, the late-Carboniferous high-elevation hinterland precipitation records have been compared to age-equivalent δD_{water} values preserved in the foreland geological record. One of the best proxies amenable to record the isotope composition of surface-derived water at sea level is represented by fossil sharks that evolved in late-Carboniferous freshwater environments in the Bourbon l'Archambault basin. Using the $\delta^{18}O_{phosphate}$ values of shark tooth and spines from Fischer et al. (2013), a temperature of isotope exchange based

on modern and Jurassic euryhaline sharks water temperature (29 ± 7°C; e.g. Dera et al., 2009; Carlson et al., 2010; Fischer et al., 2012) and the phosphate-water fractionation equation of Lécuyer et al. (2013) (**Table V-3**), an average $\delta^{18}O_{water}$ value of -3.1 ± 1.0‰ was calculated (**Fig. V-9; Table V-6**).

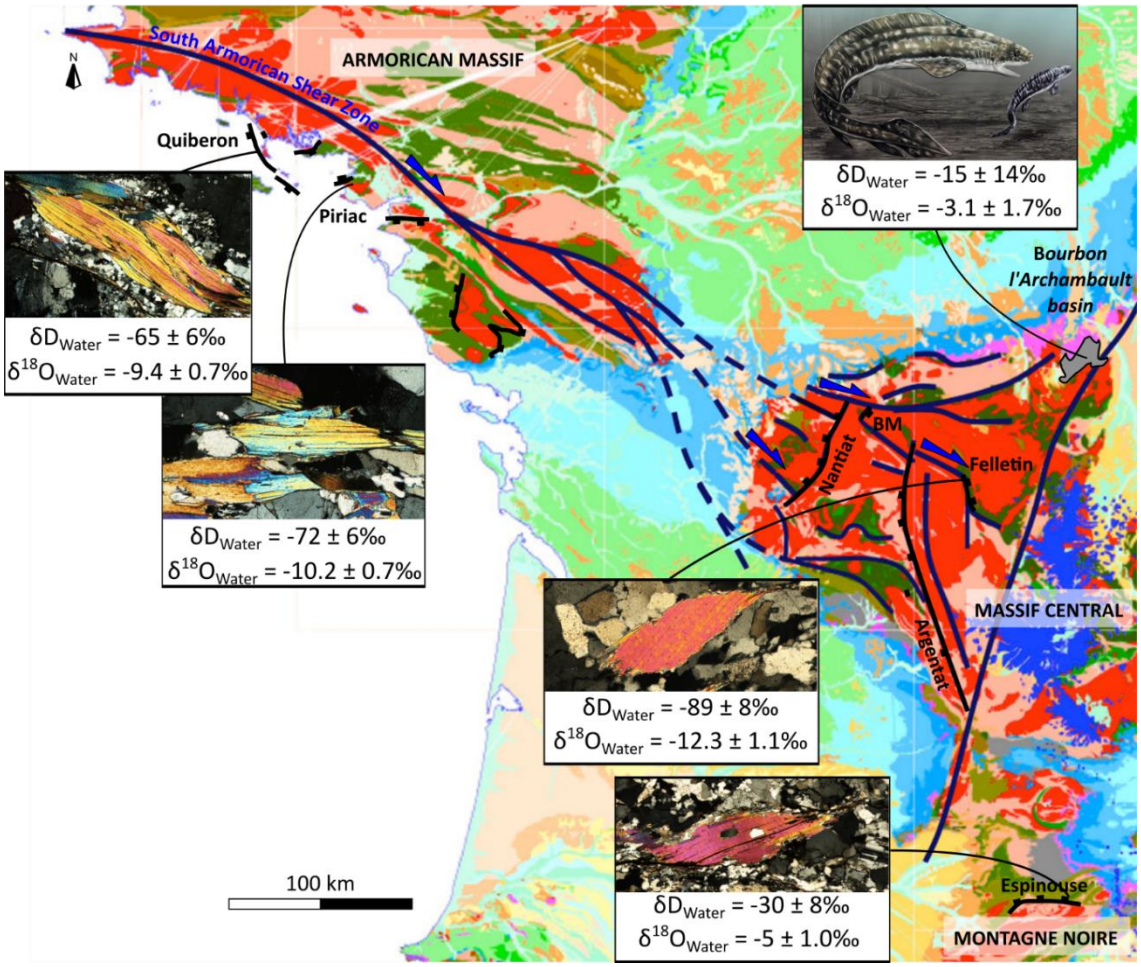

Figure V-9: Geological map of France showing the sampled proxies (hydrous silicates and shark remains) and associated average calculated δD_{water} and $\delta^{18}O_{water}$ values calculated in the hinterland of the Variscan Belt (Armorican Massif and French Massif Central) and the foreland (Montagne Noire and Bourbon l'Archambault basin). Black line: detachment shear zone. Purple line: strike-slip shear zone. Red: Variscan granite; Pink: Variscan terranes; Grey: Permo-Carboniferous basins.

Finally, the footwall of the Espinouse detachment in the Montagne Noire was sampled and the δD values of synkinematic biotite (δD_{Bt}) were measured. Combined with isotope exchange temperatures inferred from Raman Spectroscopy on

Carbonaceous Matter thermometry (566 ± 38°C; Fréville et al., 2016) and the calibration of biotite-water hydrogen isotope exchange (Suzuoki and Epstein, 1976; **Tables V-4 and V-5**), δD_{water} values as high as -23‰ with an average value of -30 ± 8‰ have been calculated (**Fig. V-9; Table V-6**).

2. Choice of the isotope lapse rate

Stable isotope ratios of precipitation systematically scale with elevation (modern lapse rate for mid to low latitude of ~22‰/km in δD or ~2.8‰/km in $\delta^{18}O$; Poage and Chamberlain, 2001; Quade et al., 2011). In the case of the Variscan belt of Western Europe, using this lapse rate would lead us to underestimate its paleoaltitude as paleomagnetic data indicate that it was located near by the Equator (**Fig. I-10; e.g.** Tait et al., 1996a, b, 1999, 2000; Zwing and Bachtadse, 2000; Domeier and Torsvik, 2014; Edel et al., 2018). Therefore, a modern lapse rate of ~−17‰/km in δD or ~−2.2‰/km in $\delta^{18}O$ calculated in Ecuador (Windhorst et al., 2013) seems to be more appropriate.

For the paleoaltimetry estimates, the two lapses rates discussed above were considered: (1) a low to middle latitude lapse rate of ~22‰/km in δD (or ~2.8‰/km in $\delta^{18}O$; Poage and Chamberlain, 2001; Quade et al., 2011) that will allow us to compare the results of this study with previous stable isotope paleoaltimetry studies; (2) an equatorial lapse rate of ~−17‰/km in δD (or ~−2.2‰/km in $\delta^{18}O$; Windhorst et al., 2013; **Figs. V-10 and V-11**) that seems to be more appropriate for the Variscan Belt of Western Europe.

Finally, the δD_{water} values were recast as $\delta^{18}O_{water}$ values, and vice-versa, by the means of the global meteoric water line ($\delta D = 8 \times \delta^{18}O + 10$, Craig, 1961; **Table V-7**) which has been assumed to be valid during the late-Palaeozoic period.

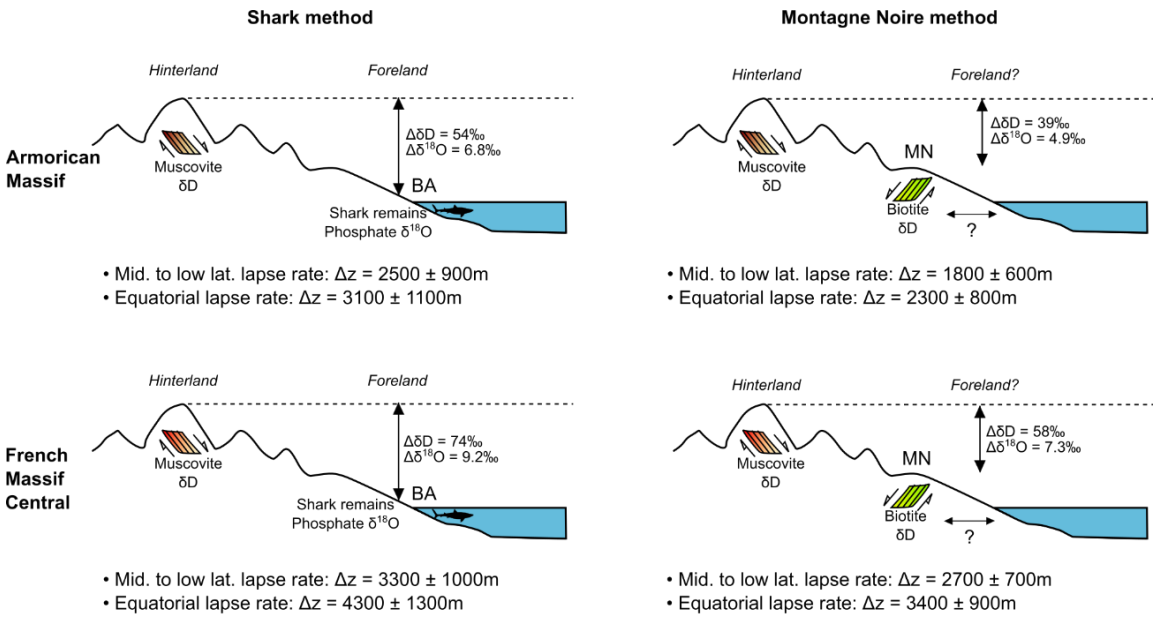

Figure V-10: Simplified late-Carboniferous paleoaltimetry reconstruction of the Armorican Massif (AM) and the French Massif Central (FMC) compared to foreland isotope record in the Montagne Noire (MN) and the Bourbon l'Archambault basin (BA). ΔδD are obtained by comparing the δD_{water} values calculated from the δD of muscovite from the Armorican Massif (Chapter III) and the French Massif Central (Chapter IV) in the internal zones with the ones from biotite in the Montagne Noire (Chapter IV) and from the $\delta^{18}O$ values of shark remains phosphate of sedimentary basins (Fischer et al., 2013) that are converted in δD using the meteoric water line of Craig (1961). Paleoaltitude reconstructions are based on isotope lapse rates of (1) ~22‰/km in δD for low to middle latitude (Poage and Chamberlain, 2001) and of (2) ~17‰/km in δD for at the equator (Windhorst et al., 2013).

3. Paleoaltitude estimates

a. French Massif Central

When comparing the hydrogen isotope record of precipitation preserved in the internal zones in the **French Massif Central** (δD_{water} value = -89‰ or $\delta^{18}O_{water}$ value = -12.3**‰**) with the one from the foreland using shark fossil from the Bourbon l'Archambault basin (δD_{water} value = -15‰ or $\delta^{18}O_{water}$ value = -3.1**‰**), the $\Delta\delta D_{water}$ is 74‰ and the $\Delta\delta^{18}O_{water}$ is 9.2‰. These values correspond to late-Carboniferous elevations of:

(1) 3300 ± 1000 m at low to mid-latitudes

(2) 4300 ± 1300 m at the equator (**Figs. V-10, V-11 and V-12; Table V-7**).

When comparing the hydrogen isotope records from the **French Massif Central** with those obtained from biotite of the Montagne Noire (δD_{water} value = -30‰ or

$\delta^{18}O_{water}$ value = -5.0‰), the $\Delta\delta D_{water}$ is 58‰ and the $\Delta\delta^{18}OD_{water}$ of 7.3‰. This is consistent with an elevation difference of:

(1) 2700 ± 700 m for mid-latitude
(2) 3400 ± 900 m at the equator (**Figs. V-10,V-11 and V-12; Table V-7**).

b. Armorican Massif

When comparing the hydrogen isotope record of precipitation preserved in the internal zones in the **Armorican Massif** (δD_{water} value = -70‰ or $\delta^{18}O_{water}$ value = -9.9‰) with the one obtained using shark fossil from the Bourbon l'Archambault basin (δD_{water} value = -15‰ or $\delta^{18}O_{water}$ value = -3.1‰), the $\Delta\delta D_{water}$ is 54‰ and the $\Delta\delta^{18}O_{water}$ of 6.8‰. It translates into an elevation difference of:

(1) 2500 ± 900m for mid-latitude
(2) 3100 ± 1100m at the equator.

When comparing the hydrogen isotope records from the **Armorican Massif** with those obtained from biotite of the Montagne Noire (δD_{water} value = -30‰ or $\delta^{18}O_{water}$ value = -5.0‰), the $\Delta\delta D_{water}$ is 39‰ and the $\Delta\delta^{18}OD_{water}$ is 4.9‰. This is consistent with an elevation difference of:

(1) 1800 ± 600 m for mid-latitude
(2) 2300 ± 800 m for low-latitude (**Figs. V-10,V-11 and V-12; Table V-7**).

The error estimate on elevation quantification includes the isotope analyses, the average of isotope ratios and the temperature estimates, but excludes uncertainty in the isotope lapse rate, which can attain ± 500 m for model elevations of ~3000 m (Rowley, 2007).

	Zone	Proxy	δD_{water} (‰)	Uncertainty (‰)	Average $\delta^{18}O_{water}$ (‰)	Uncertainty (‰)
Hinterland	AM - Armorican Massif	Muscovite	-70	6	-9.9	0.7
	MC - Massif Central	Muscovite	-89	8	-12.3	1.1
Foreland	MN - Montagne Noire	Biotite	-30	8	-5.0	1.0
	BA - Bourbon l'Archambault basin	Shark remains phosphate	-15	14	-3.1	1.7

δD

	Comparison with the Montagne Noire biotite				Comparison with the Bourbon shark remains		
Armorican Massif	*Considering a*	***22***	*‰/km gradient*	*Mid Latitude*	*Considering a*	***22***	*‰/km gradient*
	$\Delta\delta D_{water}$ AM-MN (‰)	**Elevation (m)**	Uncertainty (m)		$\Delta\delta D_{water}$ AM-BA (‰)	**Elevation (m)**	Uncertainty (m)
	39	**1782**	600		52	**2475**	900
	Considering a	***17***	*‰/km gradient*	*Low Latitude*	*Considering a*	***17***	*‰/km gradient*
	$\Delta\delta D_{water}$ AM-MN (‰)	**Elevation (m)**	Uncertainty (m)		$\Delta\delta D_{water}$ AM-BA (‰)	**Elevation (m)**	Uncertainty (m)
	39	**2269**	800		54	**3148**	1100
Massif Central	*Considering a*	***22***	*‰/km gradient*	*Mid Latitude*	*Considering a*	***22***	*‰/km gradient*
	$\Delta\delta D_{water}$ MC-MN (‰)	**Elevation (m)**	Uncertainty (m)		$\Delta\delta D_{water}$ MC-BA (‰)	**Elevation (m)**	Uncertainty (m)
	58	**2652**	700		74	**3344**	1000
	Considering a	***17***	*‰/km gradient*	*Low Latitude*	*Considering a*	***17***	*‰/km gradient*
	$\Delta\delta D_{water}$ MC-MN (‰)	**Elevation (m)**	Uncertainty (m)		$\Delta\delta D_{water}$ MC-BA (‰)	**Elevation (m)**	Uncertainty (m)
	58	**3372**	900		74	**4253**	1300

$\delta^{18}O$

	Comparision with the Montagne Noire biotite				Comparision with the Bourbon shark remains		
Armorican Massif	*Considering a*	***2,8***	*‰/km gradient*	*Mid Latitude*	*Considering a*	***2,8***	*‰/km gradient*
	$\Delta\delta^{18}O_{water}$ AM-MN (‰)	**Elevation (m)**	Uncertainty (m)		$\Delta\delta^{18}O_{water}$ AM-BA (‰)	**Elevation (m)**	Uncertainty (m)
	4.9	**1751**	600		6.8	**2431**	900
	Considering a	***2,2***	*‰/km gradient*	*Low Latitude*	*Considering a*	***2,2***	*‰/km gradient*
	$\Delta\delta^{18}O_{water}$ AM-MN (‰)	**Elevation (m)**	Uncertainty (m)		$\Delta\delta^{18}O_{water}$ AM-BA (‰)	**Elevation (m)**	Uncertainty (m)
	4.9	**2228**	800		6.8	**2955**	1100
Massif Central	*Considering a*	***2,8***	*‰/km gradient*	*Mid Latitude*	*Considering a*	***2,8***	*‰/km gradient*
	$\Delta\delta^{18}O_{water}$ MC-MN (‰)	**Elevation (m)**	Uncertainty (m)		$\Delta\delta^{18}O_{water}$ MC-BA (‰)	**Elevation (m)**	Uncertainty (m)
	7.3	**2604**	700		9.2	**3357**	1000
	Considering a	***2,2***	*‰/km gradient*	*Low Latitude*	*Considering a*	***2,2***	*‰/km gradient*
	$\Delta\delta^{18}O_{water}$ MC-MN (‰)	**Elevation (m)**	Uncertainty (m)		$\Delta\delta^{18}O_{water}$ MC-BA (‰)	**Elevation (m)**	Uncertainty (m)
	7.3	**3314**	900		9.2	**4273**	1200

Table V-7: Stable-isotope based paleoaltitude estimates of the Armorican Massif and the French Massif Central (proxy: muscovite) referend with age-equivalent isotope record in the Montagne Noire (proxy: biotite) and the Bourbon l'Archambault basin (proxy: shark remains). Calculations based on the lapse rate of Poage and Chamberlain (2001) for mid to low-latitude and Windhorst et al. (2013) at the equator. Conversion in δD_{water} or $\delta^{18}O_{water}$ values using the meteoric water line of Craig (1961).

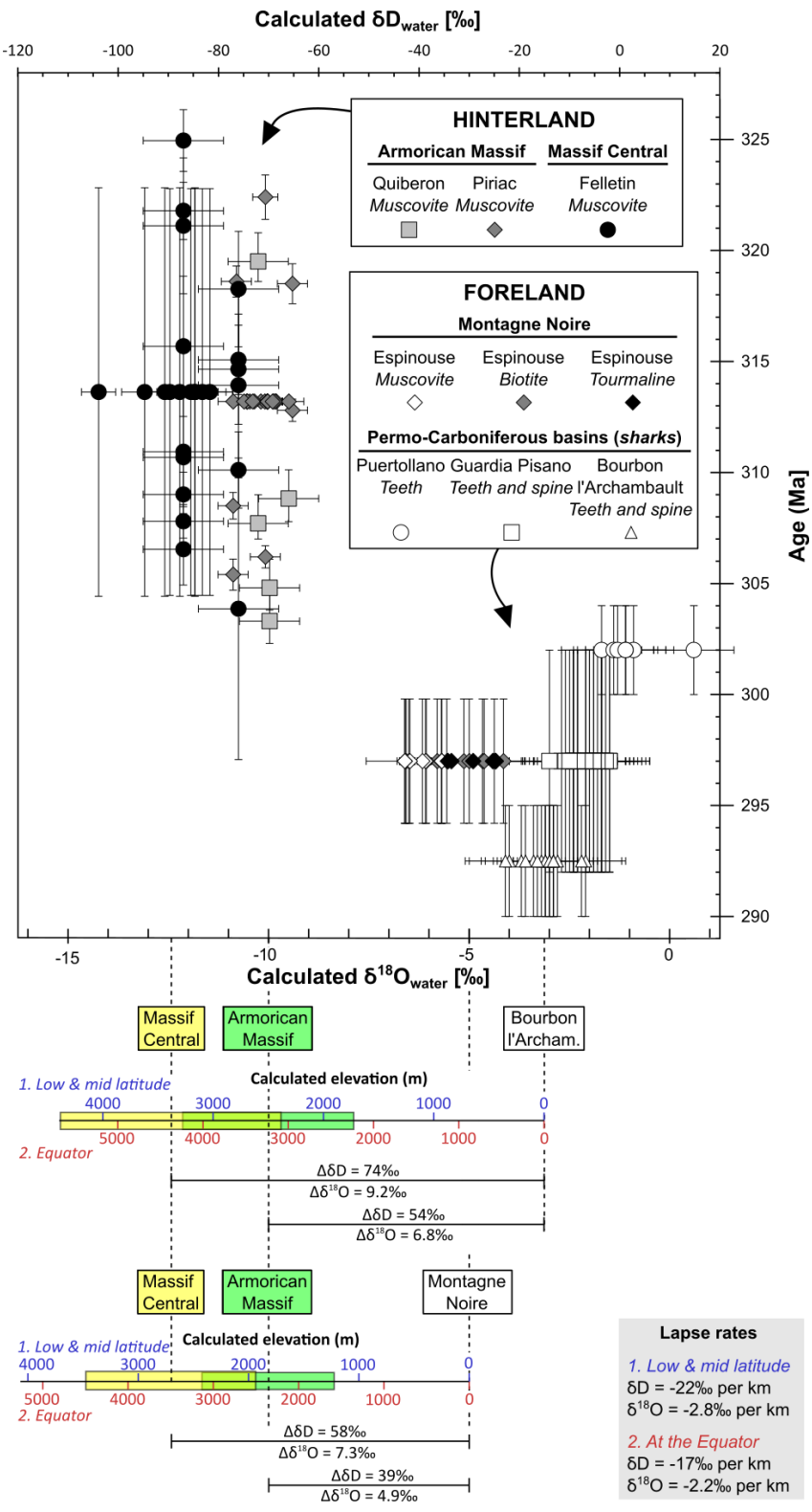

Figure V-11: Late-Carboniferous paleoaltimetry reconstruction of the Armorican Massif and the French Massif Central compared to foreland isotope records in the Montagne Noire and the Bourbon l'Archambault basin.

δD_{water} values are calculated from the δD of muscovite from the Armorican Massif (Chapter III), the French Massif Central (Chapter IV) and the Montagne Noire (Chapter IV) and the $\delta^{18}O$ of shark teeth phosphate of sedimentary basins (Fischer et al., 2013) that are converted in δD using the meteoric water line of Craig (1961).

Ages: Ar/Ar on synkinematic muscovite or biotite in the detachment footwalls of Quiberon and Piriac (Chapter IIII), Felletin (Gébelin, 2004), and Espinouse (Maluski et al., 1991); biostratigraphic and isotope geochronological data from the Permo-Carboniferous basins reported by Fischer et al. (2013).

Paleoaltitude estimates are based on the isotope lapse rates at (1) low to middle latitude (Poage and Chamberlain, 2001) and (2) the equator (Windhorst et al., 2013). Isotope and geochronology data and associated references are detailed in Tables VI-5 in the Appendix.

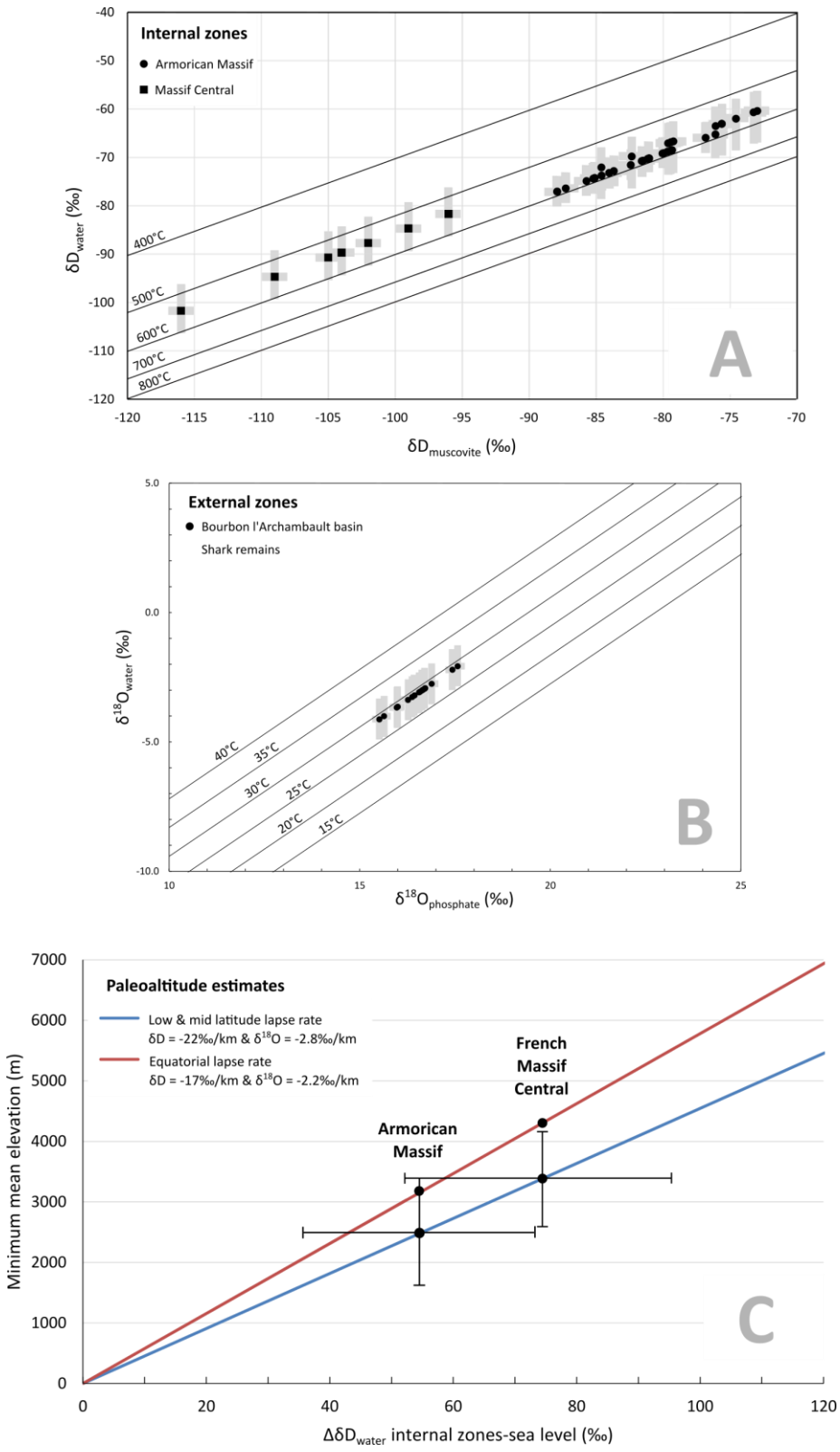

Figure V-12: Uncertainties for paleoaltitude estimate calculation. (A) Uncertainties of the hydrogen isotope composition of muscovite and temperature leading to the hydrogen isotope composition of the water in the internal zones of the belt; (B) Uncertainties of the oxygen isotope composition of shark remains and temperature leading to the oxygen isotope composition of the water in the external zones of the belt; (C) Paleoaltitude estimates uncertainties linked to the difference between the isotope composition of rainwater in the internal and external zones of the belt.

E. Discussion and conclusion

1. Uncertainties of paleoelevation estimates

The strength of the stable isotope paleoaltimetry study presented here is the comparison of age-equivalent stable isotope data from the hinterland assumed to represent a topographic high (Armorican Massif and Massif Central) with stable isotope data from the foreland located near sea level (Montagne Noire and foreland basins). The uncertainties associated with these paleoaltimetry estimates include:

a. Uncertainty of the isotope composition of meteoric waters (δD_{water} values)

The uncertainty in the calculated δD_{water} values depends on 3 parameters: (1) the precision of isotope analysis, (2) the temperature of isotope exchange and (3) the average of the isotope analyses. (see discussion in parts V - B, C and D). In summary, (1) the isotope analysis uncertainty does not exceed ± 2‰ for the δD_{proxy} values and (2) the temperature of isotope exchange, used to calibrate the fractionation factor between the proxy and the water, has an uncertainty that does not exceed ± 50°C that result in an uncertainty of maximum ± 5‰ for the δD_{water} values. In the case of the fossil sharks, the uncertainty of the water temperature (± 7°C) led to $\delta^{18}O_{water}$ values uncertainty up to ± 1.6‰. In addition, for the paleoaltitude calculations, (3) an average of the δD_{proxy} values with a standard deviation up to ± 7‰ was considered in the hinterland and in the foreland (**Figs. V-10, V-11 and V-12; Table V-7**).

(1) <u>Internal zones</u>

In the internal zones of the belt, muscovite that (re)crystallised at depth during high temperature deformation was analysed. For the paleoaltitude reconstructions, an average of -70 ± 6‰ for the δD of precipitation was considered, although δD_{water} values

as low as -77‰ were calculated in the southern Armorican domain. Similarly, δD_{water} values as low as -104‰ were determined in the French Massif Central, but an average value of -89 ± 8‰ was considered for this area. However, the downward penetration of deuterium-depleted meteoric fluids in the internal zones leads to an increase in δD_{water} values due to fluid-rock interaction. As a consequence, the δD_{water} values that were calculated from minerals that (re)crystallised at depth represents a maximum value that may have been potentially lower at the Earth's surface (e.g. Gébelin et al., 2012). Therefore, this study could have used the lowest calculated δD_{water} values (-104‰ in the French Massif Central and -77‰ in the southern Armorican domain) that approximate most closely the isotope composition of meteoric water at the surface in these two areas. Considering these lowest values instead of the averages would result in increasing the paleoaltitude estimates by 300 to 900 m.

(2) External zones

In the foreland of the French Variscan Belt, two proxies were chosen: (1) freshwater shark remains from the Bourbon l'Archambault basin and (2) biotite from the Espinouse detachment in the Montagne Noire.

(1) In the Bourbon l'Archambault basin, the sharks evolved in lacustrine to fluvial environments connected to the ocean (e.g. Fischer et al., 2013). The paralic foreland basin was situated at an altitude close to sea level (e.g. Fischer et al., 2013). Therefore, the average $\delta^{18}O_{water}$ values calculated from the $\delta^{18}O_{Phosphate}$ values of the sharks teeth and spines were considered to represent the average isotopic composition of meteoric water near sea level in the Northern part of the French Massif Central. However, these ~295 to 290 Ma δD_{water} values obtained from the Bourbon l'Archambault shark remains are the lowest δD_{water} values recorded over the European late-Carboniferous to early-

Permian basins (**Fig. V-11**). The comparison of the ~320 to 300 Ma hinterland records of precipitation from this study with the ~305 to 295 Ma $\delta^{18}O_{water}$ values calculated in the Guardia Pisano (Italy) and the Puertollano (Spain) basins (average $\delta^{18}O_{water}$ values = -2.1‰ and -1.0‰; **Table V-5**) would lead to higher paleoelevation estimates of up to +1000 m.

(2) In the Montagne Noire, the average δD_{water} value of -30 ± 8‰ could be interpreted as: (1) near sea level precipitation, or (2) metamorphic fluids. Assuming that this value reflect a meteoric fluid signature sourced at low elevation, the mixing of crustal fluids ($\delta D \leq -20‰$) with these low-altitude meteoric fluids would have led to an increase in the δD_{Bt} values at the top of the footwall. Therefore, the highest calculated δD_{water} values (-23‰) in the Espinouse detachment would approximate most closely the isotope composition of precipitation at the surface. Considering this value as a reference for near sea level precipitation instead of the average δD_{water} value (-30 ± 8‰) would increase the paleoaltitude estimates by 400m.

Referencing the hydrogen isotope record from the hinterland with those obtained from the Montagne Noire foreland proxy lead to paleoaltitudes estimates that are ~700 to 900 m lower the paleoelevations obtained by comparison with the Bourbon l'Archambault sharks. This suggests that, in agreement with previous studies ,the Montagne Noire was located at the transition between the Variscan hinterland to the north and the foreland to the south (**Fig. V-10 and V-11**; e.g. Faure, 1995; Faure et al., 2009; Whitney et al., 2015).

b. Uncertainty of the lapse rate

The paleomagnetic data indicate that the Variscan Belt of Western Europe was located near the Equator (**Fig. I-10**; Tait et al., 1996a, b, 1999, 2000; Zwing and Bachtadse, 2000; Domeier and Torsvik, 2014; Edel et al., 2018) where 65% of the evaporation occurs

before air masses get transported to the poles (e.g. Rozanski et al., 1993; Blisniuk and Stern, 2005). Therefore, the isotope composition of meteoric water tends to increase with decreasing latitude (e.g. Rozanski et al., 1993; Blisniuk and Stern, 2005). In addition, the late Palaeozoic glacial age (~340-300 Ma) was one of the prominent glacial event in Earth history with an apex of glaciation at the Carboniferous-Permian boundary (Montañez and Poulsen, 2013). Indeed, the Southern part of Gondwana was covered by thick ice sheets that are believe to be 40% more extensive than today (**Fig. I-10**; Du Toit, 1921; Martin, 1975; Banks, 1985; Visser, 1987a,b; González-Bonorino and Eyles, 1995). As a consequence, an increase of +1.5‰ in the $\delta^{18}O$ values (or +12‰ in the δD values) of ocean waters is expected as light isotopes (^{1}H and ^{16}O) preferentially concentrate in continental glaciers (Buggisch et al., 2008). These paleoenvironmental conditions would lead to a lower lapse rate between the isotope composition of meteoric water and elevation (Poulsen and Jeffery, 2011).

Therefore, two different modern lapse rates were considered to bracket the paleoaltitude estimations: (1) the lapse rate of Poage and Chamberlain (2001) obtained at mid to low latitude and (2) the equatorial lapse rate of Windhorst et al. (2013) (**Figs. V-10,V-11 and V-12; Table V-7**). Both lapse rates resulted in similar paleoaltitude estimates within uncertainty. However, the equatorial lapse rate of ~17‰/km in δD values (Windhorst et al., 2013) gives paleoaltitude estimates that are ~400 to 900 m higher than the ones calculated with the low to mid latitude lapse rate (~22‰/km in δD; Poage and Chamberlain, 2001).

c. Paleoaltitude estimates of the French Variscan Massifs

The paleoaltitudes that will be discussed in the following section are the ones estimated using the isotopic lapse rate of Poage and Chamberlain (2001) that has been calculated based on 68 studies conducted in many of the world's mountain belts located at low to mid-latitudes. The higher paleoaltitude estimates calculated using the lower isotope lapse rate calculated at the equator by Windhorst et al. (2013) provide an upper limit regarding the paleoaltitude of the Variscan Belt of Western Europe (**Fig. V-12**).

The paleoaltitude obtained by comparison between the hinterland isotope records of precipitation with the one obtained in the foreland from shark remains of the Bourbon l'Archambault basin will be discussed. Indeed, the sharks teeth and spines allow recovering directly the average isotopic composition of meteoric water near sea level in the northern part of the French Massif Central, whereas the paleogeography of the Montagne Noire is less constrained (including its position relative to the Sillon Houiller fault and to the foreland itself, see discussion above).

In conclusion, this study argues that the paleoelevation estimates using the l**apse rate of Poage and Chamberlain (2001)** and referencing the **hinterland records** to the **Bourbon l'Archambault record** reflect **minimum mean elevations** despite all the above potential biases, and taking into account the above parameters that may have changed the isotope composition of Variscan rainfall. This study therefore estimates the following minimum mean paleoelevation (**Figs. V-10, V-11 and V-12; Table V-7**):

- **2500 ± 900 m for the Armorican Massif (southern Armorican domain);**
- **3300 ± 1000 m for the French Massif Central (Limousin).**

2. Paleoaltitude of the Variscan Belt of Western Europe

a. Comparison with stable isotope paleoaltimetry studies of other orogens

The results from the present study fall within the same range as the calculated mean Miocene paleoaltitudes of 1850 - 3050m in the European Alps of Campani et al. (2012), obtained by comparing the δD values of precipitation recovered from chlorite in the Simplon fault (δD_{water} ~ -107‰) to those obtained from carbonate nodules in the North Alpine foreland basin (δD_{water} ~ -69 to -61‰). In comparison, this study's elevation estimates are much lower than the 5100–5400m calculated in the Himalayas during the Miocene (Gébelin et al., 2013), obtained by referencing the rainfalls isotope compositions calculated from muscovite from the South Tibetan Detachment (δD_{water} ~ 156‰) to age-equivalent $\delta^{18}O$ values of foreland basin paleosols (δD_{water} ~ -36‰).

b. Comparison with the fossil record and paleoclimate modelling

The late-Carboniferous minimum mean elevations of 2500 ± 900 m calculated for the Armorican Massif and 3300 ± 1000 m for the Massif Central points to a subdued elevation. These results agree with the uniform flora (mostly fern-type plants) found in the late-Carboniferous/early-Permian coal-bearing basins of the European Variscan belt. Some of these basins located in the foreland during the Late Carboniferous also preserved fossils of shark species, whose distribution was consistent in all the European basins (e.g. Schneider et al., 2000). The shark taxa distribution became more diverse during the Early Permian as various types of sharks (diadromous to marine) were preserved in the European basins (Fischer et al., 2010, 2013). To conclude, in agreement with the results of this study, the European basins do not show any significant evidence of high topography-related differentiation and argue for "Alpine-type" elevation during

the end of the Carboniferous (e.g. Franke and Engel, 1986; Kerp, 2000; Fischer et al., 2013; Franke, 2014).

This study's paleoaltitude estimates of ~2500 and ~3300 m also fit well with paleoclimate studies. Indeed, the Late Permian atmospheric general circulation model of Fluteau et al. (2001) favours a mean elevation of ~2000 to 3000 m for the Variscan belt of Europe. In their model, for any configuration of Pangea, a Variscan paleoaltitude of ~2000 m is needed to account for the arid climate of Laurussia to the north of the E-W trending Variscan Belt (Fluteau et al., 2001). Indeed, the presence of a subdued-altitude range would still allow the deflection of the moisture coming from the Tethys ocean to the south of the Variscan orogen (Fluteau et al., 2001). Based on denudation rates inferred from stratigraphic correlations, Roscher and Schneider (2006) argued for a mean Variscan elevation of ~2000 m that falls within the uncertainty window suggested by this study. However, in contrast to Fluteau et al. (2001), Roscher and Schneider (2006) argue that the Variscan Belt has never reached a sufficient elevation to trigger an orographic rain shadow, explaining the progressive aridification of Laurussia by the closure of the Rheic ocean.

c. Comparison with geodynamic models

This study's paleoaltitude estimates (2500 ± 900 m for the AM and 3300 ± 1000 m for the FMC) are in good agreement with crustal thickening evidenced by the discovery of nappes stacking and of high-pressure metamorphism that occurred from the Late Carboniferous to the Early Devonian in both massifs (e.g. Ledru et al., 1989; Aerden and Malavieille, 1999; Matte, 2001, 2007; Lotout et al., 2018). Indeed, the Variscan belt displays tectonic similarities with the Himalaya-Tibet orogen as a result of collision tectonics such as leucogranite emplacement within large-scale ductile shear zones (e.g.

Dewey and Burke, 1973; Mattauer, 1986; Mattauer et al., 1988; Ménard and Molnar, 1988; Matte, 2001; Dörr and Zulauf, 2010). However, the topography estimates are not comparable to the modern mean elevation of the Himalayan range (~5200 m at the longitude of Mount Everest).

One explanation lies in the development of orogen-parallel extensional faults and strike-slip shear zones that could have counterbalanced crustal thickening (e.g. Lardeaux et al., 2001; Franke, 2014). Indeed, large-scale NW-SE dextral shear zones (such as the South Armorican Shear Zone or la Marche shear zone) developed as a result of tectonic escape during the late Carboniferous (e.g. Matte, 1986; Gébelin et al., 2007; Rolin et al., 2009; Augier et al., 2015). At the same time, widespread syn- to post-orogenic NW-SE extension is recorded by laccolith leucogranite emplacement along low-angle detachment shear zones and exhumation of partially molten crust in migmatite domes (e.g. Malavieille et al., 1990; Faure, 1995; Gébelin, 2004, 2009; Rolin et al., 2009; Faure et al., 2009; Turrillot et al., 2011; Tartèse et al., 2012; Lardeaux et al., 2014; Ballouard et al., 2015; Gapais et al., 2015). However, many topographic highs exceed 8000m of altitude in the Himalayas, despite similar structures such as the strike-slip Red River Fault (e.g. Searle, 2006), the E-W striking South Tibetan detachment (e.g. Chi-Hsiang and Shih-Tseng, 1978; Burchfiel and Royden, 1985; Carosi et al., 1998) and N-S striking normal faults perpendicular to the trend of the Himalayan orogen (e.g. Jessup and Cottle, 2010). Despite some similarities, these structures also found in the Variscan are not sufficient to explain the subdued elevation of the AM and FMC estimated in this study.

An explanation for the results of this study is the material rheology during the Late Carboniferous: the Variscan belt is often described as a “hot orogen” (e.g. Lardeaux et al., 2001; Chardon et al., 2009; Franke, 2014). The high Variscan geothermal gradient

(35°C/km; e.g. Vigneresse and Burg, 2003) and the low viscosity of crustal materials would have triggered deformation mechanisms associated with plastic flow. Indeed, the Archean ultra-hot crust accommodated strain through a different type of of tectonics ("dome and keel"), where crustal thickening was evenly distributed, homogeneous over long distances but limited with flat interfaces, lateral flow and gravitational spreading (e.g. Chardon et al., 1996, 2009; Cagnard, 2005). In contrast, the modern cold crust accommodates collision tectonics along narrow but elevated orogens that allow the juxtaposition of highly contrasting metamorphic rocks.

In conclusion, the paleoaltitude of ~2500 - 3300 m estimated in this study for the Palaeozoic Variscan Belt argue for an intermediate model between Archean and modern tectonics, where the continental collisions were accommodated by a mix of density contrasts and tectonic movements that would have not allowed Himalayan-type elevations. Therefore, the rheology of the crust would have allowed only narrow thickened zones along shear zones or active margin (Franke, 2014; Franke et al., 2017), such as the southern Armorican domain and the Limousin.

VI. APPENDICES

This chapter includes supplementary material for Chapters III, IV and V:

Table VI-1. Result tables of Ar/Ar geochronology on muscovite from the Quiberon detachment footwall (discussed in **Chapter III-B**).

Table VI-2. Result tables of Ar/Ar geochronology and trace elements of monazite from Port-Navalo migmatite below the Quiberon detachment footwall (discussed in **Chapter III-B**).

Table VI-3. Fluid inclusions microthermometry results for samples QUIB03, QUIB07, PIR01, PIR06 and PIR16 (discussed in **Chapter III-C**).

Table VI-4. Result tables of microprobe analysis of muscovite grains from the NE corner of the Millevaches Massif (French Massif Central) and calculation of temperature using the Ti-in-Ms geothermometer (discussed in **Chapter IV**).

Table VI-5. **Isotope and geochronology data** used to build the graph of **Figure V-11**.

Table VI-1: $^{40}Ar/^{39}Ar$ muscovite step heating data from mylonitic leucogranite of the footwall of Quiberon detachment zone (1/3)

QUIB01 Muscovite		J parameter		error J		Mass Discrimination (1+e)		Err Discrimination								
		2,76E-02		1,14E-04		1,007978		1,32E-03								
Laser power	^{40}Ar	Error ^{40}Ar	^{39}Ar	Error ^{39}Ar	^{38}Ar	Error ^{38}Ar	^{37}Ar	Error ^{37}Ar	^{36}Ar	Error ^{36}Ar	$^{40}Ar^*/^{39}Ar_K$	Error $^{40}Ar^*/^{39}Ar_K$	Apparent age (My)	Error Age (My)	Delay to irradiation (day)
280	255.545034	0.403286	14.402492	0.047867	0.000001	0.016572	0.015417	0.021433	0.770531	0.016444	2.345477	0.355844	113.6	16.7	326.2
330	137.375000	0.179805	13.334150	0.083972	0.000001	0.033689	0.000001	0.030111	0.203545	0.017500	5.918678	0.410386	273.9	17.7	326.2
360	180.030537	0.263747	24.598807	0.068691	0.000001	0.017944	0.000051	0.018513	0.070978	0.012159	6.518824	0.153466	299.5	6.6	326.3
390	143.353241	0.154360	19.885900	0.060761	0.000001	0.019464	0.000001	0.026140	0.035960	0.015698	6.721500	0.245507	308.1	10.4	326.3
400	147.640595	0.237346	20.931277	0.045744	0.000001	0.014571	0.039845	0.018358	0.039162	0.012090	6.667706	0.178442	305.8	7.7	326.3
430	445.350368	0.506812	64.807842	0.132840	0.000001	0.018901	0.000001	0.032727	0.044492	0.017153	6.708938	0.085451	307.6	3.9	326.3
440	413.060014	0.504543	60.702175	0.134315	0.008620	0.024727	0.055686	0.031453	0.036110	0.015759	6.726224	0.084691	308.3	3.8	326.3
460	794.779944	0.898278	117.558239	0.062735	0.000001	0.016187	0.039753	0.018042	0.049214	0.016212	6.696532	0.043203	307.0	2.3	326.4
490	1289.310573	0.823835	181.201349	0.180843	0.000504	0.028623	0.000001	0.030204	0.288553	0.016757	6.690306	0.032077	306.8	1.9	326.4
550	1684.105321	1.902628	252.102150	0.049202	0.000001	0.012411	0.036987	0.023236	0.034885	0.012697	6.684978	0.019778	306.6	1.6	326.4
560	26747.902919	13.348384	3994.804737	1.741449	0.000001	0.020735	0.194222	0.030341	0.246640	0.019121	6.716558	0.010200	307.9	1.5	326.5
590	4280.941815	2.833848	642.094409	0.388756	0.000001	0.019552	0.023534	0.032940	0.078457	0.011413	6.669526	0.012498	305.9	1.5	327.1
700	9802.012750	3.484397	1471.604473	0.652592	0.000001	0.021853	0.162777	0.037005	0.119394	0.009357	6.679800	0.010096	306.3	1.4	327.1
900	15305.866702	10.083013	2287.133237	2.100116	0.000001	0.013113	0.140531	0.025102	0.174800	0.017409	6.709587	0.012046	307.6	1.5	327.1
1100	5032.071524	2.625916	754.518737	0.597008	0.003763	0.021697	0.037061	0.022248	0.062850	0.015052	6.683748	0.012620	306.5	1.5	327.1
Fusion	12474.267680	5.955269	1856.387998	1.157473	0.000001	0.017311	0.077576	0.031440	0.092068	0.014668	6.743769	0.010811	309.0	1.5	327.2

Table VI-1: 40Ar/39Ar muscovite step heating data from mylonitic leucogranite of the footwall of Quiberon detachment zone (2/3)

QUIB01 Muscovite		J parameter		error J		Mass Discrimination (1+e)		Err Discrimination							
		2.76E-02		1.14E-04		1.007978		1.32E-03							
laser power	^{40}Ar	Error ^{40}Ar	^{39}Ar	Error ^{39}Ar	^{38}Ar	Error ^{38}Ar	^{37}Ar	Error ^{37}Ar	^{36}Ar	Error ^{36}Ar	$^{40}Ar^*/^{39}Ar_K$	Error $^{40}Ar^*/^{39}Ar_K$	Apparent age (My)	Error Age (My)	Delay to irradiation (day)
280	75.806313	0.149606	7.221265	0.051852	0.000001	0.019863	0.000001	0.031184	0.076948	0.021629	7.455685	0.917356	338.8	38.0	327.2
330	143.947594	0.119259	18.404572	0.060677	0.000001	0.010697	0.020261	0.025414	0.059428	0.014298	6.995417	0.244690	319.6	10.3	327.2
350	390.774767	0.775506	53.746927	0.122199	0.000001	0.016134	0.000001	0.016924	0.057522	0.015206	6.998359	0.088152	319.7	4.0	327.3
360	274.229976	0.497814	32.365916	0.156020	0.000001	0.012553	0.000001	0.016795	0.165304	0.015637	7.033106	0.150186	321.2	6.4	327.3
390	1293.621823	1.491861	180.591361	0.190789	0.000001	0.024026	0.000001	0.026851	0.135057	0.012633	6.984123	0.027187	319.1	1.8	327.3
410	107.541633	0.204595	15.175038	0.039091	0.003863	0.021237	0.001898	0.022849	0.000001	0.020577	7.132856	0.407124	325.3	17.1	327.3
500	2559.931604	2.698463	364.597315	0.714352	0.000001	0.021468	0.015761	0.027578	0.093263	0.016495	6.987240	0.023099	319.3	1.7	327.4
Fusion	2954.026095	2.761252	420.695639	0.354966	0.000001	0.022382	0.033739	0.024278	0.089099	0.014889	7.002950	0.017074	319.9	1.6	327.4

QUIB03 Muscovite		J parameter		error J		Mass Discrimination (1+e)		Err Discrimination							
		2.76E-02		1.14E-04		1.007978		1.32E-03							
laser power	^{40}Ar	Error ^{40}Ar	^{39}Ar	Error ^{39}Ar	^{38}Ar	Error ^{38}Ar	^{37}Ar	Error ^{37}Ar	^{36}Ar	Error ^{36}Ar	$^{40}Ar^*/^{39}Ar_K$	Error $^{40}Ar^*/^{39}Ar_K$	Apparent age (My)	Error Age (My)	Delay to irradiation (day)
280	103.560052	0.157668	9.811209	0.046761	0.000001	0.014428	0.001664	0.019557	0.172322	0.018466	5.515032	0.564145	256.0	24.4	327.4
350	115.772051	0.117300	16.615895	0.046006	0.012282	0.018532	0.023358	0.017106	0.048402	0.014072	6.248333	0.256317	287.4	11.0	327.4
370	1974.923056	1.862449	294.957972	0.317916	0.000001	0.020675	0.068016	0.021025	0.089816	0.023186	6.657672	0.026883	304.7	1.8	327.5
420	438.752711	0.552050	65.856870	0.086805	0.000001	0.019703	0.000001	0.021212	0.000001	0.010738	6.697694	0.054081	306.4	2.7	328.1
470	580.123758	0.286542	87.503576	0.139554	0.013046	0.020934	0.020473	0.028615	0.006135	0.014864	6.659983	0.055729	304.8	2.7	328.1
Fusion	1212.653658	0.776786	181.188236	0.154938	0.000151	0.017138	0.042835	0.017799	0.060671	0.012721	6.646541	0.024430	304.3	1.7	328.1

Table VI-1: 40Ar/39Ar muscovite step heating data from mylonitic leucogranite of the footwall of Quiberon detachment zone (3/3)

QUIB03 Muscovite		J parameter		error J		Mass Discrimination (1+e)		Err Discrimination							
		2.76E-02		1.14E-04		1.007978		1.32E-03							
laser power	^{40}Ar	Error ^{40}Ar	^{39}Ar	Error ^{39}Ar	^{38}Ar	Error ^{38}Ar	^{37}Ar	Error ^{37}Ar	^{36}Ar	Error ^{36}Ar	$^{40}Ar^*/^{39}Ar_K$	Error $^{40}Ar^*/^{39}Ar_K$	Apparent age (My)	Error Age (My)	Delay to irradiation (day)
280	163.194140	0.233158	19.554194	0.030023	0.000001	0.032593	0.000001	0.025239	0.120635	0.014670	6.596364	0.235308	302.2	10.0	328.1
350	285.695948	0.264367	41.900289	0.094537	0.009342	0.020071	0.023842	0.022973	0.046066	0.008345	6.572429	0.070850	301.1	3.3	328.2
380	198.063872	0.439558	26.490224	0.045347	0.000001	0.018182	0.020427	0.028926	0.085573	0.015446	6.628029	0.185824	303.5	8.0	328.2
400	2848.065124	4.163100	425.322465	0.457266	0.000001	0.019455	0.012635	0.030262	0.133533	0.016082	6.642545	0.019445	304.1	1.6	328.2
430	365.479555	0.419926	54.785413	0.080519	0.002388	0.021114	0.023367	0.029353	0.023195	0.031261	6.611532	0.170426	302.8	7.3	328.2
510	1542.909876	1.185632	233.228676	0.266362	0.000001	0.019675	0.016746	0.035908	0.023241	0.016074	6.626376	0.025863	303.4	1.8	328.3
Fusion	721.109509	0.490489	108.738708	0.118001	0.000001	0.018792	0.000001	0.031332	0.026606	0.015050	6.595701	0.046222	302.1	2.4	328.3

Table VI-2: U-Th/Pb geochronology monazite data from Port Navalo migmatite. Uncertainties include instrumental drift and were increased in quadrature to include 2% reproducibility of the secondary reference material. Isoplot function ^{207}Pb-corrected $^{206}Pb/^{238}U$ dates are reported (Compston et al., 1992) (1/2)

	Ratios											Ages (Ma)									
	$^{238}U/^{206}Pb$	$2\sigma^1$	$^{207}Pb/^{206}Pb$	$2\sigma^1$	$^{207}Pb/^{235}U$	$2\sigma^1$	$^{206}Pb/^{238}U$	$2\sigma^1$	Rho	$^{208}Pb/^{232}Th$	$2\sigma^1$	$^{207}Pb/^{206}Pb$	$2\sigma^1$	$^{206}Pb/^{238}U$	$2\sigma^1$	$^{207}Pb/^{235}U$	$2\sigma^1$	$^{208}Pb/^{232}Th$	$2\sigma^1$	age7corr[2]	$2\sigma^1$
NAV04_mnz1182A	21.97	0.61	0.0525	0.0023	0.333	0.02	0.0455	0.001	0.403	0.0148	0.0004	306.4	98.0	287.0	7.8	291.9	11.7	296.4	7.0	286.8	0.4
NAV04_mnz1399A	20.19	0.57	0.0534	0.0024	0.357	0.02	0.0495	0.001	0.425	0.0154	0.0004	345.0	99.8	311.6	8.6	310.3	12.4	308.1	7.5	311.3	0.4
NAV04_mnz1399B	20.86	0.60	0.0535	0.0024	0.351	0.02	0.0479	0.001	0.302	0.0151	0.0004	350.1	103.4	301.9	8.5	305.3	13.0	302.3	7.3	301.4	0.4
NAV04_mnz1410A	21.19	0.60	0.0535	0.0024	0.350	0.02	0.0472	0.001	0.265	0.0154	0.0004	350.1	103.4	297.2	8.2	304.4	12.4	308.1	7.4	296.8	0.4
NAV04_mnz1410B	20.56	0.58	0.0529	0.0024	0.354	0.02	0.0486	0.001	0.456	0.0155	0.0004	324.5	100.9	306.2	8.4	308.0	12.4	309.9	7.4	306.0	0.4
NAV04_mnz1410C	21.08	0.59	0.0531	0.0024	0.345	0.02	0.0474	0.001	0.457	0.0154	0.0004	333.5	100.5	298.7	8.2	301.2	12.4	309.1	7.3	298.4	0.4
NAV04_mnz1646B	20.40	0.61	0.0528	0.0024	0.355	0.02	0.0490	0.001	0.532	0.0153	0.0004	320.2	101.2	308.4	9.0	308.1	13.0	307.5	7.7	308.3	0.4
NAV04_mnz1646C	20.29	0.57	0.0537	0.0024	0.364	0.02	0.0493	0.001	0.390	0.0156	0.0004	358.9	99.1	310.1	8.4	315.3	12.3	312.9	7.5	309.7	0.4
NAV04_mnz1646D	20.19	0.57	0.0526	0.0023	0.360	0.02	0.0495	0.001	0.321	0.0153	0.0004	312.4	101.6	311.6	8.6	311.9	12.3	306.7	7.9	311.6	0.4
NAV04_mnz2014A	21.07	0.60	0.0524	0.0023	0.340	0.02	0.0475	0.001	0.348	0.0149	0.0004	302.5	102.1	298.9	8.3	297.2	11.7	299.3	7.0	298.9	0.4
NAV04_mnz2014B	21.09	0.65	0.0542	0.0025	0.350	0.02	0.0474	0.001	0.494	0.0151	0.0004	379.4	105.5	298.6	8.9	304.9	13.1	303.7	8.8	297.9	0.4
NAV04_mnz2045A	20.69	0.66	0.0528	0.0024	0.352	0.02	0.0483	0.002	0.545	0.0159	0.0004	320.2	105.0	304.3	9.5	305.9	13.0	318.6	8.2	304.1	0.5
NAV04_mnz2045B	21.28	0.57	0.0526	0.0023	0.341	0.02	0.0470	0.001	0.287	0.0155	0.0004	313.3	97.7	296.1	7.8	298.0	11.7	311.5	7.2	295.9	0.4
NAV04_mnz2048A	20.06	0.57	0.0536	0.0024	0.364	0.02	0.0498	0.001	0.396	0.0158	0.0004	355.1	99.3	313.5	8.7	315.2	13.0	317.5	7.7	313.2	0.4
NAV04_mnz2048B	20.38	0.56	0.0528	0.0024	0.353	0.02	0.0491	0.001	0.312	0.0157	0.0004	321.1	101.1	308.7	8.3	307.0	12.4	314.5	7.2	308.6	0.4
NAV04_mnz2080A	20.46	0.62	0.0530	0.0024	0.355	0.02	0.0489	0.001	0.471	0.0154	0.0004	328.8	104.5	307.6	9.0	308.2	13.0	308.1	7.9	307.4	0.4
NAV04_mnz2080B	20.00	0.57	0.0531	0.0024	0.363	0.02	0.0500	0.001	0.372	0.0156	0.0004	333.1	100.5	314.5	8.7	314.5	13.0	312.3	8.2	314.4	0.4
NAV04_mnz2245A	19.88	0.55	0.0551	0.0025	0.377	0.02	0.0503	0.001	0.294	0.0158	0.0004	416.3	99.8	316.4	8.6	325.0	13.0	317.5	7.7	315.5	0.4
NAV04_mnz2245B	19.89	0.59	0.0526	0.0023	0.362	0.02	0.0503	0.001	0.458	0.0157	0.0004	311.6	101.6	316.2	9.1	313.4	13.0	315.3	8.9	316.3	0.5
NAV04_mnz2245C	20.08	0.56	0.0531	0.0023	0.361	0.02	0.0498	0.001	0.430	0.0159	0.0004	334.8	96.6	313.3	8.6	312.7	12.3	318.8	7.5	313.1	0.4
NAV04_mnz2318	20.47	0.59	0.0532	0.0024	0.360	0.02	0.0489	0.001	0.369	0.0154	0.0004	339.0	100.2	307.5	8.6	311.8	12.3	307.9	7.8	307.2	0.4
NAV04_mnz2395A	20.31	0.56	0.0533	0.0024	0.357	0.02	0.0492	0.001	0.267	0.0160	0.0004	339.5	100.1	309.9	8.4	309.7	12.4	319.8	7.6	309.6	0.4
NAV04_mnz2395B	19.77	0.54	0.0533	0.0024	0.367	0.02	0.0506	0.001	0.274	0.0161	0.0004	341.2	100.0	318.1	8.4	317.1	12.3	322.0	7.7	317.9	0.4
NAV04_mnz2592A	20.19	0.57	0.0543	0.0024	0.369	0.02	0.0495	0.001	0.420	0.0156	0.0004	383.5	97.8	311.7	8.6	318.6	13.0	313.1	7.4	311.1	0.4
NAV04_mnz2913A	20.26	0.56	0.0533	0.0024	0.357	0.02	0.0494	0.001	0.181	0.0158	0.0004	341.2	100.0	310.5	8.3	309.6	12.4	316.7	7.7	310.3	0.4
NAV04_mnz2913B	20.59	0.56	0.0529	0.0023	0.349	0.02	0.0486	0.001	0.460	0.0155	0.0004	325.8	97.1	305.7	8.1	304.2	11.7	311.5	7.4	305.5	0.4
NAV04_mnz3007A	20.07	0.54	0.0536	0.0024	0.362	0.02	0.0498	0.001	0.379	0.0162	0.0004	354.3	99.4	313.5	8.3	314.0	12.3	324.4	7.8	313.1	0.4
NAV04_mnz3007B	20.30	0.56	0.0530	0.0023	0.355	0.02	0.0493	0.001	0.293	0.0156	0.0004	328.4	96.9	309.9	8.3	308.3	12.4	313.5	7.6	309.8	0.4
NAV04_mnz3028A	21.40	0.60	0.0532	0.0024	0.346	0.02	0.0467	0.001	0.339	0.0152	0.0004	337.3	100.3	294.4	8.1	301.4	12.4	305.3	7.5	294.0	0.4
NAV04_mnz3028B	20.70	0.58	0.0527	0.0023	0.355	0.02	0.0483	0.001	0.439	0.0156	0.0004	317.6	97.5	304.2	8.3	308.5	12.4	313.7	7.4	304.1	0.4
NAV04_mnz3028C	20.63	0.59	0.0531	0.0023	0.356	0.02	0.0485	0.001	0.434	0.0155	0.0004	333.5	96.7	305.1	8.5	308.8	12.4	309.9	7.2	304.9	0.4
NAV04_mnz3028E	20.82	0.59	0.0539	0.0024	0.356	0.02	0.0480	0.001	0.365	0.0154	0.0004	366.0	98.7	302.5	8.4	309.1	12.4	309.1	7.4	301.9	0.4
NAV04_mnz3034A	20.38	0.56	0.0533	0.0023	0.364	0.02	0.0491	0.001	0.410	0.0158	0.0004	340.3	96.3	308.8	8.3	315.0	12.3	316.1	7.8	308.5	0.4
NAV04_mnz3034B	20.76	0.58	0.0531	0.0023	0.356	0.02	0.0482	0.001	0.498	0.0156	0.0004	333.5	96.7	303.3	8.3	309.4	12.4	312.9	7.6	303.1	0.4
NAV04_mnz3034C	21.26	0.65	0.0524	0.0023	0.341	0.02	0.0470	0.001	0.339	0.0153	0.0004	302.9	102.1	296.3	8.9	298.2	11.7	307.5	8.0	296.3	0.4

Table VI-2: Trace element data from monazite in Port Navalo migmatite (Normalised to McDonough and Sun, 1995) (2/2)

			Trace element value												
	Y (ppm)	2σ	La	Pr	Nd	Sm	Eu	Gd	Tb	Dy	Ho	Er	Tm	Yb	Lu
NAV04_mnz1182A	14000	1300	516878	316129	249234	126351	18839	62211	37222	19350	10418	4738	2020	1037	496
NAV04_mnz1399A	4540	310	598312	310753	218184	100203	14232	40201	18306	8049	3564	1663	608	304	180
NAV04_mnz1399B	10560	660	530380	313978	235667	123649	13268	60603	35722	18577	7836	2531	732	323	156
NAV04_mnz1410A	4260	300	561603	300000	211379	96824	14000	39397	18139	7236	3200	1525	584	209	104
NAV04_mnz1410B	8290	810	534599	303226	214223	109392	16714	49950	26750	13252	6545	2806	1120	565	252
NAV04_mnz1410C	9800	700	509283	296774	225602	122568	17321	56633	31056	15569	7200	3475	1384	547	408
NAV04_mnz1646B	5620	280	505485	300000	225383	129054	20786	66884	44167	25163	14200	6556	2892	1130	604
NAV04_mnz1646C	5960	540	567511	298925	236324	113514	12179	49045	24000	10203	4527	1819	684	398	212
NAV04_mnz1646D	5230	450	541350	296774	224726	110135	12250	45126	21111	8740	3818	1594	644	329	164
NAV04_mnz2014A	9930	640	498734	298925	221663	118919	21446	56131	32639	16098	7018	2975	1204	652	376
NAV04_mnz2014B	12280	990	538819	320430	235230	120946	30536	59950	37222	18415	8873	4106	1544	913	612
NAV04_mnz2045A	15200	1000	529114	296774	231729	130405	18768	66533	40000	21585	11109	5275	2012	795	460
NAV04_mnz2045B	4260	360	628692	321505	242670	108784	13643	43116	20528	7480	2836	1225	468	248	88
NAV04_mnz2048A	7660	650	562025	332258	246171	128378	17268	55126	28694	11911	5709	2569	1032	590	232
NAV04_mnz2048B	9770	720	529536	334409	258206	135135	19286	61508	33333	15081	7782	3450	1652	727	416
NAV04_mnz2080A	7380	480	607595	337634	256674	132432	15929	57085	26667	11951	5400	2475	1048	491	252
NAV04_mnz2080B	17000	1400	508861	303226	229978	131757	20179	67286	41111	23171	12036	6425	3060	1435	832
NAV04_mnz2245A	8450	600	564135	315054	237637	123649	16054	56633	28944	13252	6036	2575	1024	472	228
NAV04_mnz2245B	9300	1000	570886	325806	242888	131081	13286	59497	32444	14431	6727	2700	1228	460	236
NAV04_mnz2245C	9800	1000	599156	333333	264770	131081	15071	59146	34694	15610	7818	3138	1088	429	284
NAV04_mnz2318	12850	790	533755	308602	245295	125000	19964	62663	37528	20569	9909	4444	1500	634	296
NAV04_mnz2395A	15200	1300	569620	333333	255361	135135	16696	67839	43611	21748	10836	3900	1520	696	184
NAV04_mnz2395B	9110	760	599156	347312	266521	133108	18357	59296	31444	14512	6945	3013	1336	652	364
NAV04_mnz2592A	4330	410	536709	303226	217746	100676	13214	40352	17111	8008	3545	1506	560	267	224
NAV04_mnz2913A	26900	1700	578059	317204	239606	111486	13036	45729	21056	9390	3945	1706	720	366	180
NAV04_mnz2913B	5200	500	561181	331183	253173	143243	18036	74372	49167	25366	12164	5100	1972	820	492
NAV04_mnz3007A	18400	2000	607595	334409	265208	147973	23214	79899	48056	26016	14418	6250	2688	1143	816
NAV04_mnz3007B	20100	1800	545992	331183	244420	140541	23804	75879	47778	27114	14873	6500	2436	1056	420
NAV04_mnz3028A	14300	1200	587764	330108	260613	133108	18643	69849	40611	21707	9927	4150	1676	807	324
NAV04_mnz3028B	5550	420	573418	304301	238512	123649	15125	48191	23722	10163	4309	1713	724	217	156
NAV04_mnz3028C	4430	320	546835	297849	217287	106757	12643	42915	19500	8293	3873	1450	560	174	216
NAV04_mnz3028E	17100	1400	535021	324731	255142	146622	22304	75879	48611	25447	12509	4900	1472	584	184
NAV04_mnz3034A	6860	460	539241	303226	226039	111554	15196	47789	24222	11260	5655	2469	1008	497	228
NAV04_mnz3034B	7510	660	569620	307527	233917	117568	15214	51357	25583	11707	6000	2475	1060	559	392
NAV04_mnz3034C	6700	600	224945	106081	14232	44874	22833	10203	5109	2419	984	373	308		

Table VI-3: Fluid inclusions microthermometry results for samples QUIB03, QUIB07, PIR01, PIR06 and PIR16. FIA: Fluid Inclusion Assemblage; Inclusion: Inclusion number within the FIA; T_{im}: ice melting temperature (°C); Salinity (wt% eq. NaCl); T_h: homogeneisation temperature (°C); n: number of data; SD: Standard Deviation. (1/3)

Sample	FIA	Inclusion	T_{im}	Salinity	T_h
QUIB03	1	2	-1.4	2.4	384
		6	-1.3	2.3	284
		1	-0.3	0.6	366
		9	-0.3	0.6	
	2	1	-4.3	6.9	218
		2	-4.6	7.3	208
		3	-4.2	6.7	262
		4	-4.5	7.2	
		5	-4.5	7.2	201
		6	-4.5	7.2	197
		7	-4.5	7.2	253
		8	-4.5	7.2	190
		9	-4.3	6.9	258
		10	-4.7	7.4	203
		11	-4.6	7.3	216
		12	-4.4	7.0	226
		13	-1.3	2.3	
		14	-4.7	7.4	208
		15	-4.3	6.9	213
		16	-4.3	6.9	207
		17	-4.3	6.9	207
		18	-4.0	6.4	243
		19	-4.0	6.4	275
		20	-4.4	7.0	260
		21	-2.5	4.2	245
	3	1	-2.1	3.6	182
		2	-4.8	7.6	180
		3	-5.4	8.4	178
		4	-5.7	8.8	173
		5	-2.4	4.0	183
	4	1	-1.5	2.6	172
		2	-1.3	2.3	180
		3	-1.2	2.1	198
		4	-0.5	0.9	176
		5	-1.5	2.6	192

Average of the 5 five samples

	T_{im}	Salinity	T_h
n	402	239	369
average	**-0.6**	**3.7**	**225**
SD	2.6	2.9	62
Minimum	-9.4	0.0	113
Maximum	5.0	13.3	393

Sample	FIA	Inclusion	T_{im}	Salinity	T_h
QUIB07	1	1	-1.0	1.8	203
		2	-1.0	1.8	208
		3	-1.3	2.3	234
		4	-1.1	1.9	277
		5	-0.8	1.4	287
		6	-1.3	2.3	287
		7	-1.6	2.8	
		8	-0.8	1.4	
		9	-1.0	1.8	287
		10	-0.9	1.6	267
		11	-1.2	2.1	267
		12	-1.1	1.9	267
		13	-1.1	1.9	270
	2	1	-0.9	1.6	297
		2	-1.0	1.8	296
		3	-1.2	2.1	295
		4	-0.9	1.6	292
		5	-1.2	2.1	277
		6	-0.9	1.6	276
		7	-1.3	2.3	280
		8	-0.9	1.6	274
		9	-1.4	2.4	296

Sample	FIA	Inclusion	T_{im}	Salinity	T_h
PIR16	1	1	-1.8	3.1	149
		2	-1.9	3.3	
		3	-1.9	3.3	
		4	-1.3	2.3	
		5	-1.5	2.6	
	2	1	-1.5	2.6	157
		2	-1.6	2.8	225
		3	-1.7	2.9	
		4	-1.7	2.9	149
		5	-1.4	2.4	159
		6	-1.6	2.8	278
		7	-1.6	2.8	157
		8	-1.6	2.8	169
		9	-1.8	3.1	199
	3	1	-2.3	3.9	166
		2	-1.8	3.1	177
		3	-1.5	2.6	178
		4	-2.0	3.4	167
		5	-1.7	2.9	194
		6	-1.2	2.1	153
		7	-1.6	2.8	160
		8	-1.7	2.9	195
		9	-2.2	3.7	250
		10	-1.9	3.3	160

Sample	FIA	Inclusion	T_{im}	Salinity	T_h
PIR06	F3	1	0.0	0.0	307
		2	-0.2	0.4	303
		3	-0.4	0.7	342
		4	-0.8	1.4	200
		5	0.0	0.0	301
		6	-0.7	1.2	290
		7	-1.2	2.1	221
		8	0.5		263
		9	-0.7	1.2	260
		10	-0.8	1.4	244
		11	-0.5	0.9	225
		12	1.0		174
		13	2.8		
		14	-2.1	3.6	201
		15	-1.8	3.1	198
		16	-1.7	2.9	233
	F4	1	1.4		194
		2	1.6		391
		3	3.3		336
		4	3.3		393
		5	2.5		343
		6	1.6		181
		7	2.3		179
		8	1.8		182
		9	2.1		263
		10	3.1		178
		11	3.2		285
		12	0.8		298
		13	0.6		134
	F5	1	2.0		210
		2	0.8		190
		3	1.3		223
		4	1.3		241
		5	1.1		220
		6	1.4		263
		7	0.8		236
		8	0.6		201
		9	1.0		239
		10	2.6		
		11	2.6		293
		12	2.7		289
		13	2.8		374
		14	1.9		300
		15	1.8		253
		16	1.9		255
	F6	1	0.6		233
		2	0.3		193
		3	0.7		353
		4	0.4		356
		5	0.0	0.0	348
		6	0.0	0.0	175
		7	0.0	0.0	179
		8	1.4		183
		9	0.3		195
		10	0.4		244
		11	0.4		224
		12	1.6		
		13	0.7		192
		14	0.8		198
		15	2.2		265
		16	1.4		245
		17	1.3		220
		18	0.9		207
	F7	1	1.2		286
		2	0.4		174
		3	0.2		197
		4	0.0	0.0	188
		5	1.0		274
		6	0.0	0.0	199
		7	0.5		232
		8	0.8		264
		9	1.3		178
		10	1.7		162
		11	0.7		149
		12	0.6		176
		13	0.6		283
		14	1.3		183
		15	0.1		141

Sample	FIA	Inclusion	T_{im}	Salinity	T_h
PIR06	F8	1	-6.7	10.1	282
		2	-5.3	8.3	240
		3	-9.4	13.3	220
		4	-7.2	10.7	298
		5	-8.7	12.5	324
		6	-5.2	8.1	303
		7	-8.2	11.9	292
		8	-6.6	10.0	232
		9	-7.3	10.9	287
		10	-7.1	10.6	289
		11	-8.8	12.6	
		12	-7.6	11.2	284
		13	-8.4	12.2	223
	F9	1	-2.5	4.2	207
		2	-4.4	7.0	223
		3	-3.1	5.1	143
		4	-2.2	3.7	148
		5	-3.0	5.0	163
		6	-2.3	3.9	217
		7	-4.6	7.3	242
		8	-3.0	5.0	172
		9	-3.8	6.2	214
		10	-2.5	4.2	200
		11	-2.7	4.5	168
		12	-1.8	3.1	152
		13	-1.9	3.2	209
		14	-1.8	3.1	142
	F10	1	-1.6	2.7	163
		2	-4.4	7.0	247
		3	-1.3	2.2	170
		4	-1.7	2.9	174
		5	-2.0	3.4	193
		6	-1.6	2.7	166
		7	-1.8	3.1	176
		8	-3.8	6.2	235
		9	-3.2	5.3	182
		10	-3.6	5.9	222
		11	-3.4	5.6	228
		12	-2.8	4.7	201
		13	-2.7	4.5	207
		14	-2.8	4.7	220
		15	-2.9	4.8	225
	F11	1	-4.2	6.7	248
		2	-3.2	5.3	238
		3	-3.0	5.0	218
		4	-2.7	4.5	210
		5	-1.0	1.7	179
		6	-1.3	2.2	187
		7	-1.1	1.9	185
		8	-1.7	2.9	214
		9	-1.7	2.9	218
		10	-1.6	2.7	218
		11	-1.8	3.1	221
		12	-4.4	7.0	253
		13	-1.8	3.1	179
		14	-1.5	2.6	183
		15	-2.7	4.5	154
	F12	1	2.8		258
		2	2.8		263
		3	3.2		276
		4	2.8		135
		5	3.1		273
		6	3.1		364
		7	3.2		354
		8	3.4		302
		9	2.8		185
		10	3.6		198
		11	3.4		152
		12	4.0		205
		13	3.1		137
		14	2.9		143
		15	3.0		128
		16	3.8		139
		17	2.6		179
		18	2.9		141

Sample	FIA	Inclusion	T_{im}	Salinity	T_h
PIR01	F3	1	2.4		260
		2	2.2		381
		3	-1.6	2.7	
		4	5.0		113
		5	2.1		227
		6	-0.4	0.7	
		7	3.2		337
		8	4.1		261
		9	4.2		
		10	1.8		272
		11	2.8		273
		12	3.6		232
		13	1.8		256
		14	-1.2	2.1	212
		15	1.6		229
	F4	1	-0.4	0.7	
		2	-0.1	0.2	362
		3	-1.0	1.7	
		4	0.0	0.0	312
		5	-0.1	0.2	348
		6	-0.8	1.4	261
		7	-0.6	1.1	230
		8	-0.4	0.7	286
		9	-1.9	3.2	324
		10	-3.2	5.3	313
		11	-2.6	4.3	302
		12	-1.2	2.1	327
		13	-1.1	1.9	270
		14	-0.8	1.4	294
		15	-0.7	1.2	327
		16	-0.9	1.6	241
		17	-1.2	2.1	216
		18	-2.0	3.4	274
		19	-1.0	1.7	360
	F5	1	0.0	0.0	289
		2	-2.2	3.7	300
		3	-1.3	2.2	174
		4	-2.8	4.6	183
		5	-2.5	4.2	142
		6	-3.0	5.0	228
		7	-2.6	4.3	247
		8	-2.6	4.3	211
		9	-6.1	9.3	
		10	-0.7	1.2	240
		11	-0.7	1.2	269
		12	-0.6	1.1	222
		13	-3.1	5.1	302
		14	-3.2	5.3	245
		15	-3.4	5.6	
		16	-2.6	4.3	222
		17	-2.2	3.7	260
	F6	1	-3.2	5.3	259
		2	-3.9	6.3	145
		3	-5.1	8.0	123
		4	-5.0	7.9	184
		5	-2.2	3.7	164
		6	-2.2	3.7	171
		7	-2.0	3.4	200
		8	-4.2	6.7	217
		9	-1.0	1.7	227
		10	-5.4	8.4	
		11	-3.6	5.9	
		12	-2.4	4.0	155
		13	-1.6	2.7	234
		14	0.8		201
		15	-3.7	6.0	
		16	-0.8	1.4	133
		17	-2.5	4.2	
		18	0.0	0.0	174
	F7	1	3.0		248
		2	3.0		276
		3	1.8		223
		4	2.8		275
		5	0.0	0.0	207
		6	0.8		264
		7	2.2		270
		8	0.2		302
		9	0.6		150
		10	0.8		114
		11	0.9		

FIA	Inclusion	T_{im}	Salinity	T_h
F7	12	1.7		210
	13	0.7		142
	14	3.8		
	15	2.1		259
	16	1.3		244
	17	1.2		228
	18	1.8		191
F8	1	4.0		349
	2	4.2		141
	3	3.2		129
	4	2.5		210
	5	1.8		189
	6	2.2		192
	7	2.4		153
	8	0.5		164
	9	-0.7	1.2	158
	10	0.7		324
	11	-0.4	0.7	197
	12	-0.4	0.7	199
	13	0.6		206
	14	-1.6	2.7	168
	15	-0.9	1.6	164
	16	1.8		178
	17	0.8		183
F9	1	4.4		
	2	0.6		262
	3	0.4		214
	4	0.3		258
	5	1.6		163
	6	3.5		182
	7	1.2		173
	8	3.0		158
	9	1.7		232
	10	0.6		
	11	1.1		286
	12	1.7		270
	13	2.7		
	14	0.6		254
	15	0.3		264
	16	0.6		189
F10	1	-3.2	5.3	209
	2	-0.5	0.9	173
	3	-0.5	0.9	188
	4	-3.6	5.9	205
	5	1.0		
	6	1.0		183
	7	1.3		176
	8	0.1		189
	9	1.4		242
	10	1.4		267
	11	2.7		254
	12	2.5		174
	13	4.2		172
	14	1.3		163
	15	1.5		145
	16	1.7		256
F11	1	1.4		234
	2	0.3		228
	3	1.5		212
	4	1.7		192
	5	2.1		200
	6	2.5		162
	7	1.6		146
	8	1.9		290
	9	0.2		174
	10	1.9		183
	11	0.6		153
	12	3.3		127
	13	1.3		213
	14	2.1		235
	15	2.2		
F12	1	-0.9	1.6	241
	2	-0.9	1.6	246
	3	-1.2	2.1	211
	4	-2.2	3.7	224
	5	-1.6	2.7	185
	6	-0.1	0.2	213
	7	-0.6	1.1	141
	8	-0.8	1.4	
	9	-1.1	1.9	331

FIA	Inclusion	T_{im}	Salinity	T_h
F12	10	-0.8	1.4	284
	11	-1.0	1.7	285
	12	-2.8	4.6	199
	13	0.0	0.0	144
	14	-1.4	2.4	182
	15	-1.1	1.9	152
	16	-1.3	2.2	139
	17	-0.6	1.1	202

Table VI-4: Microprobe analysis of muscovite grains and calculation of temperature using the Ti-in-Ms geothermometer (Wu and Chen, 2015) for sample MIL18H (1/6)

Sample		MIL18H																					
Zone		A						B		C		D				E							
DataSet/Point		1	2	3	4	5	6	7	8	9	10	11	12	13	14	15	16	17	18	19	20	21	22
Oxydes (Wt. %)	SiO2	45.72	46.41	46.02	46.14	45.54	46.10	46.61	46.21	45.78	46.00	45.38	45.51	45.78	45.98	45.27	46.50	45.43	45.69	45.49	45.40	46.24	45.54
	Al2O3	35.66	35.76	35.11	35.79	35.39	34.98	35.49	35.61	35.05	35.28	35.15	34.98	34.76	35.37	35.35	34.13	35.24	35.46	35.04	34.83	34.37	35.32
	K2O	11.56	11.38	11.57	11.22	11.32	11.32	11.14	11.25	11.39	11.25	11.72	11.26	11.31	11.73	11.18	11.02	11.20	11.25	11.63	11.73	11.22	11.54
	CaO	0.00	0.00	0.00	0.00	0.00	0.00	0.00	0.00	0.00	0.00	0.00	0.00	0.00	0.00	0.00	0.00	0.00	0.00	0.00	0.00	0.00	0.00
	TiO2	0.55	0.56	0.57	0.57	0.55	0.42	0.51	0.45	0.28	0.27	0.58	0.54	0.52	0.65	0.63	0.52	0.59	0.57	0.52	0.61	0.67	0.46
	Cr2O3	0.00	0.00	0.00	0.00	0.00	0.00	0.00	0.00	0.00	0.00	0.00	0.00	0.00	0.00	0.00	0.00	0.00	0.00	0.00	0.00	0.00	0.00
	MnO	0.01	0.01	0.02	0.02	-0.02	0.02	0.03	0.00	0.02	0.02	0.01	0.01	0.02	0.00	0.03	0.02	0.01	0.04	0.01	0.01	0.00	-0.03
	FeO	1.27	1.27	1.32	1.31	1.42	1.35	1.47	1.44	1.45	1.44	1.43	1.31	1.56	1.37	1.38	1.65	1.32	1.37	1.43	1.39	1.52	1.37
	Na2O	0.55	0.58	0.52	0.69	0.46	0.58	0.52	0.49	0.54	0.51	0.53	0.60	0.46	0.46	0.65	0.54	0.73	0.70	0.52	0.42	0.54	0.51
	MgO	0.77	0.80	0.79	0.76	0.79	0.81	0.80	0.83	0.89	0.80	0.77	0.75	0.86	0.79	0.75	1.10	0.75	0.77	0.80	0.79	0.91	0.84
	Sum	96.05	96.76	95.87	96.48	95.47	95.55	96.55	96.27	95.37	95.57	95.56	94.92	95.25	96.28	95.25	95.51	95.22	95.85	95.44	95.17	95.47	95.53
Conversion factor		4.00	3.96	4.01	3.97	4.02	4.01	3.96	3.98	4.03	4.01	4.03	4.03	4.03	4.00	4.02	4.01	4.03	4.00	4.04	4.04	4.01	4.02
Moles (normalised for 11 oxygens)	Si	3.04	3.06	3.07	3.04	3.05	3.08	3.07	3.06	3.07	3.07	3.05	3.05	3.07	3.06	3.03	3.10	3.05	3.04	3.06	3.05	3.09	3.05
	Al	2.79	2.77	2.76	2.78	2.79	2.75	2.76	2.78	2.77	2.77	2.78	2.77	2.75	2.77	2.79	2.68	2.79	2.78	2.77	2.76	2.70	2.79
	K	0.98	0.96	0.98	0.94	0.97	0.96	0.94	0.95	0.97	0.96	1.00	0.96	0.97	1.00	0.95	0.94	0.96	0.96	1.00	1.01	0.95	0.99
	Ca	0.00	0.00	0.00	0.00	0.00	0.00	0.00	0.00	0.00	0.00	0.00	0.00	0.00	0.00	0.00	0.00	0.00	0.00	0.00	0.00	0.00	0.00
	Ti	**0.03**	**0.03**	**0.03**	**0.03**	**0.03**	**0.02**	**0.03**	**0.02**	**0.01**	**0.01**	**0.03**	**0.03**	**0.03**	**0.03**	**0.03**	**0.03**	**0.03**	**0.03**	**0.03**	**0.03**	**0.03**	**0.02**
	Cr	0.00	0.00	0.00	0.00	0.00	0.00	0.00	0.00	0.00	0.00	0.00	0.00	0.00	0.00	0.00	0.00	0.00	0.00	0.00	0.00	0.00	0.00
	Mn	0.00	0.00	0.00	0.00	0.00	0.00	0.00	0.00	0.00	0.00	0.00	0.00	0.00	0.00	0.00	0.00	0.00	0.00	0.00	0.00	0.00	0.00
	Fe	0.07	0.07	0.07	0.07	0.08	0.08	0.08	0.08	0.08	0.08	0.08	0.07	0.09	0.08	0.08	0.09	0.07	0.08	0.08	0.08	0.08	0.08
	Na	0.07	0.07	0.07	0.09	0.06	0.08	0.07	0.06	0.07	0.07	0.07	0.08	0.06	0.06	0.08	0.07	0.10	0.09	0.07	0.05	0.07	0.07
	Mg	0.08	0.08	0.08	0.08	0.08	0.08	0.08	0.08	0.09	0.08	0.08	0.07	0.09	0.08	0.07	0.11	0.08	0.08	0.08	0.08	0.09	0.08
[Mg/(Fe+Mg)]		0.52	0.53	0.52	0.51	0.50	0.52	0.49	0.51	0.52	0.50	0.49	0.50	0.49	0.51	0.49	0.54	0.50	0.50	0.50	0.50	0.52	0.52
T(°C) at 4 kbar		571	572	575	574	567	529	552	535	469	465	577	567	560	596	592	564	580	574	559	587	602	543
SD (P ± 1kbar)		5	5	5	5	5	5	5	5	4	4	5	5	5	5	5	5	5	5	5	5	5	5
Average T per sample		**568**																					
SD (°C) on average		42																					

Table VI-4: Microprobe analysis of muscovite grains and calculation of temperature using the Ti-in-Ms geothermometer (Wu and Chen, 2015) for sample MIL18H (2/6)

Sample		MIL18H																						
Zone		F							G							H								
DataSet/Point		23	24	25	26	27	28	29	31	32	33	34	35	36	37	38	39	40	41	42	43	44	47	48
Oxydes (Wt. %)	SiO2	46.00	45.75	45.74	45.62	45.28	45.82	46.02	45.52	46.03	46.08	45.95	45.70	45.76	46.10	45.86	45.99	46.27	46.35	46.08	46.15	46.11	46.25	46.52
	Al2O3	35.62	35.21	35.27	35.47	34.61	34.94	33.64	34.11	35.00	35.05	34.75	35.02	35.10	35.13	35.08	34.76	35.20	34.67	34.13	34.73	35.39	35.08	35.40
	K2O	11.30	11.14	11.17	11.12	10.90	11.11	11.66	11.53	11.30	11.50	11.42	11.32	11.01	11.43	11.67	11.18	11.29	11.25	11.32	11.44	11.73	11.23	11.32
	CaO	0.00	0.00	0.00	0.00	0.00	0.00	0.00	0.00	0.00	0.00	0.00	0.00	0.00	0.00	0.00	0.00	0.00	0.00	0.00	0.00	0.00	0.00	0.00
	TiO2	0.56	0.56	0.58	0.61	0.52	0.59	0.70	0.62	0.53	0.54	0.62	0.49	0.50	0.51	0.12	0.50	0.62	0.70	0.70	0.70	0.66	0.75	0.36
	Cr2O3	0.02	0.00	0.01	0.01	0.00	0.00	0.02	0.00	0.01	0.01	0.00	0.01	0.01	0.03	0.00	0.00	0.01	0.01	0.03	0.01	0.00	0.00	0.00
	MnO	0.02	0.00	0.01	0.03	0.03	0.03	0.00	0.02	0.01	0.03	0.02	0.00	0.02	0.02	0.04	0.04	0.02	0.02	0.01	0.03	0.05	0.02	0.02
	FeO	1.26	1.39	1.35	1.50	1.38	1.38	1.67	1.68	1.37	1.42	1.59	1.32	1.42	1.45	1.33	1.58	1.38	1.50	1.58	1.44	1.50	1.44	1.25
	Na2O	0.63	0.61	0.59	0.55	0.66	0.53	0.55	0.40	0.57	0.56	0.40	0.57	0.63	0.55	0.46	0.50	0.60	0.54	0.51	0.54	0.47	0.55	0.37
	MgO	0.73	0.76	0.76	0.74	0.73	0.75	1.07	0.92	0.76	0.79	0.84	0.76	0.79	0.81	0.88	0.91	0.83	0.93	1.04	0.89	0.78	0.92	0.76
	Sum	96.12	95.35	95.43	95.62	94.10	95.12	95.33	94.80	95.54	95.94	95.56	95.17	95.21	95.99	95.44	95.46	96.20	95.91	95.39	95.93	96.66	96.19	95.98
Conversion factor		3.98	4.02	4.02	4.01	4.07	4.03	4.05	4.25	4.01	4.00	4.02	4.03	4.02	4.00	4.03	4.01	3.99	4.00	4.03	4.00	3.98	4.16	3.98
Moles (normalised for 11 oxygens)	Si	3.05	3.06	3.06	3.04	3.06	3.07	3.10	3.22	3.07	3.07	3.07	3.06	3.06	3.07	3.07	3.07	3.07	3.08	3.09	3.08	3.06	3.21	3.08
	Al	2.78	2.77	2.78	2.79	2.76	2.76	2.67	2.84	2.75	2.75	2.74	2.77	2.77	2.76	2.77	2.73	2.75	2.72	2.70	2.73	2.76	2.87	2.77
	K	0.96	0.95	0.95	0.95	0.94	0.95	1.00	1.04	0.96	0.98	0.97	0.97	0.94	0.97	1.00	0.95	0.96	0.95	0.97	0.97	0.99	0.99	0.96
	Ca	0.00	0.00	0.00	0.00	0.00	0.00	0.00	0.00	0.00	0.00	0.00	0.00	0.00	0.00	0.00	0.00	0.00	0.00	0.00	0.00	0.00	0.00	0.00
	Ti	**0.03**	**0.03**	**0.03**	**0.03**	**0.03**	**0.03**	**0.04**	**0.03**	**0.03**	**0.03**	**0.03**	**0.02**	**0.03**	**0.03**	**0.01**	**0.03**	**0.03**	**0.04**	**0.04**	**0.04**	**0.03**	**0.04**	**0.02**
	Cr	0.00	0.00	0.00	0.00	0.00	0.00	0.00	0.00	0.00	0.00	0.00	0.00	0.00	0.00	0.00	0.00	0.00	0.00	0.00	0.00	0.00	0.00	0.00
	Mn	0.00	0.00	0.00	0.00	0.00	0.00	0.00	0.00	0.00	0.00	0.00	0.00	0.00	0.00	0.00	0.00	0.00	0.00	0.00	0.00	0.00	0.00	0.00
	Fe	0.07	0.08	0.08	0.08	0.08	0.08	0.09	0.10	0.08	0.08	0.09	0.07	0.08	0.08	0.07	0.09	0.08	0.08	0.09	0.08	0.08	0.08	0.07
	Na	0.08	0.08	0.08	0.07	0.09	0.07	0.07	0.06	0.07	0.07	0.05	0.07	0.08	0.07	0.06	0.06	0.08	0.07	0.07	0.07	0.06	0.07	0.05
	Mg	0.07	0.08	0.08	0.07	0.07	0.07	0.11	0.10	0.08	0.08	0.08	0.08	0.08	0.08	0.09	0.09	0.08	0.09	0.10	0.09	0.08	0.09	0.08
[Mg/(Fe+Mg)]		0.51	0.49	0.50	0.47	0.48	0.49	0.53	0.49	0.50	0.50	0.49	0.50	0.50	0.50	0.54	0.51	0.52	0.52	0.54	0.52	0.48	0.53	0.52
T(°C) at 4 kbar		572	570	577	582	560	581	613	598	562	564	588	551	553	557	372	553	588	611	614	611	595	630	505
SD (P ± 1kbar)		5	5	5	5	5	5	5	5	5	5	5	5	5	5	3	5	5	5	5	5	5	6	4
Average T per sample		**568**																						
SD (°C) on average		42																						

Table VI-4: Microprobe analysis of muscovite grains and calculation of temperature using the Ti-in-Ms geothermometer (Wu and Chen, 2015) for sample MIL18H (3/6).

Sample		MIL18H																	
Zone		I								J						K			
DataSet/Point		49	50	51	52	53	54	55	56	57	58	59	60	61	62	63	64	65	66
Oxydes (Wt. %)	SiO2	45.75	46.10	45.73	45.77	45.90	46.08	46.32	46.73	46.23	45.76	45.48	45.93	45.84	45.85	45.52	45.94	46.13	45.74
	Al2O3	34.58	35.24	34.95	35.52	33.85	35.32	34.31	33.46	33.77	35.13	34.46	34.91	35.04	34.87	35.63	35.14	34.93	35.23
	K2O	11.34	11.48	11.44	10.95	11.54	11.25	11.71	11.40	11.57	11.56	11.24	11.14	11.09	11.32	11.66	11.50	11.38	11.32
	CaO	0.00	0.00	0.00	0.00	0.00	0.00	0.00	0.00	0.00	0.00	0.00	0.00	0.00	0.00	0.00	0.00	0.00	0.00
	TiO2	0.60	0.44	0.71	0.67	0.68	0.66	0.69	0.71	0.62	0.51	0.57	0.55	0.52	0.67	0.32	0.43	0.47	0.58
	Cr2O3	0.02	0.00	0.01	0.01	0.00	0.02	0.01	0.00	0.01	0.00	0.01	0.00	0.01	0.00	0.00	0.00	0.02	0.00
	MnO	0.00	0.02	0.00	0.04	0.02	0.05	0.06	0.04	0.02	0.02	0.00	0.02	0.01	0.03	0.05	0.00	0.01	0.01
	FeO	1.53	1.35	1.50	1.37	1.67	1.42	1.44	1.99	1.69	1.36	1.70	1.58	1.42	1.41	1.42	1.39	1.58	1.43
	Na2O	0.45	0.61	0.48	0.66	0.39	0.65	0.49	0.31	0.39	0.47	0.61	0.51	0.59	0.54	0.44	0.50	0.56	0.51
	MgO	0.92	0.86	0.83	0.70	0.98	0.78	0.94	1.20	1.14	0.76	0.80	0.85	0.82	0.85	0.70	0.77	0.90	0.84
	Sum	95.13	96.06	95.65	95.68	94.99	96.18	95.91	95.81	95.41	95.53	94.84	95.47	95.31	95.53	95.71	95.59	95.96	95.66
Conversion factor		4.03	4.00	4.02	3.99	4.06	3.98	4.02	4.01	4.03	4.02	4.05	4.01	4.02	4.02	4.02	4.01	4.00	4.01
Moles (normalised for 11 oxygens)	Si	3.07	3.07	3.06	3.04	3.10	3.05	3.10	3.12	3.10	3.06	3.06	3.07	3.07	3.07	3.05	3.07	3.07	3.05
	Al	2.74	2.76	2.75	2.78	2.69	2.76	2.70	2.63	2.67	2.77	2.74	2.75	2.76	2.75	2.81	2.76	2.74	2.77
	K	0.97	0.97	0.98	0.93	0.99	0.95	1.00	0.97	0.99	0.99	0.97	0.95	0.95	0.97	0.99	0.98	0.97	0.96
	Ca	0.00	0.00	0.00	0.00	0.00	0.00	0.00	0.00	0.00	0.00	0.00	0.00	0.00	0.00	0.00	0.00	0.00	0.00
	Ti	**0.03**	**0.02**	**0.04**	**0.03**	**0.03**	**0.03**	**0.03**	**0.04**	**0.03**	**0.03**	**0.03**	**0.03**	**0.03**	**0.03**	**0.02**	**0.02**	**0.02**	**0.03**
	Cr	0.00	0.00	0.00	0.00	0.00	0.00	0.00	0.00	0.00	0.00	0.00	0.00	0.00	0.00	0.00	0.00	0.00	0.00
	Mn	0.00	0.00	0.00	0.00	0.00	0.00	0.00	0.00	0.00	0.00	0.00	0.00	0.00	0.00	0.00	0.00	0.00	0.00
	Fe	0.09	0.08	0.08	0.08	0.09	0.08	0.08	0.11	0.10	0.08	0.10	0.09	0.08	0.08	0.08	0.08	0.09	0.08
	Na	0.06	0.08	0.06	0.09	0.05	0.08	0.06	0.04	0.05	0.06	0.08	0.07	0.08	0.07	0.06	0.06	0.07	0.07
	Mg	0.09	0.09	0.08	0.07	0.10	0.08	0.09	0.12	0.11	0.08	0.08	0.08	0.08	0.08	0.07	0.08	0.09	0.08
[Mg/(Fe+Mg)]		0.52	0.53	0.49	0.48	0.51	0.49	0.54	0.52	0.54	0.50	0.46	0.49	0.51	0.52	0.47	0.50	0.50	0.51
T(°C) at 4 kbar		584	535	610	599	608	597	610	614	594	557	573	568	561	604	485	529	544	578
SD (P ± 1kbar)		5	5	5	5	5	5	5	5	5	5	5	5	5	5	4	5	5	5
Average T per sample		**568**																	
SD (°C) on average		42																	

Table VI-4: Microprobe analysis of muscovite grains and calculation of temperature using the Ti-in-Ms geothermometer (Wu and Chen, 2015) for sample MIL18C (4/6).

Sample		MIL18C																							
Zone		A					B							D											
DataSet/Point		69	70	71	72	73	74	75	76	77	78	79	80	84	85	86	87	88	89	90	91	92	93	94	95
Oxydes (Wt. %)	SiO2	45.59	45.79	45.46	45.53	45.75	45.62	45.61	45.61	45.84	45.82	45.69	45.18	45.32	45.68	45.52	45.68	45.71	46.01	45.62	45.50	45.67	45.99	45.82	46.13
	Al2O3	35.05	34.99	34.93	35.04	33.50	34.54	35.11	35.36	35.21	35.17	33.98	28.92	34.77	35.32	35.19	34.54	34.38	33.94	34.28	34.44	35.42	35.65	35.37	33.71
	K2O	11.58	11.37	11.53	11.49	11.71	11.55	11.45	11.38	11.06	10.98	11.41	10.98	11.66	11.08	10.85	11.42	11.27	11.47	11.60	11.40	11.37	11.45	11.45	11.34
	CaO	0.00	0.00	0.00	0.00	0.00	0.00	0.00	0.00	0.00	0.00	0.00	0.00	0.00	0.00	0.00	0.00	0.00	0.00	0.00	0.00	0.00	0.00	0.00	0.00
	TiO2	0.43	0.33	0.41	0.44	0.24	0.48	0.53	0.43	0.44	0.44	0.51	0.59	0.38	0.46	0.43	0.47	0.38	0.44	0.34	0.37	0.35	0.38	0.36	0.26
	Cr2O3	0.00	0.00	0.00	0.00	0.00	0.01	0.00	0.02	0.02	0.00	0.00	0.01	0.01	0.02	0.00	0.00	0.00	0.00	0.00	0.01	0.01	0.00	0.01	0.01
	MnO	0.06	0.05	0.02	0.01	0.08	0.00	0.08	0.07	0.02	0.02	0.02	0.15	0.07	0.02	0.05	0.04	0.01	0.03	0.07	0.03	0.01	0.03	0.04	0.09
	FeO	1.86	1.81	1.73	1.85	2.89	1.97	1.72	1.53	1.43	1.39	2.32	6.38	1.92	1.43	1.42	1.67	2.04	2.06	2.14	2.16	1.70	1.66	1.64	2.45
	Na2O	0.43	0.42	0.55	0.42	0.33	0.42	0.49	0.61	0.67	0.77	0.33	0.14	0.34	0.73	0.80	0.69	0.55	0.50	0.45	0.38	0.52	0.52	0.66	0.37
	MgO	0.69	0.64	0.63	0.65	0.98	0.68	0.63	0.60	0.63	0.64	0.84	1.77	0.71	0.64	0.64	0.68	0.77	0.88	0.83	0.78	0.72	0.60	0.62	0.95
	Sum	95.65	95.38	95.23	95.37	95.41	95.20	95.57	95.58	95.28	95.19	95.05	94.11	95.14	95.36	94.87	95.19	95.09	95.30	95.31	95.06	95.75	96.25	95.93	95.26
Conversion factor		3.95	4.02	4.04	4.03	4.06	4.04	4.02	4.02	4.01	4.02	4.06	4.19	3.96	4.01	4.03	4.05	4.04	4.05	4.05	4.05	4.01	3.99	4.01	4.04
Moles (normalised for 11 oxygens)	Si	3.00	3.07	3.06	3.06	3.09	3.07	3.05	3.05	3.06	3.07	3.09	3.15	2.99	3.05	3.06	3.08	3.08	3.10	3.08	3.07	3.05	3.05	3.06	3.11
	Al	2.71	2.76	2.77	2.77	2.67	2.74	2.77	2.79	2.77	2.77	2.71	2.37	2.70	2.78	2.78	2.74	2.73	2.69	2.72	2.74	2.79	2.79	2.78	2.67
	K	0.97	0.97	0.99	0.98	1.01	0.99	0.98	0.97	0.94	0.94	0.98	0.98	0.98	0.94	0.93	0.98	0.97	0.98	1.00	0.98	0.97	0.97	0.97	0.97
	Ca	0.00	0.00	0.00	0.00	0.00	0.00	0.00	0.00	0.00	0.00	0.00	0.00	0.00	0.00	0.00	0.00	0.00	0.00	0.00	0.00	0.00	0.00	0.00	0.00
	Ti	**0.02**	**0.02**	**0.02**	**0.02**	**0.01**	**0.02**	**0.03**	**0.02**	**0.02**	**0.02**	**0.03**	**0.03**	**0.02**	**0.02**	**0.02**	**0.02**	**0.02**	**0.02**	**0.02**	**0.02**	**0.02**	**0.02**	**0.02**	**0.01**
	Cr	0.00	0.00	0.00	0.00	0.00	0.00	0.00	0.00	0.00	0.00	0.00	0.00	0.00	0.00	0.00	0.00	0.00	0.00	0.00	0.00	0.00	0.00	0.00	0.00
	Mn	0.00	0.00	0.00	0.00	0.00	0.00	0.00	0.00	0.00	0.00	0.00	0.01	0.00	0.00	0.00	0.00	0.00	0.00	0.00	0.00	0.00	0.00	0.00	0.00
	Fe	0.10	0.10	0.10	0.10	0.16	0.11	0.10	0.09	0.08	0.08	0.13	0.37	0.11	0.08	0.08	0.09	0.11	0.12	0.12	0.12	0.09	0.09	0.09	0.14
	Na	0.05	0.05	0.07	0.05	0.04	0.06	0.06	0.08	0.09	0.10	0.04	0.02	0.04	0.09	0.10	0.09	0.07	0.06	0.06	0.05	0.07	0.07	0.08	0.05
	Mg	0.07	0.06	0.06	0.07	0.10	0.07	0.06	0.06	0.06	0.06	0.08	0.18	0.07	0.06	0.06	0.07	0.08	0.09	0.08	0.08	0.07	0.06	0.06	0.09
[Mg/(Fe+Mg)]		0.40	0.39	0.39	0.39	0.38	0.38	0.39	0.41	0.44	0.45	0.39	0.33	0.40	0.45	0.44	0.42	0.40	0.43	0.41	0.39	0.43	0.39	0.40	0.41
T(°C) at 4 kbar		518	481	515	524	439	537	553	521	527	529	547	571	499	535	527	538	505	528	487	498	495	502	493	451
SD (P ± 1kbar)		5	4	5	5	4	5	5	5	5	5	5	5	4	5	5	5	4	5	4	4	4	4	4	4
Average T per sample		**493**																							
SD (°C) on average		94																							

Table VI-4: Microprobe analysis of muscovite grains and calculation of temperature using the Ti-in-Ms geothermometer (Wu and Chen, 2015) for sample MIL18C (5/6)

Sample		MIL18C																	
Zone		E						F											
DataSet/Point		96	97	98	99	100	101	102	103	104	105	106	107	108	109	110	111	112	113
Oxydes (Wt. %)	SiO2	46.18	45.86	45.91	45.77	46.13	44.68	45.62	45.70	45.47	45.49	45.37	46.50	45.22	44.94	45.75	46.27	46.09	45.55
	Al2O3	33.64	34.93	34.40	34.52	34.35	33.36	34.43	34.78	34.39	33.09	33.02	34.37	34.73	34.20	34.81	34.90	35.41	33.71
	K2O	11.20	11.59	11.42	11.36	11.51	11.64	11.32	11.47	11.58	11.49	11.34	11.36	11.40	11.13	11.34	11.82	11.63	10.77
	CaO	0.00	0.00	0.00	0.00	0.00	0.00	0.00	0.00	0.00	0.00	0.00	0.00	0.00	0.00	0.00	0.00	0.00	0.02
	TiO2	0.25	0.41	0.30	0.26	0.22	0.65	0.36	0.35	0.34	0.27	0.26	0.33	0.48	0.37	0.54	0.14	0.05	0.17
	Cr2O3	0.01	0.00	0.00	0.01	0.01	0.01	0.02	0.00	0.00	0.01	0.00	0.01	0.00	0.00	0.00	0.00	0.00	0.00
	MnO	0.05	0.06	0.07	0.04	0.05	0.02	0.04	0.02	0.04	0.06	0.06	0.04	0.04	0.05	0.02	0.05	0.05	0.05
	FeO	2.14	1.81	1.98	2.34	2.09	2.11	1.84	1.70	1.90	2.55	2.51	2.13	1.71	1.89	1.62	2.10	2.03	2.93
	Na2O	0.38	0.51	0.42	0.44	0.43	0.41	0.49	0.60	0.48	0.40	0.47	0.49	0.43	0.44	0.37	0.41	0.50	0.42
	MgO	0.97	0.63	0.79	0.73	0.84	0.76	0.68	0.67	0.75	0.98	0.90	0.86	0.61	0.69	0.65	0.63	0.43	0.84
	Sum	94.78	95.76	95.22	95.43	95.60	93.59	94.76	95.25	94.90	94.34	93.89	96.08	94.57	93.67	95.06	96.28	96.13	94.46
Conversion factor		4.05	4.03	4.04	4.04	4.03	4.13	4.05	4.04	4.06	4.10	4.11	4.00	4.07	4.10	4.04	4.01	4.00	4.07
Moles (normalised for 11 oxygens)	Si	3.12	3.07	3.08	3.08	3.09	3.07	3.08	3.07	3.07	3.10	3.10	3.10	3.06	3.07	3.08	3.09	3.07	3.08
	Al	2.67	2.76	2.72	2.73	2.72	2.70	2.74	2.76	2.74	2.66	2.66	2.70	2.77	2.75	2.76	2.75	2.78	2.69
	K	0.96	0.99	0.98	0.97	0.99	1.02	0.97	0.98	1.00	1.00	0.99	0.97	0.98	0.97	0.97	1.01	0.99	0.93
	Ca	0.00	0.00	0.00	0.00	0.00	0.00	0.00	0.00	0.00	0.00	0.00	0.00	0.00	0.00	0.00	0.00	0.00	0.00
	Ti	**0.01**	**0.02**	**0.02**	**0.01**	**0.01**	**0.03**	**0.02**	**0.02**	**0.02**	**0.01**	**0.01**	**0.02**	**0.02**	**0.02**	**0.03**	**0.01**	**0.00**	**0.01**
	Cr	0.00	0.00	0.00	0.00	0.00	0.00	0.00	0.00	0.00	0.00	0.00	0.00	0.00	0.00	0.00	0.00	0.00	0.00
	Mn	0.00	0.00	0.00	0.00	0.00	0.00	0.00	0.00	0.00	0.00	0.00	0.00	0.00	0.00	0.00	0.00	0.00	0.00
	Fe	0.12	0.10	0.11	0.13	0.12	0.12	0.10	0.10	0.11	0.15	0.14	0.12	0.10	0.11	0.09	0.12	0.11	0.17
	Na	0.05	0.07	0.05	0.06	0.06	0.05	0.06	0.08	0.06	0.05	0.06	0.06	0.06	0.06	0.05	0.05	0.06	0.06
	Mg	0.10	0.06	0.08	0.07	0.08	0.08	0.07	0.07	0.08	0.10	0.09	0.09	0.06	0.07	0.07	0.06	0.04	0.08
[Mg/(Fe+Mg)]		0.45	0.38	0.42	0.36	0.42	0.39	0.40	0.41	0.41	0.41	0.39	0.42	0.39	0.39	0.42	0.35	0.27	0.34
T(°C) at 4 kbar		450	513	472	450	428	591	495	493	488	459	455	485	539	501	558	371	266	393
SD (P ± 1kbar)		4	5	4	4	4	5	4	4	4	4	4	4	5	4	5	3	2	3
Average T per sample		**493**																	
SD (°C) on average		57																	

Table VI-4: Microprobe analysis of muscovite grains and calculation of temperature using the Ti-in-Ms geothermometer (Wu and Chen, 2015) for sample MIL18I (6/6)

Sample		MIL18I														
Zone		A				B					C				D	
DataSet/Point		115	116	117	118	119	120	121	122	124	125	126	127	128	131	132
Oxydes (Wt. %)	SiO2	46.56	46.29	46.50	46.19	46.59	46.17	46.83	46.66	46.34	45.88	45.30	45.92	46.49	46.32	46.42
	Al2O3	34.92	34.54	34.71	35.19	34.92	35.30	34.30	33.58	33.74	34.32	34.66	34.21	34.46	33.46	35.20
	K2O	11.22	11.29	11.39	11.10	11.23	11.21	11.28	11.50	11.50	11.33	11.43	11.70	11.43	11.50	11.16
	CaO	0.00	-0.03	-0.03	0.00	-0.02	-0.02	-0.01	0.01	-0.03	-0.02	-0.04	-0.05	0.00	-0.03	-0.03
	TiO2	0.41	0.47	0.45	0.55	0.48	0.44	0.55	0.44	0.55	0.93	0.92	0.48	0.27	0.87	0.42
	Cr2O3	0.02	0.01	0.02	-0.02	0.01	0.00	0.00	0.01	0.00	0.01	0.00	-0.01	0.02	-0.01	0.00
	MnO	0.02	0.04	0.06	0.05	0.07	0.02	0.04	0.07	0.04	0.02	0.04	0.04	0.03	0.05	0.02
	FeO	1.60	1.65	1.83	1.60	1.65	1.56	1.67	2.12	1.88	1.66	1.54	1.81	1.82	1.99	1.50
	Na2O	0.61	0.53	0.46	0.63	0.57	0.53	0.61	0.39	0.40	0.65	0.66	0.48	0.46	0.40	0.68
	MgO	0.91	0.84	0.92	0.74	0.84	0.75	0.97	1.09	0.98	0.74	0.73	0.91	0.97	1.05	0.81
	Sum	96.26	95.64	96.31	96.04	96.32	95.95	96.25	95.87	95.42	95.52	95.22	95.51	95.95	95.61	96.16
Conversion factor		4.07	4.01	3.99	3.99	3.98	3.99	3.99	4.02	3.95	4.02	4.04	3.97	4.00	3.97	3.98
Moles (normalised for 11 oxygens)	Si	3.16	3.09	3.09	3.07	3.09	3.07	3.11	3.12	3.05	3.07	3.05	3.03	3.09	3.06	3.07
	Al	2.79	2.72	2.72	2.75	2.73	2.77	2.68	2.65	2.62	2.71	2.75	2.66	2.70	2.61	2.75
	K	0.97	0.96	0.96	0.94	0.95	0.95	0.96	0.98	0.97	0.97	0.98	0.99	0.97	0.97	0.94
	Ca	0.00	0.00	0.00	0.00	0.00	0.00	0.00	0.00	0.00	0.00	0.00	0.00	0.00	0.00	0.00
	Ti	**0.02**	**0.02**	**0.02**	**0.03**	**0.02**	**0.02**	**0.03**	**0.02**	**0.03**	**0.05**	**0.05**	**0.02**	**0.01**	**0.04**	**0.02**
	Cr	0.00	0.00	0.00	0.00	0.00	0.00	0.00	0.00	0.00	0.00	0.00	0.00	0.00	0.00	0.00
	Mn	0.00	0.00	0.00	0.00	0.00	0.00	0.00	0.00	0.00	0.00	0.00	0.00	0.00	0.00	0.00
	Fe	0.09	0.09	0.10	0.09	0.09	0.09	0.09	0.12	0.10	0.09	0.09	0.10	0.10	0.11	0.08
	Na	0.08	0.07	0.06	0.08	0.07	0.07	0.08	0.05	0.05	0.08	0.09	0.06	0.06	0.05	0.09
	Mg	0.09	0.08	0.09	0.07	0.08	0.07	0.10	0.11	0.10	0.07	0.07	0.09	0.10	0.10	0.08
[Mg/(Fe+Mg)]		0.50	0.48	0.47	0.45	0.47	0.46	0.51	0.48	0.48	0.44	0.46	0.47	0.49	0.49	0.49
T(°C) at 4 kbar		524	541	533	564	542	527	567	531	566	657	656	543	460	646	522
SD (P ± 1kbar)		5	5	5	5	5	5	5	5	5	6	6	5	4	6	5
Average T per sample		**559**														
SD (°C) on average		55														

Table VI-5: Isotope and geochronology data used to build the graph of Figure V-11. Ms: Muscovite (1/5)

Hinter Land /Foreland	Zone	Rock type and sampling area	Sample	Proxy	δD_{water} [‰]	Uncertainty [‰]	$\delta^{18}O_{water}$ [‰]	Uncertainty [‰]	Age [Ma]	Uncertainty [Ma]	Isotope data (reference) Ages (reference)
HINTERLAND	Southern part of the Armorican Massif, France	Quiberon granite, Quiberon detachment footwall	QUIB01	Ms	-72	6	*-10.3*	*0.8*	319.5	0.9	
			QUIB01	Ms	-72	6	*-10.3*	*0.8*	307.7	0.7	δD_{Ms} values (this study)
			QUIB03	Ms	-70	6	*-10.0*	*0.8*	304.8	1.0	Ar/Ar on muscovite (this study)
			QUIB03	Ms	-70	6	*-10.0*	*0.8*	303.3	1.0	
			QUIB02	Ms	-66	6	*-9.5*	*0.8*	*308.8*	*1.0*	δD_{Ms} values (this study) Average from Ar/Ar dates (samples QUIB01 and 03, this study)
		Guérande granite. Piriac-sur-mer detachment footwall	PIR01	Ms	-71	3	*-10.1*	*0.3*	322.4	1.0	
			PIR01	Ms	-71	3	*-10.1*	*0.4*	306.2	0.5	
			PIR06	Ms	-65	3	*-9.4*	*0.4*	318.5	0.9	δD_{Ms} values (this study)
			PIR06	Ms	-65	3	*-9.4*	*0.4*	312.8	0.5	
			PIR11	Ms	-76	3	*-10.8*	*0.4*	318.6	0.7	Ar/Ar on muscovite (this study)
			PIR16	Ms	-77	3	*-10.9*	*0.4*	308.5	0.6	
			PIR16	Ms	-77	3	*-10.9*	*0.4*	305.4	0.7	
			PIR02	Ms	-72	3	*-10.2*	*0.4*	*313.2*	*1.3*	
			PIR03	Ms	-70	3	*-10.0*	*0.4*	*313.2*	*1.3*	
			PIR04	Ms	-69	3	*-9.8*	*0.4*	*313.2*	*1.3*	
			PIR05	Ms	-74	3	*-10.5*	*0.4*	*313.2*	*1.3*	
			PIR07	Ms	-68	3	*-9.8*	*0.4*	*313.2*	*1.3*	
			PIR08	Ms	-69	3	*-9.9*	*0.4*	*313.2*	*1.3*	
			PIR09	Ms	-71	3	*-10.1*	*0.4*	*313.2*	*1.3*	
			PIR10	Ms	-74	3	*-10.5*	*0.4*	*313.2*	*1.3*	
			PIR12	Ms	-66	3	*-9.5*	*0.4*	*313.2*	*1.3*	
			PIR13	Ms	-73	3	*-10.4*	*0.4*	*313.2*	*1.3*	δD_{Ms} values (this study)
			PIR14	Ms	-70	3	*-10.0*	*0.4*	*313.2*	*1.3*	
			PIR15	Ms	-77	3	*-10.9*	*0.4*	*313.2*	*1.3*	Average from Ar/Ar ages (samples PIR01, 06, 11 and 16, this study)
			GUE6	Ms	-74	3	*-10.5*	*0.4*	*313.2*	*1.3*	
			GUE7	Ms	-69	3	*-9.9*	*0.4*	*313.2*	*1.3*	
			GUE9	Ms	-74	3	*-10.5*	*0.4*	*313.2*	*1.3*	
			GUE21	Ms	-75	3	*-10.6*	*0.4*	*313.2*	*1.3*	
			GUE12-11	Ms	-70	3	*-10.0*	*0.4*	*313.2*	*1.3*	
			GUE12-12	Ms	-73	3	*-10.4*	*0.4*	*313.2*	*1.3*	
			GUE12-13	Ms	-70	3	*-10.0*	*0.4*	*313.2*	*1.3*	
			GUE12-14	Ms	-70	3	*-10.0*	*0.4*	*313.2*	*1.3*	
			GUE12-17	Ms	-69	3	*-9.9*	*0.4*	*313.2*	*1.3*	

Table VI-5: Isotope and geochronology data used to build the graph of Figure V-11. Ms: Muscovite (2/5)

Hinter Land /Forel and	Zone	Rock type and sampling area	Sample	Proxy	δD_{water} [‰]	Uncertainty [‰]	$\delta^{18}O_{water}$ [‰]	Uncertainty [‰]	Age [Ma]	Uncertainty [Ma]	Isotope data (reference) Ages (reference)
HINTERLAND	Western part of the French Massif Central	Mille vaches granite, Felletin detachment footwall	MIL18A	Ms	-82	5	*-11.5*	*0.6*	*313.6*	*9.2*	
			MIL18B	Ms	-88	5	*-12.2*	*0.6*	*313.6*	*9.2*	
			MIL18C	Ms	-86	8	*-11.9*	*1.0*	*313.6*	*9.2*	
			MIL18D	Ms	-91	5	*-12.6*	*0.6*	*313.6*	*9.2*	δD_{Ms} values (this study)
			MIL18E	Ms	-90	5	*-12.5*	*0.6*	*313.6*	*9.2*	
			MIL18F	Ms	-85	5	*-11.8*	*0.6*	*313.6*	*9.2*	Average from samples 524 and 3 (Gébelin, 2004)
			MIL18G	Ms	-85	5	*-11.8*	*0.6*	*313.6*	*9.2*	
			MIL18H	Ms	-104	3	*-14.2*	*0.4*	*313.6*	*9.2*	
			MIL18I	Ms	-83	5	*-11.7*	*0.6*	*313.6*	*9.2*	
			MIL19	Ms	-95	5	*-13.1*	*0.6*	*313.6*	*9.2*	
			3	Ms	-87	8	*-12.1*	*1.0*	321.1	3.1	
			3	Ms	-87	8	*-12.1*	*1.0*	310.7	2.9	
			3	Ms	-87	8	*-12.1*	*1.0*	321.8	1.3	
			3	Ms	-87	8	*-12.1*	*1.0*	325.0	1.4	
			3	Ms	-87	8	*-12.1*	*1.0*	310.9	2.5	
			3	Ms	-87	8	*-12.1*	*1.0*	306.5	1.6	
			3	Ms	-87	8	*-12.1*	*1.0*	307.8	0.8	δD_{Ms} values (this study)
			3	Ms	-87	8	*-12.1*	*1.0*	309.0	1.0	
			3	Ms	-87	8	*-12.1*	*1.0*	315.7	3.2	Ar/Ar on muscovite (Gébelin. 2004)
			524	Ms	-76	8	*-10.8*	*1.0*	310.1	1.7	
			524	Ms	-76	8	*-10.8*	*1.0*	315.1	1.6	
			524	Ms	-76	8	*-10.8*	*1.0*	303.9	6.8	
			524	Ms	-76	8	*-10.8*	*1.0*	318.3	2.6	
			524	Ms	-76	8	*-10.8*	*1.0*	313.9	4.2	
			524	Ms	-76	8	*-10.8*	*1.0*	314.7	2.5	

Table VI-5: Isotope and geochronology data used to build the graph of Figure V-11. Ms: Muscovite (3/5)

Hinterland /Foreland	Zone	Rock type and sampling area	Sample	Proxy	δD_{water} [‰]	Uncertainty [‰]	$\delta^{18}O_{water}$ [‰]	Uncertainty [‰]	Age [Ma]	Uncertainty [Ma]	Isotope data (reference) Ages (reference)
FORELAND	Southern Spain	Puertollano basin	LP1	Shark tooth	*-3.6*	*13*	-1.7	1.6	302	2	$\delta^{18}O_{Phosphate}$ values of shark remains (Fischer et al. 2013) Stephanian C (Gzhelian/Asselian; (e.g. Schneider et al., 2000)
			TP1	Shark tooth	*-1.2*	*13*	-1.4	1.6	302	2	
			OP1	Shark tooth	*2.8*	*13*	-0.9	1.6	302	2	
			OP2	Shark tooth	*1.2*	*13*	-1.1	1.6	302	2	
			OP3	Shark tooth	*-0.4*	*13*	-1.3	1.6	302	2	
			OP4	Shark tooth	*1.2*	*13*	-1.1	1.6	302	2	
			OP5	Shark tooth	*14.8*	*13*	0.6	1.6	302	2	
	NW part of the French Massif Central	Bourbon l'Archambault basin	LBS 1A	Shark spine	*-13.2*	*13*	-2.9	1.6	292.5	2.5	$\delta^{18}O_{Phosphate}$ values of shark remains (Fischer et al. 2013) Sakmarian (e.g. Roscher and Schneider, 2005; Schneider and Werneburg, 2006)
			LBS 1B	Shark spine	*-12.4*	*13*	-2.8	1.6	292.5	2.5	
			LBS 2	Shark spine	*-15.6*	*13*	-3.2	1.6	292.5	2.5	
			LBS 2A	Shark spine	*-14.8*	*13*	-3.1	1.6	292.5	2.5	
			LBS 2B	Shark spine	*-13.2*	*13*	-2.9	1.6	292.5	2.5	
			LBS 2C	Shark spine	*-14*	*13*	-3	1.6	292.5	2.5	
			LBS 3	Shark spine	*-22*	*13*	-4	1.6	292.5	2.5	
			LBS 3A	Shark spine	*-19.6*	*13*	-3.7	1.6	292.5	2.5	
			LBS 3B	Shark spine	*-22.8*	*13*	-4.1	1.6	292.5	2.5	
			OB1	Shark tooth	*-14.8*	*13*	-3.1	1.6	292.5	2.5	
			OBS 1a	Shark spine	*-14*	*13*	-3	1.6	292.5	2.5	
			OBS 2a	Shark spine	*-17.2*	*13*	-3.4	1.6	292.5	2.5	
			OBS 1b	Shark spine	*-18.8*	*13*	-3.6	1.6	292.5	2.5	
			OBS 2b	Shark spine	*-13.2*	*13*	-2.9	1.6	292.5	2.5	
			OBS 3b	Shark spine	*-6.8*	*13*	-2.1	1.6	292.5	2.5	
			OBS 4b	Shark spine	*-7.6*	*13*	-2.2	1.6	292.5	2.5	
			OBS 5b	Shark spine	*-16.4*	*13*	-3.3	1.6	292.5	2.5	

Table VI-5: Isotope and geochronology data used to build the graph of Figure V-11. Ms: Muscovite (4/5)

Hinterland /Foreland	Zone	Rock type and sampling area	Sample	Proxy	δD_{water} [‰]	Uncertainty [‰]	$\delta^{18}O_{water}$ [‰]	Uncertainty [‰]	Age [Ma]	Uncertainty [Ma]	Isotope data (reference) Ages (reference)
FORELAND	southwestern Sardinia, Italy	Guardia Pisano basin	LS 1	Shark tooth	*-6.8*	*13*	-2.1	1.6	297	5	$\delta^{18}O_{Phosphate}$ values of shark remains (Fischer et al. 2013) U–Pb SHRIMP - Gzhelian to Asselian (Pittau et al., 2002; Fischer et al., 2010)
			LS 2	Shark tooth	*-2*	*13*	-1.5	1.6	297	5	
			LS 3	Shark tooth	*-3.6*	*13*	-1.7	1.6	297	5	
			LS 4	Shark tooth	*-3.6*	*13*	-1.7	1.6	297	5	
			LS 5	Shark tooth	*-3.6*	*13*	-1.7	1.6	297	5	
			LS 6	Shark tooth	*-2*	*13*	-1.5	1.6	297	5	
			LS 7	Shark spine	*-11.6*	*13*	-2.7	1.6	297	5	
			LS 8	Shark spine	*-6*	*13*	-2	1.6	297	5	
			LS 9	Shark spine	*-6*	*13*	-2	1.6	297	5	
			LS 10	Shark spine	*-6.8*	*13*	-2.1	1.6	297	5	
			LS 11	Shark spine	*-9.2*	*13*	-2.4	1.6	297	5	
			LS 12	Shark spine	*-9.2*	*13*	-2.4	1.6	297	5	
			LS 13	Shark spine	*-9.2*	*13*	-2.4	1.6	297	5	
			LS 14	Shark spine	*-8.4*	*13*	-2.3	1.6	297	5	
			LS 15	Shark spine	*-2.8*	*13*	-1.6	1.6	297	5	
			LS 16	Shark spine	*-4.4*	*13*	-1.8	1.6	297	5	
			LS 17	Shark spine	*-5.2*	*13*	-1.9	1.6	297	5	
			LS 18	Shark spine	*-5.2*	*13*	-1.9	1.6	297	5	
			LS 19	Shark spine	*-6.8*	*13*	-2.1	1.6	297	5	
			LS 20	Shark spine	*-10.8*	*13*	-2.6	1.6	297	5	
			LS 21	Shark scale	*-8.4*	*13*	-2.3	1.6	297	5	
			LS 22	Shark scale	*-10*	*13*	-2.5	1.6	297	5	
			LS 23	Shark scale	*-14*	*13*	-3	1.6	297	5	

Table VI-5: Isotope and geochronology data used to build the graph of Figure V-11. Ms: Muscovite (5/5)

Hinterland /Foreland	Zone	Rock type and sampling area	Sample	Proxy	δD_{water} [‰]	Uncertainty [‰]	$\delta^{18}O^{water}$ [‰]	Uncertainty [‰]	Age [Ma]	Uncertainty [Ma]	Isotope data (reference) Ages (reference)
	Southern part of the French Massif Central	Espinouse detachment, Montagne Noire	MNC01A	Muscovite	-42	3	*-6.5*	*0.4*	297	2.8	
			MNC01B	Muscovite	-39	3	*-6.1*	*0.4*	297	2.8	
			MN12-15	Muscovite	-39	3	*-6.1*	*0.4*	297	2.8	
			MNC02	Muscovite	-39	3	*-6.2*	*0.4*	297	2.8	
			MNC03	Muscovite	-42	3	*-6.5*	*0.4*	297	2.8	
			MNC04	Muscovite	-35	3	*-5.7*	*0.4*	297	2.8	
			MNC05	Muscovite	-43	3	*-6.6*	*0.4*	297	2.8	
			MNC06A	Muscovite	-36	3	*-5.7*	*0.4*	297	2.8	
			MNC06B	Muscovite	-34	3	*-5.6*	*0.4*	297	2.8	
			MN12-10	Muscovite	-35	3	*-5.7*	*0.4*	297	2.8	
			MN12-05	Muscovite	-43	3	*-6.6*	*0.4*	297	2.8	
			MNC01A	Biotite	-43	3	*-6.6*	*0.4*	297	2.8	δD values of muscovite. biotite and tourmaline (this study)
			MNC01B	Biotite	-31	3	*-5.1*	*0.4*	297	2.8	
			MN12-15	Biotite	-30	3	*-5.0*	*0.4*	297	2.8	Ar/Ar on muscovite (Maluski et al. 1991)
			MNC02	Biotite	-36	3	*-5.8*	*0.4*	297	2.8	
			MNC04	Biotite	-23	3	*-4.1*	*0.4*	297	2.8	
			MNC06B	Biotite	-27	3	*-4.7*	*0.4*	297	2.8	
			MN12-10	Biotite	-25	3	*-4.4*	*0.4*	297	2.8	
			MN12-05	Biotite	-27	3	*-4.6*	*0.4*	297	2.8	
			MNC01A	Tourmaline	-34	4	*-5.5*	*0.5*	297	2.8	
			MNC01B	Tourmaline	-29	4	*-4.9*	*0.5*	297	2.8	
			MNC02	Tourmaline	-25	4	*-4.4*	*0.5*	297	2.8	
			MNC03	Tourmaline	-34	4	*-5.4*	*0.5*	297	2.8	
			MNC04	Tourmaline	-25	4	*-4.3*	*0.5*	297	2.8	
			MNC06A	Tourmaline	-25	4	*-4.3*	*0.5*	297	2.8	

VII. REFERENCES

Aerden, D.G.A.M., and Malavieille, J., 1999, Origin of a large-scale fold nappe in the Montagne Noire, Variscan belt, France: Journal of Structural Geology, v. 21, p. 1321–1333, doi:10.1016/S0191-8141(99)00098-X.

Aldaz, L., and Deutsch, S., 1967, On a relationship between air temperature and oxygen isotope ratio of snow and firn in the south pole region: Earth and Planetary Science Letters, v. 3, p. 267–274, doi:10.1016/0012-821X(67)90047-7.

Ambach, W., Dansgaard, W., Eisner, H., and Mollner, J., 1968, The altitude effect on the isotopic composition of precipitation and glacier ice in the Alps: Tellus, v. 20, p. 595–600.

Amiot, R., Lécuyer, C., Escarguel, G., Billon-Bruyat, J.-P., Buffetaut, E., Langlois, C., Martin, S., Martineau, F., and Mazin, J.-M., 2007, Oxygen isotope fractionation between crocodilian phosphate and water: Palaeogeography, Palaeoclimatology, Palaeoecology, v. 243, p. 412–420, doi:10.1016/j.palaeo.2006.08.013.

Arthaud, F., 1970, Etude tectonique et microtectonique comparée de deux domaines hercyniens: les Nappes de la Montagne Noire (France) et l'anticlinorium de l'Iglesiente (Sardaigne): style des déformations successives, notions de sous-faciès, de faciès et de profils tectoniq: Université des Sciences et Techniques du Languedoc, 175 p.

Augier, R., Choulet, F., Faure, M., and Turrillot, P., 2015, A turning-point in the evolution of the Variscan orogen: the ca. 325 Ma regional partial-melting event of the coastal South Armorican domain (South Brittany and Vendée, France): Bulletin de la Société Géologique de France, doi:10.2113/gssgfbull.186.2-3.63.

Bakker, R., 2017, Re-Equilibration Processes in Fluid Inclusion Assemblages: Minerals, v. 7, p. 117, doi:10.3390/min7070117.

Ballèvre, M., Bosse, V., Dabard, M., Fourcade, S., Paquette, J., Peucat, J., and Pitra, P., 2013, Histoire géologique du Massif armoricain : actualité de la recherche: Bull. Soc. géol. minéral. Bretagne, v. 10–11, p. 5–96, https://hal-insu.archives-ouvertes.fr/insu-00873116.

Ballèvre, M., Fourcade, S., Capdevila, R., Peucat, J.-J., Cocherie, A., and Fanning, C.M., 2012, Geochronology and geochemistry of Ordovician felsic volcanism in the Southern Armorican Massif (Variscan belt, France): Implications for the breakup of Gondwana: Gondwana Research, v. 21, p. 1019–1036, doi:10.1016/j.gr.2011.07.030.

Ballouard, C. et al., 2017, Magmatic and hydrothermal behavior of uranium in syntectonic leucogranites: The uranium mineralization associated with the Hercynian Guérande granite (Armorican Massif, France): Ore Geology Reviews, v. 80, p. 309–331, doi:10.1016/j.oregeorev.2016.06.034.

Ballouard, C., Boulvais, P., Poujol, M., Gapais, D., Yamato, P., Tartèse, R., and Cuney, M., 2015, Tectonic record , magmatic history and hydrothermal alteration in the Hercynian Guérande leucogranite , Armorican Massif , France: LITHOS, v. 220–223, p. 1–22, doi:10.1016/j.lithos.2015.01.027.

Ballouard, C., Poujol, M., Boulvais, P., Branquet, Y., Tart??se, R., Vigneresse, J.L., Tartèse, R., and Vigneresse, J.L., 2016, Nb-Ta fractionation in peraluminous granites: A marker of the magmatic-hydrothermal transition: Geology, v. 44, p. 231–234, doi:10.1130/G37475.1.

Ballouard, C., Poujol, M., Mercadier, J., Deloule, E., Boulvais, P., Baele, J.M., Cuney, M., and Cathelineau, M., 2018, Uranium metallogenesis of the peraluminous leucogranite from the Pontivy-Rostrenen magmatic complex (French Armorican Variscan belt): the result of long-term oxidized hydrothermal alteration during strike-slip deformation: Mineralium Deposita, v. 53, p. 601–628, doi:10.1007/s00126-017-0761-5.

Banks, M.R., 1985, Paleogeographic development of the Tasmania Basin in the late Paleozoic, *in* Sixth Gondwana Symposium, Columbus, Ohio, p. 7.

Barth, N.C., Hacker, B.R., Seward, G.G.E., Walsh, E.O., Young, D., and Johnston, S., 2010, Strain within the ultrahigh-pressure Western Gneiss region of Norway recorded by quartz CPOs: Geological Society, London, Special Publications, v. 335, p. 663–685, doi:10.1144/SP335.27.

Bauer, P., Palm, S., and Handy, M.R., 2000, Strain localization and fluid pathways in mylonite: inferences from in situ deformation of a water-bearing quartz analogue (norcamphor):, www.elsevier.com/locate/tecto (accessed January 2019).

Beaudoin, G., Taylor, B.E., and Sangster, D.F., 1991, Silver-lead-zinc veins, metamorphic core complexes, and hydrologic regimes during crustal extension: Geology, v. 19, p. 1217, doi:10.1130/0091-7613(1991)019<1217:SLZVMC>2.3.CO;2.

Beaumont, C., Jamieson, R. a., Nguyen, M.H., and Lee, B., 2001, Himalayan tectonics explained by extrusion of a low-viscosity crustal channel coupled to focused surface denudation: Nature, v. 414, p. 738–742, doi:10.1038/414738a.

Becq-Giraudon, J.-F., and Van Den Driessche, J., 1994, Stephano-Autunian periglacial deposits in the French Massif Central as markers of the collapse of a high Hercynian plateau: Comptes Rendus de l'Académie des Sciences, v. 318, p. 675–682.

Becq-Giraudon, J.-F., Montenat, C., and Van Den Driessche, J., 1996, Hercynian high-altitude phenomena in the French Massif Central: tectonic implications: Palaeogeography, Palaeoclimatology, Palaeoecology, v. 122, p. 227–241, doi:10.1016/0031-0182(95)00081-X.

Bellot, J.P., 2007, Extensional deformation assisted by mineralised fluids within the brittle-ductile transition: Insights from the southwestern Massif Central, France: Journal of Structural Geology, v. 29, p. 225–240, doi:10.1016/j.jsg.2006.09.004.

Bellot, J.P., 2008, Hydrothermal fluids assisted crustal-scale strike-slip on the Argentat fault zone: Tectonophysics, v. 450, p. 21–33, doi:10.1016/j.tecto.2007.12.00.

Bernard-Griffiths, J., Peucat, J.J., Sheppard, S., and Vidal, P., 1985, Petrogenesis of Hercynian leucogranites from the southern Armorican Massif: contribution of REE and isotopic (Sr, Nd, Pb and O) geochemical data to the study of source rock characteristics and ages: Earth and Planetary Science Letters, v. 74, p. 235–250, doi:10.1016/0012-821X(85)90024-X.

Bernard, A. et al., 2010, Regulation of Body Temperature by Some Mesozoic Marine Reptiles: Science, v. 328, p. 1379–1382, doi:10.1126/science.1187443.

Blamart, D., Pichavant, M., and Sheppard S.M.F., 1989, Détemination du fractionnement isotopique D/H entre tourmaline et eau à 600, 500 C et 3 Kb: Comptes rendus de l'Académie des Sciences (Paris), v. 308, p. 39–44.

Blisniuk, P.M., and Stern, L.A., 2005, Stable Isotope Paleoaltimetry: a critical review: American Journal of Science, v. 305, p. 1033–1074.

Blumenfeld, P., Mainprice, D., and Bouchez, J.L.L., 1986, C-slip in quartz from subsolidus deformed granite: Tectonophysics, v. 127, p. 97–115, doi:10.1016/0040-1951(86)90081-8.

Bodnar, R.J., 1993, Revised equation and table for determining the freezing point depression of H2O-NaCl solutions: Geochimica et Cosmochimica Act1, v. 57, p. 683–684.

Boiron, M.C., Cathelineau, M., Banks, D.A., Fourcade, S., and Vallance, J., 2003, Mixing of metamorphic and surficial fluids during the uplift of the Hercynian upper crust: Consequences for gold deposition: Chemical Geology, v. 194, p. 119–141, doi:10.1016/S0009-2541(02)00274-7.

Boos, W.R.W.R.W.R., and Kuang, Z., 2010, Dominant control of the South Asian monsoon by orographic insulation versus plateau heating.: Nature, v. 463, p. 218–222, doi:10.1038/nature08707.

Bosse, V., Ballèvre, M., and Vidal, O., 2002, Ductile thrusting recorded by the garnet isograd from blueschist-facies metapelites of the Ile de Groix, Armorican Massif, France: Journal of Petrology, v. 43, p. 485–510, doi:10.1093/petrology/43.3.485.

Bosse, V., Féraud, G., Ballèvre, M., Peucat, J.-J., and Corsini, M., 2005, Rb–Sr and 40Ar/39Ar ages in blueschists from the Ile de Groix (Armorican Massif, France): Implications for closure mechanisms in isotopic systems: Chemical Geology, v. 220, p. 21–45, doi:10.1016/j.chemgeo.2005.02.019.

Bossière, G., 1988, Evolutions chimico-minéralogiques du grenat et de la muscovite au voisinage de l'isograde biotite-staurotide dans un métamorphisme prograde de type barrovien: un exemple en Vendée littorale (Massif Armoricain).: Comptes rendus de l'Académie des sciences. Série 2, Mécanique, Physique, Chimie, Sciences de l'univers, Sciences de la Terre, v. 306, p. 135–140.

Boucot, A.J., Xu, C., Scotese, C.R., and Morley, R.J., 2013, Phanerozoic Paleoclimate: An Atlas of Lithologic Indicators of Climate: Tulsa, Oklahoma, U.S.A., SEPM (Society for Sedimentary Geology), doi:10.2110/sepmcsp.11.

Braun, J., 2010, The many surface expressions of mantle dynamics: Nature Geoscience, v. 3, p. 825–833, doi:10.1038/ngeo1020.

BRGM, 2003, Carte géologique de la France au 1/1 000 000ème,6ème édition révisée.:

Brown, M., and Dallmeyer, R.D.R., 1996, Rapid Variscan exhumation and the role of magma in core complex formation: southern Brittany metamorphic belt, France: Journal of Metamorphic Geology, v. 14, p. 361–379, doi:10.1111/j.1525-1314.1996.00361.x.

Bruguier, O., Becq-Giraudon, J.., Champenois, M., Deloule, E., Ludden, J., and Mangin, D., 2003, Application of in situ zircon geochronology and accessory phase chemistry to constraining basin development during post-collisional extension: a case study

from the French Massif Central: Chemical Geology, v. 201, p. 319–336, doi:10.1016/j.chemgeo.2003.08.005.

Brun, J.-P., and van den Driessche, J., 1994, Extensional gneiss domes and detachment fault systems; structure and kinematics: Bulletin de la Societe Geologique de France, v. 165, p. 519–530.

Buggisch, W., Joachimski, M.M., Sevastopulo, G., and Morrow, J.R., 2008a, Mississippian δ13Ccarb and conodont apatite δ18O records — Their relation to the Late Palaeozoic Glaciation: Palaeogeography, Palaeoclimatology, Palaeoecology, v. 268, p. 273–292, doi:10.1016/j.palaeo.2008.03.043.

Buggisch, W., Joachimski, M.M., Sevastopulo, G., and Morrow, J.R., 2008b, Mississippian δ13Ccarb and conodont apatite δ18O records — Their relation to the Late Palaeozoic Glaciation: Palaeogeography, Palaeoclimatology, Palaeoecology, v. 268, p. 273–292, doi:10.1016/j.palaeo.2008.03.043.

Bukovská, Z., Jeřábek, P., and Morales, L.F.G., 2016, Major softening at brittle-ductile transition due to interplay between chemical and deformation processes: An insight from evolution of shear bands in the South Armorican Shear Zone: Journal of Geophysical Research: Solid Earth, v. 121, p. 1158–1182, doi:10.1002/2015JB012319.

Burchfiel, B.C., and Royden, L.H., 1985, North-south extension within the convergent Himalayan region: Geology, v. 13, p. 679, doi:10.1130/0091-7613(1985)13<679:NEWTCH>2.0.CO;2.

Burg, J.P., 1983, Tectogenèse comparée de deux segments de chaîne de collision: Le Sud du Tibet (Suture du Tsangpo) et La Chaîne Hercynienne en Europe (sutures du Massif Central). Thèse d'Ètat, Université des Sciences et Techniques du Languedoc, Montpellier,: Université des Sciences et Techniques du Languedoc, Montpellier, France, 361 p.

Cagnard, F., 2005, Compression de lithosphères continentales "chaudes" : application à la tectonique précambrienne: Rennes 1, http://www.theses.fr/2005REN1S182 (accessed June 2015).

Cagnard, F., Gapais, D., Brun, J.P., Gumiaux, C., and Van den Driessche, J., 2004, Late pervasive crustal-scale extension in the south Armorican Hercynian belt (Vendée, France): Journal of Structural Geology, v. 26, p. 435–449, doi:10.1016/j.jsg.2003.08.006.

Campani, M., Mulch, A., Kempf, O., Schlunegger, F., and Mancktelow, N., 2012, Miocene paleotopography of the Central Alps: Earth and Planetary Science Letters, v. 337–338, p. 174–185, doi:10.1016/j.epsl.2012.05.017.

Capetta, H., 1987, Chondrichthyes II, Mesozoic and Cenozoic Elasmobranchii, *in* Handbook of Paleoichthyology 3B., Stuttgart–New York., Gustav Fischer Verlag, doi:10.1080/02724634.1988.10011678.

Le Carlier de Veslud, C., Alexandre, P., Cuney, M., Ruffet, G., Cheilletz, A., and Virlogeux, D., 2004, Thermochronology 40Ar/39Ar et évolution thermique des granitoïdes mésovarisques du complexe plutonique de Charroux-Civray (Seuil du Poitou): Bulletin de la Societé Géologique de France, v. 2, p. 95–106.

Carlson, J.K., Ribera, M.M., Conrath, C.L., Heupel, M.R., and Burgess, G.H., 2010, Habitat

use and movement patterns of bull sharks Carcharhinus leucas determined using pop-up satellite archival tags: Journal of Fish Biology, v. 77, p. 661–675, doi:10.1111/j.1095-8649.2010.02707.x.

Carosi, R., Lombardo, B., Molli, G., Musumeci, G., and Pertusati, P.C., 1998, The south Tibetan detachment system in the Rongbuk valley, Everest region. Deformation features and geological implications: Journal of Asian Earth Sciences, v. 16, p. 299–311, doi:10.1016/S0743-9547(98)00014-2.

Cartannaz, C., Rolin, P., Cocherie, A., Marquer, D., Legendre, O., Fanning, C.M., and Rossi, P., 2007, Characterization of wrench tectonics from dating of syn- to post-magmatism in the north-western French Massif Central: International Journal of Earth Sciences, v. 96, p. 271–287, doi:10.1007/s00531-006-0101-y.

Carter, M.J., Siebenaller, L., and Teyssier, C., 2015, Orientation, composition, and entrapment conditions of fluid inclusions in the footwall of the northern Snake Range detachment, Nevada: Journal of Structural Geology, v. 81, p. 106–124, doi:10.1016/j.jsg.2015.11.001.

Cassel, E.J., Graham, S.A., and Chamberlain, C.P., 2009, Cenozoic tectonic and topographic evolution of the northern Sierra Nevada, California, through stable isotope paleoaltimetry in volcanic glass: Geology, v. 37, p. 547–550, doi:10.1130/G25572A.1.

Castonguay, S., Ruffet, G., and Tremblay, A., 2007, Dating polyphase deformation across low-grade metamorphic belts: An example based on 40Ar/39Ar muscovite age constraints from the southern Quebec Appalachians, Canada: Geological Society of America Bulletin, v. 119, p. 978–992, doi:10.1130/B26046.1.

Castonguay, S., Ruffet, G., Tremblay, A., and Féraud, G., 2001, Tectonometamorphic evolution of the southern Quebec Appalachians: 40Ar/39Ar evidence for Middle Ordovician crustal thickening and Silurian–Early Devonian exhumation of the internal Humber zone: Geological Society of America Bulletin, v. 113, p. 144–160, doi:10.1130/0016-7606(2001)113<0144:TEOTSQ>2.0.CO;2.

Cawood, P.A., and Buchan, C., 2007, Linking accretionary orogenesis with supercontinent assembly: Earth-Science Reviews, v. 82, p. 217–256, doi:10.1016/j.earscirev.2007.03.003.

Chacko, T., Hu, X., Mayeda, T.K., Clayton, R.N., and Goldsmith, J.R., 1996, Oxygen isotope fractionations in muscovite, phlogopite, and rutile: Geochimica et Cosmochimica Acta, v. 60, p. 2595–2608, doi:10.1016/0016-7037(96)00112-3.

Chamberlain, C.P. et al., 2012, The cenozoic climatic and topographic evolution of the western north American Cordillera: American Journal of Science, v. 312, p. 213–262, doi:10.2475/02.2012.05.

Chardon, D., Choukroune, P., and Jayananda, M., 1996, Strain patterns, décollement and incipient sagducted greenstone terrains in the Archaean Dharwar craton (south India): Journal of Structural Geology, v. 18, p. 991–1004, doi:10.1016/0191-8141(96)00031-4.

Chardon, D., Gapais, D., and Cagnard, F., 2009, Flow of ultra-hot orogens: A view from the Precambrian, clues for the Phanerozoic: Tectonophysics, v. 477, p. 105–118, doi:10.1016/j.tecto.2009.03.008.

Châteauneuf, J.-J. et al., 1989, Synthèse géologique des bassins permiens français: Mémoire du BRGM, v. 128, p. 304 p.

Cherniak, D.., Lanford, W.., and Ryerson, F.., 1991, Lead diffusion in apatite and zircon using ion implantation and Rutherford Backscattering techniques: Geochimica et Cosmochimica Acta, v. 55, p. 1663–1673, doi:10.1016/0016-7037(91)90137-T.

Cherniak, D.., and Watson, E.., 2001, Pb diffusion in zircon: Chemical Geology, v. 172, p. 5–24, doi:10.1016/S0009-2541(00)00233-3.

Chi-Hsiang, Y., and Shih-Tseng, K., 1978, Stratigraphy of the Mont JolmoLungma and its north slope: Sci. Sin., v. 5, p. 629–644.

Chi, G.X., and Lu, H.Z., 2008, Validation and representation of fluid inclusion microthermometric data using the fluid inclusion assemblage (FIA) concept.: Acta Petrologica Sinica, doi:10.1017/CBO9781107415324.004.

Cocherie, A., 2005, Electron-microprobe dating as a tool for determining the closure of Th-U-Pb systems in migmatitic monazites: American Mineralogist, v. 90, p. 607–618, doi:10.2138/am.2005.1303.

Cocks, L.R.M., and Torsvik, T.H., 2002, Earth geography from 500 to 400 million years ago: a faunal and palaeomagnetic review: Journal of the Geological Society, v. 159, p. 631–644, doi:10.1144/0016-764901-118.

Cogné, J., 1960, Métamorphismes et granitisations en liaison avec l'évolution orogénique en Bretagne méridionale: Bulletin de la Société Géologique de France, v. 187, p. 213–226, doi:10.2113/gssgfbull.S7-II.2.213.

Compston, W., Williams, I.S., Kirschvink, J.L., Zichao, Z., and Guogan, M.A., 1992, Zircon U-Pb ages for the Early Cambrian time-scale: Journal of the Geological Society, v. 149, p. 171–184, doi:10.1144/gsjgs.149.2.0171.

Coney, P.J., 1980, Cordilleran metamorphic core complexes: An overview.: Cordilleran metamorphic core complexes: Geological Society of America Memoir, v. 153, p. 7–31.

Coplen, T.B. et al., 2002, Compilation of minimum and maximum isotope ratios of selected elements in naturally occurring terrestrial materials and reagents.:

Courtnadge, J., 2016, Fluid-rock interaction and microstructure development of a Variscan detachment shear zone: Plymouth University, 59 p.

Craig, H., 1961, Isotopic Variations in Meteoric Waters: Science, v. 133, p. 1702–1703, doi:10.1126/science.133.3465.1702.

Cuney, M., Friedrich, M., Blumenfeld, P., Bourguignon, A., Boiron, M.C., Vigneresse, J.L., and Poty, B., 1990, Metallogenesis in the French part of the Variscan orogen. Part I: U preconcentrations in pre-Variscan and Variscan formations — a comparison with Sn, W and Au: Tectonophysics, v. 177, p. 39–57, doi:10.1016/0040-1951(90)90273-B.

Currie, B.S., Rowley, D.B., and Tabor, N.J., 2005, Middle Miocene paleoaltimetry of southern Tibet: Implications for the role of mantle thickening and delamination in the Himalayan orogen: Geology, v. 33, p. 181, doi:10.1130/G21170.1.

Dansgaard, W., 1964, Stable isotopes in precipitation: Tellus, v. 16, p. 436–468, doi:10.3402/tellusa.v16i4.8993.

Davis, G.H., 1983, Shear-zone model for the origin of metamorphic core complexes: Geology, v. 11, p. 342, doi:10.1130/0091-7613(1983)11<342:SMFTOO>2.0.CO;2.

Dera, G., Pucéat, E., Pellenard, P., Neige, P., Delsate, D., Joachimski, M.M., Reisberg, L., and Martinez, M., 2009, Water mass exchange and variations in seawater temperature in the NW Tethys during the Early Jurassic: Evidence from neodymium and oxygen isotopes of fish teeth and belemnites: Earth and Planetary Science Letters, v. 286, p. 198–207, doi:10.1016/J.EPSL.2009.06.027.

Dettman, D.L., and Lohmann, K.C., 2000, Oxygen isotope evidence for high-altitude snow in the Laramide Rocky Mountains of North America during the Late Cretaceous and Paleogene: Geology, v. 28, p. 243, doi:10.1130/0091-7613(2000)28<243:OIEFHS>2.0.CO;2.

Dewey, J.F., 1988, Extensional collapse of orogens: Tectonics, v. 7, p. 1123–1139, doi:10.1029/TC007i006p01123.

Dewey, J.F., and Burke, K.C.A., 1973, Tibetan, Variscan, and Precambrian Basement Reactivation: Products of Continental Collision: The Journal of Geology, v. 81, p. 683–692, doi:10.1086/627920.

Domeier, M., and Torsvik, T.H., 2014, Plate tectonics in the late Paleozoic: Geoscience Frontiers, v. 5, p. 303–350, doi:10.1016/j.gsf.2014.01.002.

Dörr, W., and Zulauf, G., 2010, Elevator tectonics and orogenic collapse of a Tibetan-style plateau in the European Variscides: the role of the Bohemian shear zone: International Journal of Earth Sciences, v. 99, p. 299–325, doi:10.1007/s00531-008-0389-x.

Van Den Driessche, J., and Brun, J.-P., 1992, Tectonic evolution of the Montagne Noire (french Massif Central): a model of extensional gneiss dome: Geodinamica Acta, v. 5, p. 85–97, doi:10.1080/09853111.1992.11105221.

Drummond, C.N., Wilkinson, B.H., Lohmann, K.C., and Smith, G.R., 1993, Effect of regional topography and hydrology on the lacustrine isotopic record of Miocene paleoclimate in the Rocky Mountains: Palaeogeography, Palaeoclimatology, Palaeoecology, v. 101, p. 67–79, doi:10.1016/0031-0182(93)90152-9.

Dusséaux, C., Gébelin, A., Boulvais, P., Gardien, V., Grimes, S., and Mulch, A., 2019, Meteoric fluid-rock interaction in Variscan shear zones: Terra Nova, v. accepted, doi:10.1111/ter.12392.

Echtler, H., 1990, Geometry and kinematics of recumbent folding and low-angle detachment in the Pardailhan nappe (Montagne Noire, Southern French Massif Central): Tectonophysics, v. 177, p. 109–123, doi:10.1016/0040-1951(90)90276-E.

Edel, J.B., Schulmann, K., Lexa, O., and Lardeaux, J.M., 2018, Late Palaeozoic palaeomagnetic and tectonic constraints for amalgamation of Pangea supercontinent in the European Variscan belt: Earth-Science Reviews, v. 177, p. 589–612, doi:10.1016/j.earscirev.2017.12.007.

Eggleton, R.A., and Buseck, P.R., 1980, The orthoclase-microcline inversion: A high-resolution transmission electron microscope study and strain analysis: Contributions to Mineralogy and Petrology, v. 74, p. 123–133, doi:10.1007/BF01131998.

Enax, J., Prymak, O., Raabe, D., and Epple, M., 2012a, Structure, composition, and mechanical properties of shark teeth: Journal of Structural Biology, v. 178, p. 290–299, doi:10.1016/j.jsb.2012.03.012.

Enax, J., Prymak, O., Raabe, D., and Epple, M., 2012b, Structure, composition, and mechanical properties of shark teeth: Journal of Structural Biology, v. 178, p. 290–299, doi:10.1016/j.jsb.2012.03.012.

Famin, V., Hébert, R., Philippot, P., and Jolivet, L., 2005, Ion probe and fluid inclusion evidence for co-seismic fluid infiltration in a crustal detachment: Contributions to Mineralogy and Petrology, v. 150, p. 354–367, doi:10.1007/s00410-005-0031-x.

Famin, V., Philippot, P., Jolivet, L., and Agard, P., 2004, Evolution of hydrothermal regime along a crustal shear zone, Tinos Island, Greece: Tectonics, v. 23, p. n/a-n/a, doi:10.1029/2003TC001509.

Fan, M., Constenius, K.N., and Dettman, D.L., 2017, Prolonged high relief in the northern Cordilleran orogenic front during middle and late Eocene extension based on stable isotope paleoaltimetry: Earth and Planetary Science Letters, v. 457, p. 376–384, doi:10.1016/j.epsl.2016.10.038.

Fan, M., Heller, P., Allen, S.D., and Hough, B.G., 2014, Middle Cenozoic uplift and concomitant drying in the central Rocky Mountains and adjacent Great Plains: Geology, v. 42, p. 547–550, doi:10.1130/G35444.1.

Faure, M., 1995, Late orogenic carboniferous extensions in the Variscan French Massif Central: Tectonics, v. 14, p. 132–153, doi:10.1029/94TC02021.

Faure, M., Bé Mézème, E., Duguet, M., Cartier, C., and Talbot, J.-Y., 2005, Paleozoic tectonic evolution of medio-europa from the example of the french massif central and massif armoricain: Journal of the Virtual Explorer, v. 19.

Faure, M., Cocherie, A., Gaché, J., Esnault, C., Guerrot, C., Rossi, P., Wei, L., and Qiuli, L., 2014, Middle Carboniferous intracontinental subduction in the Outer Zone of the Variscan Belt (Montagne Noire Axial Zone, French Massif Central): multimethod geochronological approach of polyphase metamorphism: Geological Society, London, Special Publications, v. 405, p. 289–311, doi:10.1144/SP405.2.

Faure, M., Lardeaux, J.-M., and Ledru, P., 2009, A review of the pre-Permian geology of the Variscan French Massif Central: Comptes Rendus Geoscience, v. 341, p. 202–213, doi:10.1016/j.crte.2008.12.001.

Faure, M., Leloix, C., and Roig, J.-Y., 1997, Polycyclic evolution of the Hercynian belt: Bulletin de la Société Géologique de France, v. 168, p. 695–705, http://apps.webofknowledge.com.elib.tcd.ie/full_record.do?product=UA&search_mode=GeneralSearch&qid=11&SID=P1nDeBx994FIWX4kLGl&page=1&doc=3&cacheurlFromRightClick=no.

Faure, M., Monié, P., Pin, C., Maluski, H., and Leloix, C., 2002, Late Visean thermal event in the northern part of the French Massif Central: new 40Ar/39Ar and Rb–Sr isotopic constraints on the Hercynian syn-orogenic extension: International Journal of Earth Sciences, v. 91, p. 53–75, doi:10.1007/s005310100202.

Favre, A., Päckert, M., Pauls, S.U., Jähnig, S.C., Uhl, D., Michalak, I., and Muellner-Riehl, A.N., 2014, The role of the uplift of the Qinghai-Tibetan Plateau for the evolution of Tibetan biotas.: Biological reviews, v. 90, p. 236–253, doi:10.1111/brv.12107.

Feist, R., and Galtier, J., 1985, Découverte de flores d'âge namurien probable dans le flysch à olistolites de Cabrières (Hérault). Implication sur la durée de la sédimentation synorogénique dans la Montagne Noire (France méridionale).: Comptes-rendus des séances de l'Académie des sciences. Série 2, Mécanique-physique, chimie, sciences de l'univers, sciences de la terre, v. 300, p. 207–2012.

Feng, R., Poulsen, C.J., Werner, M., Chamberlain, C.P., Mix, H.T., and Mulch, A., 2013, Early Cenozoic evolution of topography, climate, and stable isotopes in precipitation in the North American Cordillera: American Journal of Science, v. 313, p. 613–648, doi:10.2475/07.2013.01.

Field, C.W., and Fifarek, R.H., 1985, Light stable-isotope systematics in the epithermal environment, *in* Berger, B.R. and Bethke, P.M. eds., Geology and Geochemistry of Epithermal Systems, Boulder, Colorado, Colorado, Soc. of Econ. Geol., p. 99–128, doi:10.5382/Rev.02.06.

Fischer, J., Schneider, J.W., and Ronchi, A., 2010, New Hybondontoid Shark from the Permocarboniferous (Gzhelian—Asselian) of Guardia Pisano (Sardinia, Italy): Acta Palaeontologica Polonica, v. 55, p. 241–264, doi:10.4202/app.2009.0019.

Fischer, J., Schneider, J.W., Voigt, S., Joachimski, M.M., Tichomirowa, M., Tütken, T., Götze, J., and Berner, U., 2013, Oxygen and strontium isotopes from fossil shark teeth: Environmental and ecological implications for Late Palaeozoic European basins: Chemical Geology, v. 342, p. 44–62, doi:10.1016/j.chemgeo.2013.01.022.

Fischer, J., Voigt, S., Franz, M., Schneider, J.W., Joachimski, M.M., Tichomirowa, M., Götze, J., and Furrer, H., 2012, Palaeoenvironments of the late Triassic Rhaetian Sea: Implications from oxygen and strontium isotopes of hybodont shark teeth: Palaeogeography, Palaeoclimatology, Palaeoecology, v. 353–355, p. 60–72, doi:10.1016/J.PALAEO.2012.07.002.

Fluteau, F., Besse, J., Broutin, J., and Ramstein, G., 2001, The late Permian climate. What can be inferred from climate modelling concerning Pangea scenarios and Hercynian range altitude? Palaeogeography, Palaeoclimatology, Palaeoecology, v. 167, p. 39–71, doi:10.1016/S0031-0182(00)00230-3.

Fontes, J.-C., and Gonfiantini, R., 1967, Comportement isotopique au cours de l'evaporation de deux bassins sahariens: Earth and Planetary Science Letters, v. 3, p. 258–266, doi:10.1016/0012-821X(67)90046-5.

Franke, W., 2012, Comment on Dörr and Zulauf: Elevator tectonics and orogenic collapse of a Tibetan-style plateau in the European Variscides: the role of the Bohemian shear zone. Int J Earth Sci (Geol Rundsch) (2010) 99: 299–325: International Journal of Earth Sciences, v. 101, p. 2027–2034, doi:10.1007/s00531-012-0766-3.

Franke, W., 2014, Topography of the Variscan orogen in Europe: Failed-not collapsed: International Journal of Earth Sciences, v. 103, p. 1471–1499, doi:10.1007/s00531-014-1014-9.

Franke, W., Cocks, L.R.M., and Torsvik, T.H., 2017, The Palaeozoic Variscan oceans revisited: Gondwana Research, v. 48, p. 257–284, doi:10.1016/j.gr.2017.03.005.

Franke, W., Doublier, M.P., Klama, K., Potel, S., and Wemmer, K., 2011, Hot metamorphic core complex in a cold foreland: International Journal of Earth Sciences, v. 100, p. 753–785, doi:10.1007/s00531-010-0512-7.

Franke, W., and Engel, W., 1986a, Synorogenic sedimentation in the Variscan Belt of Europe: Bulletin de la Société géologique de France, http://bsgf.geoscienceworld.org/content/II/1/25.abstract (accessed June 2017).

Franke, W., and Engel, W., 1986b, Synorogenic sedimentation in the Variscan Belt of Europe: Bulletin de la Société Géologique de France, v. II, p. 25–33, doi:10.2113/gssgfbull.II.1.25.

Fréville, K., Cenki-Tok, B., Trap, P., Rabin, M., Leyreloup, A., Régnier, J.-L., and Whitney, D.L., 2016, Thermal interaction of middle and upper crust during gneiss dome formation: example from the Montagne Noire (French Massif Central): Journal of Metamorphic Geology, v. 34, p. 447–462, doi:10.1111/jmg.12188.

Freytet, P., Lebreton, M.L., and Paquette, Y., 1992, The carbonates of the Permian Lakes of North Massif central, France: Carbonates and Evaporites, v. 7, p. 122–131, doi:10.1007/BF03175626.

Fricke, H.C., Wickham, S.M., and O'Neil, J.R., 1992, Oxygen and hydrogen isotope evidence for meteoric water infiltration during mylonitization and uplift in the Ruby Mountains-East Humboldt Range core complex, Nevada: Contributions to Mineralogy and Petrology, v. 111, p. 203–221, doi:10.1007/BF00348952.

Gapais, D., 1989, Shear structures within deformed granites: mechanical and thermal indicators: Geology, v. 17, p. 1144–1147, doi:10.1130/0091-7613(1989)017<1144:SSWDGM>2.3.CO.

Gapais, D., and Barbarin, B., 1986, Quartz fabric transition in a cooling syntectonic granite (Hermitage Massif, France): Tectonophysics, v. 125, p. 357–370, doi:10.1016/0040-1951(86)90171-X.

Gapais, D., and Boundi, A.L.B., 2014, Pegmatite mylonites: origin and significance: Geological Society, London, Special Publications, v. 409, p. SP409.7, doi:10.1144/SP409.7.

Gapais, D., Brun, J.-P., Gumiaux, C., Cagnard, F., Ruffet, G., and Le Carlier De Veslud, C., 2015, Extensional tectonics in the Hercynian Armorican belt (France). An overview: Bulletin de la Société Géologique de France, v. 186, p. 117–129, doi:10.2113/gssgfbull.186.2-3.117.

Gapais, D., Cagnard, F., Gueydan, F., Barbey, P., and Ballèvre, M., 2009, Mountain building and exhumation processes through time: inferences from nature and models: Terra Nova, v. 21, p. 188–194, http://archenv.geo.uu.nl/pdf/Gapais et al 2009 Terra Nova Mountain Building Exhumation.pdf (accessed May 2015).

Gapais, D., Lagarde, J.-L.J.L., Le Corre, C., Audren, C., Jegouzo, P., Casas Sainz, A., and Van Den Driessche, J., 1993, La zone de cisaillement de Quiberon : témoin d'extension de la chaîne varisque en Bretagne méridionale au Carbonifère: Comptes Rendus de l'Académie des Sciences - Series II - Mécanique, physique, chimie, sciences de l'univers, sciences de la Terre, v. 316, p. 1123–1129.

Gardien, V., Leloup, P.-H., Maheo, G., Monnié, P., and Arnaud, N., 2017, New paleo-altimeter based on Hydrogen and Oxygen Isotopes of aqueous Fluid Inclusions in hydrothermal quartz, *in* Goldschmidt2017 Abstract,.

Gardien, V., Michel, R., Jean-Louis, V., Michel, D., Philippe, B., and Rossana, M., 2016, Long-lived interaction between hydrothermal and magmatic fluids in the Soultz-

sous-Forêts granitic system (Rhine Graben, France): Lithos, v. 246–247, p. 110–127, doi:10.1016/j.lithos.2015.12.002.

Garzione, C.N., Dettman, D.L., and Horton, B.K., 2004, Carbonate oxygen isotope paleoaltimetry: evaluating the effect of diagenesis on paleoelevation estimates for the Tibetan plateau: Palaeogeography, Palaeoclimatology, Palaeoecology, v. 212, p. 119–140, doi:10.1016/j.palaeo.2004.05.020.

Garzione, C.N., Hoke, G.D., Libarkin, J.C., Withers, S., MacFadden, B., Eiler, J., Ghosh, P., and Mulch, a., 2008, Rise of the Andes: Science, v. 320, p. 1304–1307, doi:10.1126/science.1148615.

Garzione, C.N., Quade, J., DeCelles, P.G., and English, N.B., 2000, Predicting paleoelevation of Tibet and the Himalaya from d18O versus altitude gradients in meteoric water across the Nepal Himalaya: Earth and Planetary Science Letters, v. 183, p. 215–229, doi:10.1016/S0012-821X(00)00252-1.

Gébelin, A., 2004, Déformation et mise en place des granites (360-300Ma) dans un segment de la cha\^{\i}ne Varisque (plateau de Millevaches, Massif Central): Université des Sciences et Techniques du Languedoc.

Gébelin, A., Brunel, M., Monié, P., Faure, M., and Arnaud, N., 2007, Transpressional tectonics and Carboniferous magmatism in the Limousin, Massif Central, France: Structural and 40Ar/39Ar investigations: Tectonics, v. 26, doi:10.1029/2005TC001822.

Gébelin, A., Jessup, M.J., Teyssier, C., Cosca, M.A., Law, R.D., Brunel, M., and Mulch, A., 2017, Infiltration of meteoric water in the South Tibetan Detachment (Mount Everest, Himalaya): When and why? Tectonics, v. 36, p. 690–713, doi:10.1002/2016TC004399.

Gebelin, A., Martelet, G., Brunel, M., Faure, M., and Rossi, P., 2004, Late Hercynian leucogranites modelling as deduced from new gravity data: The example of the Millevaches massif (Massif Central, France): Bulletin de la Societe Geologique de France, v. 175, p. 239–248, doi:10.2113/175.3.239.

Gébelin, A., Martelet, G., Chen, Y., Brunel, M., and Faure, M., 2006, Structure of late Variscan Millevaches leucogranite massif in the French Massif Central: AMS and gravity modelling results: Journal of Structural Geology, v. 28, p. 148–169, doi:10.1016/j.jsg.2005.05.021.

Gébelin, A., Mulch, A., Teyssier, C., Heizler, M., Vennemann, T., and Seaton, N.C.A., 2011, Oligo-Miocene extensional tectonics and fluid flow across the Northern Snake Range detachment system, Nevada: Tectonics, v. 30, doi:10.1029/2010TC002797.

Gébelin, A., Mulch, A., Teyssier, C., Jessup, M.J., Law, R.D., and Brunel, M., 2013, The Miocene elevation of Mount Everest: Geology, v. 41, p. 799–802, doi:10.1130/G34331.1.

Gébelin, A., Mulch, A., Teyssier, C., Page Chamberlain, C., and Heizler, M., 2012, Coupled basin-detachment systems as paleoaltimetry archives of the western North American Cordillera: Earth and Planetary Science Letters, v. 335–336, p. 36–47, doi:10.1016/j.epsl.2012.04.029.

Gébelin, A., Roger, F., and Brunel, M., 2009, Syntectonic crustal melting and high-grade metamorphism in a transpressional regime, Variscan Massif Central, France:

Tectonophysics, v. 477, p. 229–243, doi:10.1016/j.tecto.2009.03.022.

Gébelin, A., Teyssier, C., Heizler, M.T., and Mulch, A., 2015, Meteoric water circulation in a rolling-hinge detachment system (northern Snake Range core complex, Nevada): Bulletin of the Geological Society of America, v. 127, p. 149–161, doi:10.1130/B31063.1.

Geze, B., de Sitter, L.U., and Truempy, R., 1952, Sur le sens de déversement des nappes de la Montagne Noire: Bulletin de la Société Géologique de France Jan 1952, S6-II (7-9) 491-535, v. S6-II (7-9, p. 491–535, doi:10.2113/gssgfbull.S6-II.7-9.491.

Ginter, M., Hampe, O., and Duffin, C.J., 2010, Chondrichthyes — Paleozoic Elasmobranchii: teeth, *in* Handbook of Paleoichthyology 3D, München, Verlag Dr. Friedrich Pfeil.

Goldstein, R.H., and Reynolds, T.J., 1994, Systematics of fluid inclusions in diagenetic minerals: SEPM Short Course 31.: Society for Sedimentary Geology, v. 1999.

Goldstein, R.H., Samson, I., and Anderson, A., 2003, Petrographic analysis of fluid inclusions, *in* Fluid inclusions: Analysis and interpretation, Mineralogical Association of Canada, p. 9–53.

Gonçalves, G.O. et al., 2016, An assessment of monazite from the Itambé pegmatite district for use as U–Pb isotope reference material for microanalysis and implications for the origin of the “Moacyr” monazite: Chemical Geology, v. 424, p. 30–50, doi:10.1016/j.chemgeo.2015.12.019.

González-Bonorino, G., and Eyles, N., 1995, Inverse relation between ice extent and the late Paleozoic glacial record of Gondwana: Geology, v. 23, p. 1015, doi:10.1130/0091-7613(1995)023<1015:IRBIEA>2.3.CO;2.

Gottardi, R., Teyssier, C., Mulch, A., Vennemann, T.W., and Wells, M.L., 2011, Preservation of an extreme transient geotherm in the Raft River detachment shear zone: Geology, v. 39, p. 759–762, doi:10.1130/G31834.1.

Goujou, J.-C., 1992, Analyse pétro-structurale d’un avant-pays métamorphique: influence du plutonisme tardi-orogénique Varisque sur l’encaissant épi à mésozonal de Vendée: Université de Montpellier 2, Montpellier, France.

Gower, R.J.., and Simpson, C., 1992, Phase boundary mobility in naturally deformed, high-grade quartzofeldspathic rocks: evidence for diffusional creep: Journal of Structural Geology, v. 14, p. 301–313, doi:10.1016/0191-8141(92)90088-E.

Graham, C.M., Atkinson, J., and Harmon, R.S., 1984, Hydrogen isotope fractionation in the system chlorite-water.: Progress in Experimental Petrology (N.E.R.C.),.

Graham, C.M., Sheppard, S.M.F., and Heaton, T.H.E., 1980, Experimental hydrogen isotope studies—I. Systematics of hydrogen isotope fractionation in the systems epidote-H2O, zoisite-H2O and AlO(OH)-H2O: Geochimica et Cosmochimica Acta, v. 44, p. 353–364, doi:10.1016/0016-7037(80)90143-X.

ten Grotenhuis, S.M., Trouw, R.A.J., and Passchier, C.W., 2003, Evolution of mica fish in mylonitic rocks: Tectonophysics, v. 372, p. 1–21, doi:10.1016/S0040-1951(03)00231-2.

Guggenheim, S., Chang, Y.H., and Koster Van Groos, A.F., 1987, Muscovite dehydroxylation: high-temperature studies.: American Mineralogist, v. 72, p. 537–

550.

Gunnell, 2000, Apatite fission track thermochronology: an overview of its potential and limitations in geomorphology: Basin Research, v. 12, p. 115–132, doi:10.1046/j.1365-2117.2000.00114.x.

Guy, A., Edel, J.-B., Schulmann, K., Tomek, Č., and Lexa, O., 2011, A geophysical model of the Variscan orogenic root (Bohemian Massif): Implications for modern collisional orogens: Lithos, v. 124, p. 144–157, doi:10.1016/j.lithos.2010.08.008.

Haar, L., Gallagher, J.S., and Kell, G.S., 1984, NBS/NRC steam tables: Thermodynamic and transport properties and computer programs for vapor and liquid states of water in SI units: Washington, DC, Hemisphere, 324 p.

Hartley, A.J., and Otava, J., 2001, Sediment provenance and dispersal in a deep marine foreland basin: the Lower Carboniferous Culm Basin, Czech Republic: Journal of the Geological Society, v. 158, p. 137–150, doi:10.1144/jgs.158.1.137.

Le Hebel, F., 2002, Déformation continentale et histoire des fluides au cours d'un cycle subduction, exhumation, extension. Exemples des porphyroïdes sud-armoricains.: Université de Rennes.

Le Hébel, F., Fourcade, S., Boiron, M.C., Cathelineau, M., Capdevila, R., and Gapais, D., 2007, Fluid history during deep burial and exhumation of oil-bearing volcanics, Hercynian Belt of southern Brittany, France: American Journal of Science, v. 307, p. 1096–1125, doi:10.2475/09.2007.03.

Le Hébel, F., Vidal, O., Kienast, J., and Gapais, D., 2002, Les « Porphyroïdes » de Bretagne méridionale : une unité de HP–BT dans la chaîne hercynienne: Comptes Rendus Geoscience, v. 334, p. 205–211, doi:10.1016/S1631-0713(02)01746-7.

Hetzel, R., Zwingmann, H., Mulch, A., Gessner, K., Akal, C., Hampel, A., Güngör, T., Petschick, R., Mikes, T., and Wedin, F., 2013, Spatiotemporal evolution of brittle normal faulting and fluid infiltration in detachment fault systems: A case study from the Menderes Massif, western Turkey: Tectonics, v. 32, p. 364–376, doi:10.1002/tect.20031.

Hirth, G., and Tullis, J., 1992, Dislocation creep regimes in quartz aggregates: Journal of Structural Geology, v. 14, p. 145–159, doi:10.1016/0191-8141(92)90053-Y.

Hoefs, J., 2004, Stable isotope geochemistry - 5th, completely rev., updated, and enl. (Springer, Ed.): 244 p.

Hoke, G.D., Liu-Zeng, J., Hren, M.T., Wissink, G.K., and Garzione, C.N., 2014, Stable isotopes reveal high southeast Tibetan Plateau margin since the Paleogene: Earth and Planetary Science Letters, v. 394, p. 270–278, doi:10.1016/j.epsl.2014.03.007.

Holk, G.J., and Taylor, H.P., 2007, 18O/16O Evidence for Contrasting Hydrothermal Regimes Involving Magmatic and Meteoric-Hydrothermal Waters at the Valhalla Metamorphic Core Complex, British Columbia: Economic Geology, v. 102, p. 1063–1078, doi:10.2113/gsecongeo.102.6.1063.

Holk, G.J., and Taylor, H.P., 2008, $^{18}O/^{16}O$ Evidence for Contrasting Hydrothermal Regimes Involving Magmatic and Meteoric-Hydrothermal Waters at the Valhalla Metamorphic Core Complex, British Columbia: Economic Geology, v. 102, p. 1063 LP – 1078, http://economicgeology.org/content/102/6/1063.abstract.

Holliger, P., Cuney, M., Friedrich, M., and Turpin, L., 1986, Age Carbonifère de l'unité de Brâme du complexe granitique peralumineux de Saint Sylvestre (N.O. Massif Central) défini par les données isotopiques U-Pb sur zircon et monazite: Comptes rendus de l'Académie des sciences. Série II, Mécanique, physique, chimie, sciences de l'univers, sciences de la terre., v. 303, p. 1309–1314, https://inis.iaea.org/search/search.aspx?orig_q=RN:18044669 (accessed February 2019).

Hoorn, C. et al., 2010, Amazonia through time: Andean uplift, climate change, landscape evolution, and biodiversity: Science, v. 330, p. 927–931, doi:10.1126/science.1194585.

Horton, T.W., and Chamberlain, C.P., 2006, Stable isotopic evidence for Neogene surface downdrop in the central Basin and Range Province: Geological Society of America Bulletin, v. 118, p. 475–490, doi:10.1130/B25808.

Hunter, N.J.R., Hasalová, P., Weinberg, R.F., and Wilson, C.J.L., 2016, Fabric controls on strain accommodation in naturally deformed mylonites: The influence of interconnected micaceous layers: Journal of Structural Geology, v. 83, p. 180–193, doi:10.1016/j.jsg.2015.12.005.

Huntington, K.W., Saylor, J., Quade, J., and Hudson, A.M., 2015, High late Miocene-Pliocene elevation of the Zhada Basin, southwestern Tibetan Plateau, from carbonate clumped isotope thermometry: Bulletin of the Geological Society of America, v. 127, p. 181–199, doi:10.1130/B31000.1.

Jegouzo, P., 1980, The South Armorican Shear Zone: Journal of Structural Geology, v. 2, p. 39–57.

Jenkin, G.R.T., Craw, D., and Fallick, A.E., 1994, Stable isotopic and fluid inclusion evidence for meteoric fluid penetration into an active mountain belt; Alpine Schist, New Zealand: Journal of Metamorphic Geology, v. 12, p. 429–444, doi:10.1111/j.1525-1314.1994.tb00033.x.

Jessell, M.W., 1987, Grain-boundary migration microstructures in a naturally deformed quartzite: Journal of Structural Geology, v. 9, p. 1007–1014, doi:10.1016/0191-8141(87)90008-3.

Jessup, M.J., and Cottle, J.M., 2010, Progression from South-Directed Extrusion to Orogen-Parallel Extension in the Southern Margin of the Tibetan Plateau, Mount Everest Region, Tibet: The Journal of Geology, v. 118, p. 467–486, doi:10.1086/655011.

Jibao, G., and Yaqian, Q., 1997a, Hydrogen isotope fractionation and hydrogen diffusion in the tourmaline-water system: Geochimica et Cosmochimica Acta, v. 61, p. 4679–4688, doi:10.1016/S0016-7037(97)00252-4.

Jibao, G., and Yaqian, Q., 1997b, Hydrogen isotope fractionation and hydrogen diffusion in the tourmaline-water system: Geochimica et Cosmochimica Acta, v. 61, p. 4679–4688, doi:10.1016/S0016-7037(97)00252-4.

Jones, K.A., and Brown, M., 1990, High-temperature 'clockwise' P-T paths and melting in the development of regional migmatites: an example from southern Brittany, France: Journal of Metamorphic Geology, v. 8, p. 551–578.

Jourdan, F., and Renne, P.R., 2007, Age calibration of the Fish Canyon sanidine

40Ar/39Ar dating standard using primary K–Ar standards: Geochimica et Cosmochimica Acta, v. 71, p. 387–402, doi:10.1016/j.gca.2006.09.002.

Jourdan, F., Verati, C., and Féraud, G., 2006, Intercalibration of the Hb3gr 40Ar/39Ar dating standard: Chemical Geology, v. 231, p. 177–189, doi:10.1016/j.chemgeo.2006.01.027.

Jouzel, J., Genthon, C., Lorius, C., Petit, J.R., and Barkov, N.I., 1987, Vostok ice core - A continuous isotope temperature record over the last climatic cycle (160,000 years): Nature, v. 329, p. 403–408.

Kerp, H., 2000, The Modernization of Landscapes during the Late Paleozoic-Early Mesozoic: The Paleontological Society Papers, v. 6, p. 79–114, doi:10.1017/S1089332600000723.

Kerrich, R., La Tour, T.E., and Willmore, L., 1984, Fluid participation in deep fault zones: Evidence from geological, geochemical, and 18 O/ 16 O relations: Journal of Geophysical Research: Solid Earth, v. 89, p. 4331–4343, doi:10.1029/JB089iB06p04331.

Kilian, R., and Heilbronner, R., 2017, Analysis of crystallographic preferred orientations of experimentally deformed Black Hills Quartzite: Solid Earth, v. 8, p. 1095–1117, doi:10.5194/se-8-1095-2017.

Kishima, N., and Sakai, H., 1980, Oxygen-18 And Deuterium Determination On a Single Water Sample Of a Few Milligrams: Analytical Chemistry, doi:10.1021/ac50052a038.

Koch, P.L., 2008, Isotopic Study of the Biology of Modern and Fossil Vertebrates, *in* Stable Isotopes in Ecology and Environmental Science, Oxford, UK, Blackwell Publishing Ltd, p. 99–154, doi:10.1002/9780470691854.ch5.

Koch, P.L., Halliday, A.N., Walter, L.M., Stearley, R.F., Huston, T.J., and Smith, G.R., 1992, Sr isotopic composition of hydroxyapatite from recent and fossil salmon: the record of lifetime migration and diagenesis: Earth and Planetary Science Letters, v. 108, p. 277–287, doi:10.1016/0012-821X(92)90028-T.

Kocsis, L., Vennemann, T.W., and Fontignie, D., 2007, Migration of sharks into freshwater systems during the Miocene and implications for Alpine paleoelevation: Geology, v. 35, p. 451, doi:10.1130/G23404A.1.

Kocsis, L., Vennemann, T.W., Hegner, E., Fontignie, D., and Tütken, T., 2009, Constraints on Miocene oceanography and climate in the Western and Central Paratethys: O-, Sr-, and Nd-isotope compositions of marine fish and mammal remains: Palaeogeography, Palaeoclimatology, Palaeoecology, v. 271, p. 117–129, doi:10.1016/j.palaeo.2008.10.003.

Kohn, M.J., and Cerling, T.E., 2002, Stable Isotope Compositions of Biological Apatite: Reviews in Mineralogy and Geochemistry, v. 48, p. 455–488, doi:10.2138/rmg.2002.48.12.

Kohn, M.J., and Dettman, D.L., 2007, Paleoaltimetry from Stable Isotope Compositions of Fossils: Reviews in Mineralogy and Geochemistry, v. 66, p. 119–154, doi:10.2138/rmg.2007.66.5.

Kolodny, Y., and Luz, B., 1991, Oxygen isotopes in phosphates of fossil fish—Devonian

to Recent, *in* The Geochemical Society, Special Publication, v. 3, p. 105–119.

Kolodny, Y., and Luz, B., 1992, The isotopic record of oxygen in phosphates of fossil fish - Devonian to Recent: The Paleontological Society Special Publications, v. 6, p. 171, doi:10.1017/S2475262200007310.

Kolodny, Y., Luz, B., and Navon, O., 1983a, Oxygen isotope variations in phosphate of biogenic apatites, I. Fish bone apatite—rechecking the rules of the game: Earth and Planetary Science Letters, v. 64, p. 398–404, doi:10.1016/0012-821X(83)90100-0.

Kolodny, Y., Luz, B., and Navon, O., 1983b, Oxygen isotope variations in phosphate of biogenic apatites, I. Fish bone apatite—rechecking the rules of the game: Earth and Planetary Science Letters, v. 64, p. 398–404, doi:10.1016/0012-821X(83)90100-0.

Kolodny, Y., and Raab, M., 1988a, Oxygen isotopes in phosphatic fish remains from Israel: Paleothermometry of tropical cretaceous and tertiary shelf waters: Palaeogeography, Palaeoclimatology, Palaeoecology, v. 64, p. 59–67, doi:10.1016/0031-0182(88)90142-3.

Kolodny, Y., and Raab, M., 1988b, Oxygen isotopes in phosphatic fish remains from Israel: Paleothermometry of tropical cretaceous and tertiary shelf waters: Palaeogeography, Palaeoclimatology, Palaeoecology, v. 64, p. 59–67, doi:10.1016/0031-0182(88)90142-3.

El Korh, A.A., Schmidt, S.T., Vennemann, T., and Ulianov, A., 2011, Trace Element and O-Isotope Composition of Polyphase Metamorphic Veins of the Ile de Groix (Armorican Massif, France): Implication for Fluid Flow During HP Subduction and Exhumation Processes, *in* Ultrahigh-Pressure Metamorphism, p. 243–291, doi:10.1016/B978-0-12-385144-4.00008-4.

Kotzer, T.., Kyser, T.., King, R.., and Kerrich, R., 1993, An empirical oxygen- and hydrogen-isotope geothermometer for quartz-tourmaline and tourmaline-water: Geochimica et Cosmochimica Acta, v. 57, p. 3421–3426, doi:10.1016/0016-7037(93)90548-B.

Kroner, U., and Romer, R.L., 2013, Two plates - Many subduction zones: The Variscan orogeny reconsidered: Gondwana Research, v. 24, p. 298–329, doi:10.1016/j.gr.2013.03.001.

Lambrecht, G., and Diamond, L.W., 2014, Morphological ripening of fluid inclusions and coupled zone-refining in quartz crystals revealed by cathodoluminescence imaging: Implications for CL-petrography, fluid inclusion analysis and trace-element geothermometry: Geochimica et Cosmochimica Acta, v. 141, p. 381–406, doi:10.1016/j.gca.2014.06.036.

Langille, J.M., Jessup, M.J., Cottle, J.M., Newell, D., and Seward, G., 2010, Kinematic evolution of the Ama Drime detachment: Insights into orogen-parallel extension and exhumation of the Ama Drime Massif, Tibet-Nepal: Journal of Structural Geology, v. 32, p. 900–919, doi:10.1016/j.jsg.2010.04.005.

Lardeaux, J.., Ledru, P., Daniel, I., and Duchene, S., 2001, The Variscan French Massif Central - a new addition to the ultra-high pressure metamorphic “club”: exhumation processes and geodynamic consequences: Tectonophysics, v. 332, p. 143–167, doi:10.1016/S0040-1951(00)00253-5.

Lardeaux, J.M., Schulmann, K., Faure, M., Janoušek, V., Lexa, O., Skrzypek, E., Edel, J.B., and Štípská, P., 2014, The Moldanubian Zone in the French Massif Central,

Vosges/Schwarzwald and Bohemian Massif revisited: differences and similarities: Geological Society, London, Special Publications, v. 405, p. 7–44, doi:10.1144/SP405.14.

Lécuyer, C., Amiot, R., Touzeau, A., and Trotter, J., 2013, Calibration of the phosphate δ18O thermometer with carbonate–water oxygen isotope fractionation equations: Chemical Geology, v. 347, p. 217–226, doi:10.1016/j.chemgeo.2013.03.008.

Lécuyer, C., Bogey, C., Garcia, J.-P., Grandjean, P., Barrat, J.-A., Floquet, M., Bardet, N., and Pereda-Superbiola, X., 2003, Stable isotope composition and rare earth element content of vertebrate remains from the Late Cretaceous of northern Spain (Laño): did the environmental record survive? Palaeogeography, Palaeoclimatology, Palaeoecology, v. 193, p. 457–471, doi:10.1016/S0031-0182(03)00261-X.

Ledru, P., and Autran, A., 1987, L'édification de la chaîne varisque dans le Limousin, rôle de la faille d'Argentat à la limite Limousin-Millevaches: Géol. Prof. France, p. 51–91, https://scholar.google.fr/scholar?hl=fr&q=Ledru+P.+and+Autran+A+%281987%29+L%27édification+de+la+chaîne+Varisque+dans+le+Limousin.+Rôle+de+la+faille+d%27Argenta+à+la+limite+Limousin-Millevaches.+In%3A+Prog.+Géol.+Profonde+de++la+F (accessed June 2017).

Ledru, P., Lardeaux, J.M., Santallier, D., Autran, A., Quenardel, J.M., Floc'h, J.P., Lerouge, G., Maillet, N., Marchand, J., and Ploquin, A., 1989, Ou sont les nappes dans le massif central francais? Bulletin de la Société Géologique de France, v. V, p. 605–618, doi:10.2113/gssgfbull.v.3.605.

Lee, D., Severn, G., Oksuz, L., and Hershkowitz, N., 2006, Laser-induced fluorescence measurements of argon ion velocities near the sheath boundary of an argon–xenon plasma: Journal of Physics D: Applied Physics, v. 39, p. 5230–5235, doi:10.1088/0022-3727/39/24/020.

Lemarchand, J., Boulvais, P., Gaboriau, M., Boiron, M.-C., Tartese, R., Cokkinos, M., Bonnet, S., and Jegouzo, P., 2012, Giant quartz vein formation and high-elevation meteoric fluid infiltration into the South Armorican Shear Zone: geological, fluid inclusion and stable isotope evidence: Journal of the Geological Society, v. 169, p. 17–27, doi:10.1144/0016-76492010-186.

Lin, W., Faure, M., Li, X., Chu, Y., Ji, W., and Xue, Z., 2016, Detrital zircon age distribution from Devonian and Carboniferous sandstone in the Southern Variscan Fold-and-Thrust belt (Montagne Noire, French Massif Central), and their bearings on the Variscan belt evolution: Tectonophysics, v. 677–678, p. 1–33, doi:10.1016/j.tecto.2016.03.032.

Longinelli, A., and Nuti, S., 1973a, Oxygen isotope measurements of phosphate from fish teeth and bones: Earth and Planetary Science Letters, v. 20, p. 337–340, doi:10.1016/0012-821X(73)90007-1.

Longinelli, A., and Nuti, S., 1973b, Oxygen isotope measurements of phosphate from fish teeth and bones: Earth and Planetary Science Letters, v. 20, p. 337–340, doi:10.1016/0012-821X(73)90007-1.

Losh, S., 1997, Stable isotope and modeling studies of fluid-rock interaction associated with the Snake Range and Mormon Peak detachment faults, Nevada: Geological Society of America Bulletin, v. 109, p. 300–323, doi:10.1130/0016-7606(1997)109<0300:SIAMSO>2.3.CO;2.

Lotout, C., Pitra, P., Poujol, M., Anczkiewicz, R., and Van Den Driessche, J., 2018, Timing and duration of Variscan high-pressure metamorphism in the French Massif Central: A multimethod geochronological study from the Najac Massif: Lithos, v. 308–309, p. 381–394, doi:10.1016/j.lithos.2018.03.022.

Mainprice, D., Bouchez, J.-L., Blumenfeld, P., and Tubia, J.M., 1986, Dominant c slip in naturally deformed quartz: Implications for dramatic plastic softening at high temperature: Geology, v. 14, p. 819–822, doi:10.1130/0091-7613(1986)14.

Mainprice, D.H., and Paterson, M.S., 1984, Experimental studies of the role of water in the plasticity of quartzites: Journal of Geophysical Research: Solid Earth, v. 89, p. 4257–4269, doi:10.1029/JB089iB06p04257.

Malavieille, J., 1993, Late Orogenic extension in mountain belts: Insights from the Basin and Range and the Late Paleozoic Variscan Belt: Tectonics, v. 12, p. 1115–1130, doi:10.1029/93TC01129.

Malavieille, J., Guihot, P., Costa, S., Lardeaux, J.M., and Gardien, V., 1990, Collapse of the thickened Variscan crust in the French Massif Central: Mont Pilat extensional shear zone and St. Etienne Late Carboniferous basin: Tectonophysics, v. 177, p. 139–149, doi:10.1016/0040-1951(90)90278-G.

Maluski, H., Costa, S., and Echtler, H., 1991, Late variscan tectonic evolution by thinning of earlier thickened crust. An 40Ar/39Ar study of the Montagne Noire, southern Massif Central, France: Lithos, v. 26, p. 287–304, doi:10.1016/0024-4937(91)90034-I.

Mariani, E., Brodie, K.H., and Rutter, E.H., 2006, Experimental deformation of muscovite shear zones at high temperatures under hydrothermal conditions and the strength of phyllosilicate-bearing faults in nature: Journal of Structural Geology, v. 28, p. 1569–1587, doi:10.1016/j.jsg.2006.06.009.

Mark, D.F., Stuart, F.M., and de Podesta, M., 2011, New high-precision measurements of the isotopic composition of atmospheric argon: Geochimica et Cosmochimica Acta, v. 75, p. 7494–7501, doi:10.1016/j.gca.2011.09.042.

Martin, H., 1975, Structural and palaeogeographical evidence for an upper Palaeozoic sea between souhern Africa and South America, *in* IUGS 3rd Gondwana Symposium, Canberra, Australia, p. 37–51.

Mattauer, M., 1986, Intracontinental subduction, crust-mantle decollement and crustal-stacking wedge in the Himalayas and other collision belts: Geological Society, London, Special Publications, v. 19, p. 37–50, doi:10.1144/GSL.SP.1986.019.01.02.

Mattauer, M., Brunel, M., and Matte, P., 1988, Failles normales ductiles et grands chevauchements. Une nouvelle analogie entre l'Himalaya et la chaîne Hercynienne du Massif Central français: Comptes rendus de l'Académie des sciences. Série 2, Mécanique, Physique, Chimie, Sciences de l'univers, Sciences de la Terre, v. 306, p. 671–676.

Mattauer, M., and Matte, P., 1998, Le bassin Stéphanien de St-Etienne ne resulte pas d'une extension tardi-hercynienne généralisée : c'est un bassin pull-apart en relation avec un décrochement dextre: Geodinamica Acta, v. 11, p. 23–31.

Matte, P., 1986, Tectonics and plate tectonics model for the Variscan belt of Europe: Tectonophysics, v. 126, p. 329–374, doi:10.1016/0040-1951(86)90237-4.

Matte, P., 2001, The Variscan collage and orogeny (490-290 Ma) and the tectonic definition of the Armorica microplate: a review: Terra Nova, v. 13, p. 122–128.

Matte, P., 2007, Variscan thrust nappes, detachments, and strike-slip faults in the French Massif Central: Interpretation of the lineations: Geological Society of America Memoirs, v. 200, p. 391–402, doi:10.1130/2007.1200(20).

McCaig, A.M., 1988, Deep fluid circulation in fault zones: Geology, v. 16, p. 867, doi:10.1130/0091-7613(1988)016<0867:DFCIFZ>2.3.CO;2.

McDonough, W.F., and Sun, S. -s., 1995, The composition of the Earth: Chemical Geology, v. 120, p. 223–253, doi:10.1016/0009-2541(94)00140-4.

McDougall, I., and Harrison, T., 1988, Geochronology and Thermochronology by the 40Ar/39Ar Method, *in* Press, O.U. ed., Oxford Monographs on Geology and Geophysics No. 9, New York, p. 212, https://books.google.com/books?hl=fr&lr=&id=FgeSnj9OnFsC&oi=fnd&pg=PA3&ots=--t2SXc_U4&sig=En8DG3_HHTofUttDuoNa9afDZ5k (accessed April 2019).

Ménard, G., and Molnar, P., 1988, Collapse of a Hercynian Tibetan Plateau into a late Palaeozoic European Basin and Range province: Nature, v. 334, p. 235–237, doi:10.1038/334235a0.

Menzies, C.D., Teagle, D.A.H., Craw, D., Cox, S.C., Boyce, A.J., Barrie, C.D., and Roberts, S., 2014, Incursion of meteoric waters into the ductile regime in an active orogen: Earth and Planetary Science Letters, v. 399, p. 1–13, doi:10.1016/j.epsl.2014.04.046.

Methner, K., Mulch, A., Teyssier, C., Wells, M.L., Cosca, M.A., Gottardi, R., Gébelin, A., and Chamberlain, C.P., 2015, Eocene and Miocene extension, meteoric fluid infiltration, and core complex formation in the Great Basin (Raft River Mountains, Utah): Tectonics, v. 34, p. 680–693, doi:10.1002/2014TC003766.

Miller, C.F., Stoddard, E.F., Bradfish, L.J., and Dollase, W.A., 1981, Composition of plutonic muscovite; genetic implications: The Canadian Mineralogist, v. 19, p. 25–34, https://pubs.geoscienceworld.org/canmin/article-abstract/19/1/25/11497/composition-of-plutonic-muscovite-genetic?redirectedFrom=fulltext (accessed February 2019).

Mix, H.T., Ibarra, D.E., Mulch, A., Graham, S. a., and Page Chamberlain, C., 2016, A hot and high Eocene Sierra Nevada: Bulletin of the Geological Society of America, v. 128, p. 531–542, doi:10.1130/B31294.1.

Molnar, P., and England, P., 1990, Late Cenozoic uplift of mountain rangesand global climate change: chicken or egg? Nature, v. 346, p. 29–34, doi:10.1038/346029a0.

Montañez, I.P., and Poulsen, C.J., 2013, The Late Paleozoic Ice Age: An Evolving Paradigm: Annual Review of Earth and Planetary Sciences, v. 41, p. 629–656, doi:10.1146/annurev.earth.031208.100118.

Morrill, C., and Koch, P.L. Elevation or alteration? Evaluation of isotopic constraints on paleoaltitudes surrounding the Eocene Green River Basin:, https://websites.pmc.ucsc.edu/~pkoch/pdfs/Koch papers/2002/Morrill & Koch 02 Geo 30-151.pdf (accessed January 2019).

Morrison, J., and Anderson, J.L., 1998, Footwall refrigeration along a detachment fault: implications for the thermal evolution of core complexes: Science, v. 279, p. 63–66,

doi:10.1126/science.279.5347.63.

Mulch, A., 2016, Stable isotope paleoaltimetry and the evolution of landscapes and life: Earth and Planetary Science Letters, v. 433, p. 180–191, doi:10.1016/j.epsl.2015.10.034.

Mulch, A., and Chamberlain, C.P., 2007, Stable Isotope Paleoaltimetry in Orogenic Belts The Silicate Record in Surface and Crustal Geological Archives: Reviews in Mineralogy and Geochemistry, v. 66, p. 89–118, doi:10.2138/rmg.2007.66.4.

Mulch, A., Chamberlain, C.P., Cosca, M.A., Teyssier, C., Methner, K., Hren, M.T., and Graham, S.A., 2015, Rapid change in high-elevation precipitation patterns of western North America during the Middle Eocene Climatic Optimum (MECO): American Journal of Science, v. 315, p. 317–336, doi:10.2475/04.2015.02.

Mulch, A., and Cosca, M., 2004, Recrystallization or cooling ages: in situ UV-laser 40Ar/39Ar geochronology of muscovite in mylonitic rocks: Journal of the Geological Society, v. 161, p. 573–582, doi:10.1144/0016-764903-110.

Mulch, A., Cosca, M.A., Andresen, A., and Fiebig, J., 2005, Time scales of deformation and exhumation in extensional detachment systems determined by high-spatial resolution in situ UV-laser 40Ar/39Ar dating: Earth and Planetary Science Letters, v. 233, p. 375–390, doi:10.1016/j.epsl.2005.01.042.

Mulch, A., Graham, S.A., and Chamberlain, C.P., 2006a, Hydrogen Isotopes in Eocene River Gravels and Paleoelevation of the Sierra Nevada: Science, v. 313, p. 87–89, doi:10.1126/science.1125986.

Mulch, A., Sarna-Wojcicki, A.M., Perkins, M.E., and Chamberlain, C.P., 2008, A Miocene to Pleistocene climate and elevation record of the Sierra Nevada (California): Proceedings of the National Academy of Sciences of the United States of America, v. 105, p. 6819–6824, doi:10.1073/pnas.0708811105.

Mulch, A., Teyssier, C., Cosca, M.A., and Chamberlain, C.P., 2007, Stable isotope paleoaltimetry of Eocene core complexes in the North American Cordillera: Tectonics, v. 26, p. n/a-n/a, doi:10.1029/2006TC001995.

Mulch, A., Teyssier, C., Cosca, M. a., Vanderhaeghe, O., and Vennemann, T.W., 2004a, Reconstructing paleoelevation in eroded orogens: Geology, v. 32, p. 525, doi:10.1130/G20394.1.

Mulch, A., Teyssier, C., Cosca, M.A., Vanderhaeghe, O., and Vennemann, T.W., 2004b, Reconstructing paleoelevation in eroded orogens: Geology, v. 32, p. 525, doi:10.1130/G20394.1.

Mulch, A., Teyssier, C., Cosca, M.A., and Vennemann, T.W., 2006b, Thermomechanical analysis of strain localization in a ductile detachment zone: Journal of Geophysical Research: Solid Earth, v. 111, p. n/a-n/a, doi:10.1029/2005JB004032.

Mulch, A., Uba, C.E., Strecker, M.R., Schoenberg, R., and Chamberlain, C.P., 2010, Late Miocene climate variability and surface elevation in the central Andes: Earth and Planetary Science Letters, v. 290, p. 173–182, doi:10.1016/j.epsl.2009.12.019.

Murphy, J.B., Gutierrez-Alonso, G., Nance, R.D., Fernandez-Suarez, J., Keppie, J.D., Quesada, C., Strachan, R.A., and Dostal, J., 2006, Origin of the Rheic Ocean: Rifting along a Neoproterozoic suture? Geology, v. 34, p. 325, doi:10.1130/G22068.1.

Nance, R.D., Gutiérrez-Alonso, G., Keppie, J.D., Linnemann, U., Murphy, J.B., Quesada, C., Strachan, R.A., and Woodcock, N.H., 2010, Evolution of the Rheic Ocean: Gondwana Research, v. 17, p. 194–222, doi:10.1016/j.gr.2009.08.001.

Nesbitt, B.E., and Muehlenbachs, K., 1995, Geochemical studies of the origins and effects of synorogenic crustal fluids in the southern Omineca Belt of British Columbia, Canada: Geological Society of America Bulletin, v. 107, p. 1033–1050, doi:10.1130/0016-7606(1995)107<1033:GSOTOA>2.3.CO;2.

Norris, R.D., Jones, L.S., Corfield, R.M., and Cartlidge, J.E., 1996, Skiing in the Eocene Uinta Mountains? Isotopic evidence in the Green River Formation for snow melt and large mountains: Geology, v. 24, p. 403, doi:10.1130/0091-7613(1996)024<0403:SITEUM>2.3.CO;2.

O'Neil, J.R., and Adami, L.H., 1969, The oxygen isotope partition function ratio of water and the structure of liquid water: Journal of Physical Chemistry, doi:10.1021/j100725a062.

Okudaira, T., Takeshita, T., Hara, I., and Ando, J., 1995, A new estimate of the conditions for transition from basal 〈a〉 to prism [c] slip in naturally deformed quartz: Tectonophysics, v. 250, p. 31–46, doi:10.1016/0040-1951(95)00039-4.

Passchier, C.., and Simpson, C., 1986, Porphyroclast systems as kinematic indicators: Journal of Structural Geology, v. 8, p. 831–843, doi:10.1016/0191-8141(86)90029-5.

Passchier, C.W., and Trouw, R.A.J., 2005, Microtectonics: Berlin/Heidelberg, Springer-Verlag, 366 p., doi:10.1007/3-540-29359-0.

Pastor-Galán, D., Gutiérrez-Alonso, G., Murphy, J.B., Fernández-Suárez, J., Hofmann, M., and Linnemann, U., 2013, Provenance analysis of the Paleozoic sequences of the northern Gondwana margin in NW Iberia: Passive margin to Variscan collision and orocline development: Gondwana Research, v. 23, p. 1089–1103, doi:10.1016/j.gr.2012.06.015.

Paton, C., Hellstrom, J., Paul, B., Woodhead, J., and Hergt, J., 2011, Iolite: Freeware for the visualisation and processing of mass spectrometric data: Journal of Analytical Atomic Spectrometry, v. 26, p. 2508, doi:10.1039/c1ja10172b.

Person, M., Mulch, A., Teyssier, C., and Gao, Y., 2007, Isotope transport and exchange within metamorphic core complexes: American Journal of Science, v. 307, p. 555–589, doi:10.2475/03.2007.01.

Peucat, J.-J., 1983, Géochronologie des roches métamorphiques (Rb-Sr et U-Pb): exemples choisis au Groenland, en Laponie, dans le Massif armoricain et en Grande Kabylie: Société géologique et minéralogique de Bretagne, v. 28.

Pin, C., 1990, Variscan oceans: Ages, origins and geodynamic implications inferred from geochemical and radiometric data: Tectonophysics, v. 177, p. 215–227, doi:10.1016/0040-1951(90)90282-D.

Pitra, P., Poujol, M., Van Den Driessche, J., Poilvet, J.-C., and Paquette, J.-L., 2012, Early Permian extensional shearing of an Ordovician granite: The Saint-Eutrope "C/S-like" orthogneiss (Montagne Noire, French Massif Central): Comptes Rendus Geoscience, v. 344, p. 377–384, doi:10.1016/j.crte.2012.06.002.

Pittau, P., Barca, S., Cocherie, A., Del Rio, M., Fanning, M., and Rossi, P., 2002, Le bassin permien de Guardia Pisano (Sud-Ouest de la Sardaigne, Italie) : palynostratigraphie, paléophytogéographie, corrélations et âge radiométrique des produits volcaniques associés: Geobios, v. 35, p. 561–580, doi:10.1016/S0016-6995(02)00069-4.

Poage, M.A., and Chamberlain, C.P., 2001, Empirical relationships between elevation and the stable isotope composition of precipitation and surface waters: considerations for studies of paleoelevation change: American Journal of Science, v. 301, p. 1–15, doi:10.2475/ajs.301.1.1.

Poage, M.A., and Chamberlain, C.P., 2006, Rising Mountain Ranges: Science, v. 311, p. 478–479.

Poilvet, J.C., Poujol, M., Pitra, P., Van Den Driessche, J., and Paquette, J.L., 2011, The montalet granite, montagne noire, France: An early permian syn-extensional pluton as evidenced by new U-Th-Pb data on zircon and monazite: Comptes Rendus - Geoscience, doi:10.1016/j.crte.2011.06.002.

Poujol, M., Pitra, P., Van Den Driessche, J., Tartèse, R., Ruffet, G., Paquette, J.-L., and Poilvet, J.-C., 2017, Two-stage partial melting during the Variscan extensional tectonics (Montagne Noire, France): International Journal of Earth Sciences, v. 106, p. 477–500, doi:10.1007/s00531-016-1369-1.

Poulsen, C.J., and Jeffery, M.L., 2011, Climate change imprinting on stable isotopic compositions of high-elevation meteoric water cloaks past surface elevations of major orogens: Geology, v. 39, p. 595–598, doi:10.1130/G32052.1.

Pucéat, E., Joachimski, M.M., Bouilloux, A., Monna, F., Bonin, A., Motreuil, S., Morinière, P., Hénard, S., Mourin, J., and Dera, G., 2010, Revised phosphate–water fractionation equation reassessing paleotemperatures derived from biogenic apatite: Earth and Planetary Science Letters, v. 298, p. 135–142, doi:10.1016/j.epsl.2010.07.034.

Quade, J., Breecker, D.O., Daeron, M., and Eiler, J., 2011, The paleoaltimetry of Tibet: An isotopic perspective: American Journal of Science, v. 311, p. 77–115, doi:10.2475/02.2011.01.

Quade, J., Garzione, C., and Eiler, J., 2007, Paleoelevation Reconstruction using Pedogenic Carbonates: Reviews in Mineralogy and Geochemistry, v. 66, p. 53–87, doi:10.2138/rmg.2007.66.3.

Quilichini, A., Siebenaller, L., Nachlas, W.O., Teyssier, C., Vennemann, T.W., Heizler, M.T., and Mulch, A., 2015, Infiltration of meteoric fluids in an extensional detachment shear zone (Kettle dome, WA, USA): How quartz dynamic recrystallization relates to fluid-rock interaction: Journal of Structural Geology, v. 71, p. 71–85, doi:10.1016/j.jsg.2014.11.008.

Quilichini, A., Siebenaller, L., Teyssier, C., and Vennemann, T.W., 2016, Magmatic and meteoric fluid flow in the Bitterroot extensional detachment shear zone (MT, USA) from ductile to brittle conditions: Journal of Geodynamics, v. 101, p. 109–128, doi:10.1016/j.jog.2016.05.006.

Ratschbacher, L., Frisch, W., Neubauer, F., Schmid, S.M., and Neugebauer, J., 1989, Extension in compressional orogenic belts: The eastern Alps: Geology, v. 17, p. 404, doi:10.1130/0091-7613(1989)017<0404:EICOBT>2.3.CO;2.

Renne, P.R., Balco, G., Ludwig, K.R., Mundil, R., and Min, K., 2011, Response to the comment by W.H. Schwarz et al. on " Joint determination of 40K decay constants and 40Ar */ 40K for the Fish Canyon sanidine standard, and improved accuracy for 40Ar/ 39Ar geochronology" by P.R. Renne et al. (2010): Geochimica et Cosmochimica Acta, doi:10.1016/j.gca.2011.06.021.

Renne, P.R., Mundil, R., Balco, G., Min, K., and Ludwig, K.R., 2010, Joint determination of 40K decay constants and 40Ar∗/40K for the Fish Canyon sanidine standard, and improved accuracy for 40Ar/39Ar geochronology: Geochimica et Cosmochimica Acta, v. 74, p. 5349–5367, doi:10.1016/j.gca.2010.06.017.

Roddick, J.., 1983, High precision intercalibration of 40Ar-39Ar standards: Geochimica et Cosmochimica Acta, v. 47, p. 887–898, doi:10.1016/0016-7037(83)90154-0.

Roedder, E., 1984, Fluid inclusions. In Reviews in Mineralogy: v. 12.

Roger, F., Respaut, J.P., Brunel, M., Matte, P., and Paquette, J.L., 2004, Première datation U-Pb des orthogneiss œillés de la zone axiale de la Montagne noire (Sud du Massif central) : Nouveaux témoins du magmatisme ordovicien dans la cha\^{\i}ne Varisque: Comptes Rendus - Geoscience, v. 336, p. 19–28, doi:10.1016/j.crte.2003.10.014.

Roger, F.F., Teyssier, C., Respaut, J.-P.P., Rey, P.F., Jolivet, M., Whitney, D.L., Paquette, J.-L.L., and Brunel, M., 2015, Timing of formation and exhumation of the Montagne Noire double dome, French Massif Central: Tectonophysics, v. 640–641, p. 53–69, doi:10.1016/j.tecto.2014.12.002.

Roig, J.Y., Faure, M., and Maluski, H., 2002, Superimposed tectonic and hydrothermal events during the late-orogenic extension in the Western French Massif Central: A structural and 40AR/39Ar study: Terra Nova, v. 14, p. 25–32, doi:10.1046/j.1365-3121.2002.00384.x.

Rolin, P., Marquer, D., Cartannaz, C., and Rossi, P., 2014, Carboniferous magmatism related to progressive pull-apart opening in the western French Massif Central: Bulletin de la Societé Géologique de France, v. 185, p. 171–189, doi:10.2113/gssgfbull.185.3.171.

Rolin, P., Marquer, D., Colchen, M., Cartannaz, C., Cocherie, A., Thiery, V., Quenardel, J.M., and Rossi, P., 2009, Famenno-carboniferous (370-320 Ma) strike slip tectonics monitored by syn-kinematic plutons in the French Variscan belt (Massif Armoricain and French Massif Central): Bulletin de la Societé Géologique de France, v. 180, p. 231–246, doi:10.2113/gssgfbull.180.3.231.

Roscher, M., and Schneider, J.W., 2005, An annotated correlation chart for continental Late Pennsylvanian and Permian basins and the marine scale. The Nonmarine Permian.: New Mexico Museum of Natural History and Science Bulletin, v. 30, p. 282–291.

Roscher, M., and Schneider, J.W., 2006, Permo-Carboniferous climate: Early Pennsylvanian to Late Permian climate development of central Europe in a regional and global context: Geological Society, London, Special Publications, v. 265, p. 95–136, doi:10.1144/GSL.SP.2006.265.01.05.

Rowley, D.B., 2007, Stable Isotope-Based Paleoaltimetry: Theory and Validation: Reviews in Mineralogy and Geochemistry, v. 66, p. 23–52,

doi:10.2138/rmg.2007.66.2.

Rowley, D.B., and Currie, B.S., 2006, Palaeo-altimetry of the late Eocene to Miocene Lunpola basin, central Tibet: Nature, v. 439, p. 677–681, doi:10.1038/nature04506.

Rowley, D.B., and Garzione, C.N., 2007, Stable isotope-based paleoaltimetry: Annual Review of Earth and Planetary Sciences, v. 35, p. 463–508, doi:10.1146/annurev.earth.35.031306.140155.

Rowley, D.B., Pierrehumbert, R.T., and Currie, B.S., 2001, A new approach to stable isotope-based paleoaltimetry: implications for paleoaltimetry and paleohypsometry of the High Himalaya since the Late Miocene: Earth and Planetary Science Letters, v. 188, p. 253–268, doi:10.1016/S0012-821X(01)00324-7.

Rozanski, K., Araguás-Araguás, L., and Gonfiantini, R., 1993, Isotopic patterns in modern global precipitation, *in* Union, A.G. ed., Climate Change in Continental Isotopic Records, v. Geophysica, p. 1–36, doi:10.1029/GM078p0001.

Rubio Pascual, F.J., López-Carmona, A., and Arenas, R., 2016, Thickening vs. extension in the Variscan belt: P–T modelling in the Central Iberian autochthon: Tectonophysics, v. 681, p. 144–158, doi:10.1016/j.tecto.2016.02.033.

Ruffet, G., Féraud, G., and Amouric, M., 1991, Comparison of 40Ar/39Ar conventional and laser dating of biotites from the North Trégor Batholith: Geochimica et Cosmochimica Acta, v. 55, p. 1675–1688, doi:10.1016/0016-7037(91)90138-U.

Ruffet, G., Féraud, G., Balèvre, M., and Kiénast, J.-R., 1995, Plateau ages and excess argon in phengites: an 40Ar/39Ar laser probe study of Alpine micas (Sesia Zone, Western Alps, northern Italy): Chemical Geology, v. 121, p. 327–343, doi:10.1016/0009-2541(94)00132-R.

Rye, R.O., Schuiling, R.D., Rye, D.M., and Jansen, J.B.H., 1976, Carbon, hydrogen, and oxygen isotope studies of the regional metamorphic complex at Naxos, Greece: Geochimica et Cosmochimica Acta, v. 40, p. 1031–1049, doi:10.1016/0016-7037(76)90045-4.

Saylor, J.E., and Horton, B.K., 2014, Nonuniform surface uplift of the Andean plateau revealed by deuterium isotopes in Miocene volcanic glass from southern Peru: Earth and Planetary Science Letters, v. 387, p. 120–131, doi:10.1016/j.epsl.2013.11.015.

Scaillet, S., Cuney, M., le Carlier de Veslud, C., Cheilletz, A., and Royer, J.J., 1996, Cooling pattern and mineralization history of the Saint Sylvestre and western Marche leucogranite pluton, French Massif Central: II. Thermal modelling and implications for the mechanisms of uranium mineralization: Geochimica et Cosmochimica Acta, v. 60, p. 4673–4688, doi:10.1016/S0016-7037(96)00292-X.

Schmitz, B., Åberg, G., Werdelin, L., Forey, P., and Bendix-Almgreen, S.E., 1991, 87Sr/86Sr, Na, F, Sr, and La in skeletal fish debris as a measure of the paleosalinity of fossil-fish habitats: Geological Society of America Bulletin, v. 103, p. 786–794, doi:10.1130/0016-7606(1991)103<0786:SSNFSA>2.3.CO;2.

Schneider, J.W., Hampe, O., and Soler-Gijon, R., 2000, The Late Carboniferous and Permian: Aquatic vertebrate zonation in southern Spain and German basins: CFS Courier Forschungsinstitut Senckenberg,.

Schneider, D., Handler, R., Neubauer, F., Kalvoda, J., and Tomek, Č., 1999, Ar single-und multi-grain ages of detrital white mica from the Silesian Culm basin (Czech Republic): v. 8, http://geolines.gli.cas.cz/fileadmin/volumes/volume08/G8-059.pdf (accessed June 2017).

Schneider, J.W., and Werneburg, R., 2006, Insect biostratigraphy of the Euramerican continental Late Pennsylvanian and Early Permian: Geological Society, London, Special Publications, v. 265, p. 325–336, doi:10.1144/GSL.SP.2006.265.01.15.

Schultze, H.-P., and Soler-Gijón, R., 2004, A xenacanth clasper fromthe ?uppermost Carboniferous - Lower Permian of Buxières-les-Mines(Massif Central, France) and the palaeoecology of the EuropeanPermo-Carboniferous basins: Neues Jahrbuch für Geologie und Paläontologie - Abhandlungen, p. 325–363, doi:10.1127/NJGPA/232/2004/325.

Scotese, C.R., 1997, Paleogeographic Atlas, PALEOMAP Progress Report 90-0497.:

Seager, R., Battisti, D.S., Yin, J., Gordon, N., Naik, N., Clement, A.C., and Cane, M.A., 2002, Is the Gulf Stream responsible for Europe's mild winters? Quarterly Journal of the Royal Meteorological Society, v. 128, p. 2563–2586, doi:10.1256/qj.01.128.

Searle, M.P., 2006, Role of the Red River Shear zone, Yunnan and Vietnam, in the continental extrusion of SE Asia:, http://jgs.lyellcollection.org/ (accessed April 2019).

Sharp, Z.D., 2000, The effect of diagenesis on oxygen isotope ratios of biogenic phosphates: American Journal of Science, v. 300, p. 222–237, doi:10.2475/ajs.300.3.222.

Sheppard, S.M.F., 1986, Characterization and isotopic variations in natural waters: Reviews in Mineralogy and Geochemistry, v. 16, p. 165–183.

Sibson, R.H., 1981, Controls on low-stress hydro-fracture dilatancy in thrust, wrench and normal fault terrains: Nature, v. 289, p. 665–667, doi:10.1038/289665a0.

Sibson, R.H., Robert, F., and Poulsen, K.H., 1988, High-angle reverse faults, fluid-pressure cycling, and mesothermal gold-quartz deposits: Geology, v. 16, p. 551, doi:10.1130/0091-7613(1988)016<0551:HARFFP>2.3.CO;2.

Siebenaller, L., Boiron, M.-C., Vanderhaeghe, O., Hibsch, C., Jessell, M.W., Andre-Mayer, A.-S., France-Lanord, C., and Photiades, A., 2013, Fluid record of rock exhumation across the brittle-ductile transition during formation of a Metamorphic Core Complex (Naxos Island, Cyclades, Greece): Journal of Metamorphic Geology, v. 31, p. 313–338, doi:10.1111/jmg.12023.

Siegenthaler, U., and Oeschger, H., 1980, Correlation of 18O in precipitation with temperature and altitude: Nature, v. 285, p. 314–317, doi:10.1038/285314a0.

Simpson, C., and Wintsch, R., 1989, Evidence for deformation induced K-Feldspar replacement by myrmekite: Journal of metamorphic Geology, v. 7, p. 261–275.

Singleton, J.S., and Mosher, S., 2012, Mylonitization in the lower plate of the Buckskin-Rawhide detachment fault, west-central Arizona: Implications for the geometric evolution of metamorphic core complexes: Journal of Structural Geology, v. 39, p. 180–198, doi:10.1016/j.jsg.2012.02.013.

Sjostrom, D.J., Hren, M.T., Horton, T.W., Waldbauer, J.R., and Chamberlain, C.P., 2006,

Stable isotopic evidence for a pre–late Miocene elevation gradient in the Great Plains–Rocky Mountain region, USA, *in* Special Paper 398: Tectonics, Climate, and Landscape Evolution, Geological Society of America, p. 309–319, doi:10.1130/2006.2398(19).

Soler-Gijon, R., 1997, Euselachian sharks from the Late Carboniferous of the Puertollano Basin, Spain: biostratigraphic and palaeoenvironmental implications.: Modern Geology, v. 21, p. 137–170.

Soler-Gijón, R., 1997, New discoveries of xenacanth sharks from the Late Carboniferous of Spain (Puertollano Basin) and Early Permian of Germany (Saar-Nahe Basin): Implications for the phylogeny of xenacanthiform and anacanthous sharks: Neues Jahrbuch für Geologie und Paläontologie - Abhandlungen, v. 205, p. 1–31, doi:10.1127/njgpa/205/1997/1.

Soler-Gijón, R., 1999, Occipital spine ofOrthacanthus (Xenacanthidae, Elasmobranchii): Structure and growth: Journal of Morphology, v. 242, p. 1–45, doi:10.1002/(SICI)1097-4687(199910)242:1<1::AID-JMOR2>3.0.CO;2-9.

Sourirajan, S., and Kennedy, G.C., 1962, The system H 2 O-NaCl at elevated temperatures and pressures: American Journal of Science, v. 260, p. 115–141, doi:10.2475/ajs.260.2.115.

Speers-Roesch, B., and Treberg, J.R., 2010, The unusual energy metabolism of elasmobranch fishes: Comparative Biochemistry and Physiology Part A: Molecular & Integrative Physiology, v. 155, p. 417–434, doi:10.1016/j.cbpa.2009.09.031.

Stampfli, G.., and Borel, G.., 2002, A plate tectonic model for the Paleozoic and Mesozoic constrained by dynamic plate boundaries and restored synthetic oceanic isochrons: Earth and Planetary Science Letters, v. 196, p. 17–33, doi:10.1016/S0012-821X(01)00588-X.

Stampfli, G.M., Hochard, C., Vérard, C., Wilhem, C., and vonRaumer, J., 2013, The formation of Pangea: Tectonophysics, v. 593, p. 1–19, doi:10.1016/j.tecto.2013.02.037.

Steyer, J.S. et al., 2000, New data on the flora and fauna from the uppermost Carboniferous-Lower Permian of Buxieres-les-Mines, Bourbon l'Archambault Basin (Allier, France); a preliminary report: Bulletin de la Société Géologique de France, v. 171, p. 239–249, doi:10.2113/171.2.239.

Stipp, M., Stünitz, H., Heilbronner, R., and Schmid, S.M., 2002, The eastern Tonale fault zone: a 'natural laboratory' for crystal plastic deformation of quartz over a temperature range from 250 to 700°C: Journal of Structural Geology, v. 24, p. 1861–1884, doi:10.1016/S0191-8141(02)00035-4.

Suess, E., 1887, Ueber unterbrochene Gebirgsfaltung: Sitzungsberichte der Kaiserlich Akademie der Wissenschaften, v. 94, p. 111.

Suzuoki, T., and Epstein, S., 1976, Hydrogen isotope fractionation between OH-bearing minerals and water: Geochimica et Cosmochimica Acta, v. 40, p. 1229–1240, doi:10.1016/0016-7037(76)90158-7.

Tait, J., 1999, New Early Devonian paleomagnetic data from NW France: Paleogeography and implications for the Armorican microplate hypothesis: Journal of Geophysical Research: Solid Earth, v. 104, p. 2831–2839, doi:10.1029/98JB02787.

Tait, J. a, Bachtadse, V., and Dinarès-Turell, J., 2000, Paleomagnetism of Siluro-Devonian sequences, NE Spain: Journal of Geophysical Research: Solid Earth, v. 105, p. 23595–23603, doi:10.1029/2000JB900111.

Tait, J.A., Bachtadse, V., and Soffel, H., 1996a, Eastern Variscan fold belt: paleomagnetic evidence for oroclinal bending: Geology, v. 24, p. 871.

Tait, J.A., Bachtadse, V., Soffel, H.C., and Franke, W., 1996b, Palaeomagnetic constraints on the evolution of the European Variscan Fold belt: Geologica Bavarica, v. 101, p. 221–232.

Tartèse, R., and Boulvais, P., 2010, Differentiation of peraluminous leucogranites "en route" to the surface: Lithos, v. 114, p. 353–368, doi:10.1016/j.lithos.2009.09.011.

Tartèse, R., Boulvais, P., Poujol, M., Chevalier, T., Paquette, J., Ireland, T.R., and Deloule, E., 2012, Mylonites of the South Armorican Shear Zone : Insights for crustal-scale fluid flow and water – rock interaction processes: Journal of Geodynamics, v. 56–57, p. 86–107, doi:10.1016/j.jog.2011.05.003.

Tartèse, R., Boulvais, P., Poujol, M., Gloaguen, E., and Cuney, M., 2013, Uranium mobilization from the variscan questembert syntectonic granite during fluid-rock interaction at depth: Economic Geology, v. 108, p. 379–386, doi:10.2113/econgeo.108.2.379.

Tartèse, R., Poujol, M., Ruffet, G., Boulvais, P., Yamato, P., and Košler, J., 2011a, New U-Pb zircon and 40Ar/39Ar muscovite age constraints on the emplacement of the Lizio syn-tectonic granite (Armorican Massif, France): Comptes Rendus Geoscience, v. 343, p. 443–453, doi:10.1016/j.crte.2011.07.005.

Tartèse, R., Ruffet, G., Poujol, M., Boulvais, P., and Ireland, T.R., 2011b, Simultaneous resetting of the muscovite K-Ar and monazite U-Pb geochronometers: A story of fluids: Terra Nova, v. 23, p. 390–398, doi:10.1111/j.1365-3121.2011.01024.x.

Taylor, H.P., 1978, Oxygen and hydrogen isotope studies of plutonic granitic rocks: Earth and Planetary Science Letters, v. 38, p. 177–210, doi:10.1016/0012-821X(78)90131-0.

Taylor, H.P., 1974, The Application of Oxygen and Hydrogen Isotope Studies to Problems of Hydrothermal Alteration and Ore Deposition: Economic geology, v. 69, p. 843–883.

Templeton, A.S., Chamberlain, C.P., Koons, P.O., and Craw, D., 1998, Stable isotopic evidence for mixing between metamorphic fluids and surface-derived waters during recent uplift of the Southern Alps, New Zealand: Earth and Planetary Science Letters, v. 154, p. 73–92, doi:10.1016/S0012-821X(97)00143-X.

Teyssier, C., and Whitney, D.L., 2002, Gneiss domes and orogeny: Geology, v. 30, p. 1139, doi:10.1130/0091-7613(2002)030<1139:GDAO>2.0.CO;2.

Thiede, R.C., Arrowsmith, J.R., Bookhagen, B., Williams, M.M., Sobel, E.R., and Strecker, M.R., 2006, Dome formation and extension in the Tethyan Himalaya, Leo Pargil, northwest India: Geol. Soc. Am. Bull., v. 118, p. 635–650.

Du Toit, A.L., 1921, The Carboniferous glaciation of South Africa: South African Journal of Geology, v. 24, p. 188–227.

Tomascak, P.B., Krogstad, E.J., and Walker, R.J., 1996, U-Pb monazite geochronology of

granitic rocks from Maine: implications for Late Paleozoic tectonics in the northern Appalachians: The Journal of Geology, v. 104, p. 185–195, doi:10.2307/30064163.

Torne, M., Fernàndez, M., Vergés, J., Ayala, C., Salas, M.C., Jimenez-Munt, I., Buffett, G.G., and Díaz, J., 2015, Crust and mantle lithospheric structure of the Iberian Peninsula deduced from potential field modeling and thermal analysis: Tectonophysics, v. 663, p. 419–433, doi:10.1016/j.tecto.2015.06.003.

Triboulet, C.L., and Audren, C., 1988, Controls on P–T–t deformation path from amphibole zonation during progressive metamorphism of basic rocks (estuary of the River Vilaine, South Brittany, France): Journal of Metamorphic Geology, v. 6, p. 117–133, doi:10.1111/j.1525-1314.1988.tb00412.x.

Tullis, J., Christie, J.M., and Griggs, D.T., 1973, Microstructures and preferred orientations of experimentally deformed quartzites: Geological Society of America Bulletin, v. 84, p. 297, doi:10.1130/0016-7606(1973)84<297:MAPOOE>2.0.CO;2.

Turner, G., 1971, Argon 40-argon 39 dating: the optimization of irradiation parameters: Earth and Planetary Science Letters, v. 10, p. 227–234, doi:10.1016/0012-821X(71)90010-0.

Turpin, L., Cuney, M., Friedrich, M., Bouchez, J.-L., and Aubertin, M., 1990, Meta-igneous origin of Hercynian peraluminous granites in N.W. French Massif Central: implications for crustal history reconstructions: Contributions to Mineralogy and Petrology, v. 104, p. 163–172, doi:10.1007/BF00306440.

Turrillot, P., 2010, Fusion crustale et évolution tardi-orogénique du Domaine Sud Armoricain: ISTO - Institut des Sciences de la Terre d'Orléans, 365 p.

Turrillot, P., Augier, R., and Faure, M., 2009, The top-to-the-southeast Sarzeau shear zone and its place in the late-orogenic extensional tectonics of southern Armorica: Bulletin de la Societe Geologique de France, v. 180, p. 247–261, doi:10.2113/gssgfbull.180.3.247.

Turrillot, P., Augier, R., Monié, P., Faure, M., Monié, P., and Faure, M., 2011a, Late orogenic exhumation of the Variscan high-grade units (South Armorican Domain, western France), combined structural and 40 Ar/ 39 Ar constraints: Tectonics, v. 30 (TC5007, p. 1–27, doi:10.1029/2010TC002788.

Turrillot, P., Faure, M., Martelet, G., Chen, Y., and Augier, R., 2011b, Pluton-dyke relationships in a Variscan granitic complex from AMS and gravity modelling. Inception of the extensional tectonics in the South Armorican Domain France): Journal of Structural Geology, v. 33, p. 1681–1698, doi:10.1016/j.jsg.2011.08.004.

Tütken, T., Vennemann, T.W., and Pfretzschner, H.-U., 2011, Nd and Sr isotope compositions in modern and fossil bones – Proxies for vertebrate provenance and taphonomy: Geochimica et Cosmochimica Acta, v. 75, p. 5951–5970, doi:10.1016/j.gca.2011.07.024.

Upton, P., Koons, P.O., and Chamberlain, C.P., 1995, Penetration of deformation-driven meteoric water into ductile rocks: Isotopic and model observations from the Southern Alps, New Zealand: New Zealand Journal of Geology and Geophysics, v. 38, p. 535–543, doi:10.1080/00288306.1995.9514680.

Vanderhaeghe, O., 1999, Pervasive melt migration from migmatites to leucogranite in the Shuswap metamorphic core complex, Canada: control of regional deformation:

Tectonophysics, v. 312, p. 35–55, doi:10.1016/S0040-1951(99)00171-7.

Vanderhaeghe, O., Laurent, O., Moyen, J., Gardien, V., Gébelin, A., Chelle-Michoul, C., Couzinie, S., Bellanger, M., Villaros, A., and Berger, J., 2018, Flow of partially molten crust controlling construction, growth and collapse of the Variscan orogenic belt, *in* Réunion des Sciences de la Terre, https://rst2018-lille.sciencesconf.org/data/book_rst2018_lille_fr_final_DEF_web.pdf (accessed January 2019).

Vennemann, T.W., and Hegner, E., 1998, Oxygen, strontium, and neodymium isotope composition of fossil shark teeth as a proxy for the palaeoceanography and palaeoclimatology of the Miocene northern Alpine Paratethys: Palaeogeography, Palaeoclimatology, Palaeoecology, v. 142, p. 107–121, doi:10.1016/S0031-0182(98)00062-5.

Vennemann, T.., Hegner, E., Cliff, G., and Benz, G.., 2001, Isotopic composition of recent shark teeth as a proxy for environmental conditions: Geochimica et Cosmochimica Acta, v. 65, p. 1583–1599, doi:10.1016/S0016-7037(00)00629-3.

Vigneresse, J.-L., and Burg, J., 2003, The paradoxical aspect of the Himalayan granites: Journal of the Virtual Explorer, v. 11, p. 1–24, doi:10.3809/jvirtex.2003.00070.

Villa, 1998, Isotopic closure: Terra Nova, v. 10, p. 42–47, doi:10.1046/j.1365-3121.1998.00156.x.

Virlogeux, D., Roux, J.T., and Guillemot, D., 1999, Apport de la géophysique ala connaissance du massif de Charroux-Civray et du socle poitevin, *in* Etudes du massif de Charroux-Civray, Poitiers, CNRS/ANDRA, Journées scientifiques, p. 33–62.

Visser, J.N.J., 1987a, The influence of topography on the Permo-Carboniferous glaciation in the Karoo basin and adjoining areas, southern Africa, *in* Gondwana Six: Stratigraphy, Sedimentology, and Paleontology, p. 123–129, doi:10.1029/GM041p0123.

Visser, J.N.J., 1987b, The palaeogeography of part of southwestern Gondwana during the Permo-Carboniferous glaciation: Palaeogeography, Palaeoclimatology, Palaeoecology, v. 61, p. 205–219, doi:10.1016/0031-0182(87)90050-2.

Watson, E.B., Harrison, T.M., and Ryerson, F.J., 1985, Diffusion of Sm, Sr, and Pb in fluorapatite: Geochimica et Cosmochimica Acta, v. 49, p. 1813–1823, doi:10.1016/0016-7037(85)90151-6.

Webster, T.J., Gébelin, A., Law, R.D., Stahr, D.W., and Mulch, A., 2018, Meteoric fluid-rock interaction in the footwall of the South Tibetan Detachment (Sutlej Valley and Zanskar, NW India), *in* Himalaya-Karakorum-Tibet workshop, Lausanne, Switzerland.

Wenner, D.B., 1979, Hydrogen, oxygen and carbon isotopic evidence for the origin of rodingites in serpentinized ultramafic rocks: Geochimica et Cosmochimica Acta, v. 43, p. 603–614, doi:10.1016/0016-7037(79)90168-6.

Werneburg, R., 2003, The branchiosaurid amphibians from the Lower Permian of Buxières-les-Mines, Bourbon l'Archambault Basin (Allier, France) and their biostratigraphic significance: Bulletin de la Societé Géologique de France, v. 174, p. 343–349, doi:10.2113/174.4.343.

Whitney, D.L., Roger, F., Teyssier, C., Rey, P.F., and Respaut, J.P., 2015, Syn-collapse eclogite metamorphism and exhumation of deep crust in a migmatite dome: The P-T-t record of the youngest Variscan eclogite (Montagne Noire, French Massif Central): Earth and Planetary Science Letters, v. 430, p. 224–234, doi:10.1016/j.epsl.2015.08.026.

Whitney, D.L., Teyssier, C., Rey, P., and Buck, W.R., 2013, Continental and oceanic core complexes: Geological Society of America Bulletin, v. 125, p. 273–298, doi:10.1130/B30754.1.

Williamson, B.J., Shaw, A., Downes, H., and Thirlwall, M.F., 1996, Geochemical constraints on the genesis of Hercynian two-mica leucogranites from the Massif Central, France: Chemical Geology, v. 127, p. 25–42, doi:10.1016/0009-2541(95)00105-0.

Windhorst, D., Waltz, T., Timbe, E., Frede, H.-G., and Breuer, L., 2013, Impact of elevation and weather patterns on the isotopic composition of precipitation in a tropical montane rainforest: Hydrology and Earth System Sciences, v. 17, p. 409–419, doi:10.5194/hess-17-409-2013.

Wirth, R., and Voll, G., 1987, Cellular intergrowth between quartz and sodium-rich plagioclase (myrmekite) ? an analogue of discontinuous precipitation in metal alloys: Journal of Materials Science, v. 22, p. 1913–1918, doi:10.1007/BF01132916.

Wu, C.-M., and Chen, H.-X., 2015, Calibration of a Ti-in-muscovite geothermometer for ilmenite- and Al2SiO5-bearing metapelites: Lithos, v. 212–215, p. 122–127, doi:10.1016/j.lithos.2014.11.008.

Wu, G., Liu, Y., He, B., Bao, Q., Duan, A., and Jin, F.-F., 2012, Thermal controls on the Asian summer monsoon.: Scientific reports, v. 2, p. 1–7, doi:10.1038/srep00404.

Xu, Q., Ding, L., Zhang, L., Cai, F., Lai, Q., Yang, D., and Liu-Zeng, J., 2013, Paleogene high elevations in the Qiangtang Terrane, central Tibetan Plateau: Earth and Planetary Science Letters, v. 362, p. 31–42, doi:10.1016/j.epsl.2012.11.058.

York, D., 1968, Least squares fitting of a straight line with correlated errors: Earth and Planetary Science Letters, v. 5, p. 320–324, doi:10.1016/S0012-821X(68)80059-7.

Zacke, A., Voigt, S., Joachimski, M.M., Gale, A.S., Ward, D.J., and Tütken, T., 2009, Surface-water freshening and high-latitude river discharge in the Eocene North Sea: Journal of the Geological Society, v. 166, p. 969–980, doi:10.1144/0016-76492008-068.

Žák, J., Sláma, J., and Burjak, M., 2017, Rapid extensional unroofing of a granite–migmatite dome with relics of high-pressure rocks, the Podolsko complex, Bohemian Massif: Geological Magazine, v. 154, p. 354–380, doi:10.1017/S0016756816000030.

Žák, J., Svojtka, M., and Opluštil, S., 2018, Topographic inversion and changes in the sediment routing systems in the Variscan orogenic belt as revealed by detrital zircon and monazite U Pb geochronology in post-collisional continental basins: Sedimentary Geology, v. 377, p. 63–81, doi:10.1016/j.sedgeo.2018.09.008.

Zhang, Y.G., and Frantz, J.D., 1987, Determination of the homogenization temperatures and densities of supercritical fluids in the system NaClKClCaCl2H2O using synthetic fluid inclusions: Chemical Geology, v. 64, p. 335–350, doi:10.1016/0009-

2541(87)90012-X.

Zheng, Y.-F., 1993, Calculation of oxygen isotope fractionation in hydroxyl-bearing silicates: Earth and Planetary Science Letters, v. 120, p. 247–263, doi:10.1016/0012-821X(93)90243-3.

Zwing, A., and Bachtadse, V., 2000, Paleoposition of the northern margin of Armorica in Late Devonian times: Paleomagnetic and rock magnetic results from the Frankenstein Intrusive Complex (Mid-German Crystalline Rise): Journal of Geophysical Research: Solid Earth, v. 105, p. 21445–21456, doi:10.1029/2000JB900167.